

What the president's budget
means for science p. 599

Making the most of student
lab experiences p. 627

How oxygen lends strength
to titanium p. 635

Science

\$10
6 FEBRUARY 2015
sciencemag.org

AAAS



Grassland guardians

Termite mounds help dryland
habitats resist climate change

pp. 597 & 651

CONTENTS

6 FEBRUARY 2015 • VOLUME 347 • ISSUE 6222



612

How do neurons “code” for space?

NEWS

IN BRIEF

590 Roundup of the week's news

IN DEPTH

593 SEAFLOOR GROOVES RECORD THE BEAT OF THE ICE AGES

Sea level changes influence the underwater eruptions that build abyssal hills *By E. Hand*

► REPORT BY CROWLEY ET AL.
10.1126/science.1261508

594 U.S. HOUSE REVEALS AMBITIOUS BIOMEDICAL INNOVATION PLAN

Lawmakers seek feedback on “21st Century Cures” proposal *By K. Servick*

595 MISFIRE ASIDE, SIGNS OF COSMIC INFLATION COULD COME SOON

Even as the BICEP result bites the dust, observers like their chances of spotting big-bang gravitational waves *By A. Cho*

596 AFRICA'S SOIL ENGINEERS: TERMITES

Kenyan plots show that termite mounds promote ecological health and may slow desertification *By E. Pennisi*

► REPORT P. 651

598 JAPANESE NEUTRINO PHYSICISTS THINK REALLY BIG

Hyper-Kamiokande would be the largest neutrino detector ever *By D. Normile*

599 BUDGET FOR 2016 ACCENTUATES THE PRACTICAL

White House proposal lifts (almost) all boats, but applied research floats to the top *By J. Mervis*

601 Biomedical initiatives get top billing in budget rollout

By J. Kaiser and K. Servick

FEATURE

602 A CLASSROOM EXPERIMENT

NSF has spent \$500 million to train thousands of science and math teachers. But what has that meant for kids?

By J. Mervis

INSIGHTS

PERSPECTIVES

606 WHERE IS SILICON VALLEY?

Forecasting and mapping entrepreneurial quality

By J. Guzman and S. Stern

609 THERE GOES THE MACROPHAGE NEIGHBORHOOD

Migrating dendritic cells disrupt lymph node macrophages and limit the immune response to secondary infection *By H. D. Hickman*

► REPORT P. 667

611 TAKING TEMPERATURE AT THE NANOSCALE

A local probe technique can determine temperature with nanometer-scale resolution *By C. Collier*

► REPORT P. 629

612 OUR SKEWED SENSE OF SPACE

The distribution of neuron activity reveals an organization that supports the brain's spatial mapping capacity

By G. Buzsáki

► PODCAST

614 A MEGAGE FOR PLURIPOTENCY

Methylation of messenger RNA on the adenine base is critical for stem cell commitment and differentiation

By H. G. Stunnenberg et al.

615 THE COORDINATION CHEMISTRY OF NANOCRYSTAL SURFACES

The luminescence and electronic properties of inorganic nanocrystals depend on surface-layer structure

By J. Owen

616 HOW A VIRUS TRAVELS THE WORLD

Wild birds may spread the H5N8 virus

By J. H. Verhagen et al.



BOOKS ET AL.

618 LIFE ON DISPLAY

By K. A. Rader and V. E. M. Cain, reviewed by K. R. Johnson

619 I THINK YOU'LL FIND IT'S A BIT MORE COMPLICATED THAN THAT

By B. Goldacre, reviewed by J. Best

LETTERS

620 THE CURTAILED CAREERS OF WOMEN IN CHINA

By C. Yan

620 CONVERTING BIG DATA INTO PUBLIC HEALTH

By I. C.-H. Fung et al.

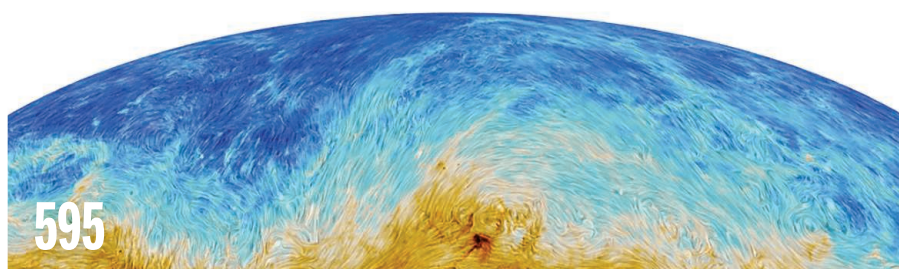
620 COMMON DISEASES IN CHINA OVERLOOKED

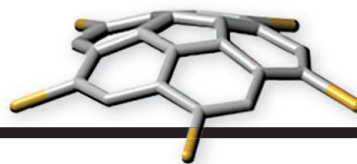
By X.-Z. Shan

621 NEXTGEN VOICES: LAST CALL

621 TECHNICAL COMMENT ABSTRACTS

Science Staff	586
Information for Authors.....	678
New Products.....	680
Science Careers	681





RESEARCH

IN BRIEF

623 From *Science* and other journals

REVIEW

627 EDUCATION

Undergraduate research experiences: Impacts and opportunities *M. C. Linn et al.*

REVIEW SUMMARY; FOR FULL TEXT:

dx.doi.org/10.1126/science.1261757

RESEARCH ARTICLE

628 EXPRESSION PROFILING

Combinatorial labeling of single cells for gene expression cytometry *H. C. Fan et al.*

RESEARCH ARTICLE SUMMARY; FOR FULL TEXT:

dx.doi.org/10.1126/science.1258367

REPORTS

629 THERMAL MEASUREMENT

Nanoscale temperature mapping in operating microelectronic devices *M. Mecklenburg et al.*

► PERSPECTIVE P. 611



632 EXOPLANET DYNAMICS

Asynchronous rotation of Earth-mass planets in the habitable zone of lower-mass stars *J. Leconte et al.*

635 METALLURGY

Origin of dramatic oxygen solute strengthening effect in titanium *Q. Yu et al.*

639 DNA NANOTECHNOLOGY

Programming colloidal phase transitions with DNA strand displacement *W. B. Rogers and V. N. Manoharan*

643 CARBON RADICALS

Direct observation and kinetics of a hydroperoxyalkyl radical (QOOH) *J. D. Savee et al.*

646 NONCOVALENT ASSEMBLY

A rational strategy for the realization of chain-growth supramolecular polymerization *J. Kang et al.*

651 ECOLOGICAL FEEDBACKS

Termite mounds can increase the robustness of dryland ecosystems to climatic change *J. A. Bonachela et al.*

► NEWS STORY P. 596

655 PLANT DEVELOPMENT

Genetic control of distal stem cell fate within root and embryonic meristems *B. C. W. Crawford et al.*

659 ADDICTION THERAPY

Refining deep brain stimulation to emulate optogenetic treatment of synaptic pathology *M. Creed et al.*

664 GENOMIC VARIATION

Impact of regulatory variation from RNA to protein *A. Battle et al.*

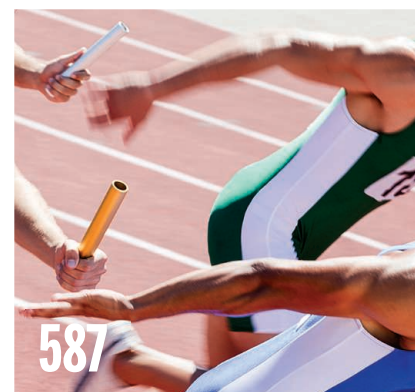
667 HOST RESPONSE

Inflammation-induced disruption of SCS macrophages impairs B cell responses to secondary infection *M. Gaya et al.*

► PERSPECTIVE P. 609

673 PROTEIN EVOLUTION

Pervasive degeneracy and epistasis in a protein-protein interface *A. I. Podgornaia and M. T. Laub*



DEPARTMENTS

587 EDITORIAL

Passing the CEO baton
By Alan I. Leshner

686 WORKING LIFE

Science by any means necessary
By Rachel Bernstein

ON THE COVER



Termite mounds (shown here in the Tanami Desert, Australia) are ubiquitous in tropical grasslands and savannas, where they generate distinctive spatial patterns and influence key

ecological processes. These regularly spaced mounds are often resource-rich relative to surrounding soils, enhancing plant growth on and/or around the mounds. Mathematical models show that these local enhancements can reduce the susceptibility of arid ecosystems to catastrophic desertification following drought. See pages 596 and 651.

Photo: © William D. Bachman/
Science Source

Editor-in-Chief Marcia McNutt

Executive Editor Monica M. Bradford **News Editor** Tim Appenzeller

Managing Editor, Research Journals Katrina L. Kelner

Deputy Editors Barbara R. Jasny, Andrew M. Sugden(UK), Valda J. Vinson, Jake S. Yeston

Research and Insights

SR. EDITORS Caroline Ash(UK), Gilbert J. Chin, Lisa D. Chong, Maria Cruz(UK), Julia Fahrenkamp-Uppenbrink(UK), Pamela J. Hines, Stella M. Hurtley(UK), Paula A. Kiberstis, Marc S. Lavine(Canada), Kristen L. Mueller, Ian S. Osborne(UK), Beverly A. Purnell, L. Bryan Ray, Guy Riddihough, H. Jesse Smith, Jelena Stajic, Peter Stern(UK), Phillip D. Szurmi, Brad Wible, Nicholas S. Wigginton, Laura M. Zahn **ASSOCIATE EDITORS** Brent Grocholski, Melissa R. McCartney, Margaret M. Moerchen, Sacha Vignieri **ASSOCIATE BOOK REVIEW EDITOR** Valerie B. Thompson **ASSOCIATE LETTERS EDITOR** Jennifer Sills **CHIEF CONTENT PRODUCTION EDITOR** Cara Tate **SR. CONTENT PRODUCTION EDITORS** Harry Jach, Trista Wagoner **CONTENT PRODUCTION EDITORS** Jeffrey E. Cook, Chris Filiatreau, Cynthia Howe, Lauren Kmec, Barbara P. Ordway **SR. EDITORIAL COORDINATORS** Carolyn Kyle, Beverly Shields **EDITORIAL COORDINATORS** Ramatoulaye Diop, Joi S. Granger, Lisa Johnson, Anita Wynn **PUBLICATIONS ASSISTANTS** Aneera Dobbins, Jeffrey Hearn, Dona Mathieu, Le-Toya Mayne Flood, Shannon McMahon, Scott Miller, Jerry Richardson, Rachel Roberts(UK), Alice Whaley(UK), Brian White **EXECUTIVE ASSISTANT** Anna Bashkirova **ADMINISTRATIVE SUPPORT** Janet Clements(UK), Michael Crabtree(UK, Intern), Lizanne Newton(UK), Maryrose Madrid, John Wood(UK)

News

NEWS MANAGING EDITOR John Travis **INTERNATIONAL EDITOR** Richard Stone **DEPUTY NEWS EDITORS** Daniel Clery(UK), Robert Coontz, Elizabeth Culotta, David Grimm, David Malakoff, Leslie Roberts **CONTRIBUTING EDITORS** Martin Enserink(Europe), Mara Hvistendahl **SR. CORRESPONDENTS** Jeffrey Mervis, Elizabeth Pennisi **NEWS WRITERS** Adrian Cho, Jon Cohen, Jennifer Couzin-Frankel, Carolyn Gramling, Eric Hand, Jocelyn Kaiser, Kelly Servick, Robert F. Service, Erik Stokstad(Cambridge, UK), Emily Underwood **INTERNS** Emily Conover, David Shultz, Jia You **CONTRIBUTING CORRESPONDENTS** Pallava Bagla(South Asia), Michael Balter(Paris), John Bohannon, Ann Gibbons, Sam Kean, Richard A. Kerr, Eli Kintisch, Kai Kupferschmidt(Berlin), Andrew Lawler, Christina Larson(Beijing), Mitch Leslie, Charles C. Mann, Eliot Marshall, Virginia Morell, Dennis Normile(Tokyo), Heather Pringle, Tania Rabesandratana(Brussels), Gretchen Vogel(Berlin), Lizzie Wade(Mexico City) **CAREERS** Jim Austin(Editor), Donisha Adams, Rachel Bernstein **COPY EDITORS** Kara Estelle, Nora Kelly, Jennifer Levin **ADMINISTRATIVE SUPPORT** Scherraine Mack

Executive Publisher Alan I. Leshner

Publisher Kent R. Anderson **Chief Digital Media Officer** Rob Covey

BUSINESS OPERATIONS AND ADMINISTRATION DIRECTOR Deborah Rivera-Wienhold **BUSINESS SYSTEMS AND FINANCIAL ANALYSIS DIRECTOR** Randy Yi **MANAGER OF FULFILLMENT SYSTEMS** Neal Hawkins **SYSTEMS ANALYST** Nicole Mehmedovich **ASSISTANT DIRECTOR, BUSINESS OPERATIONS** Eric Knott **MANAGER, BUSINESS OPERATIONS** Jessica Tierney **BUSINESS ANALYSTS** Cory Lipman, Cooper Tilton, Celeste Troxler **FINANCIAL ANALYST** Jeremy Clay **RIGHTS AND PERMISSIONS ASSISTANT DIRECTOR** Emilie David **PERMISSIONS ASSOCIATE** Elizabeth Sandler **RIGHTS, CONTRACTS, AND LICENSING ASSOCIATE** Lili Kiser

MARKETING DIRECTOR Ian King **MARKETING MANAGER** Julianne Wielga **MARKETING ASSOCIATE** Elizabeth Sattler **SR. MARKETING EXECUTIVE** Jennifer Reeves **SR. ART ASSOCIATE, PROJECT MANAGER** Izeitel Sorrosa **ART ASSOCIATE** Seil Lee **ASSISTANT COMMERCIAL EDITOR** Selby France **MARKETING PROJECT MANAGER** Angelissa McArthur **SR. WRITER** Bill Zimmer **PROGRAM DIRECTOR, AAAS MEMBER CENTRAL** Peggy Mihelich **FULFILLMENT SYSTEMS AND OPERATIONS** membership@aaas.org **MANAGER, MEMBER SERVICES** Pat Butler **SPECIALISTS** LaToya Casteel, Javia Flemmings, Latasha Russell **OPERATIONS, DATA ENTRY** Mickey Napoleoni **DATA ENTRY SPECIALISTS** JJ Regan, Jaimee Wise, Fiona Giblin **DIRECTOR, SITE LICENSING** Tom Ryan **DIRECTOR, CORPORATE RELATIONS** Eileen Bernadette Moran **SR. PUBLISHER RELATIONS SPECIALIST** Kiki Forsythe **PUBLISHER RELATIONS MANAGER** Catherine Holland **PUBLISHER RELATIONS, EASTERN REGION** Keith Layson **PUBLISHER RELATIONS, WESTERN REGION** Ryan Rexroth **MANAGER, SITE LICENSE OPERATIONS** Iquo Edim **FULFILLMENT ANALYST** Lana Guz **ASSOCIATE DIRECTOR, MARKETING** Christina Schlecht **MARKETING ASSOCIATES** Thomas Landreth, Minah Kim

DIRECTOR OF WEB TECHNOLOGIES Ahmed Khadr **SR. DEVELOPER** Chris Coleman **DEVELOPERS** Dan Berger, Jimmy Marks **SR. PROJECT MANAGER** Trista Smith **SYSTEMS ENGINEER** Luke Johnson **PRODUCT MANAGER** Walter Jones

CREATIVE DIRECTOR, MULTIMEDIA Martyn Green **DIRECTOR OF ANALYTICS** Enrique Gonzales **SR. WEB PRODUCER** Sarah Crespi **WEB PRODUCER** Alison Crawford **VIDEO PRODUCER** Nguyen Nguyen **SOCIAL MEDIA PRODUCER** Meghna Sachdev

DIRECTOR OF OPERATIONS PRINT AND ONLINE Elizabeth Harman **DIGITAL/PRINT STRATEGY MANAGER** Jason Hillman **QUALITY TECHNICAL MANAGER** Marcus Spiegel **DIGITAL PRODUCTION MANAGER** Lisa Stanford **ASSISTANT MANAGER DIGITAL/PRINT** Rebecca Doshi **DIGITAL MEDIA SPECIALIST** Tara Kelly **SENIOR CONTENT SPECIALISTS** Steve Forrester, Antoinette Hodal, Lori Murphy, Anthony Rosen **CONTENT SPECIALISTS** Jacob Hedrick, Kimberley Oster

DESIGN DIRECTOR Beth Rakouskas **DESIGN EDITOR** Marcy Atarod **SENIOR SCIENTIFIC ILLUSTRATORS** Chris Bickel, Katharine Sutliff **SCIENTIFIC ILLUSTRATOR** Valerie Altounian **SENIOR ART ASSOCIATES** Holly Bishop, Preston Huey **SENIOR DESIGNER** Garvin Grullón **DESIGNER** Chrystal Smith **SENIOR PHOTO EDITOR** William Douthitt **PHOTO EDITOR** Leslie Blizard

DIRECTOR, GLOBAL COLLABORATION, CUSTOM PUBLICATIONS, ADVERTISING Bill Moran **EDITOR, CUSTOM PUBLISHING** Sean Sanders: 202-326-6430 **ASSISTANT EDITOR, CUSTOM PUBLISHING** Tianna Hicklin: 202-326-6463 **ADVERTISING MARKETING MANAGER** Justin Sawyers: 202-326-7061 **science_advertising@aaas.org** **ADVERTISING MARKETING ASSOCIATE** Javia Flemmings **ADVERTISING SUPPORT MANAGER** Karen Foote: 202-326-6740 **ADVERTISING PRODUCTION OPERATIONS MANAGER** Deborah Tompkins **SR. PRODUCTION SPECIALIST/GRAPHIC DESIGNER** Amy Hardcastle **PRODUCTION SPECIALIST** Yuse Lajiminmuhip **SR. TRAFFIC ASSOCIATE** Christine Hall **SALES COORDINATOR** Shirley Young **ASSOCIATE DIRECTOR, COLLABORATION, CUSTOM PUBLICATIONS/CHINA/TAIWAN/KOREA/SINGAPORE** Ruolei Wu: +86-186 0822 9345, rwu@aaas.org **COLLABORATION/CUSTOM PUBLICATIONS/JAPAN** Adarsh Sandhu + 81532-81-5142 asandhu@aaas.org **EAST COAST/E. CANADA** Laurie Faraday: 508-747-9395, FAX 617-507-8199 **WEST COAST/W. CANADA** Lynne Stickrod: 415-931-9782, FAX 415-520-6940 **MIDWEST** Jeffrey Dembski: 847-498-4520 x3005, Steven Loerch: 847-498-4520 x3006 **UK EUROPE/ASIA** Roger Goncalves: TEL/FAX +41 43 243 1358 **JAPAN** Katsuyoshi Fukamizu(Tokyo): +81-3-3219-5777 fukamizu@aaas.org **CHINA/TAIWAN** Ruolei Wu: +186-0082-9345

WORLDWIDE ASSOCIATE DIRECTOR OF SCIENCE CAREERS Tracy Holmes: +44 (0) 1223 326525, FAX +44 (0) 1223 326532 tholmes@science-int.co.uk **CLASSIFIED** advertise@sciencecareers.org **U.S. SALES** Tina Burks: 202-326-6577 Nancy Toema: 202-326-6578 **SALES ADMINISTRATOR** Marci Gallun **EUROPE/ROW SALES** Axel Gesatzki, Sarah Lehard **SALES ASSISTANT** Kelly Grace **JAPAN** Hiroyuki Mashiki(Kyoto): +81-75-823-1109 hmashiki@aaas.org **CHINA/TAIWAN** Ruolei Wu: +86-186 0082 9345 rwu@aaas.org **MARKETING MANAGER** Allison Pritchard **MARKETING ASSOCIATE** Aimee Aponte

AAAS BOARD OF DIRECTORS **RETIRING PRESIDENT, CHAIR** Phillip A. Sharp **PRESIDENT** Gerald R. Fink **PRESIDENT-ELECT** Geraldine (Geri) Richmond **TREASURER** David Evans **SHAW CHIEF EXECUTIVE OFFICER** Alan I. Leshner **BOARD** Bonnie L. Bassler, May R. Berenbaum, Carlos J. Bustamante, Claire M. Fraser, Laura H. Greene, Elizabeth Loftus, Raymond Orbach, Inder M. Verma

SUBSCRIPTION SERVICES For change of address, missing issues, new orders and renewals, and payment questions: 866-434-AAAS (2227) or 202-326-6417, FAX 202-842-1065. Mailing addresses: AAAS, P.O. Box 96178, Washington, DC 20090-6178 or AAAS Member Services, 1200 New York Avenue, NW, Washington, DC 20005

INSTITUTIONAL SITE LICENSES 202-326-6755 **REPRINTS:** Author Inquiries 800-635-7181 **COMMERCIAL INQUIRIES** 803-359-4578 **PERMISSIONS** 202-326-6765, permissions@aaas.org **AAAS Member Services** 202-326-6417 or http://membercentral.aaas.org/discouints

Science serves as a forum for discussion of important issues related to the advancement of science by publishing material on which a consensus has been reached as well as including the presentation of minority of conflicting points of view. Accordingly, all articles published in Science—including editorials, news and comment, and books reviews—are signed and reflect the individual views of the authors and not official points of view adopted by AAAS or the institutions with which the authors are affiliated.

INFORMATION FOR AUTHORS See pages 678 and 679 of the 6 February 2015 issue or access www.sciencemag.org/about/authors

SENIOR EDITORIAL BOARD

A. Paul Alivisatos, Lawrence Berkeley Nat'l Laboratory, Ernst Fehr, U. of Zürich
Susan M. Rosenberg, Baylor College of Medicine, Ali Shalithard, Northwestern University
Feinberg School of Medicine, Michael S. Turner, U. of Chicago

BOARD OF REVIEWING EDITORS (Statistics board members indicated with \$)

Adriano Aguzzi, U. Hospital Zürich
Takuzo Aida, U. of Tokyo
Leslie Aiello, Wenner-Gren Foundation
Judith Allen, U. of Edinburgh
Sonia Altizer, U. of Georgia
Sebastian Amigorena, Institut Curie
Kathryn Anderson, Memorial Sloan-Kettering Cancer Center
Meinrat O. Andreae, Max-Planck Inst. Mainz
Paola Arlotta, Harvard U.
Johan Auwerx, EPFL
David Awschalom, U. of Chicago
Jordi Bascompte, Estación Biológica de Doñana CSIC
Facundo Batista, London Research Inst.
Ray H. Baughman, U. of Texas, Dallas
David Baum, U. of Wisconsin
Carlo Beenakker, Leiden U.
Kamran Behnia, ESPCI-ParisTech
Yasmine Belkaid, NIAID, NIH
Philip Benfey, Duke U.
Stephen J. Benkovic, Penn State U.
May Berenbaum, U. of Illinois
Gabriele Bergers, U. of California, San Francisco
Bradley Bernstein, Massachusetts General Hospital
Peer Bork, EMBL
Bernard Bourdon, Ecole Normale Supérieure de Lyon
Chris Bowler, Ecole Normale Supérieure
Ian Boyd, U. of St. Andrews
Emily Brodsky, U. of California, Santa Cruz
Ron Brookmeyer, U. of California Los Angeles (\$) **Christian Büchel**, U. Hamburg-Eppendorf
Joseph A. Burns, Cornell U.
Gyorgy Buzsaki, New York U. School of Medicine
Blanche Capel, Duke U.
Mats Carlsson, U. of Oslo
David Clapham, Children's Hospital Boston
David Clary, U. of Oxford
Joel Cohen, Rockefeller U., Columbia U.
Jonathan D. Cohen, Princeton U.
James Collins, Boston U.
Robert Cook-Deegan, Duke U.
Alan Cowman, Walter & Eliza Hall Inst.
Robert H. Crabtree, Yale U.
Roberta Croce, Vrije Universiteit
Janet Currie, Princeton U.
Jeff L. Dangl, U. of North Carolina
Tom Daniel, U. of Washington
Frans de Waal, Emory U.
Stanislas Dehaene, Collège de France
Robert Desimone, MIT
Claude Desplan, New York U.
Ap Dijksterhuis, Radboud U. of Nijmegen
Dennis Discher, U. of Pennsylvania
Gerald W. Dorn II, Washington U. School of Medicine
Jennifer A. Doudna, U. of California, Berkeley
Bruce Dunn, U. of California, Los Angeles
Christopher Dye, WHO
Todd Ehlers, U. of Tuebingen
David Ehrhardt, Carnegie Inst. of Washington
Tim Elston, U. of North Carolina at Chapel Hill
Gerhard Ertl, Fritz-Haber-Institut, Berlin
Barry Everitt, U. of Cambridge
Ernst Fehr, U. of Zurich
Anne C. Ferguson-Smith, U. of Cambridge
Michael Feuer, The George Washington U.
Kate Fitzgerald, U. of Massachusetts
Peter Fratzl, Max-Planck Inst.
Elaine Fuchs, Rockefeller U.
Daniel Geschwind, UCLA
Andrew Gewirth, U. of Illinois
Karl-Heinz Glassmeier, TU Braunschweig
Ramon Gonzalez, Rice U.
Julia R. Greer, Caltech
Elizabeth Grove, U. of Chicago
Nicolas Gruber, ETH Zurich
Kip Guy, St. Jude's Children's Research Hospital
Taekjip Ha, U. of Illinois at Urbana-Champaign
Christian Haass, Ludwig Maximilians U.
Steven Hahn, Fred Hutchinson Cancer Research Center
Michael Hasselmo, Boston U.
Martin Heimann, Max-Planck Inst. Jena
Yia Helariutta, U. of Cambridge
James A. Hendler, Rensselaer Polytechnic Inst.
Janet G. Hering, Swiss Fed. Inst. of Aquatic Science & Technology
Kai-Uwe Hinrichs, U. of Bremen
Kei Hirose, Tokyo Inst. of Technology
David Hodell, U. of Cambridge
David Holden, Imperial College
Lora Hooper, UT Southwestern Medical Ctr. at Dallas
Raymond Huey, U. of Washington
Steven Jacobson, U. of California, Los Angeles
Kai Jonsson, EPFL Lausanne
Peter Jonas, Inst. of Science & Technology (IST) Austria
Matt Kaebelrein, U. of Washington
William Kaelin Jr., Dana-Farber Cancer Inst.
Daniel Kahne, Harvard U.
Daniel Kammen, U. of California, Berkeley
Masashi Kawasaki, U. of Tokyo
Joel Kingsolver, U. of North Carolina at Chapel Hill
Robert Kingston, Harvard Medical School
Etienne Kochlin, Ecole Normale Supérieure
Alexander Koldkin, Johns Hopkins U.
Alberto R. Kornblitt, U. of Buenos Aires
Leonid Kruglyak, UCLA
Thomas Langer, U. of Cologne
Mitchell A. Lazar, U. of Pennsylvania
David Lazer, Harvard U.
Thomas Lecuit, IBDM
Virginia Lee, U. of Pennsylvania
Stanley Lemon, U. of North Carolina at Chapel Hill
Ottoline Leyser, Cambridge U.
Marcia C. Linn, U. of California, Berkeley
Guangbo Liu, Michigan State U.
Luis Liz-Marzan, CIC biomaGUNE
Jonathan Losos, Harvard U.
Ke Lu, Chinese Acad. of Sciences
Christian Lüscher, U. of Geneva
Laura Machesky, CRUK Beaton Inst. for Cancer Research
Aime Magurran, U. of St. Andrews
Oscar Marin, CSIC & U. Miguel Hernández
Charles Marshall, U. of California, Berkeley
C. Robertson McClung, Dartmouth College
Graham Medley, U. of Warwick
Yasushi Miyashita, U. of Tokyo
Mary Ann Moran, U. of Georgia
Richard Morris, U. of Edinburgh
Alison Motsinger-Reif, NC State U. (\$) **Sean Munro**, CSIC & U. of Molecular Biology
Thomas Murray, The Hastings Center
James Nelson, Stanford U. School of Med.
Daniel Neumark, U. of California, Berkeley
Timothy W. Nilsen, Case Western Reserve U.
Pär Nordlund, Karolinska Inst.
Heila Nowotny, European Research Advisory Board
Ben Oken, MIT
Joe Orenstein, U. of California
Berkeley & Lawrence Berkeley National Lab
Harry Orr, U. of Minnesota
Andrew Oswald, U. of Warwick
Steve Palumbi, Stanford U.
Jane Parker, Max-Planck Inst. of Plant Breeding Research
Giovanni Parmigiani, Dana-Farber Cancer Inst. (\$) **Donald R. Paul**, U. of Texas, Austin
John H. J. Petrini, Memorial Sloan-Kettering Cancer Center
Joshua Plotkin, U. of Pennsylvania
Alfred Polman, FOM Institute AMOLF
Philippe Poulin, CNRS
Jonathan Pritchard, Stanford U.
David Randall, Colorado State U.
Colin Renfrew, U. of Cambridge
Felix Rey, Institut Pasteur
Trevor Robbins, U. of Cambridge
Jim Roberts, Fred Hutchinson Cancer Research Ctr.
Barbara A. Romanowicz, U. of California, Berkeley
Jens Rostrup-Nielsen, Haldor Topsøe
Mike Ryan, U. of Texas, Austin
Mitinori Saitou, Kyoto U.
Shimon Sakaguchi, Kyoto U.
Miquel Salmeron, Lawrence Berkeley National Lab
Jürgen Sandkühler, Medical U. of Vienna
Alexander Schier, Harvard U.
Randy Seeley, U. of Cincinnati
Vladimir Shalae, Purdue U.
Robert Siliciano, Johns Hopkins School of Medicine
Joseph Silk, Institut d'Astrophysique de Paris
Denis Simion, Arizona State U.
Alison Smith, John Innes Centre
Richard Smith, U. of North Carolina (\$) **John Speakman**, U. of Aberdeen
Allan C. Spradling, Carnegie Institution of Washington
Jonathan Sprent, Garvan Inst. of Medical Research
Eric Steig, U. of Washington
Paula Stephan, Georgia State U. and National Bureau of Economic Research
Molly Stevens, Imperial College London
V. S. Subrahmanian, U. of Maryland
Ira Tabas, Columbia U.
Sarah Teichmann, Cambridge U.
John Thomas, North Carolina State U.
Shubha Tole, Tata Institute of Fundamental Research
Christopher Tyler-Smith, The Wellcome Trust Sanger Inst.
Herbert Virgin, Washington U.
Bernd Vogelstein, Johns Hopkins U.
Cynthia Volkert, U. of Göttingen
Douglas Wallace, Dalhousie U.
David Wallace, Weizmann Inst. of Science
Ian Walsmsley, U. of Oxford
David A. Wardle, Swedish U. of Agric. Sciences
David Waxman, Fudan U.
Jonathan Weissman, U. of California, San Francisco
Chris Wickle, U. of Missouri (\$) **Ian A. Wilson**, The Scripps Res. Inst. (\$) **Timothy D. Wilson**, U. of Virginia
Rosemary Wyse, Johns Hopkins U.
Jan Zaenen, Leiden U.
Kenneth Zaret, U. of Pennsylvania School of Medicine
Jonathan Zehr, U. of California, Santa Cruz
Len Zon, Children's Hospital Boston
Maria Zuber, MIT

BOOK REVIEW BOARD

David Bloom, Harvard U. Samuel Bowring, MIT, Angela Creager, Princeton U., Richard Swedder, U. of Chicago, Ed Wasserman, DuPont

Passing the CEO baton

As I retire from the office of chief executive of the American Association for the Advancement of Science (AAAS) and pass the baton to my very capable successor, physicist and former U.S. congressman Rush Holt, I have been reflecting on changes over the past decades both within the scientific enterprise and in its relationship with the rest of society. Many trends are cause for celebration, but others require remedial attention. On the positive side, new technologies have enabled new and very important scientific questions to be confronted, and a rise in collaborative, multidisciplinary science has fueled a remarkable pace of discovery. Science is also becoming more global in character as more countries invest in science and technology and fortify their infrastructures and science capacities. Science has never been more productive. And yet, the overall climate for science is more difficult than I have ever seen in my scientific career. This stunning state of contradiction indicates that there has never been a greater need, or a greater opportunity, for an international organization such as AAAS, whose mission is to advance science and serve society.

The pressures on the scientific enterprise are well known. In the United States, for example, federal support for research and development has fallen 16% in inflation-adjusted dollars from 2010 to 2015. The situation is similar in many other countries, although some emerging economies are enjoying large increases in science funding. At the same time, launching an independent academic research career has been taking longer, the result of constrained funding and a scarcity of jobs. For example, most U.S. investigators now get their first independent research grant when they are in their late 30s or early 40s. It is not surprising that many talented young scientists are abandoning the idea of a research career altogether.

Added to this, the relationship between scientists and

the rest of the public seems to be slipping backward.* Climate change, genetically modified foods, and the teaching of evolution are among topics that now trigger unproductive tension in the fragile relationship between the scientific community and the rest of society. A weakened science-society relationship not only undermines public support for science but also makes it difficult for science to contribute to the solutions of societal problems. This

is a no-win situation from every angle, and AAAS and many disciplinary societies have sought to address this problem through an array of public-engagement activities. These efforts include helping scientists to become better public communicators and providing forums through which scientists can work with members of the public on finding solutions to tension-provoking issues.

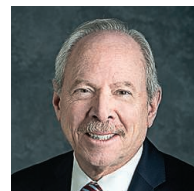
There have been many voices on this page over the years that have called for the scientific community to become more involved in nurturing a public that is receptive to science. As AAAS holds its annual meeting next week in San Jose, California, it is my hope for the organization that moving forward, all of its members and constituents will take this call to heart and

continue to pursue ambitious goals, embrace a spirit of innovation, and work with the greater scientific establishment not only to tackle the most pressing problems of the day but also to build a societal culture that champions science and thrives on the rewards of strong science-society relations. AAAS members are an untapped source of influence. By responding to calls to be involved in advocacy efforts, volunteering to serve on advisory committees, and engaging with the organization to shape its future programs and initiatives, members have the potential to turn the tide and bring the full benefits of science to society. Rush Holt is an ideal person to lead this organization, and I pass the executive officer baton to him with great confidence.

— Alan I. Leshner



“...members have the potential to turn the tide and bring the full benefits of science to society.”



Alan I. Leshner is the Chief Executive Officer of AAAS and Executive Publisher of Science.

*A. I. Leshner, *Science* **347**, 459 (2015).

“It’s pretty funny that the ideal gas law is making headlines.”

Physicist Max Tegmark of the Massachusetts Institute of Technology to *The New York Times*, on the finding that weather conditions, not tampering, reduced pressure in footballs during a playoff game.

IN BRIEF

A new eye on water in the soil

NASA’s soil moisture probe launched last week.

Globally, soils hold a tiny fraction of Earth’s water. But that moisture is crucial to water, carbon, and energy cycles: It determines how vulnerable regions are to drought and flood, how well plants grow and suck up atmospheric carbon, and how Earth heats up and cools off—a key driver for storms. Despite its importance, soil moisture has been monitored mostly by a sparse set of probes stuck in the ground. But the launch on 31 January of NASA’s Soil Moisture Active Passive probe, a \$916 million satellite, promises to change that. The mission will generate a global map of soil moisture every 2 to 3 days at a resolution of 10 kilometers, helping improve weather forecasts, flood forecasts, and drought monitoring. “This is an important factor that people have been chasing from the earliest days of optical remote sensing,” says hydrologist Dara Entekhabi of the Massachusetts Institute of Technology in Cambridge, the science team leader for the mission. <http://scim.ag/SMAPlaunch>

AROUND THE WORLD

Myriad gives up gene patent fight

SALT LAKE CITY | The molecular diagnostics company Myriad Genetics has put an end to a long battle to defend its controversial patents on genetic tests for cancer risk. Several of the companies Myriad was suing for patent infringement announced settlements last week, and the company said that it plans to settle the remaining suits. The Supreme Court in 2013 invalidated many of the company’s key patents by declaring human genes unpatentable. But Myriad still sued several companies, including LabCorp and Ambry Genetics, claiming that certain patents remain valid. A federal district court last March rejected Myriad’s request for an injunction blocking Ambry from selling its test, and the U.S. Court of Appeals for the Federal Circuit in Washington, D.C., upheld the decision in December.

Police search German institute

TÜBINGEN, GERMANY | An ongoing investigation into alleged mistreatment of rhesus macaques at the Max Planck Institute for Biological Cybernetics led to a police search of the facility on 29 January and seizure of documents related to animal care and treatment. In September, a television program that included video shot at the institute by an undercover animal rights activist triggered protests and several investigations. An inquiry by the Max Planck Society found “no serious shortcomings” in animal care. And on 16 January the state of Baden-Württemberg said it so far had found no reason to revoke the institute’s animal research licenses. Investigators with the local prosecutor’s office are now analyzing more than 100 hours of film as well as detailed experimental records.

Tamiflu helps, new study finds

BASEL, SWITZERLAND | Last week saw the latest—though likely not last—salvo over the merits of the influenza-fighting drug Tamiflu, produced by the pharmaceutical company Roche. Blending data from nine clinical trials of more than 4000 patients, Roche-funded researchers found that

BY THE NUMBERS

66

Percentage of Americans who would be more likely to vote for a candidate who says that global warming is real and is anthropogenic, according to a poll in *The New York Times*.

35

Millimeters per year that Iceland is rising due to isostatic rebound as its glaciers melt.

>50

Percentage of people born since 1960 who will develop cancer in their lifetime, according to a new study in the *British Journal of Cancer*.



Qijianglong lived in Asia with other long-necked cousins.

New dino really stuck its neck out

Many plant-eating dinosaurs had long necks, but none more impressive than the mamenchisaurids, a group of dinos that once roamed Asia. Last week, researchers reported the discovery of a new species of mamenchisaurid in southern China. Dubbed *Qijianglong guokr* (“Qijian” after the district in which it was found, “long” for dragon in Chinese, and “Guokr” for the name of a Chinese organization that supports paleontology research in Qijian), the beast’s neck made up about half of its total 15-meter length, the team reported online in the *Journal of Vertebrate Paleontology*. The 160-million-year-old skeleton is impressively well preserved: All 17 of its neck vertebrae were found, as was much of its skull. Unique among mamenchisaurids, the dinosaur’s porous vertebrae were filled with air while *Qijianglong* was alive, so its neck would have been unusually light and versatile.

Tamiflu reduces the risk of hospital admission from flu by 63%, and the drug’s use is associated with fewer cases of lower respiratory tract infections such as bronchitis. The new findings, published online on 29 January in *The Lancet*, haven’t swayed skeptics. “There are no new data presented here on complications or hospitalizations that we did not already know of,” says epidemiologist Peter Doshi of the University of Maryland School of Pharmacy in Baltimore, who belongs to the Cochrane Collaboration, an international network of scientists that has been highly critical of Tamiflu’s benefits. <http://scim.ag/tamihelp>

Fire guts academy library

MOSCOW | A fire at the Institute of Scientific Information on Social Sciences (INION) in Moscow last weekend destroyed a substantial part of its library. After breaking out on Friday night, the fire lasted more than 25 hours; researchers are describing the damage to the library’s collection of documents and books on social sciences as “catastrophic.” Vladimir Fortov, president of the Russian Academy of Sciences, puts the

losses at “about 20% of the unique scientific works that were kept in hard copies,” and others say they could be higher. Fortunately, fire brigades managed to confine the fire and save the main depository, which contains 14 million documents, including some in ancient languages and rare editions dating back to as early as the 16th century. <http://scim.ag/Russlib>



The academy fire burned for more than a day.

Boom times for academic charity

NEW YORK CITY | U.S. colleges received a record-setting amount of philanthropic gifts in 2014. And thanks to a strong stock market, the size of their endowments also soared. Two studies out last week documented those positive trends: Colleges and universities raised \$37.5 billion, and

their endowments grew by an average of 15.5%. The studies also showed that the rich got a lot richer last year: Nearly one-fourth of all donations went to only 20 colleges. Harvard University, the leader in both categories, brought in nearly \$1.2 billion in contributions and its endowment reached a new high of \$35.9 billion, some \$10 billion above the second-place University of Texas (UT) system. UT Austin raised \$529 million last year. By comparison, the median endowment size for the 832 schools surveyed was \$110 million.

Windfall for pediatric research

BETHESDA, MARYLAND | The National Institutes of Health (NIH) is scrambling to spend an unexpected \$150 million windfall for pediatric research by this fall. In December, NIH received the first installment of a 10-year, \$126 million research initiative created in memory of a 10-year-old girl who died of cancer. That same month, NIH ended its controversial National Children's Study of the environmental factors affecting a child's development and began looking for other uses for the \$165 million it had just received from Congress to continue the study. Research funded by the unforeseen bonanza will capitalize on technologies that can collect and analyze vast amounts of information on the children being studied, NIH officials told an outside advisory panel last week. <http://scim.ag/pedwind>

'Three-parent' therapy approved

LONDON | The House of Commons voted overwhelmingly this week to allow U.K. researchers to pursue a new fertility treatment that could prevent certain genetic diseases. Called mitochondrial DNA replacement therapy, it would allow women carrying mutations in mitochondrial genes to have healthy children, thanks to fresh mitochondria from a donor. The measure, which passed 382 to 128, has been controversial in part because it would alter the DNA of an embryo in a way that could be passed on to future generations, and some scientists argue that its possible side effects are uncertain. However, several ethical and scientific reviews and a public consultation in the United Kingdom supported approval. If the measure is approved by the House of Lords, the United Kingdom can then grant licenses for experimental use of the technique in humans. http://scim.ag/_mtvote

NEWSMAKERS

Three Q's

Microbiologist **Anne Glover** was the first—and sometimes controversial—chief science adviser of the European Commission (*Science*, 8 March 2013, p. 1144). In particular, some nongovernmental organizations objected to her ardent support for genetically modified (GM) crops. In November, the new commission president, Jean-Claude Juncker, eliminated her job. At a Science Media Centre briefing this week in London, she spoke to reporters about her experiences.



Debutantes dance while an art project about synesthesia lights up Vienna's City Hall.

Science has a ball

In Vienna, home of the waltz, nearly every profession and cause throws a ball. The science community inaugurated its own Ball der Wissenschaften, or Science Ball, on 31 January, with debutantes, ballgowns—and carnivorous-plant table decorations. Physicist Jörg Schmiedmayer simulated a double-slit experiment in the sweaty disco hall while computer scientist Helmut Veith lectured on probability at the roulette table. Quantum physicist Anton Zeilinger, the Austrian Academy of Sciences president (and fellow of AAAS, publisher of *Science*), gave interviews and circulated with an adoring entourage. The ball highlights Vienna's place as "the biggest university and research hub in central Europe," says organizer and science communicator Oliver Lehmann. But for many of the 2500 attendees it is also a counterpoint to the unfortunately named Akademikerball, or Academics' Ball, held the night before by a right-wing anti-immigration party. Lehmann says the Science Ball aimed to affirm that Vienna's academic community waltzes to a tune of diversity and openness.

Q: Why was your position scrapped?

A: No reason was given to me. My contract ended at the end of February. I've had no contact with the new presidency or the new team.

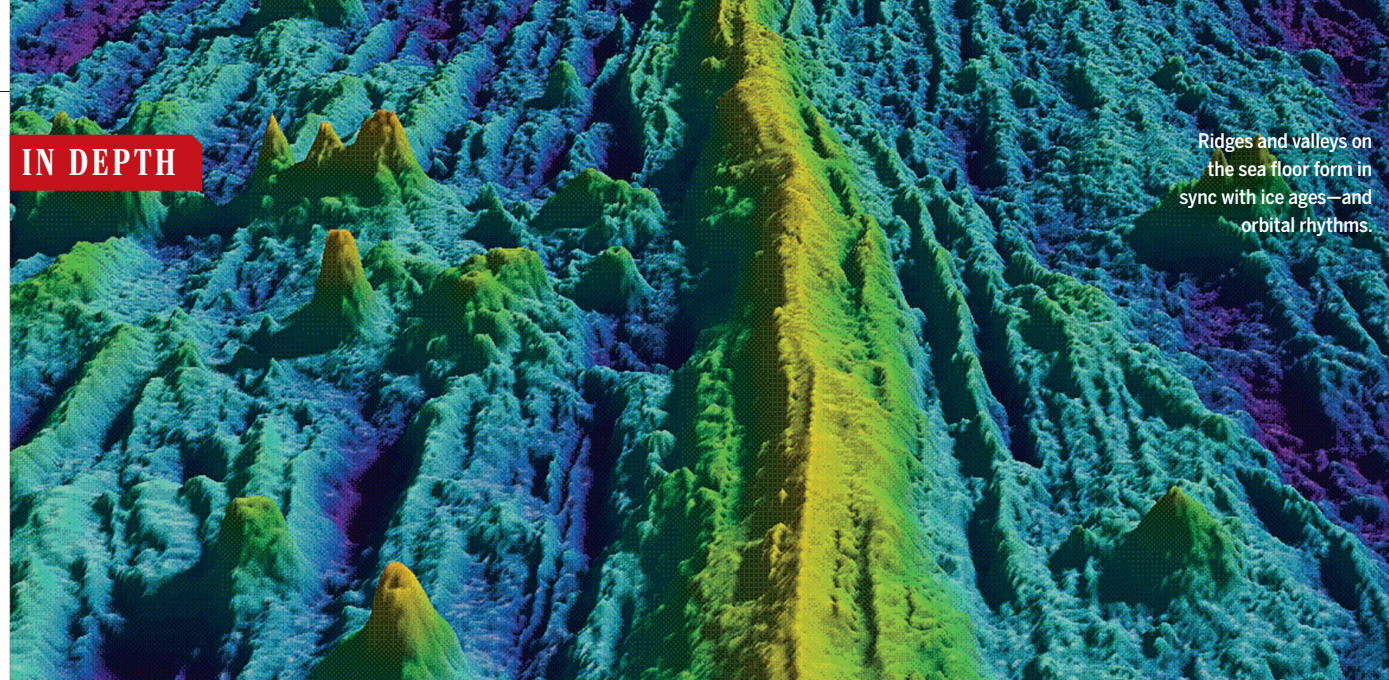
Q: Do you regret saying (in 2013) that opposing GM organisms is a form of madness?

A: No. ... As well as being a chief scientific adviser, I'm also a human being and I use

the rich variety of the English language. And my use of words expressed my frustration.

Q: Some have said your job was ill-defined. Anything you would have done differently?

A: I might have been much more energetic in asking the commission to prepare the ground for my arrival. That would have made the biggest difference: to set some ground rules before turning up.



GEOSCIENCE

Seafloor grooves record the beat of the ice ages

Sea level changes influence the underwater eruptions that build abyssal hills

By Eric Hand

With a little training, it's easy to see how ice age glaciers sculpted the land, scouring valleys and heaping up debris. This week, researchers revealed that the ancient cycles of ice also left their mark on the sea floor, thousands of meters below the ocean surface.

The evidence comes from seafloor spreading centers: sites throughout the ocean where plates of ocean crust move apart and magma erupts in between, building new crust onto the plates' trailing edges. Parallel to these spreading centers are "abyssal hills": long, 100-meter-high ridges on the diverging plates, separated by valleys. On bathymetric maps of seafloor topography, they look like grooves on a record. These grooves, it now turns out, play the tune of Earth's ice ages.

During ice ages, which are mainly driven by rhythmic variations in Earth's orbit and spin that alter sunlight in the Northern Hemisphere, growing ice caps and glaciers trap so much frozen water on land that sea levels can drop a hundred meters or more. As the pressure on the ocean floor eases, magma erupts more readily at the spreading centers, thickening the plates and creating the abyssal hills, say the authors of

two new studies, one published online this week in *Science* (<http://scim.ag/JCrowley>) and another posted online in *Geophysical Research Letters*.

"Step back and think about this: Small variations in the orbital parameters of the Earth—tilt and eccentricity and wobble—are recorded on the sea floor," says Richard Katz, a geodynamicist at the University of Oxford in the United Kingdom and a co-author of the *Science* paper. "It kind of blows my mind." Outside scientists are also impressed. "Their data provides evidence that the link is real," says David Lund, a paleoceanographer at the University of Connecticut, Avery Point. "I'm very excited about it."

The studies suggest that the bursts of

seafloor volcanism could in turn affect climate—and even play a role in bringing each ice age to an abrupt end. They may also change some minds about the origin of the abyssal hills. Ever since scientists discovered the hills more than half a century ago, many thought they resulted from cracks in Earth's crust, or faults. As new oceanic crust is made in the spreading centers (the story went), it cools, fractures, and slips along faults, creating downward-dropped blocks that could be responsible for the ridge-and-valley topography.

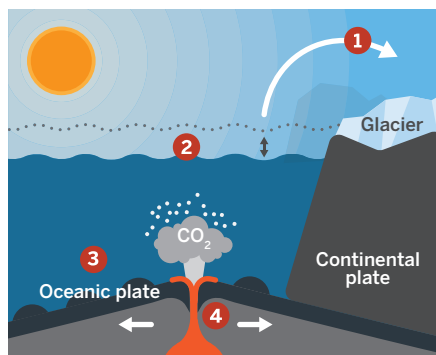
Scientists still agree that faults play a role in shaping the seafloor topography, but the new work emphasizes the importance of volcanism in creating the hills in the first place,

Lund says. "Faulting could be a secondary process as opposed to the primary one," he says.

The study in *Science* was based on fresh ocean-floor data gathered by a Korean icebreaker ship during 2011 and 2013 surveys across the Australian-Antarctic ridge, a spreading center south of Tasmania. In a transect representing more than a million years of seafloor spreading, the researchers found topographic highs and lows that seemed to have formed in synchrony with all three of Earth's astronomical cycles, which have periods of 23,000, 41,000, and 100,000 years.

Take a load off

When ice age glaciers cover continents, falling oceans stripe the sea floor with mysterious ridges. Here's how it works:



1. Water taken up in ice sheets.
2. Sea level drops.
3. Lower pressure on the mantle.
4. Increased rate of eruption.

Wondering whether the climate cycles might somehow be boosting seafloor volcanism at regular intervals, the researchers created a computer model to test the idea. When sea level drops during ice ages, they found, the decreased pressure on the mantle through the thin ocean floor would increase the rate of mantle melting. That would boost the delivery of magma to the seafloor surface by just enough to explain the bands of thicker crust that form the abyssal hills. Paul Asimow, an igneous petrologist at the California Institute of Technology in Pasadena, says the model is physically plausible. "It's additional confirmation that the basic [sea level] signal is felt by the mantle," he says.

In the *Geophysical Research Letters* paper, Maya Tolstoy, a marine geophysicist at Columbia University, reports that she found the same correlation at the East Pacific Rise, a fast seafloor spreading region off the coast of Mexico. When she estimated the ages of abyssal hills flanking the ridge, she found that they matched the strong 100,000-year ice age cycle. "It shows up very clearly," she says.

One of the *Science* co-authors, Peter Huybers, a climate scientist at Harvard University, says he was pleased by the confirmation—especially because it comes from a fast-spreading center, where the ice age signal is more difficult to observe. Because fast-spreading centers discharge more magma, lava sometimes fills valleys, overprinting the grooves left by previous lulls in volcanism during interglacial periods. Slow-spreading centers can also be hard to interpret, Huybers says, because the colder crust there is more prone to the faulting that can confuse the record. Ridges like the Australian-Antarctic are ideal, Huybers says, because they fall "in this Goldilocks range of not too fast, not too slow." Huybers and his colleagues are now working to tease out the ice age signal from another medium-rate spreading center, the Juan de Fuca Ridge, off the coast of the U.S. Pacific Northwest.

The seafloor eruptions—big sources of carbon dioxide and other gases—might also help clear up an enduring mystery about ice ages: why they start gradually and end suddenly. Perhaps extra carbon dioxide from a period of heightened seafloor eruptions eventually percolates through the ocean and into the atmosphere, allowing warming that would deliver a coup de grâce to the massive ice sheets.

Scientists had ignored that possibility because until now they assumed seafloor volcanism is constant over time, Lund says. "It's a very seductive idea, and an interesting one: The ice sheet gets so big that it seeds its own destruction." ■

BIOMEDICAL POLICY

U.S. House reveals ambitious biomedical innovation plan

Lawmakers seek feedback on long-awaited "21st Century Cures" proposal

By Kelly Servick

A high-profile effort in the U.S. House of Representatives to speed the development of new medical treatments has borne its first fruit: a sweeping draft proposal that would overhaul many policies at the National Institutes of Health (NIH) and the Food and Drug Administration (FDA).

Called the 21st Century Cures Act, the proposal has been under development by Fred Upton (R-MI) and Diana DeGette (D-CO) of the House Energy and Commerce Committee since last April, but its first draft had a bumpy rollout last week. The day before Upton's office released its 393-page "discussion document," DeGette decided she would not endorse it. She and others have reservations about provisions to extend drug companies' marketing exclusivity and redistribute NIH funds. Biomedical research advocacy and industry groups, meanwhile, welcomed the proposal but expressed some concerns.

"We're genuinely impressed by this document," says Kay Holcombe, senior vice president of science policy at the Biotechnology Industry Organization in Washington, D.C. Particularly valuable, she says, are directives to incorporate new kinds of data into the drug evaluation process. FDA would be



Fred Upton, chair of the House Energy and Commerce Committee, was eager to release a preview of the upcoming bill.

required to set standards for how it evaluates "surrogate endpoints"—measures of a patient's biological response to a drug that can indicate benefits more quickly than survival and disease progression. The agency would also be required to develop standards for incorporating patient feedback into its review process.

Other sections of the draft are intended to make certain research areas more appealing to drug companies and investors. A new FDA pathway would accelerate the approval of antibiotics for limited use in rare infections. And for complex diseases that lack effective treatments, such as Alzheimer's, the draft offers companies a hefty incentive for the time-consuming and costly drug development process: 15 years of marketing exclusivity after FDA approval. (Current exclusivity periods include 7 years for a drug to treat a rare disease and 12 for a biologic.)

These efforts could inspire more investment in research on understudied diseases, including at academic institutions, says Kenneth Kaitin, director of the Tufts Center for the Study of Drug Development in Boston. But extending marketing exclusivity could restrict competition and drive up the cost of drugs, he says. "That's one of those areas that's going to be battled out at some



Representative Diana DeGette, co-architect of the 21st Century Cures Initiative, has reservations about the draft.

point.” Those provisions were also a stumbling block for DeGette, according to a representative from her office.

Another of DeGette’s objections involves language added by Representative Andy Harris (R-MD) that would favor early-career researchers in the competition for NIH grants by setting aside funding in the director’s office for younger scientists. Benjamin Corb, public affairs director for the American Society for Biochemistry and Molecular Biology in Rockville, Maryland, says his group worries “about saying young investigators are better investigators” who should be favored over established scientists.

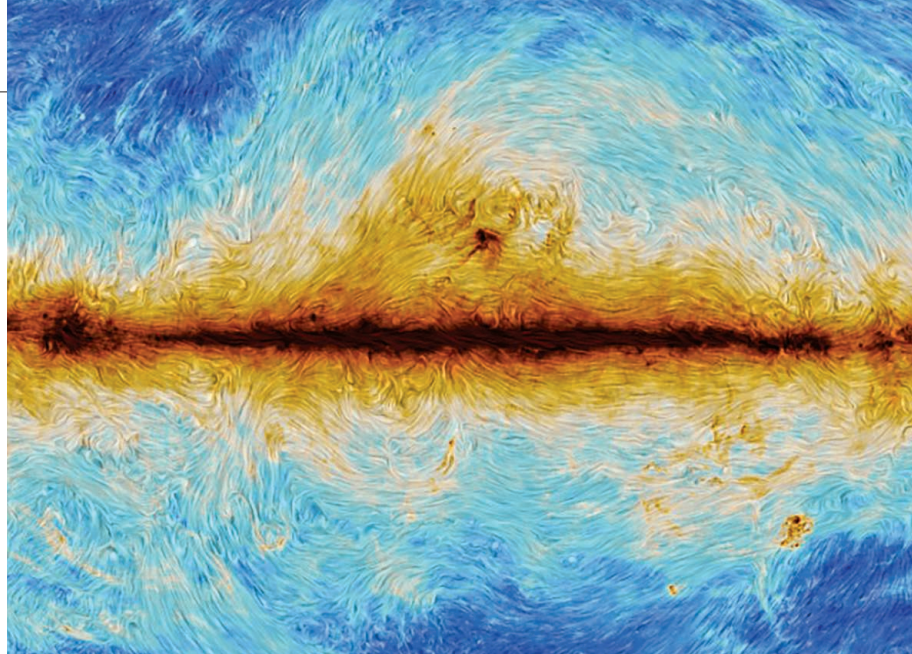
Harris also wants NIH to develop an overarching strategic plan that sets priorities for money allotted to it. That idea flopped when the agency last attempted it more than 2 decades ago. And Corb’s group is troubled by a proposal that the director of each NIH institute personally sign off on every grant, taking into account whether its goals are “a national priority and have public support” and are “worth the potential scientific discovery.” Those criteria don’t make sense for basic research, because payoffs can be difficult to predict, Corb says.

Perhaps most troubling, research advocates say, the plan doesn’t address the need to boost NIH funding after a decade of flat budgets—a trend that the 2016 budget proposal, rolled out this week, does little to change (see p. 599). “You need to get back to sustained, predictable funding instead of moving money around the margins of the budget,” says David Moore, senior director of government relations for the Association of American Medical Colleges in Washington, D.C. The Energy and Commerce Committee’s top democrat, Representative Frank Pallone (D-NJ), similarly lamented that the document “does not include any real dollars to fund additional basic research at the National Institutes of Health.”

Several sections of the draft remain to be filled in, including one on “precision medicine,” an initiative championed by President Barack Obama as part of the 2016 budget.

Upton and DeGette’s approach is attracting interest in the U.S. Senate. Senators Lamar Alexander (R-TN) and Patty Murray (D-WA), the top Republican and Democrat on the Senate’s health committee, launched a very similar initiative this week. And despite their differences, Upton and DeGette plan to work together, using feedback from this draft, to craft a formal bill, which they aim to have on the president’s desk by the end of the year. ■

With reporting by Jocelyn Kaiser.



COSMOLOGY

Misfire aside, signs of cosmic inflation could come soon

Even as the BICEP result bites the dust, observers like their chances of spotting big-bang gravitational waves

By Adrian Cho

When the biggest discovery in cosmology in years officially unraveled last Friday, nobody was surprised. Almost as soon as observers announced last March that they had detected evidence of inflation, a bizarre exponential growth spurt thought to have blown up the infant universe, others suggested the signal was merely an artifact of dust in our galaxy. “I would have been surprised if it had turned out otherwise,” said Suzanne Staggs, an observational cosmologist at Princeton University, after the last hope faded. Yet she and other cosmologists think a real signal of inflation could be found—perhaps within a few years. “The future’s so bright we’ve gotta wear shades,” she quips.

The spurious signal appeared in the big bang’s afterglow, the cosmic microwave background (CMB). Standard theory predicts that inflation would have set off ripples in space and time called gravitational waves, which would imprint faint pinwheel-like swirls—called B modes—in the CMB. Cosmologists using a specialized telescope at the South Pole called BICEP2 reported that they had detected those “primordial B modes” when they mapped the polarization of the microwaves in a patch of sky (*Science*, 21 March 2014, p. 1296). In a

Planck mapped the strength (color) and polarization (texture) of radiation from galactic dust.

press conference, the BICEP team claimed the first direct evidence of inflation.

But such swirls can come from other sources. In particular, radiating dust in our galaxy can produce them, so researchers must first strip away this “foreground” contribution to see the CMB signal properly. Ordinarily, experimenters do that by taking data at multiple microwave frequencies. However, BICEP2 took data at only one frequency to maximize sensitivity and relied on preliminary data from the European Space Agency’s Planck spacecraft to estimate the foreground contamination. The BICEP team believed it was small. But in May, others suggested that BICEP researchers may have underestimated the dust contribution. In September, Planck’s final data suggested that BICEP’s patch of sky was as dusty as an old pillow (*Science*, 26 September 2014, p. 1547).

To settle the issue, the BICEP and Planck teams decided to perform a joint analysis, which was released last week. It yields no definite sign of primordial B modes. “If gravitational waves are there, they’re probably less than half of the total signal,” says John Kovac, a cosmologist at the Harvard-Smithsonian Center for Astrophysics in Cambridge, Massachusetts, and a co-leader

of the roughly 60-member BICEP team.

BICEP researchers have taken heat from some of their peers for overstating their result. But François Boulanger, an astrophysicist at the University of Paris-Sud in Orsay, France, and a member of the Planck team, notes that the joint analysis showed that the dust emission was stronger and its polarization varied more from place to place than previously expected. “One has to be fair to the BICEP team,” he says. The delicate joint analysis took 6 months, Boulanger says, “and we went through some stages where we thought there probably was a [gravitational wave] signal.”

Researchers are optimistic about their chances of spotting the real thing soon. Physicists quantify the B-mode signal using a parameter r , which is the ratio of the strength of the peculiar oscillation of gravitational waves to the strength of more-conventional waves such as sound waves in the early universe. The joint analysis shows that r must be less than 0.12. But if r is close to that limit, then a half-dozen experiments now under way or in the works could detect primordial B modes in the next few years.

For example, John Carlstrom, a cosmologist at the University of Chicago in Illinois, and colleagues will soon deploy SPT3g, an upgrade of the 10-meter South Pole Telescope, which is also in Antarctica. Taking data at three frequencies, SPT3g should be able to detect primordial B modes if r is 0.05 or greater, Carlstrom says. Similarly, Staggs and colleagues are working on Advanced ACTpol, an upgrade of the Atacama Cosmology Telescope in Chile, that will take polarization data at five frequencies. And Kovac and colleagues have already taken data at a second frequency with BICEP2's successor, the Keck Array, and are installing BICEP3.

In case the gravitational wave signal slips past those telescopes and others, cosmologists are developing a plan for a network of telescopes that would have 10 times more sensitivity and could detect B modes if r were as low as 0.005. The \$100 million effort would link telescopes at the South Pole, in Chile, and possibly in Greenland or Tibet. In a road map for their field released last May, U.S. particle physicists strongly endorsed the idea, and researchers are hopeful that the Department of Energy will fund it and have it running in the next decade.

After the BICEP2 episode, researchers are quick to say that the discovery of primordial B modes probably won't come in one decisive measurement. “I think it will happen as these things have always happened,” Carlstrom says. “Hints will show up earlier.” Still, Kovac says, “the bottom line is that we're all feeling very optimistic.” ■



ECOLOGY

Africa's soil engineers: Termites

Kenyan plots show that termite mounds promote ecological health and may slow desertification

By Elizabeth Pennisi, in Mpala Research Centre, Kenya

Thuman Young still remembers his amazement more than a decade ago when he and his colleagues had their first aerial look at the African dryland landscape that they had been studying. From the ground, the acacia trees and bunch grasses seemed randomly distributed—and so did the termite mounds scattered across this combination ranch-field station in central Kenya. But satellite photos taken in 2003 showed these mounds were actually like polka dots, spaced far enough to avoid territorial battles. More startling, a satellite image sensitive to chlorophyll revealed that termite mounds are hotspots for plant growth.

The photo “changed the way we thought” about what shapes this landscape, recalls Young, an ecologist at the University of California, Davis. For decades, thanks primarily to National Science Foundation funding, he and his colleagues have run the Kenya Long-term Exclosure Experiment (KLEE) here, which uses fenced-in 4-hectare plots to assess how elephants, cattle, and other grazing animals affect the savanna. But after studying that image, Young suddenly realized termites had to be added to this list.

“We all tend to think about large mammals as being the big dominant driver of what's happening in the savanna, but the more we look at the termite mounds the more they

seem to be driving what's going on,” says Robert Pringle, a Princeton University ecologist who works at Mpala. A study on page 651 presents the latest example. By modeling the interactions of termites, rainfall, soil, and plants, Pringle and his colleagues conclude that the termite mounds are an insurance policy against climate change, protecting the vegetation on them from water scarcity.

Jef Huisman, a theoretical biologist at the University of Amsterdam, says the results show that “termite mounds play a key role in arid landscapes.” The work also calls into question whether land managers can forecast looming desertification based on aerial views of the landscape. “We should not blindly adopt the early warning indicators predicted by simple models,” Huisman says.

Africa's indigenous people have long recognized that the soil in termite mounds is richer than normal and good for crops. Harvester termites, such as the fungus farmers that live at Mpala, spend their days retrieving vegetation to fertilize “gardens” of microbes and fungus, which concentrate nitrogen, phosphorus, and organic matter. At the same time, the termites alter the soil profile as they build their tunnels. In some places, termites add clay to stiffen soil too sandy for tunnels. At Mpala, they dilute the clay-laden soil with sand, making it easier to excavate. “In both cases, it's making a soil that's better than background,” Young says. So plants grow more readily. The excavations also help the mounds better hold on to water. “At the right

Zebras, elephants, and other grazing animals prefer a termite mound's nutrient-rich grasses.

time of year, the mounds are all green and the rest of vegetation is all brown."

Even the savanna's iconic acacia trees benefit. They don't grow right on termite mounds, but Todd Palmer, an ecologist at the University of Florida in Gainesville, helped determine that acacia growing next to mounds have higher nitrogen concentrations and were more likely to produce fruit than trees farther away.

All told, the termite mounds create "nutrient islands" that sustain many other animals besides termites. More than a decade ago, as a graduate student, Palmer had noticed that ant colonies were biggest along the edges of termite mounds. Because of the lush plant growth, the mounds supported more of the insects that ants prey on. "These mounds are really the supermarkets of the savanna," Palmer says, also attracting zebra, buffalo, eland, and other plant-eating mammals.

By trapping all the insects flying and crawling on and away from mounds, tracking the offspring of insect-eating spiders, and counting geckos, Pringle, Palmer, and their colleagues found that all are bigger, more numerous, or more prolific near mounds. Furthermore, computer simulation studies showed that the regular spacing of the mounds enhances these beneficial effects by minimizing the average distance that animals have to travel to reach the nearest mound.

The latest termite study grew out of a collaboration between Pringle and Princeton theoretical ecologist Corina Tarnita. It exam-

ines a widely accepted theory that vegetation in dry places will arrange itself in regularly spaced clumps, instead of forming a uniform lawn as happens in wetter places. Because each plant's roots alter the soil to help concentrate water and slow its loss, plants in dry places prefer to grow close to other plants. Yet these emerging clumps suck water from more distant surrounding soil, making the space in between inhospitable to plants. As the environment dries, the space between clumps should expand. And theory predicts that "if you turn down the water enough, you get a catastrophic shift to desert," Pringle says. As a result, the presence of vegetation clumps may signal an ecosystem in danger.

Given the aridity of the climate at Mpala, Tarnita expected to see the telltale clumping in the plants. But no matter how hard she and Pringle looked, the only pattern they saw in the vegetation was the one established by the termite mounds. Then one day they visited an area that another researcher had burned to study how different grazing species affect plant regrowth. Instead of being overgrown with tall grasses, the burn area had just stubbly ground cover. When they stood on the roof of their Land Rover, Tarnita and Pringle thought they saw hints of a pattern in the vegetation. Then two graduate students rigged a fishing rod that could hoist a camera 10 meters up. The photographs showed that the new growth formed a uniform lawn

on the termite mounds. But in between, Princeton postdoc Efrat Sheffer could make out a pattern of clumps just 20 centimeters wide, created by self-organization among the plants. "There was the vegetation pattern that prior models had predicted, but it was on the scale of centimeters," Tarnita says.

To gauge how termite mounds shape the pattern, the group turned to the mathematical models that had previously suggested vegetation clumps are bellwethers for desertification. The models usually treat all soil as uniform, but Tarnita modified them to include patchy nutrient islands.

Tarnita and Juan Bonachela, now at the University of Strathclyde in the United Kingdom, provided the model with different rainfall scenarios, and it predicted what would happen to the plants on and off the mounds over time. In dry conditions, the vegetation on the termite homes per-



Plant-covered termite mounds dot Mozambique landscape.

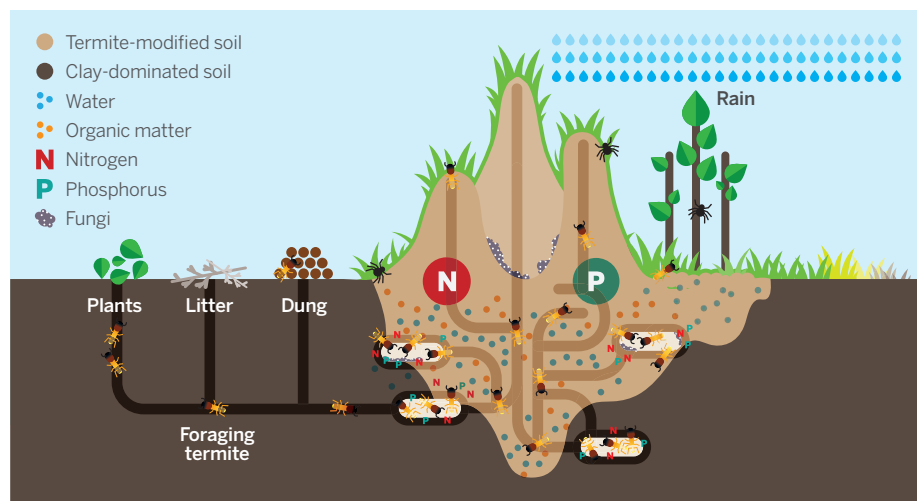
sisted, despite a 30% decline in the vegetation off the mounds, indicating termites' remodeling of the soil can slow the loss of vegetation, the Princeton team now reports. And when the group restored rainfall in the model, the remaining vegetation on the mounds helped revegetate the whole area.

But there is a downside: The modeling work suggests that there's no easy way to predict when an arid landscape is on the verge of collapsing. Vegetation clumping may be due to termite mounds rather than an unhealthy environment. "The use of vegetation patterns to predict desertification in general is in urgent need for validation," says Max Rietkerk, an ecologist at Utrecht University in the Netherlands. And the work suggests that the savanna may lose resilience when it is transformed into farms. "When agriculture takes over, we lose the termites and their mounds," Palmer explains. Cultivated lands are "likely to be much more vulnerable to climatic variability and much more likely to tip over into more permanently degraded landscapes."

Meanwhile, the termite studies at Mpala continue. Experiments by Pringle, Tarnita, and Dan Doak from the University of Colorado, Boulder, are testing the mounds' additional roles in slowing degradation of the landscape. Grace Charles, one of Young's graduate students, has been analyzing how large herbivores affect the density of the mounds or vice versa. For Young, the termites "started as noise in the background" of the KLEE research. But now, he says, "they are front and center." ■

Nutrient islands

Foraging termites concentrate plant material in mounds, where fungi process it into soil-enriching nitrogen, phosphorus, and organic material, fostering more plant and animal growth. Mounds also retain water better than surrounding soil.



CREDITS: (TOP TO BOTTOM), ROB PRINGLE, G. GRULLÓN/SCIENCE

PARTICLE PHYSICS

Japanese neutrino physicists think really big

A proposed Hyper-Kamiokande would be the largest neutrino detector ever

By **Dennis Normile**, in *Kashiwa, Japan*

Japanese physicists, already among the world's leading neutrino hunters, want to cement their position with a million-tonne instrument—dubbed Hyper-Kamiokande, or Hyper-K—capable of catching these elusive particles at 20 times the rate of its predecessor. The 250-meter-long behemoth should be a powerful tool for physics, dissecting the properties of neutrinos beamed from a remote particle accelerator. It could also boost astronomy, by capturing neutrinos spraying from supernovas in deep space. “Hyper-Kamiokande is very well placed to be the greatest experiment of its generation,” says Francesca Di Lodovico, a particle physicist at Queen Mary University of London.

The challenge will be getting the \$800 million or so needed to build it. To make their case, scientists from 13 countries this past weekend formally launched a protocol-collaboration to develop a firm plan they can take to funding agencies. Given Japan's fiscal woes, “we will have to work very hard to convince the government that this is a most important scientific project,” says Takaaki Kajita, director of the University of Tokyo's Institute for Cosmic Ray Research, which oversees the Kamioka experiments. It will also be in competition with other big physics projects. Some Japanese physicists want Japan to host the next great particle smasher, the proposed International Linear Collider. And physicists in the United States are planning a huge neutrino experiment that could beat Hyper-K to the punch (*Science*, 30 May 2014, p. 955).

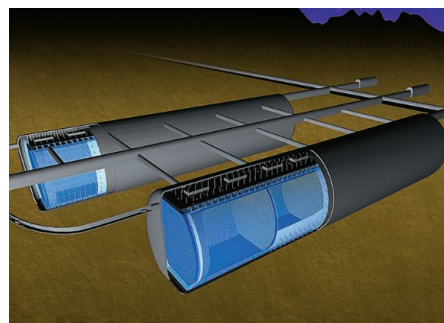
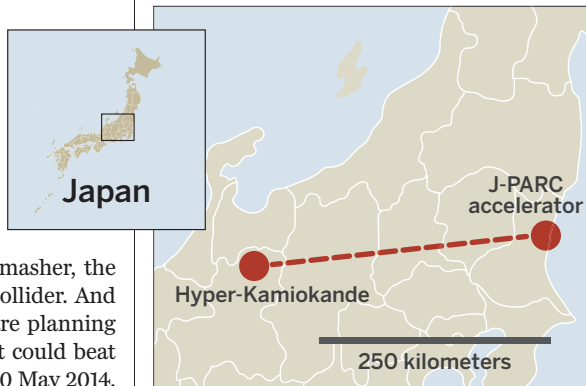
Hyper-K's grandfather, Kamiokande (for Kamioka Nucleon Decay Experiment), surprised many 3 decades ago when it demonstrated that it could pinpoint the direction and energy of incoming neutrinos from the sun, from cosmic rays colliding with particles in the atmosphere, and from a supernova. The sightings netted the head of the experiment, Masatoshi Koshiba of the University of Tokyo, a share of the 2002 Nobel Prize in physics. By then, researchers had already

moved on to the larger Super-Kamiokande, or Super-K, and showed that neutrinos have mass, upsetting previous theories. Now researchers believe an even larger detector will allow them to fill in the remaining blanks in the neutrino profiles, study the early universe, and probe why matter is more common than antimatter.

Chargeless and almost massless, neutrinos flow through matter as if it wasn't there. But occasionally a neutrino collides with another particle. In the purified water that fills the Kamiokande detectors, the interaction produces a blue cone of light known as Cherenkov radiation. By observing these flashes with photosensors, physicists can determine which of the three types, or flavors, of neutrinos produced it and the incoming particle's direction and energy. To screen out background noise, the detectors are placed 1000 meters underground in a mine near the

In the firing line

Neutrinos will beam from J-PARC to Hyper-K's giant water tanks (bottom).



Gifu Prefecture town of Kamioka.

As with many scientific instruments, size matters. Kamiokande contained 3000 tonnes of water watched by 1000 sensors. In 1996, Super-K upped the ante to 50,000 tonnes of water and 13,000 sensors. As presently planned, Hyper-K will comprise two 250-meter-long, 50-meter-high oval-shaped tubes together holding 1 million tonnes of water and 100,000 photosensors. Hyper-K will be able to collect in 5 years the amount of data Super-K would take a century to gather.

Research teams have grown proportionally. Kamiokande had a couple of dozen scientists, primarily from the University of Tokyo. About half of Super-K's 120 collaborators are from outside Japan. Hyper-K already has at least 240 researchers from 67 institutes working on R&D.

Besides snaring neutrinos from the atmosphere and from space, Super-K caught and studied neutrinos beamed from the Japan Proton Accelerator Research Complex (J-PARC), 295 kilometers to the east in Tokai. For Hyper-K, J-PARC is planning to triple the intensity of its neutrino beam. By watching the neutrinos in the beam transform from one flavor to another, researchers will try to understand why there is more matter than antimatter in the universe, a condition known as charge-parity violation that is “one of the major questions in physics,” Di Lodovico says. The neutrino changes, or oscillations, should also help researchers determine which flavor is the heaviest—a goal shared by smaller neutrino projects in other countries (*Science*, 30 January, p. 464).

Meanwhile, neutrinos from astronomical sources could shed light on how stars live and die. Should a supernova explode in our galaxy, Hyper-K could catch 250,000 neutrinos within 10 seconds, providing new clues to these cataclysms.

The same photodetectors that watch for neutrino interactions should also be sensitive to a momentous event in the water itself: the decay of one of its protons. Proton decay, postulated but never observed, would indicate that all matter in the universe will eventually break down into subatomic particles. Observing it “would be an amazing result,” says Christopher Walter, a physicist at Duke University in Durham, North Carolina.

The goal of Hyper-K's protocollaboration is now to produce a more detailed design by next December in hopes of starting construction in 2018 and taking data in 2025, a schedule that Masato Shiozawa, the University of Tokyo physicist heading the project, admits will be challenging. But, Di Lodovico says, “It's time to move forward now to keep the momentum and gather together all our efforts in order to create this experiment.” ■



Science adviser John Holdren discusses President Obama's 2016 budget for research.

U.S. RESEARCH FUNDING

Budget for 2016 accentuates the practical

White House proposal lifts (almost) all boats, but applied research floats to the top

By Jeffrey Mervis

The federal budget that President Barack Obama proposed this week for the 2016 fiscal year offers a lot of good news for scientists. But researchers conducting basic research may feel a little jealous of their colleagues in more applied fields, as the spending request released on 2 February has a distinct tilt to the practical.

Overall, the \$4 trillion spending plan includes a 7.2% hike, to \$1.09 trillion, in so-called discretionary spending—the slice of the budget that includes annual research funding. To make that increase possible, Obama is calling on Congress to shatter the spending caps imposed by a 2011 budget deal. With the economy recovering, the administration is urging “smart investments that strengthen America.”

On that list: bolstering research. “The president is thoroughly attuned to the important role that science, technology, innovation, and STEM education can and must play as the nation addresses the challenges and opportunities that lie ahead,” explained John Holdren, the president’s science adviser, during a 2 February presentation of the president’s budget at AAAS (which publishes *Science*). The request calls for total federal spending on research and development to grow by 5.5%, to \$146 billion. But basic research—the category that funds the work of most U.S. academics—

would inch up by only 2.6%, to \$32 billion.

Although most federal science agencies would see their budgets rise (see table, p. 600), those helping realize advanced manufacturing methods, new energy sources, and ways to help people cope with climate change get an extra push. Also getting top billing: efforts to move personalized, “precision medicine” into the clinic, and to fight antibiotic-resistant microbes (see sidebar, p. 601). “The United States still leads the world across most domains of science and engineering,” Holdren said at the AAAS presentation, ticking off metrics such as overall research spending, the number of scientists and engineers produced, publications, patents, and what Holdren called “the pace of actual progress” in converting discoveries into tools that help society. It’s the last metric that apparently figured prominently into the 2016 request.

Scientists generally welcomed the plan, but with a few caveats. The Association of American Universities (AAU), which represents many of the nation’s largest research universities, praised the request’s “needed investments in the ideas, discoveries, and people that can provide the foundation for our nation’s future.” But AAU scolded the administration for its “inconceivable” proposal for an 8% cut in basic research at the Defense Department, which provides major funding for academic engineering research, computer science, and math. Research!America, which

lobbies for biomedical research and has lamented recent small increases for the National Institutes of Health, called the budget a “starting point ... [that] should supplement, not supplant, the imperative of making up for a decade’s worth of lost ground.”

Republicans in Congress were critical of the overall spending hike. They generally think the number is too high, and they dislike the president’s plans to pay for much of the increase with higher taxes on the wealthy. The science budget is no exception, says the chair of the science committee in the U.S. House of Representatives. “The American people do not want increased taxes and the government spending what it doesn’t have,” said Representative Lamar Smith (R-TX). “Rather than focus on areas that have clear benefits for Americans, the president instead chose to push a partisan agenda.”

In contrast, the top Democrat on that science committee, Representative Eddie Bernice Johnson (D-TX), applauded the budget, which she said would help “solidify America’s place as a scientific and technological leader.” Johnson praised the budget’s call to undo the spending caps, which she predicted will be “very detrimental to our research, education, and innovation enterprise.”

Such partisan wrangling will now take center stage, as the president’s request moves to Congress, where it will be broken into the 12 annual appropriations bills that

fund the government. If they fail, the entire budget will likely be combined into one massive package in which science is nearly invisible.

Apply your work

Many of the research programs that did the best in the request have one thing in common: They promise what one veteran policymaker calls “news you can use”—practical information that can help businesses and communities thrive. That’s certainly the case for mission agencies such as the U.S. Geological Survey (USGS), the National Oceanic and Atmospheric Administration (NOAA), the U.S. Department of Agriculture (USDA), and NASA. But this year, the budget proposal also favored that type of research at the National Science Foundation (NSF), the backbone of academic research in nonmedical fields, and the Office of Science at the Department of Energy (DOE).

At NOAA, a proposed 6.3% boost to \$3.3 billion is the agency’s best mark in many years, says Scott Rayder, a former NOAA chief of staff and now a senior adviser at the University Corporation for Atmospheric Research in Boulder, Colorado. “There’s something there for everyone,” he says, including new weather satellites, grants to help coastal communities plan for climate change, and a push to develop better regional and seasonal forecasts, which have customers waiting. “The marketplace—agriculture, transportation, energy, water managers—they all want” such practical help, Rayder says. “So in this space, the administration and Congress can agree that it’s a good thing.”

NOAA is hoping Congress will also support a request for \$147 million to start building a new research ship. To save money, the agency hopes to build it to the same specifications as two other academic research ships already planned by NSF.

Within DOE’s six science programs, the biggest winner was the Advanced Scientific Computing Research effort. It is slated for an increase of nearly 15%, to \$621 mil-

lion. The extra funding is largely aimed at developing a new generation of computers operating at the exascale (10^{18} operations per second), which would pave the way for advanced climate modeling and myriad other applications.

Advanced computing enjoys bipartisan support in Congress. But Republicans are likely to object to funding proposals for other parts of DOE. There “the emphasis is really in the energy technology areas,” rather than science, says Michael Lubell of the American Physical Society in Washington, D.C., citing large proposed increases for programs supporting renewable energy and energy efficiency.

USGS was another big winner this year, with a proposed increase of 13.7% to nearly \$1.2 billion. The boost reflects the administration’s sense of urgency about the need to prepare for natural disasters, including those linked to a warming planet, says Lexi Shultz of the American Geophysical Union in Washington, D.C. “We’re facing a some-

Science rises, mostly, in budget request

Increases outnumber cuts for federal science agencies in president’s budget request for 2016. (Figures are in billions of dollars.)

INSTITUTIONS	2015	2016 REQUEST	% CHANGE
NIH	30.311	31.311	3.3%
NSF	7.344	7.724	5.2%
Research	5.934	6.186	4.3%
Education	0.866	0.962	11.1%
DOE Office of Science	5.071	5.340	5.3%
Basic energy	1.733	1.849	6.7%
Bio/environmental	0.592	0.612	3.4%
Fusion	0.468	0.420	-10.3%
High Energy Physics	0.766	0.788	2.9%
Nuclear Physics	0.595	0.625	5.0%
Advanced computing	0.541	0.621	14.8%
ARPA-E	0.275	0.325	18.2%
NIST	0.864	1.120	29.6%
USGS	1.052	1.196	13.7%
NASA	18.010	18.529	2.7%
Science office	5.245	5.289	0.8%
Earth science	1.773	1.947	9.8%
Planetary science	1.438	1.361	-5.4%
Astrophysics	0.684	0.709	3.7%
Heliophysics	0.662	0.651	-1.7%
USDA Agricultural Research	1.132	1.192	5.3%
AFRI	0.325	0.450	38.5%
NOAA	3.333	3.543	6.3%
Research office	0.433	0.485	12.0%
DOD Basic Research	2.292	2.101	-8.3%
DHS S&T	1.071	0.779	-27.3%
EPA S&T	0.735	0.769	4.6%

what unprecedented threat because we, as a nation, don’t have a handle on everything we need to do to protect ourselves from the effects of climate change,” she says. “So I don’t think it’s surprising that the administration would prioritize [USGS’s climate and land research programs] above all others.”

NASA’s request highlights the fine distinctions the administration made in setting priorities. NASA’s overall budget would rise by 2.7%, to \$18.5 billion. But science would grow by only 0.8%, to \$5.289 billion. And within the agency’s four science divisions—earth science, astrophysics, planetary science, and heliophysics—earth science, with its emphasis on climate and resources, is the clear winner. It gets a 10% boost, to \$1.947 billion. Part of the increase would help NASA take on responsibility for managing some of NOAA’s Earth-observing satellites.

In contrast, planetary sciences would shrink by 5%. Among operating planetary missions, the budget has proposed eliminating funding for the 11-year-old

Mars Opportunity rover, the Mars Odyssey orbiter (14 years old), and the Lunar Reconnaissance Orbiter (6 years old). But supporters are hoping that even if Congress accepts the proposal, NASA will find money to keep the missions alive, as it has in the past—if the aging spacecraft themselves are alive.

Meanwhile, some are celebrating the agency’s embrace of a mission it once resisted. The budget endorses an official start to planning a mission to Jupiter’s moon Europa—a potential habitat for alien microbes—that would launch in the mid-2020s. The start signals a detente between the administration, which had previously refused to ask for funding for Europa, and Congress, which this year appropriated \$100 million for the mission despite agency resistance. The agency asks for \$30 million for Europa in 2016 and plans to develop the mission concept this spring.

NSF officials are touting two new initiatives that also fit squarely into the administration’s thrust for solving societal problems.

One, which seeks to explore the connection between food production, energy use, and the availability of water, is proposed as a \$74 million research program. It would eventually replace a long-running initiative on environmental sustainability that is being phased out in 2017, including a proposed cut of \$58 million in 2016.

A second NSF initiative, on risk and resilience, is part of the administration's heightened focus on the effects of natural hazards and extreme events. A \$38 million boost

would go largely to ramping up a program aimed at understanding what drives geological hazards such as hurricanes, tornadoes, floods, volcanic eruptions, and earthquakes, and why they vary.

At USDA, the administration is looking to boost research aimed at ensuring future supplies of food and other agricultural products. It wants to expand the Agriculture and Food Research Initiative, a competitive grants program, by 38%, to \$450 million. And the White House is dedi-

cating \$77 million to help USDA find alternatives to using antibiotics in livestock, a practice believed to contribute to drug resistance (see sidebar, below).

But a green economy, climate change, and other themes in the White House's proposal are unlikely to be embraced in Congress. Monday's proposal marks the opening volley in a budget clash that could easily last deep into the year. ■

With reporting by the Science News staff.

Biomedical initiatives get top billing in budget rollout

By Jocelyn Kaiser and Kelly Servick

The White House began trumpeting two flagship elements of its scientific agenda well before the 2 February release of the overall federal budget. One is a \$215 million Precision Medicine Initiative, first mentioned in President Barack Obama's 20 January State of the Union address, which aims to advance personalized medicine. The other is a roughly \$1.2 billion effort to combat the mounting public health crisis of antibiotic-resistant infections.

The National Institutes of Health (NIH), the nation's leading funder of basic biomedical research, would play a key role in both campaigns. The Obama administration has requested a 3.3% overall increase for NIH, to \$31.3 billion, an amount that didn't wow many biomedical research advocates. Still, the two initiatives have drawn encouraging words from members of Congress in both parties.

The centerpiece of the precision medicine initiative, funded at \$130 million, would be an NIH effort to assemble a database containing genetic and medical information from at least 1 million Americans. Researchers would then comb through the cohort, looking for disease-gene associations and other information that could help them harness genomic and other molecular information to find drug targets and improve medical care. The cohort would not be created from scratch, but would instead recruit participants already enrolled in studies that collect and combine health and genetic information.

Other countries have already built such large population databases, and a similar U.S. study has long been on the wish list of NIH Director Francis Collins, who led the effort to sequence the human genome as director of the National Human Genome Research Institute.

A blue-ribbon panel will guide the cohort study, and participants will be involved in the study design and will control use of their data, officials said. Planning begins with a workshop next week to discuss topics such as which cohorts to include and how to pool electronic medical records.

An additional \$70 million will go to the NIH's National Cancer Institute to continue efforts to catalog cancer-driving DNA glitches in tumors and to conduct clinical trials testing drugs

based on such mutations. This area is "the leading edge of precision medicine," Collins said; many patients, such as those with breast cancer, already receive genetic or other molecular tests to determine the best drug.

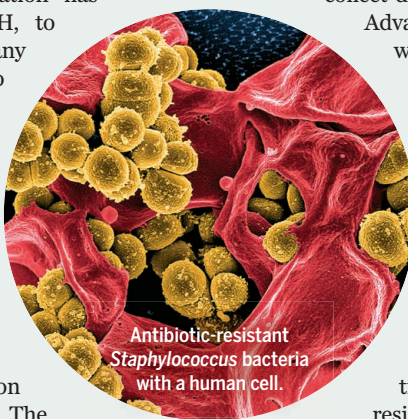
The Food and Drug Administration (FDA) will get \$10 million to help evaluate diagnostic tests based on sequencing large parts of a patient's genome. Another \$5 million will go to the Department of Health and Human Services (HHS), NIH's parent body, to develop ways to protect the privacy of patient data.

The effort to develop new antibiotics to combat resistance would steer \$100 million to NIH for basic research and a clinical trial network that would let drug developers more easily collect data across multiple clinics. HHS's Biomedical Advanced Research and Development Authority would also get an additional \$100 million to study how bacteria become resistant to antibiotics and promote the development of new drugs and diagnostics.


The U.S. Centers for Disease Control and Prevention (CDC) would receive \$280 million to nearly double its spending on "emerging and zoonotic infectious disease" programs. The \$699 million effort would include efforts to create an "isolate bank" of resistant strains and educate hospitals about how to use antibiotics while minimizing the emergence of resistant strains. CDC also plans to double the number of sites, to 20, in its Emerging Infections Program—a research and surveillance network.

Meanwhile, FDA would receive \$47 million to evaluate new drugs and diagnostics and to continue phasing out the use of certain antibiotics in feed animals—a major threat to the value of these drugs as human medicines. The U.S. Department of Agriculture would also see a quadrupling of its funding, to \$77 million, for exploring alternatives to antibiotic use in livestock.

The bipartisan backing that the antibiotics and precision medicine initiatives have already drawn suggests they will fare well as the White House and Congress clash over spending. "The federal budget picture is going to be challenging," predicts Amanda Jezek, vice president of public policy at the Infectious Diseases Society of America in Arlington, Virginia. But in the jockeying for new money, the hunt for new lifesaving drugs "stands a better shot than most." ■



FEATURES



Middle school teacher Tami May helps students run an experiment showing the relationship of mass to acceleration.

A classroom experiment

NSF has spent \$500 million to train thousands of science and math teachers. But what has that meant for kids?

By Jeffrey Mervis

After earning her undergraduate degree in biology, Tami May found herself in a dead-end job in a marine biology lab that was draining her passion for science. As an engineering major, Drew Shelton felt that he had more to contribute to society than obtaining another building permit for a shopping mall. Now, after receiving retrain-

ing funded by the federal government, both have found a new calling in the classroom: May is a science teacher at Semmes Middle School outside Mobile, Alabama, and Shelton is teaching environmental science at North Carroll Middle School in the exurbs of Baltimore, Maryland.

May and Shelton have joined thousands of other college graduates lured into becoming science educators through the Rob-

ert Noyce Teacher Scholarship Program run by the National Science Foundation (NSF). NSF has poured half a billion dollars into the program, created by Congress in 2002 to draw those with STEM (science, technology, engineering, and mathematics) degrees into teaching at high-needs schools. The lawmakers' key premise: Students would learn more science and math if taught by those who knew—and loved—the subjects.

PHOTO: © JEFF HALLER/KEYHOLE PHOTO

The program provides a variety of ways to achieve that goal, including fellowships for career changers like May and Shelton to earn a master's degree in science education and scholarships for undergraduates earning a STEM degree who want to be teachers. To protect taxpayers, the legislation requires that, for every year of support, each recipient teach 2 years in a school district where a majority of students are poor enough to qualify for federally subsidized meals.

Noyce is one of many efforts across the country aimed at improving STEM education. It is getting increased attention as a key federal contribution to the Obama administration's pledge to train 100,000 new science and math teachers over a decade. So far, 5008 teachers working in a high-needs district have received funding from one of 494 Noyce programs that NSF has funded at universities in every state.

But helping individuals pursue satisfying careers in education is not one of the program's main goals. Instead, Noyce was created specifically to both increase the number of highly qualified science and math teachers in the nation's poorest schools and raise the achievement levels of students in those schools.

Those are lofty aims, especially when many of the factors that will ultimately determine success or failure—including attitudes toward the teaching profession and the myriad factors that affect how students learn—lie outside NSF's power to control. Still, a recently completed evaluation by Abt Associates of Cambridge, Massachusetts, suggests that the initiative is not having nearly the effect its supporters anticipated.

As part of a broader program evaluation, Abt examined the impact of Noyce grants on teacher production and student achievement in six states. It found that students in science and math classes with Noyce-supported teachers did significantly better on standardized tests than their peers in two of the states, no better in three others, and worse in one state. Similarly, Abt found a small rise in teacher production in two states with Noyce programs, but no impact in three other Noyce states and a drop in one. "Overall, we think that some of the results were expected, some were disappointing, and in one state a big negative," the Abt team reported to an NSF-sponsored conference of Noyce grantees and participants held last summer in Washington, D.C.

NSF officials say they aren't surprised at the lackluster results. Noyce has so many moving parts, agency officials say, that it's unrealistic to expect more than small, halt-

ing steps toward its expansive goals. Besides, they note, any program run by NSF also has a research component that is often difficult to connect to real-time outcomes.

"Noyce is mainly about getting scholarships to kids," says Joan Ferrini-Mundy, head of NSF's education directorate, which runs the Noyce program, describing the program's short-term goal. "But it's also helping us learn more about learning and teaching, and about effective teaching in high-needs districts with a diverse population. Ideally, you'd want that knowledge to feed into the preparation of these teachers."

"And then they go out into the schools," Ferrini-Mundy explains. "It's hard for us to get our hands around that. And frankly, it's not a major focus for us right now."

THE FOUNDATION for the Noyce program was laid in the late 1980s by a moderate Republican congressman from upstate New York named Sherwood Boehlert. Boehlert and many other policymakers were dismayed by the middle-of-the-pack

"There's no way I would have forked out \$28,000 to get trained as a teacher. So yes, I would not be teaching without Noyce."

Tami May, science teacher

performance of U.S. students on international tests in science and math, viewing it as a warning that the country's global lead in science and innovation was imperiled. They were also shocked by the number of classes taught by teachers who had taken few or no math and science courses in college. One study found that 55% of high school physical science classes and 28% of middle school math classes were being led by teachers with little or no training in those fields.

So in 1989 Boehlert, now retired, proposed a new scholarship program at NSF to train math and science teachers. "By offering STEM students prestigious, highly competitive NSF scholarships in return for teaching," he told his colleagues during floor debate on the bill, "the federal government can both attract top students into teaching and send a message about the importance of the field." Lawmakers agreed that NSF was the best federal agency to run a program that awards competitive grants to universities and lets them choose the participants.

In October 1990, Congress gave its final approval, and Noyce was born. (The program's name honors Robert Noyce, co-founder of Intel and the unofficial "mayor"

of Silicon Valley, who had died unexpectedly earlier that year after a heart attack.) But there was no money attached to the legislation, and NSF was loath to shift resources from other programs.

Boehlert didn't give up, however. In 2001 he became chair of the House science committee, and the next year, along with reauthorizing the Noyce program, he convinced appropriators to put \$5 million into NSF's 2003 budget to launch the effort.

Fueled by bipartisan support, Noyce grew to \$55 million in 2008. The next year its budget soared to \$115 million, roughly half of which came from NSF's share of stimulus spending, the massive, one-time infusion of funds to counter the recent financial meltdown. In recent years, the program's annual budget has plateaued at about \$60 million, with \$61 million set aside in 2015.

Besides supporting undergraduates and career changers like Noyce and Shelton, the program offers money to existing teachers, some just learning their way around the classroom and others, so-called master teachers, who want to hone their skills and share their expertise. Noyce also gives scientifically inclined college freshmen and sophomores the chance to spend time in the classroom before deciding whether they want to become teachers. The amount of support varies greatly, from the cost of

tuition and a stipend for full-time students to a \$10,000-a-year salary stipend for master teachers.

THERE ARE MANY REASONS for the current dearth of good STEM teachers. Despite the terrible job market for academic scientists, many mentors of undergraduate STEM students still express disapproval if one mentions a desire to teach in the public schools after graduation instead of pursuing a research career. There's also the low prestige, poor salary, and difficult working conditions attached to the profession.

"In Wisconsin our political leaders have decimated education and made it very unattractive for young people to go into teaching," says Michael Beeth, a science educator who runs a Noyce program for career changers at the University of Wisconsin, Oshkosh. "Frankly, at this point it's hard for me to see how you'd make a career of teaching."

It often takes an external force—a boring job, perhaps, or the relocation of a partner—for a STEM professional to turn to teaching. The principal investigators who run Noyce programs told the Abt evaluators that recruitment remains their biggest challenge.

That certainly was the case for André Green, a chemist and professor of science ed-

ucation at the University of South Alabama in Mobile. In his 2009 Noyce application, Green had promised to crank out 24 well-qualified science teachers over 5 years. But after getting the \$900,000 grant, he wasn't sure how to find them.

May was his first recruit. She was running a pet-sitting business after hours and on the weekends that was more fun—and more profitable—than her day job as a lab tech, tending mosquito traps. But “science comes naturally to me. It's what I love,” she says.

May decided to go back to school for the additional training she would need to become an independent researcher. But she didn't know how she would pay for it. Then a friend told May that the university, where she earned her undergraduate degree in 2006, had money for people who wanted to become science teachers.

“There's no way I would have forked out \$28,000 to get trained as a teacher,” says May, who is now in her third year at Semmes Middle School. “So yes, I would not be teaching without Noyce.”

She is happy she made the move. The aquarium and terrarium in her classroom reflect not just her love of the natural world but also its value as a teaching tool. “Seventh-graders do vertebrates and adaptations, and in eighth grade we do water chemistry,” she explains.

But the chance to indulge her passions doesn't mean she expects to stay in teaching indefinitely, much less at her current school. “Science at our school is barely above an elective,” she says. “It's a core subject, but it's not treated like one.” And that's when she actually gets to teach science. “I'd estimate that a third of my time is spent teaching them how to be a person—learning manners, organizational skills, and the rest.”

Last year, May applied to the district's science and math magnet school, where she says “the kids are higher functioning.” But she wasn't offered a job. And now she's not sure she even wants it. “My heart is getting settled at Semmes,” she says. And she doesn't mind the 20-mile commute from the city to the rural school.

Shelton, too, is committed to teaching, though perhaps not at his current school. He says he had pretty much decided to make the switch into teaching before he learned about the Noyce scholarship.

“I was working myself to the bone for not a lot of money, and not making the world a better place,” he says about his job at an environmental consulting firm. And he didn't balk at the requisite 2-year payback for his 1-year Noyce scholarship (he graduated in 2011 from a master's program at Towson University in Maryland), because, he says,

“I knew that I wanted to stay until I got tenure, which is 3 years.”

He expects money and working conditions to play a major role in deciding where he teaches after that. “I have a long commute to work in a low-paying district, where teachers haven't gotten a raise in 4 years,” he says. And he's confident he has other teaching options. “I drive past three private schools on my way to work,” he notes. At schools like those, he says, “I could teach at a higher level, under better conditions.”

But then he remembers the reason he switched careers. “Those kids will probably get a great education anyway and go on to college,” he says. “So if my goal is to do good on a global scale, then maybe I should teach kids who otherwise might not even realize that college is an option.”

SIMPLY BY REMAINING in the classroom, May and Shelton are doing better than some Noyce participants. NSF data show that 1130 would-be teachers (from a 2013 sample of 8294) have left the program without satisfying the service requirement and, therefore,

Noyce by the numbers

The long-range goals of the Noyce teacher training program are hard to quantify. But here are some simple metrics for assessing the sprawling program.

**\$490
MILLION**

Total NSF investment
(FY 2003–2015)

**\$115
MILLION**

Peak budget
(FY 2009)

494

Total number
of awards

114

Awards made in
peak year (2009)

37%

Success rate for
all applicants

78%

Success rate in
peak year (2009)

8294

Total number of
recipients (as of 2013)

1130

Total who left program
and must repay award

5008

Teaching in high-needs
district (as of 2013)

86%

Only Noyce teacher
in their school

must repay their awards. How long those who do fulfill that requirement actually stick with teaching is anyone's guess. Universities with Noyce grants are not required to track their graduates after they complete their service obligation, Ferrini-Mundy says. In addition, teachers who move out of the district or state are hard to track. There are also no data on how long those who stay in the profession continue to teach in high-needs schools. Like May and Shelton, many undoubtedly feel the lure of better prepared students and better facilities, or simply want a shorter commute.

As important as it is to attract scientifically trained people into teaching, some education experts argue that retaining current science teachers may ultimately be more important to improving STEM education. Researchers have found, for example, that as many as one-fifth of high school science teachers leave the profession after their first year in the classroom. And 5-year attrition rates rise to 50% or higher across the entire profession. “A leaky bucket means not only that there is high attrition, but also that you are losing your investment,” says Richard Ingersoll of the University of Pennsylvania's Consortium for Policy Research in Education.

Ingersoll worries that, by emphasizing recruitment, the Noyce program may not be getting the biggest bang for its buck. “That's a lot of money,” he says about the overall Noyce budget since the program began. “Think what you could do to improve conditions for those already in the classroom with that kind of an investment.”

When John Ewing ran the numbers for the New York City-based teacher training program that he leads, he came to the same conclusion. So last year Ewing decided to shut down Math for America's (MfA's) successful fellowship program, which sent a small number of well-qualified math teachers each year into New York City schools, and switch to supporting the much larger pool of excellent teachers who are already in the city's classrooms.

“We liked our fellows. And the program was very successful,” says Ewing about MfA, which was begun in 2004 by billionaire philanthropist James Simons and has now spread to seven cities around the country. “But training 30 or 40 a year was a blip on the national landscape. Now we're bringing in 250 master teachers, and we plan to grow to 1000. We think it's the missing ingredient in trying to improve the quality of teachers in the country.”

“You're not going to attract the best people into any profession if the profession itself is unattractive,” adds Ewing, who is a mathematician and former executive director



May and André Green, who runs the Noyce program at the University of South Alabama, supervise 7th-grade students dissecting a chicken wing.

of the American Mathematical Society. He notes that teachers lack the peer community that is available to faculty members at a university. “Teaching is one of the loneliest professions,” he says. “That may sound weird, because teachers are around students all day. But they don’t have much of a chance to interact professionally with other teachers in the way that almost every other profession does.”

Under the new program, the master teachers receive \$15,000 a year for 5 years to create and run workshops for their peers, attend seminars taught by professional mathematicians, and become models and mentors for less-experienced teachers. If Ewing reaches his goal, MfA will be supporting roughly 10% of the math and science teachers in the city. And supporting a master teacher is much less expensive than training a new teacher, he says, notwithstanding “the vast quantities of pizza that they eat.”

James Wyckoff, a professor of education and policy at the University of Virginia in Charlottesville who has studied alternative teacher-training programs like MfA, thinks that besides acting as mentors for existing teachers, master

teachers may point to better ways to train new ones. “What are they learning in their first 3 to 5 years that makes them better?” he asks. “And can those things be learned while they are still in school?”

The Woodrow Wilson National Fellowship Foundation in Princeton, New Jersey, is also shifting its focus away from attracting new blood into teaching and toward helping those already in the classroom, says its president, Arthur Levine. The ability to have a larger impact on the profession is one reason, says Levine, the former head of Columbia University’s Teachers College, but so is

the need to adapt to local economic conditions and state education laws.

“In Michigan, for example, they aren’t hiring very many teachers,” explains Levine, whose foundation partners with governors and school officials in seven states to improve teacher training programs at universities and offers individual fellowships. “So we don’t want to overproduce. Instead, we want to work with existing teachers whose knowledge has become outdated or who are teaching out of field. Michigan also requires interdisciplinary science, and most people aren’t trained to teach that.”

Noyce graduates, however, are largely on their own once they leave the program. NSF data show that 86% of them work in schools with no other Noyce-supported teachers.

The program continues to receive strong support from Congress. And poor schools continue to need more well-trained STEM teachers. But the extent to which Noyce can close that gap remains an open question.

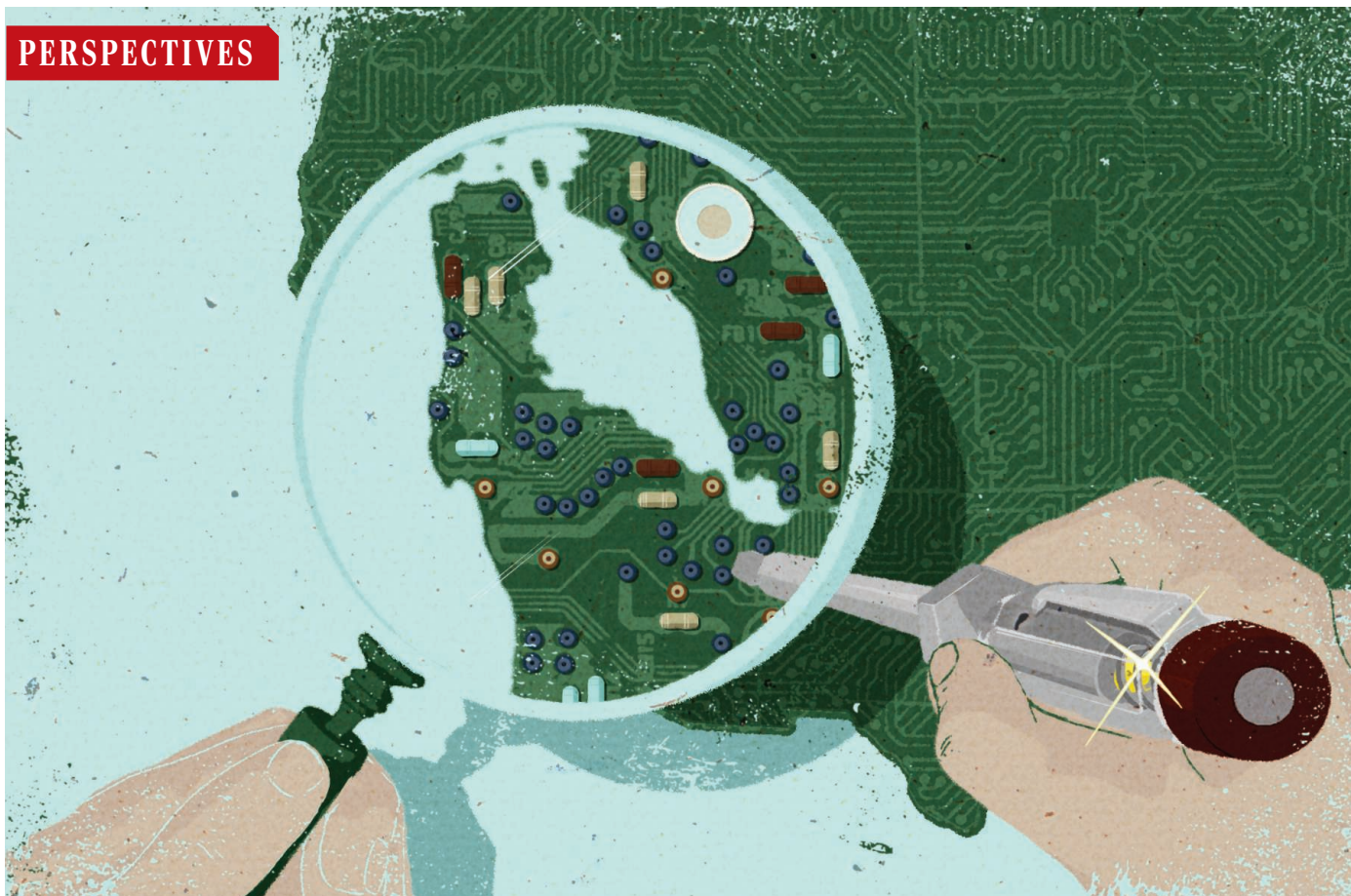
“We actually know very little about what works best and why,” Levine says. “We’re doing a lot, but we don’t have hard data to back it up.” ■

“Teaching is one of the loneliest professions. ... [They] are around students all day. But they don’t have much of a chance to interact professionally with other teachers in the way that almost every other profession does.”

John Ewing, Math for America



PERSPECTIVES



INNOVATION ECONOMICS

Where is Silicon Valley?

Forecasting and mapping entrepreneurial quality

By **Jorge Guzman¹** and **Scott Stern^{1,2*}**

Although economists, politicians, and business leaders have long emphasized the importance of entrepreneurship (1, 2), defining and characterizing entrepreneurship has been elusive (3, 4). Researchers have been unable to systematically connect the type of high-impact entrepreneurship found in regions such as Silicon Valley with the overall incidence of entrepreneurship in the population (5–7). This has important implications: Researchers arrive at alternative conclusions

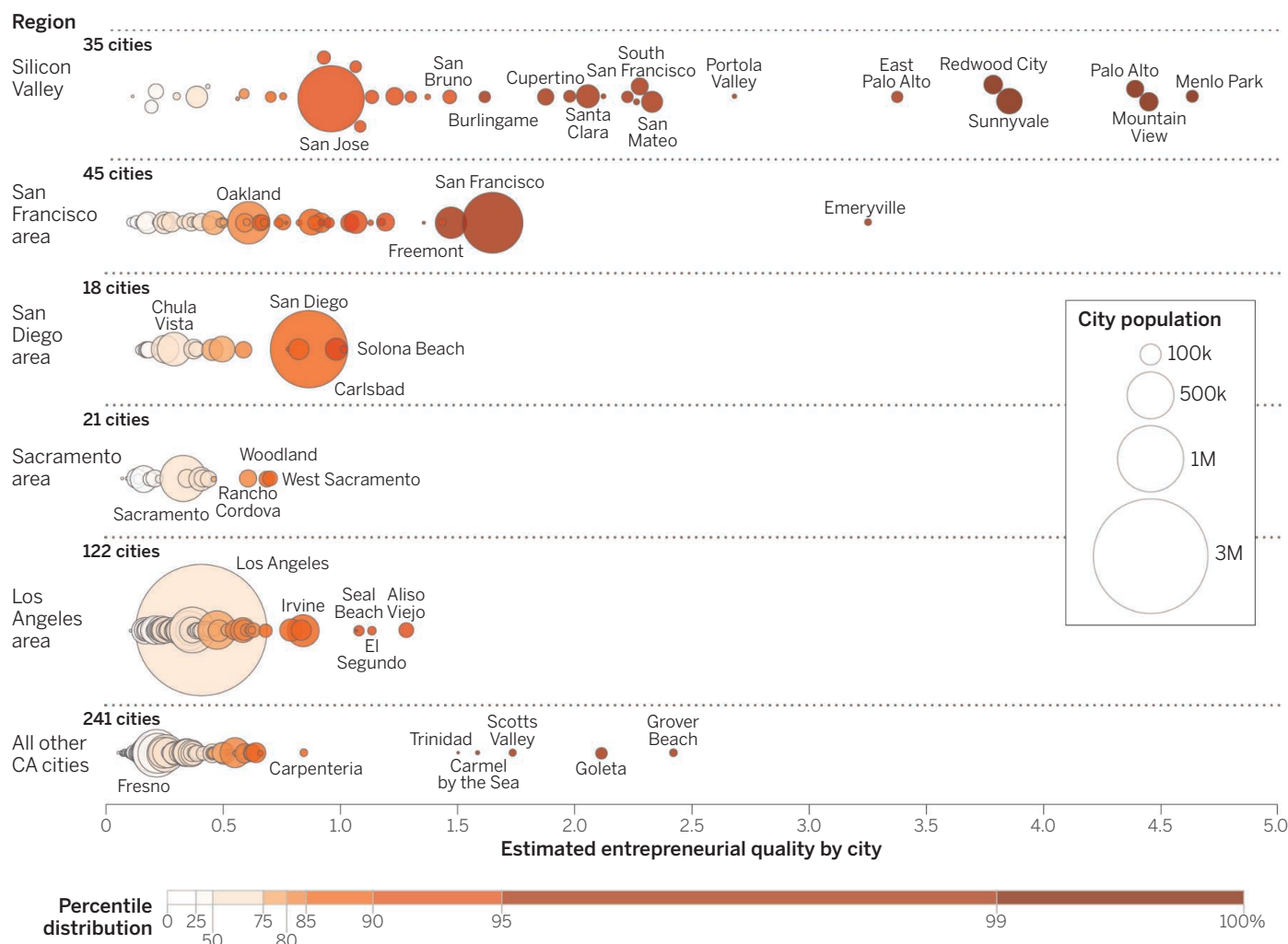
about roles and patterns of entrepreneurship (8–10), and policy-makers are given conflicting recommendations about whether or how to promote entrepreneurship for economic and social progress (11, 12).

To break this impasse, we introduce a new method for studying the founding and growth of entrepreneurial ventures. Whereas most prior studies have focused on the quantity of entrepreneurial ventures (e.g., the number of new businesses per capita in a given region), we focus on characterizing their quality. Rather than assume that all ventures have

an equal ex ante probability of success, our method allows us to estimate the probability of growth based on information publicly available at or near the time of founding.

We implement our approach using for-profit business registrations in California from 2001 to 2011 (13), combined with data from the U.S. Patent and Trademark Office and SDC Platinum [details on data and methods are in the supplementary materials (SM)]. We estimate outcomes on the basis of a small number of start-up characteristics: (i) firm name characteristics, including whether the firm name is eponymous [named after

California quality is all over the map



the founder (14)], is short or long, is associated with local business activity or regionally traded clusters (e.g., dry cleaning versus manufactured goods), or is associated with a set of high-technology industry clusters (15, 16); (ii) how the firm is registered, including whether it is a corporation [rather than partnership or limited liability company (LLC)] and whether it is incorporated in Delaware (17); and (iii) whether the firm establishes control over formal intellectual property (IP) rights within 1 year of registration (18).

To ensure that our estimate reflects the quality of start-ups in a location rather than assuming that start-ups from a given location are associated with a given level of quality, we exclude location-specific measures from the set of observable start-up characteristics.

Estimating entrepreneurial quality by city. Each bubble represents a city. Bubble size reflects city population. Bubble color varies according to quality scale at bottom of figure. Each row represents distinct geographic region. See SM.

We estimate entrepreneurial quality as the probability of achieving a meaningful growth outcome—defined as an initial public offering (IPO) or an acquisition (19) within 6 years of founding—as a function of these start-up characteristics. This predictive, location-agnostic algorithm can then be used to independently characterize the entrepreneurial quality of firms and locations.

ESTIMATING ENTREPRENEURIAL QUALITY. We estimate entrepreneurial quality through a logit model with a randomly selected sample of 70% of all firms registered in 2001–2006 (keeping the other 30% as a test sample). Our model incorporates business registration and IP factors in a single

regression, with all coefficients significant at the 5% level (20) (table S1). When we look at firm name characteristics, eponymous firms are more than 70% less likely to grow than noneponymous firms, whereas firms with short names are 50% more likely to grow than firms with long names, and firms that include words associated with high-technology clusters are 92% more likely to grow than others. Looking at legal form and IP, corporations are >6 times more likely to grow than noncorporations, and firms with trademarks are >5 times more likely to grow than nontrademarked firms. Patenting and Delaware jurisdiction play an outsized role: Each alone is associated with a >25 times increase in the probability of growth relative to not being present. When both are present at the same time, there is nearly a 200 times increase in the probability of growth.

As a validation test, we estimate entrepreneurial quality for the test sample withheld from the original regression and so

¹Sloan School of Management, Massachusetts Institute of Technology, Cambridge, MA 02142, USA. ²National Bureau of Economic Research, Cambridge, MA 02138, USA. *E-mail: sstern@mit.edu

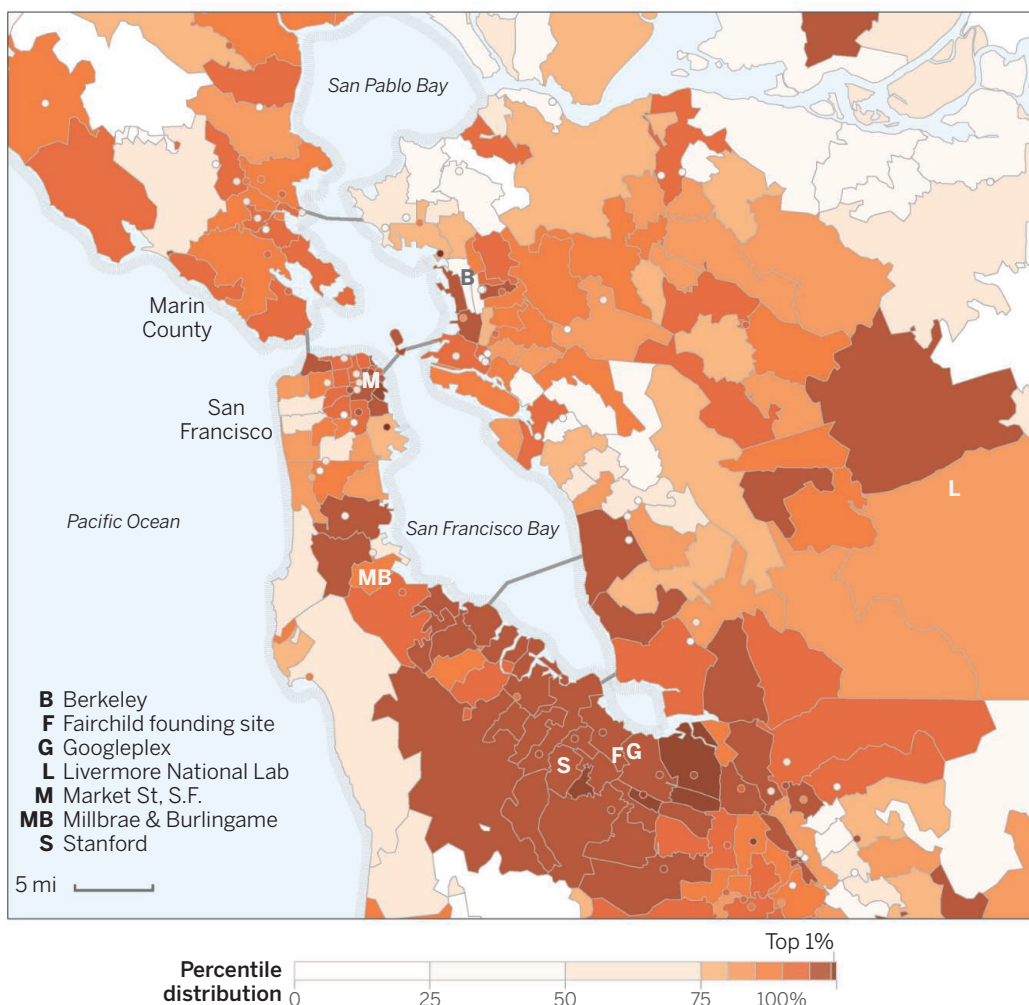
compare our predictions of entrepreneurial quality to the actual outcome distribution. Our estimate of entrepreneurial quality is strongly related to out-of-sample outcomes: 76% of all growth outcomes in the test sample are within the top 5% of the distribution of estimated entrepreneurial quality, with 56% drawn from the top 1% of that distribution (fig. S1). Highlighting the extreme uncertainty associated with entrepreneurship, growth is still rare: Even within the top 1% of estimated entrepreneurial quality, the average firm has only a 5% chance of realizing a growth outcome. This is consistent with recent findings that start-up growth is skewed relative to overall firm growth—Gibrat's law (21).

MAPPING ENTREPRENEURSHIP. The centerpiece of our analysis focuses on recent cohorts before a growth outcome has occurred (i.e., all start-ups from 2007 to 2011). We estimate the entrepreneurial quality for each firm and then calculate the average estimated quality of firms by city and, separately, by ZIP Code. These scores can be interpreted as the expected number of growth outcomes per 1000 start-ups in the 2007–2011 cohorts.

Average quality across municipalities is shown in the first figure. Silicon Valley stands out from other regions across California: Start-ups in Menlo Park, Mountain View, Palo Alto, and Sunnyvale have 20 times the average quality of the median city and 90 times that of the lowest-ranked cities in California. Among large cities, San Francisco registers an entrepreneurial quality level nearly 8 times that of Fresno.

Entrepreneurial quality is mapped for the San Francisco Bay area at the ZIP Code level in the second figure. The quality of entrepreneurial activity is distinctively higher in the area that ranges just north of San Jose through San Francisco, with a contiguous mass of intense entrepreneurial quality from just southeast of Google (and the founding location of Fairchild) through Millbrae and Burlingame. In contrast, the Los Angeles region has a much lower level of entrepreneurial quality (fig. S2). Large economic areas can vary significantly in their quality. We investigated the statistical relation between

Better by the Bay



Mapping estimated entrepreneurial quality by ZIP Code. San Francisco Bay area. Dots indicate single-address ZIP Codes. See SM.

quality and quantity (fig. S3): At best, the relation is weak and noisy. Intriguingly, across regions, entrepreneurial quality is centered around research institutions, such as universities and national laboratories. Stanford is at the heart of Silicon Valley, and University of California (UC) Berkeley; Lawrence Livermore; Caltech; University of California, Los Angeles (UCLA); and UC Irvine each host a region of distinctive entrepreneurial quality.

IMPLICATIONS. By focusing on entrepreneurial quality, we can evaluate more clearly the role of location and institutions in firm growth. For example, our method allows us to estimate a locational entrepreneurship “premium” as the difference between realized and expected growth outcomes for a region. Between 2001 and 2006, Silicon Valley had 60% more actual growth events than predicted by our model, whereas Los Angeles registered 13% fewer than predicted.

Our method can be extended to evaluate entrepreneurial quality at arbitrary levels of geographic aggregation (e.g., a specific street in Palo Alto) (fig. S4). This facilitates fine-grained analysis of entrepreneurial dynamics (22), distinguishing empirically (although not causally) between locations at a high level of granularity.

Finally, beyond our characterization of Silicon Valley in the aggregate, our results highlight the role of research institutions as centers of entrepreneurial quality. Characterizing the two-way relation between entrepreneurial quality and scientific research activity is a promising agenda for future research. Although one would need to be cautious about using these estimates as a policy tool (for example, one could imagine “gaming” of various sorts), clarifying the conditions that facilitate positive growth outcomes has important implications for policy-makers and regional stakeholders.

REFERENCES AND NOTES

1. Z. Acs, D. Audretsch, *Innovation and Small Firms* (MIT Press, Cambridge, MA, 1990).
2. W. Baumol, R. Litan, C. J. Schramm, *Good Capitalism, Bad Capitalism, and the Economics of Growth and Prosperity* (Yale Univ. Press, New Haven, CT, 2007).
3. E. Hurst, B. W. Pugsley, "What do small businesses do?" (Brookings paper 73-118, Brookings Institution, Washington, DC, 2011).
4. M. Henrekson, T. Sanandaji, *Proc. Natl. Acad. Sci. U.S.A.* **111**, 1760 (2014).
5. R. W. Fairlie, *Kaufman Index of Entrepreneurial Activity: 1996–2013* (Ewing Marion Kaufman Foundation, Kansas City, MO, 2014).
6. L. Klapper, R. Amit, M. F. Guillén, in *International Differences in Entrepreneurship*, J. Lerner, A. Schoar, Eds. (Univ. of Chicago Press, Chicago, 2010), pp. 130–158.
7. J. E. Amorós, N. Bosma, *Global Entrepreneurship Monitor: 2013 Executive Report* (London Business School, London, and Babson College, Wellesley, MA, 2014).
8. R. Decker, J. Haltiwanger, R. Jarmin, J. Miranda, *J. Econ. Perspect.* **28**, 3 (2014).
9. S. Kaplan, F. Murray, *Technology and Organization*, N. Phillips, G. Sewell, D. Griffiths, Eds. (Emerald Group, Bingley, UK, 2010), pp. 107–147.
10. S. Shane, S. Venkatamaran, *Acad. Manage. Rev.* **25**, 217 (2000).
11. J. Lerner, *Boulevard of Broken Dreams* (Princeton Univ. Press, Princeton, NJ, 2009).
12. S. Samila, O. Sorenson, *Res. Policy* **39**, 1348 (2010).
13. Formal registration includes corporation, LLC, limited partnership, and general partnership.
14. S. Belenzon, A. K. Chatterji, B. Daley, *Eponymous Entrepreneurs* (2014); https://faculty.fuqua.duke.edu/~bd28/BCD_EE.pdf.
15. M. Delgado, M. E. Porter, S. Stern, "Defining clusters of related industries" (NBER Working Paper 20375, National Bureau of Economic Research, Cambridge, MA, 2014); www.nber.org/papers/w20375.
16. We define traded and local industries in line with the definition used in the economic cluster literature [e.g., (15)], and high-technology clusters are drawn from the U.S. Cluster Mapping Project [see (15)].
17. Many firms with the intention to grow register in the state of Delaware, where corporate law is beneficial owing to a large legal canon. Venture capitalists often prefer companies to incorporate in Delaware.
18. Our use of firm names builds on a basic assumption that entrepreneurs choose firm names conscientiously to serve as a signal to consumers, investors, and employees and that there are costs in impersonating a different type of firm.
19. An IPO or acquisition represents a significant and observable equity growth outcome from the perspective of the founders. Our ongoing research agenda also explores alternative growth outcomes in terms of employment, firm revenues, and so on.
20. Results are similar when we look at business registration and IP factors alone; see columns 1 and 2 in fig. S1.
21. L. M. B. Cabral, J. Mata, *Am. Econ. Rev.* **93**, 1075 (2003).
22. J. Guzman, S. Stern, *Nowcasting and Placecasting Entrepreneurial Quality and Performance* (NBER, Cambridge, MA, 2014); www.nber.org/chapters/c13493.pdf.

ACKNOWLEDGMENTS

We thank the Jean Hammond (1986) and Michael Krasner (1974) Entrepreneurship Fund and the Edward B. Roberts (1957) Entrepreneurship Fund for financial support. We thank participants in the Massachusetts Institute of Technology (MIT) Innovation and the Digital Economy Seminar, the MIT Regional Entrepreneurship Acceleration Program, the Micro@Sloan Seminar, the Asian Innovation and Entrepreneurship Association–NBER Conference, and three anonymous referees for comments. I. Cockburn, M. Delgado, J. Gans, H. Varian, and C. Fazio provided valuable advice. We thank R. J. Andrews for excellent development of figures and visualizations, A. Carracuzzo and MIT Libraries for data support, and I. DiMambro for editorial assistance.

SUPPLEMENTARY MATERIALS

www.sciencemag.org/content/347/6222/606/suppl/DC1

10.1126/science.aaa0201

IMMUNOLOGY

There goes the macrophage neighborhood

Migrating dendritic cells disrupt lymph node macrophages and limit the immune response to secondary infection

By Heather D. Hickman

The lymph node is a highly structured organ optimized for generating adaptive immune responses. Lymph fluid carrying pathogens and their antigens from infected tissue is first distributed into a large cavity just beneath the node's surface, which is populated by a dense layer of specialized macrophages. These subcapsular sinus (SCS) macrophages filter incoming lymph, capture pathogens, and relay pathogen-derived antigen to B cells in subadjacent follicles, provoking them to produce antibodies (see the figure). At the original infection site, migratory dendritic cells (DCs) are activated, acquire antigen, and deliver it to the node through the lymph, generating a secondary wave of immune cell activation. Until now, this influx of DCs has been viewed as beneficial to the host, as they activate T cells within the node's paracortex. However, on page 667 of this issue, Gaya *et al.* (1) demonstrate that incoming DCs can be harmful. These cells can disrupt the SCS macrophage layer and reduce the host's ability to mount a humoral (antibody) response to a secondary pathogen.

Resident antigen-presenting cells in the lymph node are commonly classified into two major subsets: DCs and macrophages. Both populations are a complex, heterogeneous mixture of cells with somewhat nebulous differences and overlapping capabilities. Even so, it is clear that different cellular subsets within each population preferentially localize to distinct regions of the lymph node where they can optimally activate discrete aspects of immune responses (2). For example, CD8 α DCs reside in the interior of the node, are efficient exogenous antigen gatherers, and are needed for optimal T cell activation after viral infection (3). Several subsets of DCs are not present (in appreciable numbers) in steady-state lymph nodes, but traffic to nodes from peripheral tissue sites after infection or inflammation. Because activation, and particularly migration, take time, hours to days may elapse before immigrant DCs can influence the immune response. It is unclear how these migratory DCs precisely navigate

nodal architecture to situate themselves in the node's interior; however, their arrival is essential for eliciting maximal T cell responses to many pathogens (4).

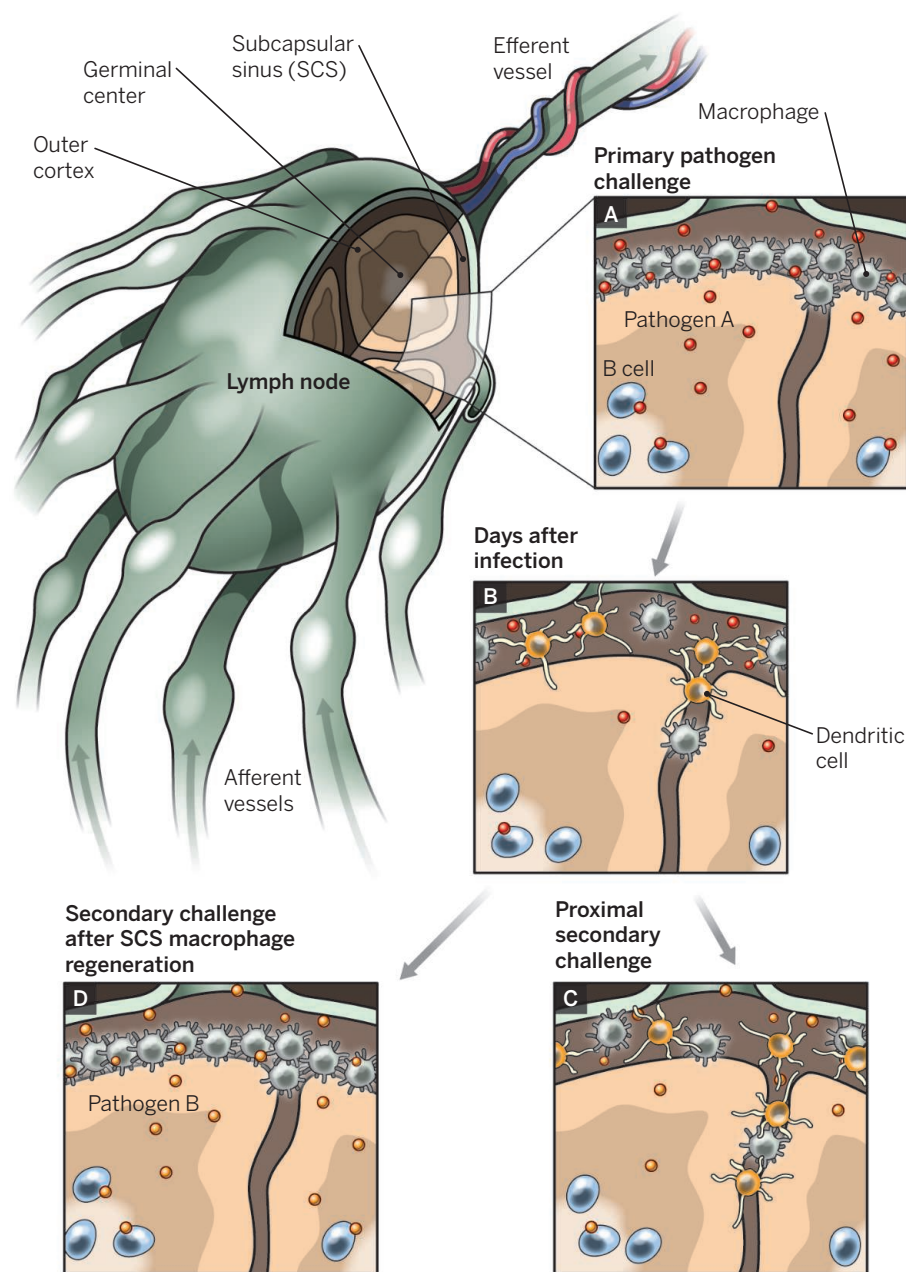
SCS macrophages, typically distinguished by the expression of the cell surface marker CD169 and the absence of F4/80 (found on medullary macrophages in the node), form a sessile, carpet-like layer along the floor of the SCS. After subcutaneous injection of viruses or antigen-antibody immune complexes, SCS macrophages transfer antigen on cellular processes to closely apposed B cells that lack direct access to SCS contents

"The evolutionary advantage of reduced responses to ... secondary challenges is puzzling."

(5–8). This antigen-capture process both activates B cells and removes infectious material from the lymph, preventing entry into the bloodstream. Accordingly, depletion of SCS macrophages from the node before infection can result in failure to control pathogen dissemination, leading to the infection of distal organs (6, 9, 10).

Although carefully scrutinized previously with primary infection models, the behavior and function of SCS macrophages have not been systematically followed for extended periods after infection. To close this gap, Gaya *et al.* used sophisticated techniques to image skin-draining murine lymph nodes 1 week after cutaneous infection with a variety of pathogens (including *Staphylococcus*, group B *Streptococcus*, and vaccinia virus). Intriguingly, the authors observed fragmentation of the SCS macrophage layer after infection with any of the pathogens, with as much as 80% of the layer disrupted. Gaya *et al.* also assessed the ability of various additional stimuli to deplete the SCS macrophage layer. Whereas the injection of inert beads or dead

National Institutes of Health, Bethesda, MD, USA. E-mail: hhickman@mail.nih.gov



Node, disrupted. (A) Pathogens (red) entering tissue at a site of infection drain into the lymph node. A layer of sessile macrophages filters pathogens from the subcapsular sinus (SCS). (B) SCS macrophages present pathogen-derived antigen to B cells (blue) in the underlying follicles. The activated B cells form germinal centers and produce antibody. (C) After the primary infection, dendritic cells (yellow) migrate into the node and disrupt the macrophage layer. If another pathogen (orange) drains into the node, B cells cannot mount a maximal antibody response. (D) When the macrophage layer regenerates, B cells can again participate in humoral immunity.

virus left SCS macrophages intact, delivery of agonists (microbe-derived products) of toll-like receptors altered SCS macrophage continuity. Activation of toll-like receptors leads to the production of inflammatory cytokines, DC maturation, and DC migration. Thus, inflammation, rather than particulate-carrying lymph per se, is needed for this dramatic breakdown in lymph node architecture.

Remarkably, lymph nodes can expand to at least 10-fold their original volume within

a few hours of infection—a feat dependent upon DCs (11, 12). Gaya *et al.* ruled out SCS macrophage disruption as a generalized consequence of nodal expansion by unlinking nodal expansion and the ability of DCs to respond to inflammation. Only nodes with immigrating DCs exhibited SCS macrophage discontinuity. Disruption of the SCS macrophage layer was attributed both to macrophage death and to macrophage migration into the interior of the node. Because most

of the stimuli Gaya *et al.* studied do not infect and/or otherwise kill macrophages, these observations raise questions regarding the precise mechanism for displacement of the SCS macrophage layer by DCs. If this event is simply a consequence of macrophage disturbance by incoming DCs as they traverse the SCS floor, then migration would have to be remarkably equitably distributed above areas of the node that typically do not house large numbers of migratory DCs (e.g., the B cell follicles) (2). Alternatively, rather than displacing macrophages, incoming DCs might signal them to migrate as well.

How well does a fragmented SCS macrophage layer function in generating an antibody response to secondary infections? Not very. Gaya *et al.* transferred B cells deficient in toll-like receptor 9 into normal mice. Delivering an activating signal for the receptor to disrupt the SCS macrophage layer (without activating the transferred B cells) decreased B cell capture of subsequent lymph-borne antigen by a factor of 15. Further, B cells responding to secondary infection after SCS macrophage disruption generated diminished numbers of germinal center B cells and fewer antibody-secreting cells.

The evolutionary advantage of reduced responses to temporally proximal secondary challenges is puzzling. Perhaps disrupting SCS macrophage function focuses immune responses on the primary pathogen or plays an essential role in this response. Indeed, the centripetal movement of pathogen-laden macrophages in the lymph node could be an important source of antigen for follicular DCs, driving the development of B cells (antibody affinity maturation). A non-mutually exclusive possibility is that, because inflammation alone can trigger SCS macrophage disruption and shut down antibody responses, this phenomenon may minimize autoimmune responses that develop after lymph drainage of self-antigens that are liberated during chronic inflammatory responses. ■

REFERENCE AND NOTES

1. M. Gaya *et al.*, *Science* **347**, 667 (2015).
2. M.Y. Gerner *et al.*, *Immunity* **37**, 364 (2012).
3. K. Hildner *et al.*, *Science* **322**, 1097 (2008).
4. W.R. Heath, F.R. Carbone, *Nat. Immunol.* **14**, 978 (2013).
5. C.C. Norbury *et al.*, *Nat. Immunol.* **3**, 265 (2002).
6. T. Jun *et al.*, *Nature* **450**, 110 (2007).
7. H.D. Hickman *et al.*, *Nat. Immunol.* **9**, 155 (2008).
8. T.G. Phan *et al.*, *Nat. Immunol.* **10**, 786 (2009).
9. M. Iannaccone *et al.*, *Nature* **465**, 1079 (2010).
10. W. Kastenmüller *et al.*, *Cell* **150**, 1235 (2012).
11. S. Chyow *et al.*, *J. Immunol.* **187**, 5558 (2011).
12. S.E. Acton *et al.*, *Nature* **514**, 498 (2014).

ACKNOWLEDGMENTS

H.D.H. is supported by the Intramural Research Program, National Institute of Allergy and Infectious Diseases, National Institutes of Health.

10.1126/science.aaa6919

Taking temperature at the nanoscale

A local probe technique can determine temperature with nanometer-scale resolution

By Christian Colliex

Measuring temperature has become commonplace since Fahrenheit, Celsius, and others introduced thermometers and temperature scales in the 18th century. However, the definition of temperature is not at all obvious, as it is now described as a statistical quantity given by the rate of change of entropy with respect to the internal energy of a system with volume and number of particles held constant. This is by itself not an easy concept to grasp. In addition, determining temperature raises thermodynamical questions when considering systems with further and further reduced dimensions (1). Consequently, measuring temperature at the nanoscale constitutes a challenge in many fields of science and technology. On page 629 of this issue, Mecklenburg *et al.* (2) report how they have elegantly met this challenge.

In practice, one has to invent or adapt a new form of thermometry, sensing at the relevant spatial scale the variation of a measurable physical property such as electrical resistivity, color and/or intensity of photon emission, and volume and/or pressure. As even smaller scales are considered, it is also important to use a noninvasive geometry, avoiding the introduction of a temperature gradient between the thermometer and the material to be measured. Several approaches describe promising routes to nanoscale thermometry. They markedly depend on the environment under study (inorganic versus organic), the temperature range of concern, and the required sensitivity in position and in temperature.

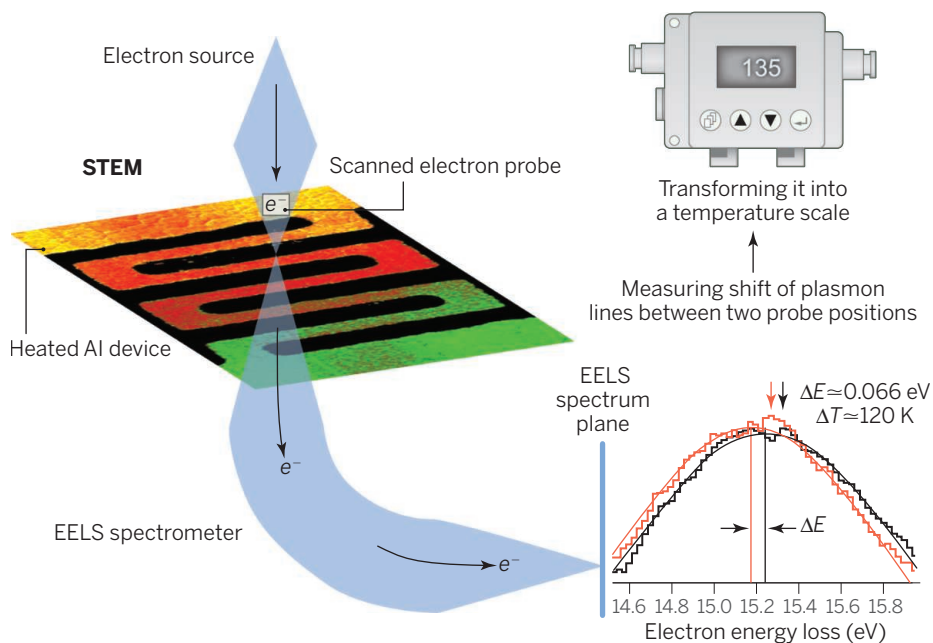
As an example, for nanometer-scale thermometry in a living cell, the temperature dependence of the electron spin resonance signal associated with the nitrogen-vacancy color centers in nanodiamonds was measured (3). The length scale of this technique is ~200 nm under confocal optical microscopy, while the accuracy of this type of sensor is quite high (~50 μ K) in the temperature domain of interest for the study of living materials (around 25°C).

The transmission electron microscope (TEM) is the preeminent instrument for

observing, analyzing, and measuring at the subnanometer scale. Consequently, temperature indicators on a specimen prepared as a thin foil have been sought in the different signals (images of atomic structure, lattice parameters in diffraction patterns) that TEMs deliver, but so far without practical development. Electron energy-loss spectroscopy (EELS) is another important channel of information. As early as 1956, Watanabe (4) pointed out that the energy of the bulk plasmon line (that is, the collective response of the quasi-free electrons in the solid) should depend on the temperature through the associated volume expansion and consequent reduction in electron density. But this was undetectable by his instrument at that time. More recently, the volume plasmon energy in aluminum was measured over the range of temperature between -175° and 500°C, with a high-resolution energy-loss spectroscopy TEM (5). From the results, it seems that the variation in energy loss of the plasmon line for this element is ~0.5 to ~0.6 meV/K, the detection of which constitutes a challenge. Furthermore, in these early studies, the spatial resolution was not mentioned, although Seah and Smith (6) argued for the use of plasmons as “quanta for microregion tem-

perature measurement” after an analysis of the shifts in the plasmon loss energies measured in the reflection EELS spectrum of 1-keV electrons from the surface of pure tin.

Mecklenburg *et al.* report the two-dimensional mapping, with ~5-nm resolution, of the temperature variation in a serpentine aluminum microdevice that can be locally heated (see the figure). In a scanning TEM (STEM) environment, they measure the value of the energy loss associated with the excitation of the plasmons, for each position of the primary electron probe on the specimen. The recorded EELS spectra encompass both the zero-loss peak and the plasmon peak at 15.2 eV, which exhibit typical full width at half-maximum in the 1-eV range (i.e., much broader than the scale required for useful thermometry). Consequently, a specific procedure for handling the data has been established: It consists in measuring the center of the plasmon peak, best-fitted to a Gaussian curve, and deducing from its relative variation with respect to a reference spectrum, recorded at temperature T_0 , the associated change in temperature $T - T_0$. The accuracy in T measurement (standard deviations of ~3 to ~5 K) is made possible by averaging over



Getting the temperature spot-on. The chain of components from the electron beam source in the electron microscope to the display of the temperature of a nanoscale area of the specimen.

several tens of pixels in the image (typically 64) and by the high signal-to-noise ratio in the spectra. The authors extensively describe the sources of errors, both of a statistical nature at different stages of the data processing (signal, plasmon energy, temperature) and of an intrinsic nature due to the specimen itself (nonhomogeneity of the specimen, role of gain boundaries, influence of thickness variations). They also justify the noninvasive character of their thermometer, noting that the current in the electron probe should not provoke an appreciable temperature rise in a thermal conductor about 100 nm thick. The technique paves the way for a more thorough investigation of the factors governing the spatial resolution, as it distinguishes those contributions related to the measurement technique (delocalization arising from the use of a high-energy electron beam) from those associated with the quantity (temperature) under measurement depending on the local transport of heat via electrons or phonons.

Another emerging application of STEM-EELS, made accessible by the implementation of monochromators, is that of vibrational spectroscopy (7). In the case of high-angle impact scattering of incident electrons on the nuclei of the specimen, the same type of data processing as that used by Mecklenburg *et al.* could provide a way to the mapping of masses and isotopes with atomic resolution (8). To distinguish ^{12}C from ^{13}C , for instance, it would be necessary to measure shifts of a few milli-electron volts on the center of characteristic peaks situated in the tens of milli-electron volts loss range.

The work of Mecklenburg *et al.* opens new routes for pushing the limits in the micro (nano)-electronics domain. In particular, the combination of fabrication techniques for devices of smaller sizes and STEM instruments with aberration correctors for the probe (more current in a probe of given size) and with monochromators (with typical 10-meV energy resolution giving access to the natural width of the involved excitations) could enable fundamental studies of the quantum aspects of heat conduction. ■

REFERENCES

1. M. Hartmann, G. Mahler, O. Hess, *Phys. Rev. Lett.* **93**, 080402 (2004).
2. M. Mecklenburg *et al.*, *Science* **347**, 629 (2015).
3. G. Kucsko *et al.*, *Nature* **500**, 54 (2013).
4. H. Watanabe, *J. Phys. Soc. Jpn.* **11**, 112 (1956).
5. H. Abe *et al.*, *J. Electron Microsc. (Tokyo)* **41**, 465 (1992).
6. M. P. Seah, G. C. Smith, *J. Mater. Sci.* **21**, 1305 (1986).
7. O. L. Krivanek *et al.*, *Nature* **514**, 209 (2014).
8. G. Argentero *et al.*, *Ultramicroscopy* **10.1016/j.ultramic.2014.11.031** (2015).

10.1126/science.aaa5311

NEUROSCIENCE

Our skewed sense of space

The distribution of neuron activity reveals an organization that supports the brain's spatial mapping capacity

By György Buzsáki

The hippocampus is the brain region where spatial maps of our surroundings are encoded. A specific location will activate a set of neurons called place cells to represent the particular place. What happens as the number of environments encountered increases? Does the hippocampus continually create and store distinct independent “maps” for each locale, or can place cells be recruited for more than one map to generalize across locales? It appears that both mechanisms contribute in unique ways.

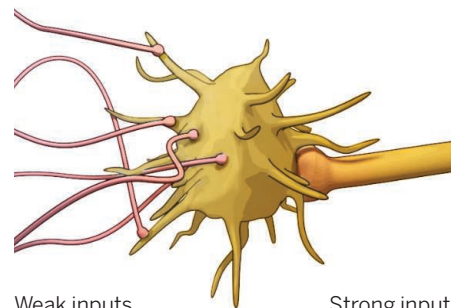
At any given position of space, a subset of hippocampal pyramidal cells is active (hence they are called “place cells”), and the firing fields of single neurons (“place fields”) can be regarded as units of spatial representation (1). Collectively, the active sets of place cells track the position of the animal in the environment, and thus they are hypothesized to provide a “code” for space. But the exact nature of this code is unknown.

Several overlapping stories emerged recently about the statistical structure of hippocampal neuronal activity (firing patterns) and its relationship to “coding” for the environment (2–5). The activity of place cells when an animal (rat) experiences a small, large, new, or familiar environment demonstrates that although the majority of these neurons have single place representation, a small minority can have many (see the second figure). Analyses of the observed skewed distribution of place fields and other log-like features of the firing patterns of hippocampal neurons offer a link between physiological organization and the long-known Weber-Fechner law of psychophysics, which describes our subjective perceptions on a logarithmic scale. Accordingly, when the stimulus strength is multiplied, the strength of our perception is only additive.

To examine the relationship between neuronal firing patterns in the hippocampus and the nature of representation of the environment, rats were tested in a familiar open field, a linear maze, and a radial arm maze. Although the majority of CA1 and CA3 pyramidal neurons had single place fields, a small fraction fired at multiple locations (2).

Thus, both the majority and the minority of hippocampal neurons tiled the environments and the distribution of space coverage by individual place cells was strongly skewed (see the second figure). The within-place field firing rates of individual neurons were also skewed and followed a lognormal form (i.e., a bell-shaped distribution on a log scale). In turn, firing rates correlated with both the number and size of place fields (5).

In a given environment, only a fraction of pyramidal neurons are active. Will every

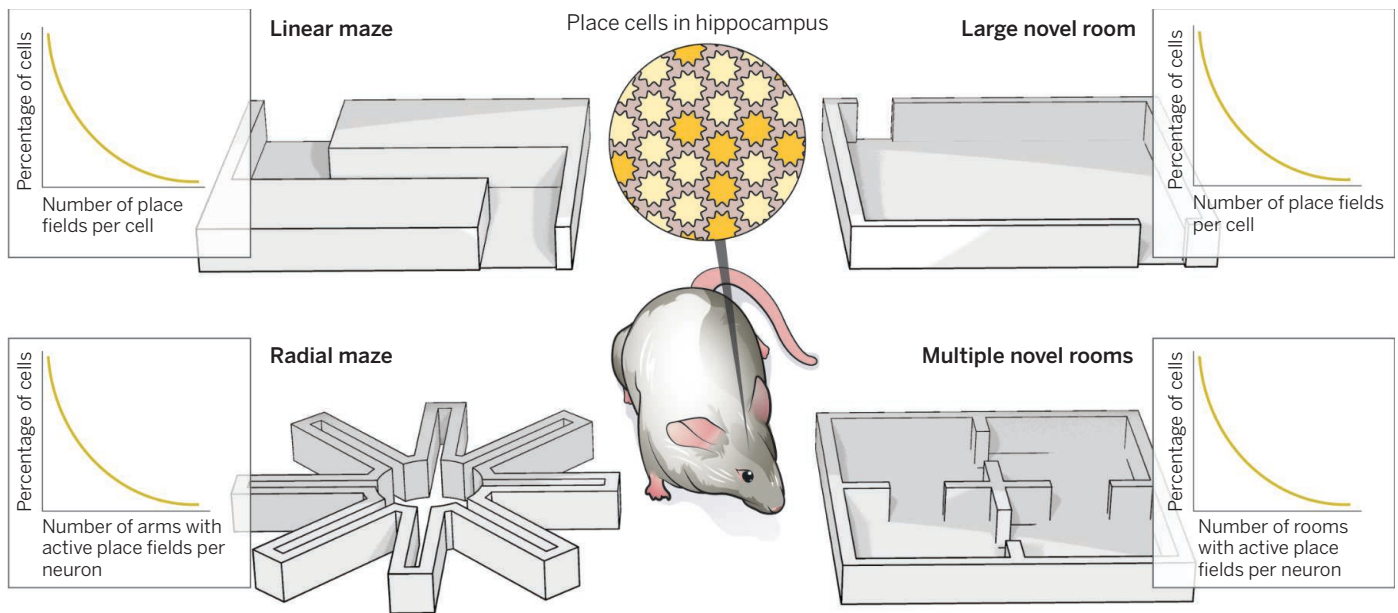


Mixed messages. Neurons with multiple place fields have higher firing rates than the majority of neurons with single place fields. Thus, neurons downstream of the hippocampus receive a mixed message—the majority of weakly active neurons convey information about the distinctness of the environment, whereas the strongly firing minority suggests similarity.

neuron eventually become a place cell if the animal explores a large environment? Another recent study explored this question by training rats to run an expandable maze track with lengths of 3, 10, 22, and 48 m in the same large room (3). Place cells active on the short tracks could form additional place fields for larger tracks, as new place cells were recruited from the pool of silent hippocampal cells. The number of fields formed by the CA1 pyramidal neurons was strongly skewed: A few neurons had many fields, whereas many neurons had only one or none. By increasing the maze length, the place fields showed a log-like recruitment, and extrapolation from the observed distributions suggested that nearly all hippocam-

New York University Neuroscience Institute, New York University Langone Center, New York, NY 10016, USA. E-mail: gyorgy.buzsaki@nyumc.org

ILLUSTRATION: V. ALTOUNIAN/SCIENCE



Skewed distribution. The number of place fields per neuron (place cell) in the hippocampus shows a skewed distribution with most place cells having none or one place field, whereas a minority have several place fields. This distribution is present in an open environment (shown as a linear maze), radial arm maze, large room [presented as linear tracks of increasing size in a single room (3)], or in multiple rooms [new or familiar (4)].

pal pyramidal cells would be active in an environment with a diameter of ~1 km.

In another study, investigators asked whether independent place cell codes are present in multiple environments (4). Rats were placed in one familiar box as well as in 10 new boxes, each placed in a different room. Most CA3 pyramidal neurons fired only in a single box, but a small minority fired in all or multiple boxes, showing a log-normal distribution of the overlap of neuronal activity in the different rooms. Thus, although the hypothesis of completely independent (or “orthogonal”) representation is supported by the majority of place cells with single-room activity, the “heavy tail” of distributions containing ~15% of the neurons active in multiple rooms suggests a more complex picture.

Overall, these studies (2–5) demonstrate that the skewed distribution of place fields is a general rule, irrespective of the nature or size of the testing environment. What could be the advantages of the skewed distributions for coding for space? From the perspective of independent coding (6), the minority of neurons with multiple place fields are regarded as “noise” or imperfection of the system. But when other physiological features of the heavy “tail-forming” minority are also considered, a different picture emerges. The small subset of place cells is not only more active in multiple environments, but their firing rates are higher, they emit more spike bursts (i.e., a higher proportion of spikes with interspike intervals less than 6 ms), and their place fields

are larger than those of the majority neurons (4, 5).

The higher mean firing rates of the active minority within their place fields correlate with their firing rates during sleep in the animal’s home cage (5). Furthermore, the diligent minority fires synchronously with other neurons more frequently in all brain states during both sleep and waking than the slower-firing majority and critically, it exerts a relatively stronger and more effective excitation on its targets. The distribution of the magnitude of collective population firing pattern is also lognormal (5). The consequence of this population organization is that in the physiological time frames of theta oscillations and sharp wave ripples of neuronal activity (4, 5), approximately half of the spikes emitted by the hippocampal neurons are contributed by the active minority; the remaining half are contributed by the great majority of neurons with single place fields. This mixed output is what the downstream observer-classifier neurons of the hippocampal output must use to generate action (see the first figure).

This emerging picture of hippocampal dynamics suggests that neurons at the opposite ends of the distributions may convey different but complementary types of information. The ever-active minority of place cells may be responsible for generalizing across environments and affords the brain the capacity to regard no situation as completely unknown because every alley, mountain, river, or room has elements of previously experienced similar situations. In many situations,

this minority provides the “best guess” of the hippocampus and offers “good enough” solutions to get by. On the other hand, the majority of less active neurons constitute a large reservoir that can be mobilized (7) to precisely distinguish one situation from another and incorporate novel ones as distinct.

The distribution of synaptic strengths, neuron firing rates, population synchrony, axon conduction velocity, and macroscopic connectivity of neuronal networks throughout the brain displays a skewed, typically log-normal form (8, 9). The relationships among these multilevel skewed distributions need to be explored to better understand network operations that underlie brain function. An important practical implication of these recent studies is that analyzing physiological data by parametric statistics is a violation because most variables are skewed. The theoretical implication is that brain dynamics supported by lognormal statistics may be the neuronal mechanism responsible for Weber-Fechner (log) perceptions, including our sense of space. ■

REFERENCES

1. J. O’Keefe, L. Nadel, *The Hippocampus as a Cognitive Map* (Oxford Univ. Press, Oxford, 1978).
2. K. Mizuseki *et al.*, *Hippocampus* **22**, 1659 (2012).
3. P. D. Rich, H. P. Liaw, A. K. Lee, *Science* **345**, 814 (2014).
4. C. B. Alme *et al.*, *Proc. Natl. Acad. Sci. U.S.A.* **111**, 18428 (2014).
5. K. Mizuseki, G. Buzsáki, *Cell Rep.* **4**, 1010 (2013).
6. B. L. McNaughton *et al.*, *Nat. Rev. Neurosci.* **7**, 663 (2006).
7. G. Dragoi, K. D. Harris, G. Buzsáki, *Neuron* **39**, 843 (2003).
8. G. Buzsáki, K. Mizuseki, *Nat. Rev. Neurosci.* **15**, 264 (2014).
9. N. T. Markov *et al.*, *Science* **342**, 1238406 (2013).

10.1126/science.aaa6505

DEVELOPMENTAL BIOLOGY

A Me6Age for pluripotency

Methylation of messenger RNA on the adenine base is critical for stem cell commitment and differentiation

By **Hendrik G. Stunnenberg**,
Michiel Vermeulen, **Yaser Atlasi**

Cell-fate decisions are orchestrated by global changes in gene expression, some of which are driven by epigenetic alterations, often including methylation of DNA. Embryonic stem cells (ESCs) have been used to decipher many of the critical factors underlying cell-fate decisions. Mouse ESCs exist in several different pluripotent states, notably naïve or ground-state ESCs and primed epiblast stem cells (EpiSCs), which resemble pre- and post-implantation-stage embryos, respectively (1, 2). New research now reveals another role for nucleic acid methylation in stem cell-fate determination, but of RNA rather than DNA—at position six of the adenosine base (m6A). Two recent papers, by Geula *et al.* (3) in *Science Express* and Batista *et al.* (4), show that m6A is involved in regulating stem cell maintenance and cell-fate decisions through its modulation of RNA stability and translation.

In eukaryotes, m6A represents an abundant RNA modification that is conserved across many different species, ranging from

plants, to yeast, to mammals (5). Similar to the 5-methylcytosine modification of DNA, m6A is a reversible chemical modification of RNA. The mark is deposited by a heterodimer of methyltransferase-like 3 and 14 (Mettl3 and Mettl14) and can be removed by the RNA demethylase enzymes FTO and ALKBH5 (5). However, until recently, it remained unclear whether m6A has any functional role in stem cell homeostasis.

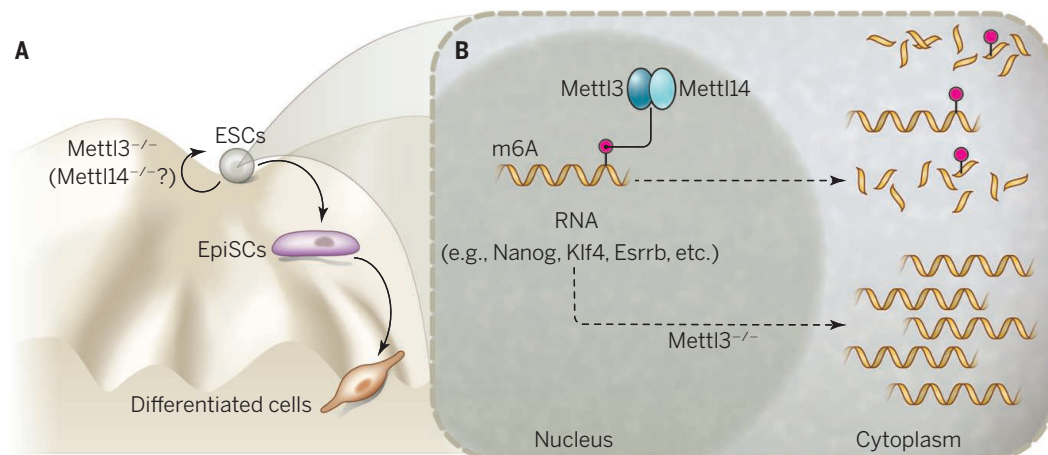
Geula *et al.* and Batista *et al.* independently depleted Mettl3 in mouse and human ESCs and found that Mettl3-depleted ESCs are “locked” in their self-renewal state; they fail to undergo differentiation in vitro or in vivo [results that are contrary to a previous report (6)]. Geula *et al.* extended these observations and found that genetically modified mice lacking Mettl3 (Mettl3^{-/-}) are embryonic lethal. Mettl3^{-/-} mouse embryos retain expression of pluripotency markers (e.g., Nanog), but fail to undergo lineage differentiation and die at the postimplantation stage. These observations suggest that Mettl3^{-/-} ESCs display a state of “hyperpluripotency” and indicate that m6A is necessary to execute lineage commitment.

m6A has previously been detected in different RNA species, including mRNAs, noncoding RNAs, ribosomal RNAs, transfer

RNAs, and small nucleolar RNAs. The two groups carried out transcriptome-wide mapping of m6A sites (“m6A-seq”) in ESCs using a specific antibody against the modification. They found that m6A is located mainly at conserved RRACU motifs (where R is G or A) enriched around the stop codon of protein-coding mRNAs, and the last exon of non-coding RNAs. These data confirm previous m6A mapping studies in somatic cells and indicate that the RRACU motif is the principal methylation site in widely different cell types and across many species (7). The largest proportion of m6A sites are similar between ESCs and their differentiated lineages; only a small number of transcripts are methylated in a cell-type-specific manner. Nonetheless, in the absence of methods to accurately quantitate the ratio of methylated to unmethylated transcript, differential or cell type-specific methylation patterns should be interpreted with caution. Notably, Mettl3/14 expression does not change during differentiation.

Both Geula *et al.* and Batista *et al.* tackled the question of how m6A affects ESC differentiation. They showed that the modification is negatively correlated with RNA stability and, to a lesser extent, with the translation rate. The majority of pluripotency gene transcripts, such as Klf2, Klf4, and Esrrb, are RNA-methylated in ESCs. For ESCs to commit to differentiation, the concentration of core pluripotency factors has to drop below a critical threshold level. Depletion of m6A results in elevated transcript levels through RNA stabilization and increased protein abundance that are sufficient to sustain stem cell self-renewal and impair lineage commitment. Geula *et al.* also report differential alternative splicing in Mettl3^{-/-} ESCs, but the implication of this observation for ESC differentiation is presently unclear.

The m6A mark is recognized by a number of m6A binding factors in the cell. YTH domain-containing proteins and the HUR protein differentially interact with m6A-containing RNA. The m6A-binding YTH domain is conserved from yeast to humans. Some YTH domain-containing proteins (Ythdf1-3) are involved in regulating RNA stability, whereas others (Ythdc1) play a role in regulating RNA splicing (6, 8, 9). The outcome of m6A methylation on mRNA fate therefore strongly



Mettl3 function in embryonic stem cells and in RNA metabolism. (A) A Waddington epigenetic landscape illustrating that ESCs can take on different cell fates that have different epigenetic states (shown as valleys). In the absence of m6A RNA methylation (by depleting either Mettl3 or Mettl14 enzymes), ESCs continue to self-renew and fail to undergo differentiation to EpiSCs and other differentiated lineages. (B) The Mettl3/14 heterodimer acts as a “writer” that marks the mRNAs (shown as wavy lines) with m6A (red labels). m6A regulates different steps of RNA metabolism, including RNA half-life and stability. In the absence of m6A, RNA abundance of pluripotency-promoting genes increases, which impairs differentiation. [Panel B modified from model originally presented by Waddington (11).]

depends on the biological function of the “reader” that interacts with that particular RNA sequence. Thus, differential cell- and state-specific expression or binding of “readers” may appreciably affect the functional readout of the m6A methylome. Currently, it is not known whether other protein domains can bind to m6A or whether different YTH-domain proteins display differential binding depending on the sequence context of m6A sites.

Mettl3 is not the only m6A-methyltransferase; both groups detected low amounts of m6A in Mettl3^{-/-} ESCs. Moreover, Geula *et al.* observed that ESCs in which the gene encoding Mettl3's binding partner Mettl14 is eliminated lose m6A to a similar extent as Mettl3^{-/-} cells and display similar in vitro differentiation defects. Reducing the expression of other regulatory proteins of the Mettl3/14 methyltransferase complex, namely WTAP and KIAA1429, resulted in the most prominent decrease of m6A levels in somatic cells, suggesting that they have an important role in m6A deposition (7). Whether depletion of these and other members of the m6A-methyltransferase complex in ESCs or during embryonic development results in phenotypes similar to those of Mettl3^{-/-} remains to be determined.

The findings of Geula *et al.* and Batista *et al.* open a new avenue for stem cell research. Whether and how RNA methylation regulates homeostasis of adult stem cells should be a fertile area of investigation. For example, genetic variations in the m6A-demethylase FTO have been linked to cancer, obesity, and metabolic disorders (10). Whether aberrant RNA methylation or defects in “writers,” “readers,” or “erasers” affect differentiation of adult stem cells and lead to disease are exciting questions for the field. Taken together, these studies highlight a role for m6A as an important posttranscriptional regulator of cell-fate decisions. It is interesting to note that there are about 100 different covalent RNA modifications, and only now are we beginning to uncover a functional role for some of them. It might be that m6A represents the tip of the iceberg in a new era of “epitranscriptomics.” ■

REFERENCES

- Q. L. Ying *et al.*, *Nature* **453**, 519 (2008).
- H. Marks *et al.*, *Cell* **149**, 590 (2012).
- S. Geula *et al.*, *Science*, 10.1126/science.1261417 (2015).
- P. J. Batista *et al.*, *Cell Stem Cell* **15**, 707 (2014).
- Y. Fu *et al.*, *Nat. Rev. Genet.* **15**, 293 (2014).
- Y. Wang *et al.*, *Nat. Cell Biol.* **16**, 191 (2014).
- S. Schwartz *et al.*, *Cell Rep.* **8**, 284 (2014).
- X. Wang *et al.*, *Nature* **505**, 117 (2014).
- C. Xu *et al.*, *Nat. Chem. Biol.* **10**, 927 (2014).
- R. J. Loos, G. S. Yeo, *Nat. Rev. Endocrinol.* **10**, 51 (2014).
- C. H. Waddington, *Organisers and Genes* (Cambridge Univ. Press, Cambridge, 1940).

10.1126/science.aaa6262

NANOCRYSTAL STRUCTURE

The coordination chemistry of nanocrystal surfaces

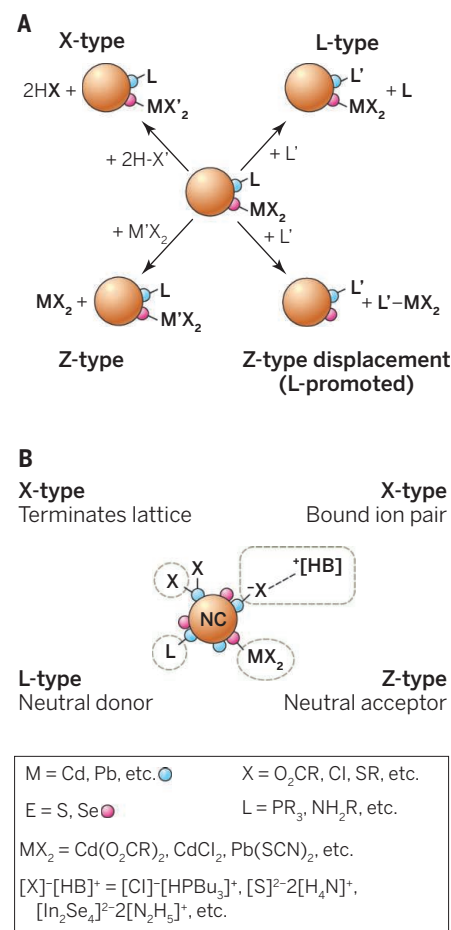
The luminescence and electronic properties of inorganic nanocrystals depends on surface-layer structure

By Jonathan Owen

In the 1990s, when quantum confined colloidal semiconductor nanocrystals (NCs, or quantum dots) were first synthesized with narrow size distributions, there was an explosion of effort to harness their bright and narrow luminescence for optoelectronic devices and fluorescence labeling (1). However, the surfactant ligands that stabilized NCs also influenced their electronic structure and optical properties. Encapsulating the NC cores within an insulating inorganic shell reduced the effect of surface structure on charge recombination (2) and forced the radiative recombination of photoexcited charges. These structures greatly increased the photoluminescence quantum yield (PLQY) and enabled their recent use in liquid crystal displays. However, PLQYs of core-shell nanocrystals remain sensitive to their surfaces and if NCs are to be useful within electrical devices, such as photovoltaic (PV) cells, the complex relation between their surface structure and their frontier orbital structure must be better understood.

Surface atoms of NCs have lower coordination than bulk atoms, which results in weaker bonds that in turn create electronic states within the semiconductor band gap that trap photoexcited charges before they can radiatively recombine. Surfactant ligands coordinate to surface atoms, which strengthens their bonding, and “passivates” these midgap electronic states, and enables luminescence. Thus, tailoring the ligand shell for its interactions with the surrounding medium, be it cellular cytoplasm or the conducting matrix of a light-emitting diode (LED), will influence the surface-derived electronic structure and the optical performance. Similarly, surface trap states define the lowest energy path for charge transport (3). Both effects limit the efficiencies of NC PV cells, LEDs, and photodetectors.

The influence of ligation on electronic structure makes surface coordination chemistry critically important in NC science. Density functional theory (DFT) simulations of surface ligand interactions can be informative, but experimental structures have only



Surface-ligand chemistry. (A) Examples of several ligand exchange reactions are shown. (B) The coordination of different types of ligands in Green's formulation (4) to metal-chalcogenide nanocrystals (NCs, such as cadmium selenide) are illustrated. R is an alkyl group; Bu is *n*-butyl.

recently reached sufficient accuracy to enable realistic DFT studies (4). Untangling the atomic structure of NC facets requires methods beyond the ones used with bulk single-crystal surfaces, many of which work well only in ultrahigh vacuum and with well-ordered, flat surfaces. Thus, two key questions remain: What is the nature of the surface li-

Department of Chemistry, Columbia University, New York, NY, USA. E-mail: jso2115@columbia.edu

gand interaction, and how do these interactions influence the frontier orbital structure and the fate of excited charge carriers?

Early investigations of II-VI NCs—in particular, cadmium selenide synthesized in tri-*n*-octylphosphine oxide—concluded that the dominant ligand type is a datively bound, neutral donor, a so-called L-type ligand (see the figure) (5). Langmuir-like adsorption should result that could be manipulated according to Le Chatelier's principle: If the NCs are placed into a solution containing a much greater concentration of a new L-type ligand, the original ligands should be displaced, regardless of their relative binding affinity. However, early

“The influence of ligation on electronic structure makes surface coordination chemistry critically important in nanocrystal science.”

attempts to exchange the ligand shell—for example, by extended heating of NCs in neutral Lewis basic ligand solutions (such as pyridine or other amines)—were only moderately successful.

Several groups then explored ligand exchange reactivity by systematically measuring the effects of ligands on PLQY (6–8). These studies revealed both a complex underlying surface coordination chemistry and a complex relation between PL and ligation that remains a difficult and central topic in colloidal crystal science. In recent years, it has been realized that L-type ligands are not the primary mode of surface-ligand stabilization. In a landmark study of lead selenide NCs, Moreels *et al.* (9) reported a size-dependent, metal-rich composition that increasingly deviated from the bulk stoichiometry as the NC radius decreased. They concluded that the NC surfaces are covered by a monolayer of lead atoms. Solution ¹H and ³¹P nuclear magnetic resonance (NMR) spectroscopy revealed that a shell of anionic or X-type ligands provided the charges needed to balance the cationic charge of a metal-rich NC (10).

The anionic ligand–cationic NC description helped explain the difficulty encountered in early exchange studies and opened the door to the design of new reactions that maintain the charge balance between the NC and its X-type ligand shell. In the past 5 years, successful ligand exchange studies have used a modified Le Chatelier's

approach in which excess anionic chalcogenide and halide salts displace the native carboxylate and phosphonate ligands, or an acid-base metathesis approach where an acidic proton, trimethylsilyl group, or alkylating agent remove the native carboxylate or phosphonate anions in exchange for another anion of interest. These strategies have led to dramatic improvements in the charge-transport mobilities of NC field-effect transistors and record efficiency of NC PV cells (11).

More recently, NMR spectroscopy revealed that the surface metal ion layer that enriches the NC formula is labile and can be displaced as a complex along with its associated ligand anions, or Z-type ligands (12). The NC stoichiometry is concentration dependent and controlled by the medium in which the NC is suspended. The same study also reported a dramatic and well-behaved dependence of the PLQY on the surface coverage of metal carboxylate complexes.

Absent better understanding of these issues, practical control over the composition and structure of metal surfactant complexes that bind the NC surface will remain erratic. Batch-to-batch variability is typical in the most common methods used to synthesize NCs and variations in the NC composition arise from methods that afford uncontrolled reactivity or terminate the precursor conversion prematurely to obtain a desired size. These effects are compounded by isolation procedures and standards for sample purity that are largely unstudied. Thus, new synthetic methods are needed that reproducibly prepare and isolate NC with known compositions on a larger scale if the structural origins of NC properties are to approach our understanding of bulk semiconductor crystals. This level of control will be necessary for NC technologies to impact not only lighting and photovoltaic technologies but also the biological sciences. ■

REFERENCES

1. C. B. Murray, D. J. Norris, M. G. Bawendi, *J. Am. Chem. Soc.* **115**, 8706 (1993).
2. M. A. Hines, P. Guyot-Sionnest, *J. Phys. Chem.* **100**, 468 (1996).
3. P. Nagpal, V. I. Klimov, *Nat. Comm.* **2**, 486 (2011).
4. D. Zherebetsky *et al.*, *Science* **344**, 1380 (2014).
5. M. L. H. Green, *J. Organomet. Chem.* **500**, 127 (1995).
6. G. Kalyuzhny, R. W. Murray, *J. Phys. Chem. B* **109**, 7012 (2005).
7. C. Bullen, P. Mulvaney, *Langmuir* **22**, 3007 (2006).
8. A. M. Munro, I. Jen-La Plante, M. S. Ng, D. S. Ginger, *J. Phys. Chem. C* **111**, 6220 (2007).
9. I. Moreels *et al.*, *Chem. Mater.* **19**, 6101 (2007).
10. J. S. Owen, J. Park, P.-E. Trudeau, A. P. Alivisatos, *J. Am. Chem. Soc.* **130**, 12279 (2008).
11. C.-H. M. Chuang, P. R. Brown, V. Bulović, M. G. Bawendi, *Nat. Mater.* **13**, 796 (2014).
12. N. C. Anderson, M. P. Hendricks, J. J. Choi, J. S. Owen, *J. Am. Chem. Soc.* **135**, 18536 (2013).

10.1126/science.1259924

INFECTIOUS DISEASE

How a virus travels the world

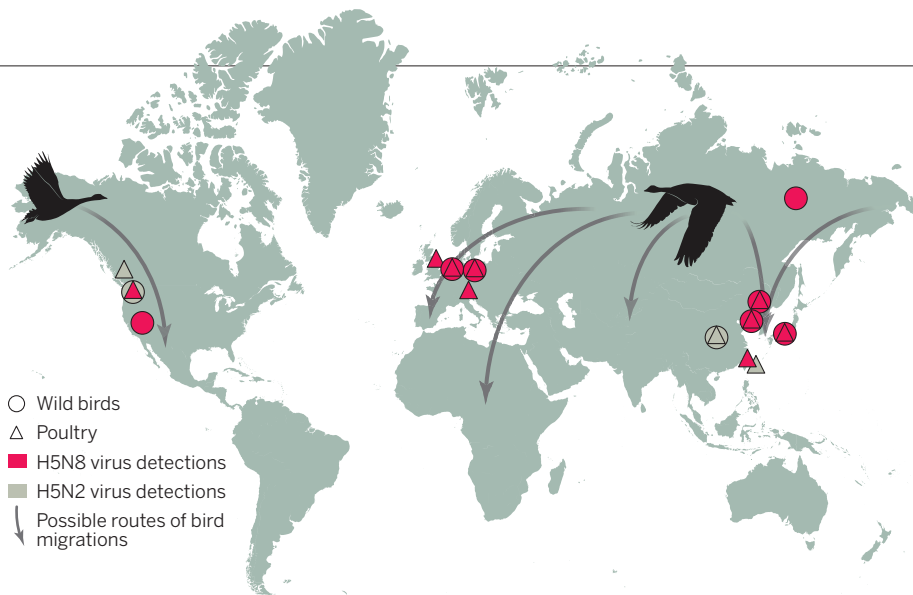
Wild birds may spread the H5N8 virus

By Josanne H. Verhagen, Sander Herfst, Ron A. M. Fouchier

In November and December 2014, highly pathogenic avian influenza (HPAI) viruses of the H5 subtype originating from China were detected in poultry and wild birds in various countries of Asia and Europe, and, for the first time, in North America. These incursions of newly emerging HPAI H5 viruses constitute a threat to animal and potentially human health and raise questions about the routes of transmission.

Wild birds of the orders Anseriformes (ducks, geese, swans) and Charadriiformes (gulls, terns, waders) are the natural reservoir for low pathogenic avian influenza (LPAI) viruses. On the basis of viral hemagglutinin (HA) and neuraminidase (NA) proteins, these viruses are classified into 16 HA subtypes and nine NA subtypes, found in numerous combinations such as H5N1 and H5N8. LPAI viruses generally do not cause substantial disease in wild birds and poultry. However, viruses of subtypes H5 and H7 can evolve into HPAI viruses upon introduction into poultry, causing up to 100% mortality in poultry species. Historically, HPAI outbreaks in poultry have been controlled rapidly by methods such as mass culling. However, since 1997, HPAI H5N1 viruses that share a common ancestral virus (A/Goose/Guangdong/1/96, GsGd) have continued to cause outbreaks in poultry populations. These outbreaks were associated with the first recorded cases of human infections with H5 influenza viruses and with spillback of HPAI viruses to wild birds.

HPAI H5N1 viruses of the GsGd lineage were first detected in poultry in Hong Kong in 1997. They resurfaced in 2001 and 2002, with frequent outbreaks in poultry in numerous Asian countries since 2003. In 2005, the viruses were detected during mass die-offs of wild birds in Mongolia, followed by reports in poultry and wild birds in Russia and Kazakhstan; the virus then spread across Europe, the Middle East, Asia, and



H5N2 and H5N8 virus detections in poultry and wild birds in 2014. The almost simultaneous detection of closely related viruses in Asia, Europe, and North America suggests linkage with wild bird migration via a large region in Russia. Data from (6).

Africa, in part associated with wild bird migrations. Since then, detections have continued to be reported in poultry and wild birds in Eurasia, with the most recent outbreaks occurring in Egypt and southeastern parts of Asia. Since 2003, 694 laboratory-confirmed human cases of H5N1 virus infection have been reported to the World Health Organization, including 402 fatalities (1).

During the initial circulation and spread of the H5N1 viruses, the HA genes diversified into multiple genetic lineages ("clades"), without evidence of gene exchange between the influenza viruses (2). However, this changed from 2009 onward, when HPAI viruses of subtypes H5N2, H5N5, H5N6, and H5N8 were found to contain the H5 gene of the GsGd lineage, together with NA and various other genes of LPAI virus origin (3–6). After numerous poultry outbreaks in eastern Asia and occasional detection in wild birds, these viruses spread into Europe and North America by December 2014 (7). H5 outbreaks were also reported from Africa and the Middle East, but whether these were also caused by H5 viruses of the GsGd lineage needs to be confirmed (8).

What explains the sudden global spread of this H5 lineage? The timing and direction of intercontinental spread coincided with fall bird migration out of Russia; the H5N8 virus was identified in a long-distance migrant bird in Russia in September 2014 and subsequently in Japan, Germany, and the Netherlands (9) and the western United States (8), which suggests that wild birds carried the virus out of Russia into other parts of the world. So far, HPAI H5N8 virus of the GsGd lineage has been isolated exclusively

from wild birds of the orders Anseriformes and Gruiformes (coots and cranes). However, given the subclinical infections in some species, other wild birds may also be susceptible. H5-specific antibodies have been detected in 10 to 53% of common teals, mallards, spot-billed ducks, Eurasian wigeons, and Baikal teals (10); these findings suggest that the virus has circulated for some time in ducks that survived infection, and this may play a role in HPAI H5N8 virus epidemiology. The almost simultaneous detection of HPAI H5 viruses in wild birds and poultry in Asia, Europe, and North America suggests that the virus was potentially introduced from a relatively large region in Russia (see the figure).

The HPAI H5N8 viruses in domestic and wild birds share a common ancestor and contain HA and a polymerase gene (PB2) derived from viruses of the GsGd H5 lineage (11). The increased geographical spread of HPAI H5 viruses and the isolation of H5N8 from live wild birds suggest that this lineage may have evolved to be better adapted to wild birds than are other poultry influenza viruses, supporting its spread.

Ferrets are frequently used to study virus replication, pathogenesis, and transmissibility as a means of assessing potential public health risk upon human exposure to virus-infected poultry, wild birds, or other animals (12, 13). Upon inoculation with HPAI H5N8 virus A/Mallard/Korea/W452/2014, ferrets did not develop any remarkable signs of illness (11). The H5N8-inoculated animals did not lose weight, in contrast with animals inoculated with human seasonal influenza viruses or H5N1 virus (13). The HPAI H5N8 virus replicated mainly in the respiratory tract of ferrets (11); this is in contrast to HPAI H5N1 viruses, which replicate abundantly in extra-respiratory organs.

Influenza viruses are mainly transmitted between humans via respiratory droplets or aerosols. In the ferret model, low, short-term shedding of A/Mallard/Korea/W452/2014 was observed from the upper respiratory tract of inoculated animals, which did not transmit the virus via the airborne route or direct contact to naïve ferrets (11). H5N8 viruses A/Duck/Shandong/Q1/2013 and A/Duck/Jiangsu/k1203/2010 did not transmit through direct contact between guinea pigs (14). Pathogenicity and transmission in animal models may not be directly extrapolated to humans, but these data suggest that the public health threat of the currently circulating HPAI H5N8 strains is low.

Vaccination and antiviral therapy are the main options for preventing human influenza virus infections. Several H5 candidate influenza vaccine strains are available but are unlikely to provide sufficient protection against H5N8 virus (15). HPAI H5N8 virus A/Mallard/Korea/W452/2014 was found to be sensitive to oseltamivir, zanamivir, and peramivir (11), which suggests that drugs can be used prophylactically or therapeutically if the need arises.

The presence of HPAI H5 viruses in migrating birds and the dispersed spatial pattern of virus detections globally are worrisome; more poultry outbreaks could occur in the future, especially in countries that are ill-prepared. Despite the currently low public health risk, the outbreaks should be monitored closely, given that several animal species are susceptible (11) and that influenza viruses are generally unpredictable. Wild birds covering multiple migratory flyways should be monitored for virus presence and for H5-specific antibodies as a cost-effective alternative to measure circulation of viruses of the GsGd H5 lineage (16). Control measures and research priorities aimed at eradicating HPAI H5 viruses from poultry populations should be redefined, as current strategies appear to be insufficient. ■

REFERENCES

1. www.who.int/influenza/human_animal_interface
2. S. S. Shepard *et al.*, *PLOS ONE* **9**, e86921 (2014).
3. G. Zhao *et al.*, *PLOS ONE* **7**, e46183 (2012).
4. C. G. Liu *et al.*, *Vet. Microbiol.* **167**, 296 (2013).
5. K. Zhao *et al.*, *Vet. Microbiol.* **163**, 351 (2013).
6. F. Y. K. Wong *et al.*, *Emerg. Infect. Dis.* **10**, 3201/eid2103.141488 (2015).
7. www.oie.int/animal-health-in-the-world/update-on-avian-influenza/2014
8. <http://promedmail.org>
9. C. Adlhoch *et al.*, *Euro Surveill.* **19**, 20996 (2014).
10. J. Jeong *et al.*, *Vet. Microbiol.* **173**, 249 (2014).
11. Y. Kim *et al.*, *Emerg. Microbes Infect.* **3**, e75 (2014).
12. S. Herfst *et al.*, *Science* **336**, 1534 (2012).
13. V. J. Munster *et al.*, *Science* **325**, 481 (2009).
14. Q. Li *et al.*, *Vet. Res.* **45**, 127 (2014).
15. http://who.int/influenza/vaccines/virus/201409_zoonotic_vaccinevirusupdate.pdf
16. M. Gilbert *et al.*, *PLOS ONE* **9**, e113569 (2014).

Department of Viroscience, Erasmus Medical Center, 3015 CE Rotterdam, Netherlands. E-mail: r.fouchier@erasmusmc.nl

10.1126/science.aaa6724

BOOKS *et al.*

MUSEUMS

Surrounded by science

Tracing the evolution of modern museums of science and natural history

By Kirk R. Johnson

The natural history museum is an example of a 19th-century invention that still has momentum in the 21st century. In a way, the continued presence of museums in our modern world is as surprising as if one were to see a fleet of horse-drawn carriages hurtling down the highway at 75 mph. *Life on Display*, by historians Karen A. Rader and Victoria E. M. Cain, focuses on the evolution of U.S. science and nature museums from the late 19th century to the early 21st century, stitching together a number of surprising insights into an excellent history.

The late 1800s was a time not unlike the present, characterized by disruptive technologies, rapid urbanization, growing monopolies, increasing wealth disparity, and scientific discovery. Global travel for the middle class was within reach. Many of the largest U.S. natural history museums emerged during this time. They joined a cohort of earlier museums that had grown as adjuncts to scientific discovery and had initially focused on the pure display of objects and specimens.

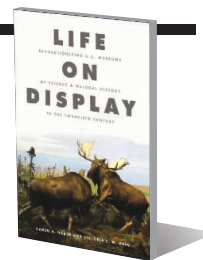
Rader and Cain begin their story with the rise of the “New Museum Idea,” a concept that gained momentum in the late 19th and early 20th centuries and maintained that educational displays should form the core of the museum visitor experience. In the 1880s, George Brown Goode, the first director of the Smithsonian’s U.S. National Museum, advocated for the advancement of three parallel missions:

“specimen preservation, scientific research and publication, and public education.” This three-pronged approach continues to this day and has been the source of both strength and strife in the management of museums.

The early application of the New Museum Idea was led by a cadre of “museum men” who produced and installed dioramas and displays based on collections and fieldwork that were intended to enlighten a growing urban audience. Dioramas remain a popular modality in large natural history museums. The American Museum of Natural History still has more than 200 on display.

Rader and Cain go on to show how the Great Depression, a pair of world wars, and a cold war shifted public attention from the natural world to one of geopolitics, technology, medicine, and the hard sciences. New museums and exhibits dedicated to educating the public about science began to open from the 1930s to the 1960s. During this time, a new breed of museum men emerged, epitomized by Frank Oppenheimer, whose San Francisco Exploratorium eschewed collections in favor of interactive participation. His East Coast counterpart, Bradford Washburn, reinvented the archaic New England Muse-

Life on Display
Revolutionizing U.S. Museums of Science and Natural History in the Twentieth Century
Karen A. Rader and Victoria E. M. Cain
University of Chicago Press, 2014. 481 pp.



value of museum scientists as communicators and vectors for citizen science, which allowed them to maintain, and even grow, their scientific programs and collections.

As suggested by the title, the book focuses mainly on the public side of museums. Curators appear primarily as curmudgeons opposing the advances in audience engagement. Collections are largely shown as elements that should be displayed in educational context. This is unfortunate because museums remain the primary tool that our culture uses to archive and preserve its recent and ancient past. Far from being “attics,” museums are the seed banks of our future. The age of discovery is still under way,

and the expertise embodied in museum scientists is a vital asset as we accelerate into an uncertain century. The compelling history of the impact of museum-based scientific research and the value of natural history collections remains to be written.

The book ends in 2005, with both natural history museums and science centers seen as trusted, articulate voices grappling with new and evolving challenges. Science literacy has been vastly complicated by a growing antisience movement. The urgent issues of preserving bio-

diversity, mitigating climate change, and promoting cultural diversity are driving some museums to take on additional roles in areas such as conservation, advocacy, and inclusion. The proclivities of the digital generation and the fragmentation of the media landscape have also focused, but narrowed, interest in both nature and science. The weight of these issues is immense, but both natural history museums and science centers have the potential to expand their role as major players and important venues for advancing science and science literacy in the 21st century.



As times change, museums work to meet new challenges and evolving expectations.

um of Natural History as the Boston Museum of Science. The result was a new focus on audience engagement, hands-on learning, and basic science.

By the 1970s and 1980s, natural history museums, with their expensive triple mission, were in direct competition with science centers, whose sole focus was on audience education. As the competition for paying audiences grew more intense from the 1980s to the 2000s, the curator count at many natural history museums began to drop. In the worst cases, natural history museums lost their entire curatorial staffs and orphaned their collections. Others recognized the increasing

The reviewer is director of the Smithsonian National Museum of Natural History, Washington, DC 20560, USA. E-mail: johnsonkr@si.edu

Breaking bad science

A physician's quest to expose the many misuses of science in the media

By Joel Best

London newsstands can strike Americans as remarkable, both for the number of different papers being sold and for their alarming headlines. Most U.S. cities are lucky to have a single daily newspaper—shrinking in both physical size and circulation—with fairly staid contents. In contrast, Britain has about 10 daily newspapers that contend for a national audience. Their circulations are also slipping, but the fact that they are competing for readers makes their coverage colorful by American standards.

The tendency of the British press toward sensationalism has provided physician and science writer Ben Goldacre with a nearly endless supply of “Bad Science”—the title of his weekly column that ran in *The Guardian* from 2003 to 2011. His new book, *I Think You'll Find It's a Bit More Complicated Than That*, collects more than 100 short pieces—many of which originally ran in his column—that break down systemic problems with how science is presented and discussed in the public forum.

To Goldacre, “bad science” is a term that encompasses a variety of problems, from reporters who write stories that favor titillation over accuracy, and those who fail to understand the research they purport to summarize, to editors who favor compelling headlines that distort a story's contents. Then there are the professional journals that issue press releases to promote their contents; the conferences that call attention to preliminary findings; the researchers who talk about their work in the media limelight before it has gone through peer review; and the ghostwriters hired by pharmaceutical corporations to produce articles reporting favorable results for their drugs. And, of course, there are the outright hucksters, who claim to have found miracle cures, effortless weight-loss schemes, and the like. Many of these figures manage to find their way into British newspapers and television programs—and those who don't can always set up shop on the Internet.

Goldacre's goal is to explain to the general public how science works by showing how bad science falls short, and he has a lot of fun doing so. He doesn't dumb down his arguments, but he favors snarky phrasings and delights in skewering politicians, activists, reporters, and purveyors of snake oil.

I Think You'll Find It's a Bit More Complicated Than That covers a lot of territory: from the value of fluoride in drinking water (“Foreign Substances in Your Precious Bodily Fluids”), to coffee-induced hallucinations (“Drink Coffee, See Dead People”), to the surprisingly resilient claims about vaccines causing autism (“MMR: The Scare Stories Are Back”). In his introduction, Goldacre says, “I hope it works as a kind of statistics toilet book, bringing satisfaction in short bursts, with a fight and an idea in each one,” and it does work on that level. Each piece offers a thoughtful critique of some dubious claim, yet can be read in a few minutes.

The underlying message is that we need to think critically about how science finds its way into the media.

The scientific literature is impossibly vast. As Goldacre points out, “there are over 24,000 academic journals in existence, 1.3 million academic papers published every year.” Yet only an infinitesimal fraction of this work attracts news coverage. Given these realities, he maintains that both reporters and readers should demand transparency from researchers. Those who are unwilling to present their data, describe their methods, and submit their work to peer review should not, in his opinion, be in the public spotlight. At the same time, he points out that the media are all too eager to publicize even highly dubious claims—for example, “Health Warning: Exercise Makes You Fat.”

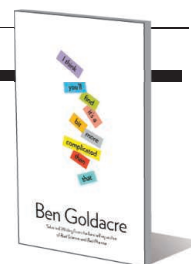
Goldacre applies the same criticism to

I Think You'll Find It's a Bit More Complicated Than That

Ben Goldacre

Fourth Estate, 2014.

496 pp.



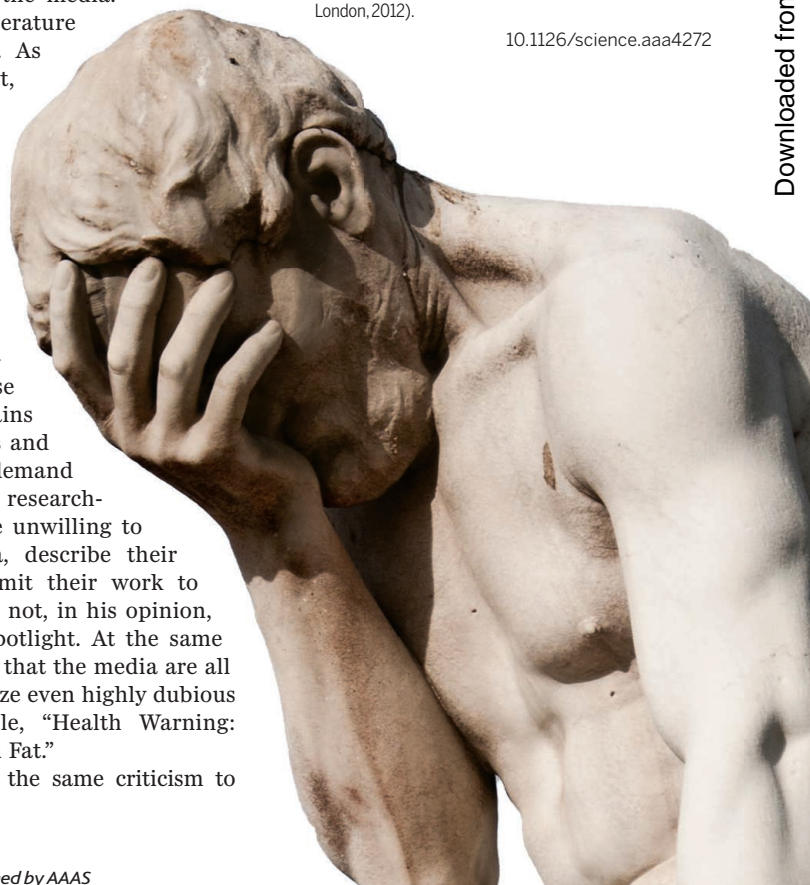
review articles, emphasizing the value of systematic reviews (where the standards for including studies are clearly defined and strictly implemented), in pieces including “Cherry-Picking Is Bad. At Least Warn Us When You Do It.” He also takes the government to task for ignoring peer-reviewed research that questions the value of their pet policies (“Why Is Evidence So Hard for Politicians?”). The book even covers the issue of the accessibility of scientific publications in a world of paywalls in “Academic Papers Are Hidden from the Public. Here's Some Direct Action.”

These are relatively sophisticated critiques for a newspaper column but—as Goldacre's “bad” examples demonstrate—they are needed. If you've read and liked his earlier books, you'll probably enjoy this one, but if you aren't familiar with his work, I'd recommend starting with his earlier best-sellers (1, 2).

REFERENCES AND NOTES

1. B. Goldacre, *Bad Science: Quacks, Hacks, and Big Pharma Flacks* (Faber & Faber, London, 2010).
2. B. Goldacre, *Bad Pharma: How Drug Companies Mislead Doctors and Harm Patients* (Faber & Faber, London, 2012).

10.1126/science.aaa4272



LETTERS

Edited by Jennifer Sills

The curtailed careers of women in China

IN THE WORKING LIFE “Reflections of a woman pioneer” (V. Venkatraman, 7 November 2014, p. 782), Mildred “Millie” Dresselhaus points out that women’s careers

often pick up steam after their childbearing years. She names a couple of examples of women who don’t want to retire and work well into their 80s and beyond. Yet in China, the statutory retirement age of Chinese female researchers is age 55, a full 5 years lower than that of Chinese male researchers.

The average childbearing age for Chinese female researchers is 30 (1). It is usually women who take care of their young children before they begin kindergarten (at about 3 years old), which prevents the female researchers from spending as much time applying for grants and publishing as male researchers. By the time they are 36 years old, Chinese male researchers have begun to attain better academic titles, publish more papers, and receive more funding (1).

To address this, China has introduced a number of policies to help female researchers deal with childbearing and raising children. For example, the National Natural Science Foundation of China stipulates that male and female researchers can apply for Young Scientist Funds before 35

and 40 years old, respectively (2). The China Association for Science and Technology stipulates that the upper age limit for female winners of the Youth Science and Technology Prize is 5 years higher than that for male winners (3). These policies have considered that female researchers can’t work on the frontlines because of childbearing and raising children. The policies are effective (1, 4, 5); after 40 years old, the gap between male and female researchers begins to narrow. After 46 years old, the percentage of senior titles is even higher among women. But after 50 years old, once again, male researchers begin to open the gap. This is mainly because female researchers have to reduce the number of research projects before the statutory retirement age. To narrow the gap between male and female researchers, we should extend the retirement age for female researchers in Chinese universities.

Chenggang Yan

Department of Automation, Tsinghua University,
Beijing, 100084, China.
E-mail: andy.cg.yan@gmail.com

REFERENCES

1. Chinese Academy of Sciences (www.cas.cn/xw/zjsd/201305/120130513_3837506.shtml) [in Chinese].
2. National Natural Science Foundation of China (www.nsf.gov.cn/nsfc/cen/xmzn/2015xmzn/08/index.html) [in Chinese].
3. China Association for Science and Technology (<http://qnkij.cast.org.cn/cms/contentmanager.do?method=view&pageid=view&id=cms0d1b2a48084b2>) [in Chinese].
4. Y. Ma, *Forum Sci. Technol. China* **11**, 126 (2011).
5. Y. Li, *Bull. Natl. Natural Sci. Foundation China* **5**, 274 (2013).

Converting Big Data into public health

WE CONCUR WITH M. J. Khoury and J. P. A. Ioannidis (“Big data meets public health,” Perspectives, 28 November 2014, p. 1054) that “a strong epidemiologic foundation, robust knowledge integration, principles of evidence-based medicine, and an expanded translation research agenda” can facilitate public health applications of Big Data. However, Big Data scientists and public health practitioners must forge better relationships if this vision is to be realized.

Big Data analysis algorithms should be accessible to health practitioners (1). This requires more than freely accessible computer code and a user-friendly Graphical User Interface. Outreach programs, self-learning modules, and textbooks that are designed for users without a programming background will help facilitate the integration of these algorithms and statistical tools into public health, medical, nursing, and other health care-related degree

programs, graduates of which are the bulk of the domestic and global public health workforce. The average public health practitioner is not a computer scientist.

The Ebola Response model from the Centers for Disease Control and Prevention (CDC) (2) provides a good example in the field of infectious disease modeling. The Modeling Task Force of CDC’s Ebola Emergency Response fits epidemiological data to a spreadsheet-based Markov chain model to provide policy-makers with incidence projections, with and without scale-up of effective interventions. Using it as a communication tool, the task force communicated the possible dire consequences of the Ebola outbreak to senior decision-makers. This simple model had a substantial policy impact on the global Ebola response because of its ability to convey a powerful message to policy-makers and facilitate resource mobilization and prompt action. Ultimately, models are tools of communication to policy-makers. Consultation with the intended audience helps ensure that the product meets their needs. Likewise, Big Data analyses should help practitioners inform policy-makers about policy options and how they should craft their messages to the general public (3).

Isaac Chun-Hai Fung,^{1*} Zion Tsz Ho Tse,²
King-Wa Fu³

¹Department of Epidemiology, Jiann-Ping Hsu College of Public Health, Georgia Southern University, Statesboro, GA 30460, USA. ²College of Engineering, The University of Georgia, Athens, GA 30602, USA.

³Journalism and Media Studies Centre, The University of Hong Kong, Hong Kong.

*Corresponding author.
E-mail: cfung@georgiasouthern.edu

REFERENCES

1. D. Lazer, R. Kennedy, G. King, A. Vespignani, *Science* **343**, 1203 (2014).
2. M. I. Meltzer et al., *MMWR Surveill. Summ.* **63** (suppl. 3), 1 (2014).
3. A. B. Heldman, J. Schindelar, J. B. Weaver III, *Public Health Rev.* **35**, 1 (2013); www.publichealthreviews.eu/show/a/129.

Common diseases in China overlooked

ENVIRONMENTAL AND public health research in China has largely focused on the effects of environmental pollution on health. Few studies have addressed the environment’s effect on noncommunicable diseases, despite the fact that almost one out of five people in China has been diagnosed with one (1). Surprisingly, the National Planning for Prevention and Treatment of Chronic Diseases of China (2012–2015), jointly promulgated by the

NEXTGEN VOICES

The Scientist's Toolbox: Last Call

You have one more week to respond to the NextGen VOICES survey! Share your thoughts:

Name and describe a currently nonexistent invention that would make you a more effective scientist.

Your invention can be realistic, futuristic, or comical, and it can aid you in any aspect of your scientific process or career.

To submit, go to http://scim.ag/NG_14

Deadline for submissions is 13 February. A selection of the best responses will be published in the 3 April 2015 issue of *Science*. Submissions should be 100 words or less. Anonymous submissions will not be considered.

Ministry of Health and other 14 national departments (1), failed to mention this research. Accordingly, this research has not been funded by the Ministry of Science and Technology or the National Natural Science Foundation of China, the two principal national funding agencies of basic research in China.

Noncommunicable diseases were emphasized as “a critical public health problem in China” in the 2012 Planning exercise (1), but relevant research has yet to be incorporated into the 2014 and 2015 National Key Basic Research Programs and Significant Research Programs of China developed by the Ministry of Science and Technology, which continues to prioritize biomedical approaches (2, 3). Moreover, this line of research is completely missing in the National Natural Science Foundation of China funding programs. Unfortunately, with approximately 260 million Chinese afflicted with noncommunicable diseases (1), the prevailing conditions hinder research development, resulting in Chinese prevention strategies that are more administrative than scientific. Given the research complexities, a long-term and systematic funding plan is required to ensure continued funding.

Xi-Zhang Shan

Department of Geography, The University of Hong Kong, Hong Kong, China.
E-mail: shanxz@graduate.hku.hk

REFERENCES

1. The Ministry of Health of China *et al.*, The National Planning for Prevention and Treatment of Chronic Diseases of China (2012–2015) [in Chinese] (2012); www.nhfp.gov.cn/zhuzhan/wsbmgz/201304/b8de7b7415ca4996b3567e5a09e43300.shtml.
2. The Ministry of Science and Technology of China, The 2014 and 2015 Priority Support Directions of National Key Basic Research Programs and Significant Research Programs of China [in Chinese] (2013); www.most.gov.cn/tztg/201302/t20130201_99485.htm.
3. The Ministry of Science and Technology of China, The 2015 Priority Support Directions of National Key Basic Research Programs and Significant Research Programs of China [in Chinese] (2014); www.most.gov.cn/tztg/201402/t20140220_111908.htm.

TECHNICAL COMMENT ABSTRACTS

Comment on “A promiscuous intermediate underlies the evolution of LEAFY DNA binding specificity”

Jacob O. Brunkard, Anne M. Runkel, Patricia C. Zambryski

Sayou *et al.* (Reports, 7 February 2014, p. 645) proposed a new model for evolution of transcription factors without gene duplication, using LEAFY as an archetype. Their proposal contradicts the evolutionary history of plants and ignores evidence that LEAFY evolves through gene duplications. Within their data set, we identified a moss with multiple LEAFY orthologs, which contests their model and supports that LEAFY evolves through duplications.

Full text at <http://dx.doi.org/10.1126/science.1255437>

Response to Comment on “A promiscuous intermediate underlies the evolution of LEAFY DNA binding specificity”

Samuel F. Brockington, Edwige Moyroud, Camille Sayou, Marie Monniaux, Max H. Nanao, Emmanuel Thévenon, Hicham Chahtane, Norman Warthmann, Michael Melkonian, Yong Zhang, Gane Ka-Shu Wong, Detlef Weigel, Renaud Dumas, François Parcy

Brunkard *et al.* propose that the identification of novel LEAFY sequences contradicts our model of evolution through promiscuous intermediates. Based on the debate surrounding land plant phylogeny and on our analysis of these interesting novel sequences, we explain why there is no solid evidence to disprove our model.

Full text at <http://dx.doi.org/10.1126/science.1256011>

TECHNICAL RESPONSE

EVOLUTION

Response to Comment on “A promiscuous intermediate underlies the evolution of LEAFY DNA binding specificity”

Samuel F. Brockington,^{1*} Edwige Moyroud,^{1*} Camille Sayou,² Marie Monniaux,³
Max H. Nanao,^{4,5†} Emmanuel Thévenon,^{6,7,8,9} Hicham Chahtane,^{6,7,8,9}
Norman Warthmann,¹⁰ Michael Melkonian,¹¹ Yong Zhang,¹² Gane Ka-Shu Wong,^{12,13}
Detlef Weigel,¹⁴ Renaud Dumas,^{6,7,8,9} François Parcy^{6,7,8,9†}

Brunkard *et al.* propose that the identification of novel *LEAFY* sequences contradicts our model of evolution through promiscuous intermediates. Based on the debate surrounding land plant phylogeny and on our analysis of these interesting novel sequences, we explain why there is no solid evidence to disprove our model.

In Sayou *et al.* (1), we explained how conserved *LEAFY* (LFY) homologs could recognize different DNA motifs (types I, II, and III) by determining the key residues affecting LFY DNA binding specificity. We identified a hypothetical promiscuous LFY variant (key residues His-Cys-His) through phylogenetic reconstruction, but also discovered a promiscuous variant (Gln-Cys-His) in a lineage of early diverging land plants, the hornworts. We proposed that these promiscuous forms acted as intermediates, enabling a gradual transition from type III to types I and II binding specificities.

Brunkard *et al.* (2) identified novel paralogous LFY sequences in a single moss species and conclude that changes in LFY binding specificity evolved only through duplication. Here, we explain why we do not agree with their conclusions.

First, Brunkard *et al.* constrain the LFY phylogeny to a single organismal topology in which liverworts, mosses, and hornworts constitute a paraphyletic grade leading to the vascular plants. This choice does not acknowledge the debate surrounding early land plant phylogeny. The topological constraint they employed is based on the phylogenetic hypothesis provided by Qiu *et al.* (3). However, Cox *et al.* reanalyzed the Qiu *et al.* data set and concluded that the paraphyly of bryophytes, and the support for the hornworts as the sister group to the tracheophytes, is a methodological artifact (4). Furthermore, other studies support alternative scenarios (5–10), and recent publications (4, 11) stress that the early land plant phylogeny remains profoundly uncertain, even in the postgenomic era. As emphasized in these publications and discussed in our original manuscript (1), there are four alternative topologies still in play [see figure S9 in (1)]. In this context, we think that it is inappropriate to constrain the LFY phylogeny to only one of several competing hypotheses of organismal relationships. Instead, in Sayou *et al.*, we evaluated the incongruence between the LFY phylogeny and these four competing organismal phylogenies, establishing that our model is robust in the context of different organismal hypotheses.

Second, on the basis of a sequence alignment alone, Brunkard *et al.* propose that the novel *Polytrichum commune* LFY sequences they isolated are the product of duplications at the base of mosses, rather than derived events. However, they did not perform the phylogenetic analysis necessary to establish whether these duplication

events occurred before or after the changes in DNA binding specificity. In addition to duplications within mosses, their model also requires a likely duplication within hornworts and a deep duplication at the base of the land plants (mediating type III to type I specificity change). In the absence of this deep duplication, their model requires an abrupt switch between different binding specificities, which would likely be deleterious. To date, there is no support for any of these additional duplications, and Brunkard *et al.* do not provide a nondeleterious mechanism to account for an abrupt switch.

Finally, Brunkard *et al.* rely on the parsimony criterion to substantiate their model. However, their parsimony reconstruction analysis [figure 2B in (2)] does not take into account that the three critical amino acid residues occupy well-separated positions and were reconstructed as such in Sayou *et al.* [figures 4 and S6 of (1)]; instead, Brunkard *et al.* appear to have reconstructed them as a single linked trait. Reanalyzing the Brunkard *et al.* data with the three amino acid sites individually reconstructed, but using their tree topology, we obtained an equal probability of the promiscuous intermediate (His-Cys-His) preceding key transitions in binding specificity (Fig. 1). Furthermore, the topology supplied by Brunkard *et al.* is the more challenging scenario for our model. In the other three competing organismal hypotheses (i.e., liverworts-plus-mosses as monophyletic, all bryophytes as monophyletic, or hornworts as sister to all land plants), a Gln-Cys-His ancestral promiscuous intermediate is always recovered. Therefore, we reject the idea that promiscuity is merely a derived state and maintain that the promiscuous model holds.

We agree that gene duplication plays a role in LFY evolution because LFY duplicates may occasionally acquire different functions, likely through divergence in expression patterns (12, 13). In Sayou *et al.*, we carefully noted all examples of known LFY duplications, even if not associated with a change in DNA binding specificity. We also agree that limited taxon sampling and genomic data make the presence of gene duplication difficult to disprove and concluded, “we cannot completely rule out the occurrence of transient ancient duplications” (1). In their Comment, Brunkard *et al.* treat the duplication and promiscuity scenarios as mutually exclusive. In contrast, we maintain that “it is plausible that the mechanisms we describe could also contribute to the evolution of TFs encoded by multigene families” (1). Promiscuous intermediates may be easier to detect in a predominantly single-copy gene lineage, but promiscuous forms could themselves be duplicated and obtain novel function in derived paralogous lineages, as recently invoked in the evolution of HOX genes (14).

In summary, we feel that Brunkard *et al.* misjudge the extent of the phylogenetic support for their model, and we suggest that their proposed scenario does not adequately explain the existence of the promiscuous form. Brunkard *et al.* highlight the need to densely sample LFY sequences from emerging genomic resources to

¹Department of Plant Sciences, University of Cambridge, Downing Street, Cambridge CB2 3EA, UK. ²Wellcome Trust Center for Cell Biology, Michael Swann Building 5.1, King's Buildings, Edinburgh, EH9 3JR, UK. ³Department of Comparative Development and Genetics, Max Planck Institute for Plant Breeding Research, Carl-von-Linne Weg 10, 50829, Köln, Germany. ⁴European Molecular Biology Laboratory (EMBL), 6 Rue Jules Horowitz, BP 181, 38042 Grenoble, France. ⁵Unit of Virus Host-Cell Interactions, Université Grenoble Alpes (UGA), Centre National de la Recherche Scientifique (CNRS), EMBL, UMI 3265, 6 Rue Jules Horowitz, 38042 Grenoble Cedex 9, France. ⁶CNRS, Laboratoire de Physiologie Cellulaire et Végétale (LPCV), UMR 5168, 38054 Grenoble, France. ⁷UGA, LPCV, F-38054 Grenoble, France. ⁸Commissariat à l'énergie atomique et aux énergies alternatives, Direction des Sciences du Vivant, Institut de Recherches en Technologies et Sciences pour le Vivant, LPCV, F-38054 Grenoble, France. ⁹Institut National de la Recherche Agronomique, LPCV, F-38054 Grenoble, France. ¹⁰Research School of Biology, The Australian National University, Acton, ACT 0200, Australia. ¹¹Botanisches Institut, Lehrstuhl I, Universität zu Köln, Biozentrum Köln, Zùlpicher Strasse 47b, 50674 Köln, Germany. ¹²Beijing Genomics Institute, Shenzhen, Beishan Industrial Zone, Yantian District, Shenzhen 518083, China. ¹³Department of Biological Sciences, Department of Medicine, University of Alberta, Edmonton AB, T6G 2E9, Canada. ¹⁴Department of Molecular Biology, Max Planck Institute for Developmental Biology, 72076 Tübingen, Germany. *These authors contributed equally to this work. †Corresponding author. E-mail: francois.parcy@cea.fr (F.P.); mnanao@embl.fr (M.H.N.)

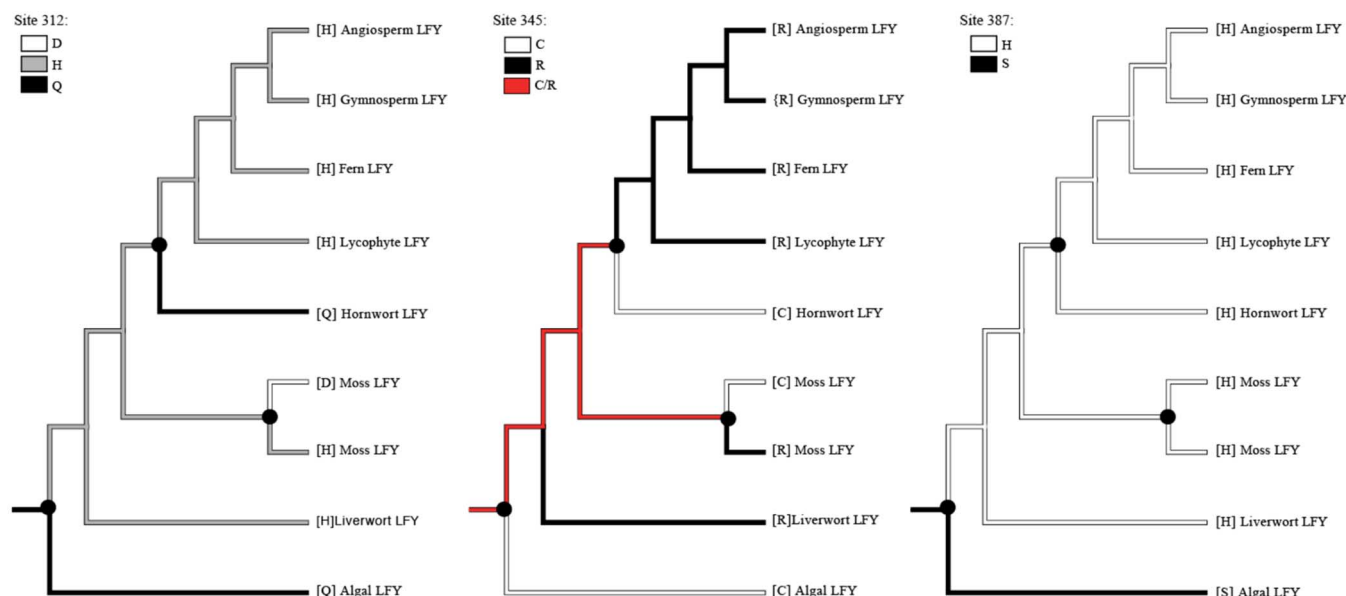


Fig. 1. Phylogenetic reconstruction with the parsimony criterion applied to the same topology and data used by Brunkard *et al.* Reconstruction analyses were implemented in Mesquite Version 2.75, with each amino-acid site (312, 345, and 387) reconstructed individually (2, 8, and 2 most parsimonious reconstructions, respectively). Reconstructions were refigured so that each lineage of *LFY* genes is represented by a single terminal branch,

following the methodology of Brunkard *et al.* Black circles indicate sites of binding specificity change inferred in the model of Brunkard *et al.* Taken together, the separate reconstructions indicate that a promiscuous intermediate (His-Cys-His) is as equally likely as the His-Arg-His variant before changes in binding specificity, even under the constrained topology imposed by Brunkard *et al.*

improve estimates of the *LFY* phylogeny and to more accurately infer changes in binding specificity. We concur, but given that the phylogenetic location of gene duplication events is revealed through reconciliation of gene and species trees, uncertain organismal relationships will continue to challenge precise inference on the timing of putative duplication events. As such, parsimony-based phylogenetic reasoning alone cannot be the sole criterion with which to distinguish among competing models of *LFY* evolution. Rather, we believe that an integrated functional, biochemical, and phylogenetic approach is essential.

REFERENCES AND NOTES

1. C. Sayou *et al.*, *Science* **343**, 645–648 (2014).
2. J. O. Brunkard, A. M. Runkel, P. C. Zambryski, *Science* **347**, 621 (2015).
3. Y.-L. Qiu *et al.*, *Proc. Natl. Acad. Sci. U.S.A.* **103**, 15511–15516 (2006).
4. C. J. Cox, B. Li, P. G. Foster, T. M. Embley, P. Cíván, *Syst. Biol.* **63**, 272–279 (2014).
5. T. Nishiyama *et al.*, *Mol. Biol. Evol.* **21**, 1813–1819 (2004).
6. K. G. Karol *et al.*, *BMC Evol. Biol.* **10**, 321 (2010).
7. T. Nishiyama, M. Kato, *Mol. Biol. Evol.* **16**, 1027–1036 (1999).
8. C. Finet, R. E. Timme, C. F. Delwiche, F. Marlétaz, *Curr. Biol.* **20**, 2217–2222 (2010).
9. S. Wodniok *et al.*, *BMC Evol. Biol.* **11**, 104 (2011).
10. F.-W. Li *et al.*, *Proc. Natl. Acad. Sci. U.S.A.* **111**, 6672–6677 (2014).
11. E. D. Cooper, *Trends Plant Sci.* **19**, 576–582 (2014).
12. K. Bomblies *et al.*, *Development* **130**, 2385–2395 (2003).
13. A. Vázquez-Lobo *et al.*, *Evol. Dev.* **9**, 446–459 (2007).
14. S. Nakagawa, S. S. Gisselbrecht, J. M. Rogers, D. L. Hartl, M. L. Bulyk, *Proc. Natl. Acad. Sci. U.S.A.* **110**, 12349–12354 (2013).

ACKNOWLEDGMENTS

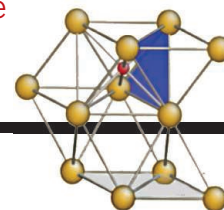
We thank J. Leebens-Mack and E. Carpenter for discussions. This work was supported by funds from the Max Planck Society (D.W.) and the Agence Nationale de la Recherche (grant Charmful SVSE2–2011). The 1000 Plants (1KP) initiative, led by G.K.-S.W., is funded by Alberta Ministry of Enterprise and Advanced Education, Alberta Innovates Technology Futures, Innovates Centre of Research Excellence, Musea Ventures, and BGI-Shenzhen.

27 May 2014; accepted 2 December 2014
10.1126/science.1256011

RESEARCH

How oxygen atoms strengthen the titanium lattice

Yu et al., p. 635



IN SCIENCE JOURNALS

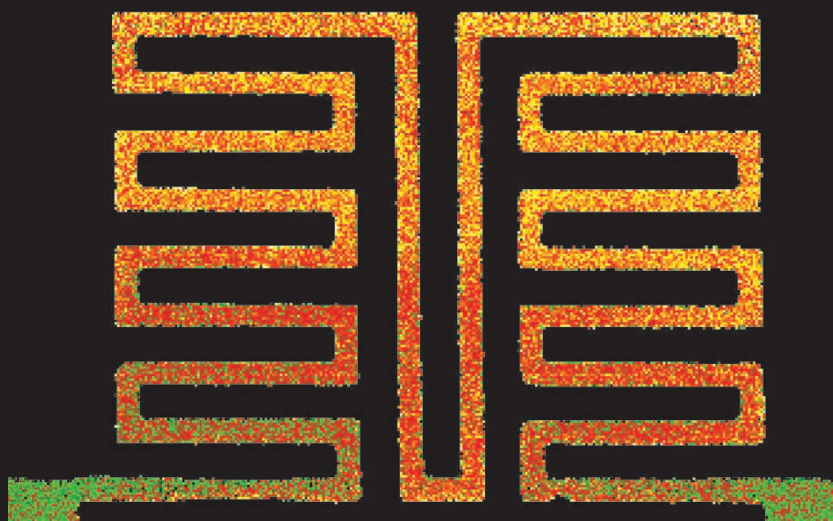
Edited by Stella Hurtley

THERMAL MEASUREMENT

Plasmons can map temperature on the nanoscale

Determining temperature on small length scales can be challenging: Direct probes can alter sample temperature, and radiation probes are limited by the wavelength of the light used. Mecklenberg *et al.* show how the bulk plasmon resonance of aluminum can be used to map the temperature on the nanoscale with transmission electron microscopy (see the Perspective by Colliex). Many other metals and semiconductors also have plasmon resonances that could also be used for temperature imaging. — PDS

Science, this issue p. 629; see also p. 611



False-color temperature map of 80-nm-thick, 100-nm-wide serpentine aluminium

EXOPLANET DYNAMICS

Can't keep hot sides hot and cold sides cold?

On Earth, we're accustomed to cycles of day and night, which drive a complex thermal relationship between the ground and atmosphere. Some exoplanets very close to their stars aren't so lucky and are generally assumed to be locked by tides into hemispheres of unchanging day and night. The thick atmosphere of Venus is thought to keep it from the same fate, but Leconte *et al.* present models showing that even a much sparser atmosphere

may suffice for lower-mass stars. The non-instantaneous thermal response of the planet (when the hottest time of day is after noon) may speed up or slow down the planet. Such thermal tides may be important in assessing potential extraterrestrial habitable zones. — MMM

Science, this issue p. 632

NONCOVALENT ASSEMBLY

Popping open one by one into polymers

We rarely board airplanes by joining the back of a single

well-ordered line. More often, we jostle around in one of several bulging crowds that merge haphazardly near the gate. Roughly speaking, these processes are analogous to the chain growth and step growth mechanisms of polymer assembly at the molecular level. Kang *et al.* present a strategy to link molecular building blocks through hydrogen bonding in accord with the well-controlled chain growth model. The molecules start out curled inward, as they engage in internal hydrogen bonding, until an initiator pulls one open; that molecule is then in the right

conformation to pull a partner into the growing chain, poising it to pull in yet another, and so forth down the line. — JSY

Science, this issue p. 646

ECOLOGICAL FEEDBACKS

Termites can stabilize tropical grasslands

Spotty vegetation patterns in tropical savannas and grasslands can be a warning sign of imminent desertification. However, Bonachela *et al.* find that termites can also produce spotty patterns. Their theoretical study, confirmed by field data from Kenya, shows that patterns produced by termite mounds are not harbingers of desertification. Indeed, the presence of termites buffers these ecosystems against climate change. — AMS

Science, this issue p. 651

TRANSPLANTATION

Long-term tracking of transplanted T cells

Clinical trials can be an untapped source of experimental data that can be leveraged to explore both basic and pathological biology in humans. Biasco *et al.* took advantage of two different gene therapy trials for inherited immunodeficiency to track T cell fate over the long term in humans. They find that the recently described T memory stem cells are able to persist and preserve their precursor potential in human recipients for up to 12 years after genetic correction and infusion into patients. The safety and long-term survival of these cells not only strengthen our knowledge

of human immunology but are also encouraging for adoptive immunotherapy. — ACC
Sci. Transl. Med. **7**, 273ra13 (2015).

ADDICTION THERAPY

Reversing cocaine-evoked behavior in mice

Therapeutic optogenetic protocols are highly effective at reversing symptoms in animal models of neuropsychiatric disease. However, translating these protocols into the clinic is challenging because we have not yet made the technical leap required to perform effective optogenetic stimulation in primates. Creed *et al.* tested whether it would be possible to circumvent these challenges by avoiding the problem altogether. They adjusted an existing therapeutic approach—deep brain stimulation—to mimic an effective optogenetic stimulation protocol to treat a mouse model of cocaine addiction. — PRS

Science, this issue p. 659

PLANT DEVELOPMENT

Genetic control of stem cell fate in plant roots

Without roots, most plants cannot thrive. Crawford *et al.* have now unearthed the robust control systems that build roots. Signaling by the plant hormone auxin triggers three genes that control the development of stem cells forming the root. With this trio of genes, any one of which can do the job, root development is backed up with fail-safe controls. The team could use the same system of controls to sprout roots in the wrong places, making roots instead of shoots. — PJH

Science, this issue p. 655



HOST RESPONSE

Bacterial infection breaks the lymph node barrier

During infections, lymph nodes are command central. Fragments from invading pathogens enter lymph nodes through the lymph. There, specialized cells called subcapsular sinus (SCS) macrophages capture these antigens and use them to initiate humoral immunity. Despite being such important players, Gaya *et al.* report that in mice, infection throws these organized sentinels into disarray (see the Perspective by Buzsáki). Disrupting SCS macrophages had important consequences: Bacterially infected mice could not respond as efficiently to a subsequent viral infection. — KLM

Science, this issue p. 667;
 see also p. 612

CANCER

Targeting Wnt signaling in lymphoma

Although several human cancers show increased activity of the Wnt/ β -catenin signaling pathway, tumors may lack mutations that would account for the increase. Walker *et al.* found that the transcription factor FOXP1 enhanced the transcription of Wnt-regulated target genes by binding to and promoting the acetylation of β -catenin. Patients with diffuse large B cell lymphomas overexpressing FOXP1 have a poor prognosis, and diffuse large B cell lymphoma cells with high FOXP1 levels were sensitive to Wnt inhibitors. Xenografted tumors in mice were smaller when they lacked FOXP1 or when Wnt signaling was blocked. — WW

Sci. Signal. **8**, ra12 (2015).

IN OTHER JOURNALS

Edited by Kristen Mueller
 and Jesse Smith



ORGANIC CHEMISTRY

How to bring two chlorines face to face

Organic chemists have known for well over a century how to chlorinate the carbons at both ends of a double bond. A vast array of different methods now exists to replace the chlorines with other molecular fragments. One persistent limitation, however, has been the tendency of the two chlorines to bond to opposite faces of the starting compound. Cresswell *et al.* now present a versatile method that adds both chlorines to the same face. The key is a selenium catalyst that probably binds to the face opposite the first chlorine, before being displaced from behind by the second. — JSY
Nat. Chem. 10.1038/nchem.2141 (2015).

products are usually only made in small quantities for local consumption. Zhou *et al.* demonstrate how thoughtful design and a bit of tinkering can lead to much greater yields of oxygenated taxanes, a precursor of the antitumor drug paclitaxel. First they split the job between a bacterium and a yeast. Second, they switched the fuel for these microbial factories from glucose (which the yeast turned into ethanol, which sedated the bacteria) to xylose (which the bacteria consumed and turned into acetate, which fed the yeast). — GJC

Nat. Biotechnol. **33**, 10.1038/nbt.3095 (2015).

WOUND HEALING

Wound healing requires senescence

Cells divide as tissues develop and regenerate, but they can only do so a limited number of times. Eventually they stop dividing and enter a state called cellular senescence. Senescent cells secrete a variety of factors,

BIOTECHNOLOGY

Outsourcing production on a small scale

Microbes are wizards at making structurally intricate and bioactive molecules, but their



CLIMATE CHANGE

California drought worst in the past millennium

Since 2012, California has been suffering a severe drought. Griffin and Anchukaitis use tree-ring records of past climate conditions to determine how the current drought compares to other droughts since 800 CE. Based on metrics for soil moisture and for precipitation, they conclude that 2014 was the worst single drought year in at least the past 1200 years, caused by very low (but not unprecedented) precipitation and record high temperatures. The 3-year period from 2012 to 2014 was the worst unbroken drought interval in the past millennium. Although the effects of climate change on rainfall patterns in California remain uncertain, higher temperatures may contribute to future droughts in the region. — JFU

Geophys. Res. Lett. 10.1002/2014GL062433 (2014).

The impact of drought on Lake Mead—pointer to California's future?

PEER REVIEW

Gauging gatekeeper performance

Researchers curse the peer review system after a rejection letter and praise it when their papers sail into publication. But do research journals make the right decisions? To find out, Siler *et al.* tracked the fates of over 1000 accepted and rejected manuscripts submitted to three leading medical journals. The authors found that overall the journals made good decisions: Manuscripts rejected without peer review received fewer citations than manuscripts rejected after peer review. However, the journals rejected the 14 most highly cited articles (12 without peer review), which may reveal issues in recognizing unconventional leaps. — BJ

Proc. Natl. Acad. Sci. U.S.A. **112**, 360 (2015).

FOREST ECOLOGY

Pathogens promote forest diversity

Environmental conditions affect the diversity of species, whether flora or fauna, in a particular habitat. But what keeps a tree that normally grows in a low-

rainfall area from growing in a tropical forest? Spear *et al.* investigated this question by transplanting drought-resistant tree seedlings into wet forests. Although both wet-forest and drier-forest species suffered pathogen attacks, the damage and mortality associated with these attacks were worse

in seedlings transplanted from drier forests. Together with the exclusion of wet-forest species from dry forests by drought, this result indicates that pathogens also promote and maintain the diversity of tree species in tropical forests. — AMS

J. Ecol. **103**, 165 (2015).

skeletal resemblances to ancient African monkeys. Now, Bond *et al.* describe three 36 million-year-old fossil teeth found in the Peruvian Amazon that support this idea: The shape of the teeth and phylogenetic analyses link



South American silvery marmosets (*Mico argentatus*) had an African ancestor.

the fossils to monkeys that inhabited Africa during the late Eocene, about 38 million years ago. The discovery also pushes back the monkeys' arrival date—perhaps by vegetation raft across the Atlantic Ocean—by 10 million years. — CG

Nature, 10.1038/nature14120 (2014).

but scientists still do not fully understand the role senescent cells play in many physiological processes, such as wound healing. Demaria *et al.* now show that wounds close more slowly in mice genetically engineered to lack senescent cells. After wounding, endothelial and mesenchymal cells undergo senescence and secrete the protein PDGF-AA. PDGF-AA helps wounds to heal more quickly by causing myfibroblast cells to differentiate. — BAP

Dev. Cell **31**, 722 (2014).

INORGANIC CHEMISTRY

Taking another look at a BB triple bond

Carbon and boron are neighbors in the periodic table, and that proximity entices chemists to make them emulate one another, akin to dressing siblings in matching outfits. An exciting achievement in this area was the preparation of a compound with a BB triple bond, analogous to the CC bond in an alkyne. Köppe and Schnöckel now

have analyzed this compound in a thermodynamic context that highlights the substantial stabilizing influence of the capping groups (N-heterocyclic carbenes) on each B atom. They further considered the stiffness of the BB bond reflected in vibrational analyses. On this basis, they suggest that the compound might be better considered to have a lower-order BB bond, with higher-order bonds to the capping groups. — JSY

Chem. Sci. 10.1039/c4sc02997f (2014).

PALEONTOLOGY

African origin for New World monkeys

New World monkeys—smallish, flat-nosed primates with prehensile tails such as silvery marmosets, golden lion tamarins, and squirrel monkeys—have inhabited South America for at least 26 million years, but it is unclear when they arrived and where they originated. Many paleontologists suspect an African origin, based on

ALSO IN SCIENCE JOURNALS

Edited by Stella Hurtley

EDUCATION

Assessing the value of undergraduate research

Undergraduate research experiences often engender enthusiasm in the students involved, but how useful are they in terms of enhancing student learning? Linn *et al.* review studies that focus on the effectiveness of undergraduate research programs. Undergraduate research experiences in a class were distinguished from those involving individualized participation in a research program. Mentoring emerges as both an important component of a successful experience and a target for improvement. — PJH

Science, this issue p. 627

INFECTIOUS DISEASE

Where will H5 flu viruses travel to next?

Avian influenza viruses can cause severe illness and even death in domestic poultry. In the past two decades, a particular group of viruses termed H5 viruses have caused repeated outbreaks after first emerging in China. In a Perspective, Verhagen *et al.* trace the recent spread of these viruses, particularly the H5N8 virus that was detected in North America in December 2014. Based on the pattern of spread, the authors argue that the virus may be spread by wild birds as they migrate via Russia to Europe, America, and beyond. The viruses currently constitute a low health threat for humans, but given the unpredictable nature of influenza viruses, they should be monitored closely. — JFU

Science, this issue p. 616

DNA NANOTECHNOLOGY

DNA control of bonding interactions

Colloidal particles have been used as atom mimics and are often connected together using complementary DNA strands. Rogers and Manoharan controlled the strength of the colloidal “bond” by using a set of competing strand displacement reactions. They capitalized on the reversible chemical equilibrium between the DNA strands connecting different particles to control the temperature dependence of the equilibrium state. — MSL

Science, this issue p. 639

EXPRESSION PROFILING

Single-cell expression analysis on a large scale

To understand why cells differ from each other, we need to understand which genes are transcribed at a single-cell level. Several methods measure messenger RNA (mRNA) expression in single cells, but most are limited to relatively low numbers of cells or genes. Fan *et al.* labeled each mRNA molecule in a cell with both a cellular barcode and a molecular barcode. Further analysis did not then require single-cell technologies. Instead, the labeled mRNA from all cells was pooled, amplified, and sequenced, and the gene expression profile of individual cells was reconstructed based on the barcodes. The technique successfully revealed heterogeneity across several thousand blood cells. — VV

Science, this issue p. 628

METALLURGY

Screw dislocations: A hard case to crack

The motion of dislocations or defects in a metal influences its strength and toughness. If these defects can be “pinned” by adding alloying elements, it should be possible to create a stronger alloy. It was thought that there shouldn’t be much of an interaction between screw dislocations and any alloying elements. However, Yu *et al.* show that for α -Ti, the profound hardening effect of oxygen is due to the strong interactions with the core of the dislocations. First-principles calculations reveal that distortion of the interstitial sites at the dislocation core creates a very strong but short-range repulsion for oxygen atoms. — MSL

Science, this issue p. 635

CARBON RADICALS

Catching a glimpse of the elusive QOOH

It’s straightforward to write down the net combustion reaction: Oxygen reacts with hydrocarbons to form water and carbon dioxide. The details of how all the bonds break and form in succession are a great deal more complicated. Savee *et al.* now report direct detection of a long-postulated piece of the puzzle, a so-called QOOH intermediate. This structure results from bound oxygen stripping a hydrogen atom from carbon, leaving a carbon-centered radical behind. The study explores the influence of the hydrocarbon’s unsaturation on the stability of QOOH, which has implications for both combustion and tropospheric oxidation chemistry. — JSY

Science, this issue p. 643

PROTEIN EVOLUTION

Exploring the limits of protein sequence space

Exploring the variability of individual functional proteins is complicated by the vast number of combinations of possible amino acid sequences. Podgornaia and Laub take on this challenge by analyzing four amino acids critical for the interaction between two signaling proteins in *Escherichia coli*. They build all the possible 160,000 variants of one of the two proteins and find that over 1650 are functional. Even though there can be very high variability in the composition of the interface between the two proteins, there are nonetheless strong context-dependent constraints for some amino acids, which suggests why many functional variants are not seen in nature. — GR

Science, this issue p. 633

GENOMIC VARIATION

How genetics affect phenotypic variation

How an individual looks depends on their genes, genetic variation, and interactions with the environment. However, the path from genotype to phenotype remains murky. Battle *et al.* examine how an individual’s genetic variation affects expression of RNA, ribosome occupancy, and protein levels. They find that RNA expression and ribosome occupancy are generally correlated. However, in contrast, protein levels appear not to depend on RNA levels or ribosome occupancy. Protein levels are thus regulated by posttranscriptional mechanisms. — LMZ

Science, this issue p. 664

REVIEW SUMMARY

EDUCATION

Undergraduate research experiences: Impacts and opportunities

Marcia C. Linn,* Erin Palmer, Anne Baranger,† Elizabeth Gerard,† Elisa Stone†

For any undergraduate contemplating a career in scientific research, participating in authentic research seems like a good opportunity. But what are authentic research experiences? How do they benefit undergraduates? What forms of mentoring are successful? What needs improvement? And how can these experiences meet the needs of interested students while at the same time be cost-effective in large research universities?

We review the research tackling these questions and find few answers. While most undergraduates give high ratings to research experiences, specific benefits have not been documented. Of the 60 empirical studies published in the last 5 years, only 4 directly measured gains in research capabilities or conceptual understanding. Most studies draw conclusions from self-report surveys or interviews, notoriously poor methods for documenting impacts. These studies leave us with few insights into what works and little idea about how to make the experiences more effective.

BACKGROUND: Most colleges and universities offer Undergraduate Research Experiences (UREs) and/or Course-based Undergraduate Research Experiences (CUREs) (Fig. 1). Two large surveys, the 2004 Freshman Survey and the 2008 College Senior Survey, administered at over 200 institutions, generated data about the impact of undergraduate research experiences on persistence in science and intention to pursue graduate school. These studies document that students appreciate undergraduate research experiences. The surveys are unable, however, to distinguish between UREs and CUREs. In addition, the value that undergraduate research adds cannot be disentangled from precollege preparation, especially for students

from groups that are underrepresented in science.

ADVANCES: Designers of UREs expect students to benefit from participating in a scientific laboratory but have not determined opti-



URE in action. Biofuel research engages a Berkeley undergraduate researcher during a summer internship with the Synthetic Biology Engineering Research Center (funded by NSF grant 1132670).

mal ways to orient and guide participants. Students often expect the URE to mimic their college laboratory experiences with procedural guidance and planned outcomes. During the first year of a URE, students often report spending most of their effort on setting up and conducting experiments and limited effort on understanding the investigation or interpreting the results. Students would benefit from an orientation that integrates their beliefs and expectations with the realities of the research experience. The

few studies that measure changes in understanding of scientific practices or relevant science concepts report little or no gains after 1 year in a URE. Students who spend over a year in a URE often learn new methodological techniques, collect their own data,

ON OUR WEB SITE

Read the full article at <http://dx.doi.org/10.1126/science.1261757>

interpret findings, and formulate new research questions. The slow enculturation into lab activities may make sense, especially when students join labs investigating

questions that do not arise in undergraduate education. The time and resources needed, however, limit the scalability of UREs. Students encounter new ideas during their research experiences but often need guidance to integrate these ideas with their expectations. We discuss ways that designers of UREs can speed up enculturation and strengthen guidance.

Individual mentoring emerges as an effective way to guide students and improve learning from research experiences. Activities that could help students benefit from research experiences include discussion with mentors, participation in group meetings where current research is discussed, guided opportunities to explore relevant research literature, reflection on observations in weekly journals, and synthesis of their insights by creating research proposals, reports, or posters. We discuss ways to prepare mentors so that they can efficiently guide students.

OUTLOOK: Undergraduate research experiences absorb a lot of time, money, and effort. The costs and benefits of research experiences for building human capital, benefitting undergraduates, improving workforce diversity, and strengthening educational outcomes need better understanding. Making the best use of extramural funds and the (often voluntary) contributions of faculty to improve undergraduate research experiences requires a strong research base.

More rigorous research is needed, and the field could benefit by building on insights from the learning sciences. We use the knowledge integration framework to interpret the available findings and to identify gaps in the research base.

We discuss ways to develop validated, generalizable assessments such as methods for measuring ability to locate and interpret primary literature. We suggest techniques for developing criteria for evaluating mentoring interactions. We identify ways to strengthen mentoring and to ensure that research experiences meet the needs of diverse students. ■

University of California, Berkeley, CA, USA.

*Corresponding author. E-mail: mcclinn@berkeley.edu

†These authors contributed equally to this work. Cite this article as M. C. Linn et al., *Science* **347**, 1261757 (2015); DOI: 10.1126/science.1261757

REVIEW

EDUCATION

Undergraduate research experiences: Impacts and opportunities

Marcia C. Linn,* Erin Palmer, Anne Baranger,† Elizabeth Gerard,† Elisa Stone†

Most undergraduates give high ratings to research experiences. Studies report that these experiences improve participation and persistence, often by strengthening students' views of themselves as scientists. Yet, the evidence for these claims is weak. More than half the 60 studies reviewed rely on self-report surveys or interviews. Rather than introducing new images of science, research experiences may reinforce flawed images especially of research practices and conceptual understanding. The most convincing studies show benefits for mentoring and for communicating the nature of science, but the ideas that students learn are often isolated or fragmented rather than integrated and coherent. Rigorous research is needed to identify ways to design research experiences so that they promote integrated understanding. These studies need powerful and generalizable assessments that can document student progress, help distinguish effective and ineffective aspects of the experiences, and illustrate how students interpret the research experiences they encounter. To create research experiences that meet the needs of interested students and make effective use of scarce resources, we encourage systematic, iterative studies with multiple indicators of success.

Many claim that undergraduate research experiences improve preparation of the next generation of scientists and increase persistence in science (1–3). The limited evidence for the impact of undergraduate research experiences makes it difficult, however, to justify the substantial resources they require. Of the 60 empirical investigations published during the last 5 years, over half rely exclusively on self-report surveys or interviews to document outcomes, although such evidence has serious flaws (4) (Fig. 1). Fewer than 10% of the studies validate self-reports with analysis of research products (such as presentations or culminating reports), direct measures of content gains, longitudinal evidence of persistence, or observations of student activities. Although researchers often call for better assessments, valid measures have yet to be designed (5–10). In addition, undergraduate research programs often select students who already intend to persist in science and primarily document that they continue to major in science. More nuanced indicators of success such as improved use of scientific practices, increased ability to interpret original sources, or a better sense of possible flaws in research designs would strengthen the research base. We draw on the most convincing studies to identify impacts and opportunities for future investigations. We identify mentoring as essential for successful support of undergraduates considering careers in science. We call for studies that distinguish which types of undergraduate research experiences

succeed for students with distinct interests, backgrounds, and preparation.

Designing research experiences to promote integrated understanding

Undergraduate research experiences provide a window on science in the making, allowing students to participate in scientific practices such as research planning, modeling of scientific observations, or analysis of data. The experiences are intended to enculturate students into scientific investigation. Faculty, postdoctoral scholars, and other members of the lab mentor students. Ideally, mentors guide students to interpret authentic images of scientific research and link their experiences to their own beliefs or expectations. Interview studies document the many inconsistent ideas about scientific research that undergraduates develop. Many expect scientific research to mimic their college laboratory experiments. Others are unprepared for the failure rate in independent research. For example, one student said, “I honestly expected it to be like my organic chemistry lab that I just finished last year [...] I’m used to ‘here is the procedure, now get to it,’ and I thought that was what the experience would be like” [(11), p.1084]. In a post-research experience interview another student reflected, “I think this experience helped me to really understand that it’s not, like, a magical experiment and you come up with magical data and some magical conclusion, and that it is frustrating, but you get through it, and you get over it, and you’ll run it again and if it’s just as frustrating, you’ll do it again” [(12), p.65].

To characterize the investigations of research experiences, analyze how they promote integrated

understanding in science, and recommend improvements, we draw on research in the learning sciences. Specifically, we use the knowledge integration framework that synthesizes extensive research on inquiry science to identify gaps and conundrums in the research on undergraduate research experiences (13–17). This framework calls for eliciting students’ initial ideas (consistent with hypothesizing) and encouraging students to test them against new ideas (18). To add new ideas, the framework documents the value of participating in personally relevant contexts, such as research experiences to make sense of science practices. The framework also highlights the value and importance of dynamic models of scientific phenomena that reveal insights into unseen processes such as molecular reactions (19). Perhaps most importantly, the framework emphasizes that new ideas can be isolated and forgotten and highlights the need to guide students to become adept at distinguishing among their initial ideas and those they encounter in courses or research experiences to build coherent understanding (17). Finally, the framework builds on research showing that learners benefit from reflecting on their investigations and observations to sort out and consolidate their ideas (20). This framework guides our analysis of the literature on research experiences and our recommendations for improving them (Fig. 2).

Distinguishing among research experiences

Research experiences include Undergraduate Research Experiences (UREs) and Course-based Undergraduate Research Experiences (CUREs) (21). UREs feature individual students in faculty research laboratories and provide the opportunity for one-on-one mentoring (Fig. 3). Typically, students spend one or more semesters in labs, although the type of activity and form of mentoring varies substantially. Selection for UREs is highly competitive because few students can be accommodated. Using grades, test scores, and essays, selection committees generally identify students who succeeded in high school and college, although a few studies use other criteria. Most students in UREs are already motivated to succeed in science. UREs may exclude students whose interests are not represented by the available research. In contrast, CUREs have a curriculum and are open to most students. CUREs put high demands on one or a few mentors to guide many students (22). Many studies demonstrate that duration for both UREs and CUREs affects outcomes (23–27). UREs and CUREs vary in selectivity, duration, setting, mentoring, and cost (Fig. 4).

Impacts and opportunities

We synthesize impacts and opportunities of undergraduate research experiences from the studies reviewed. We organize the studies in five themes: (i) mentoring participants, (ii) selecting participants and promoting identity, (iii) improving research practices, (iv) expanding conceptual understanding, and (v) communicating the nature of science.

University of California, Berkeley, CA, USA.

*Corresponding author. E-mail: mclinn@berkeley.edu †These authors contributed equally to this work.

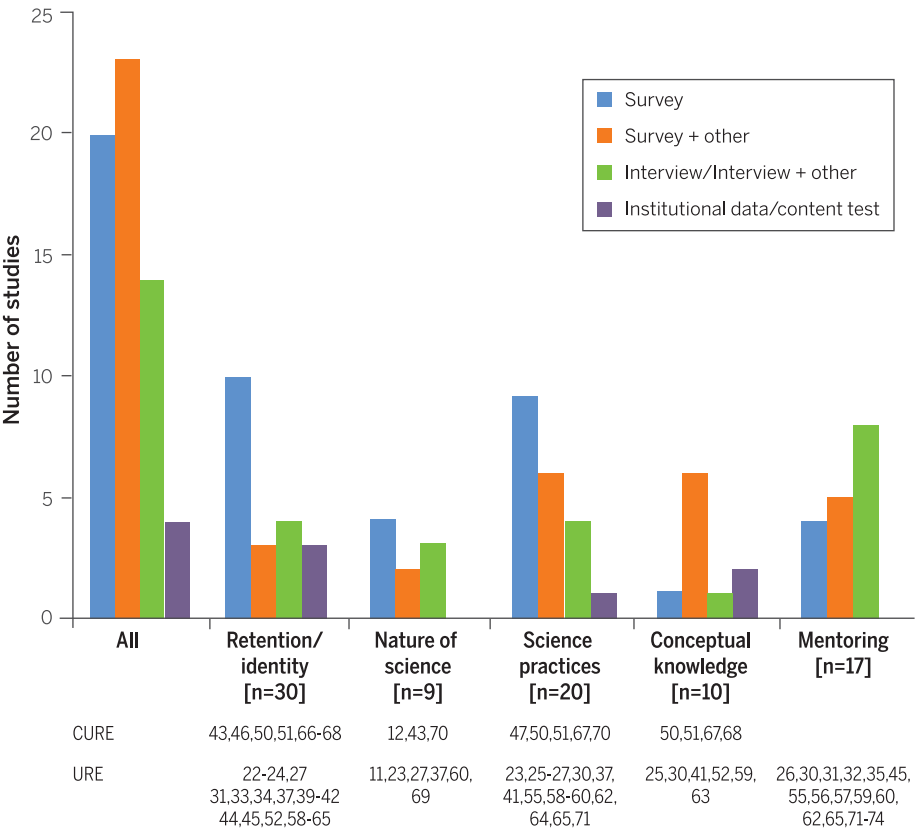


Fig. 1. Goals measured, methodologies used, and key findings. We used electronic databases and Internet search engines such as ERIC, Web of Science, SciFinder Scholar, Science Citation Index, and EdFull to identify studies. We reviewed citations in relevant articles and examined individual journals (e.g., *J. Chem. Ed.*) to locate papers missed by the search. Key words included *undergraduate research*, *research opportunities*, and *science, physics, chemistry, biology*. Computer science and psychology were excluded to keep the research experiences as similar as possible. Consistent with journal policy, we included papers published in the last 5 years (2010 to 2014). This process yielded 253 documents published in peer-reviewed journals. Review of titles and abstracts yielded 60 empirical studies. We used an emergent categorization process to analyze and score the characteristics of each study. References (1, 11, 12, 22–27, 30, 32–35, 37, 39–47, 50–52, 55–74) provided the basis of the analysis in Fig. 1. See the reference list for full citations.

Mentoring participants

Successful mentoring balances the dual goals of helping undergraduates deepen their understanding of science and guiding them to develop a scientific identity. Mentors ideally orient undergraduates to develop and integrate (i) conceptual knowledge and background information in the topic of the research experience; (ii) science practices such as developing an argument from evidence; and (iii) insights into the culture of the lab, including the requirements of the funding and the roles of the participants. Mentors guide students to form a scientific identity by helping them imagine roles they can play in the lab, recognize gaps in their knowledge that future courses will fill, and identify ways to contribute that also strengthen their current capabilities. Researchers have studied mentoring in varied professional and educational contexts using surveys and interviews (28, 29).

Typically, mentoring is shared among faculty, postdoctoral researchers, and graduate students with UREs offering an individual relationship with mentors and CUREs requiring students to share one or several mentors. Studies indicate that undergraduates interact most frequently with graduate students and postdocs, and less with faculty (26). Mentoring by graduate and postdoctoral researchers tends to focus on technical aspects of the projects, whereas faculty are likely to help students build a scientific identity by articulating their knowledge, reasoning, or problem-solving skills (30). Thus, graduate students and postdoctoral researchers may spend more time with their mentees than faculty, but rarely support development of the complex scientific reasoning skills and professional identity formation that could benefit undergraduates. Peers can also help orient and inform other undergraduates about research, especially in UREs where experienced students mentor newcomers (31).

Mentors have responsibility to orient students so they can see the connections among experiences

Mentors should guide students to:

		Elicit ideas	Add ideas	Distinguish ideas	Reflect
Mentoring	Develop practices	Identify or formulate a question in the context of the lab's research goals	Conduct experiments, collect and organize data	Analyze and interpret data Evaluate evidence Critique conclusions	Make final conclusions and plan next steps
	Expand content knowledge	Articulate hypotheses and questions about the research topic	Read literature, attend seminars, discuss with research team	Consider quality of evidence and relevance to argument	Synthesize experimental results
	Understand nature of science	Express expectations for science research experience	Attend lab meetings, experience experimental failure	Present progress reports and compare ideas in group setting	Consider how discoveries emerge from iterative processes
	Develop identity in science	Share goals for the URE relative to personal and career aspirations	Participate in social network of research team	Experience how process of criticism contributes to research progress; share ideas as a team	Recognize strengths related to career aspirations

Fig. 2. Mentoring to promote knowledge integration. Successful mentors elicit ideas to find out what students think, add relevant new ideas, encourage students to find evidence to distinguish among disparate ideas, and ask students to reflect and consolidate their experiences.

with experimental design, data collection, interpretation of findings, and scientific communication; help students understand the science concepts and practices necessary for the research project; and guide students to develop resilience to inevitable failures (32–34). Additionally, mentors

need to provide professional socialization and emotional support so that students can integrate their ideas about their scientific identity with the setbacks and confusions they encounter in their interactions with the members of the lab. One study shows that mentors can challenge students

to become aware of the tension between their own cultural norms and those of the scientific community (35). Other investigations found that students who feel supported by faculty are more likely to go to graduate school (22), that frequency of meetings with faculty mentors correlates with student confidence to perform science practices or pursue a research career (36), and that students who lack interactions with mentors and fail to get direction for research projects are likely to change career plans away from science (37). Studies suggest that mentors who function as career coaches, focusing on ways to remedy gaps in preparation, may be more effective than those who primarily emphasize social support (38). Overall, mentors play a crucial role in undergraduate research experiences, often with little preparation, support, or even rewards for their contributions.

Promoting persistence and identity

Longitudinal studies using the 2004 Freshman Survey and 2008 College Senior Survey tracked students who initially expressed an intention to pursue a STEM major (22, 39, 40). They found that students generally rated URE and CURE participation highly. Those who participated in UREs were 14 to 17% more likely to persist in science majors and more likely to retain their interest in graduate school than nonparticipants. However, the validity of this finding is undermined because intention to enroll in graduate school was inferred from a question asking for graduate school major, and those not planning to attend were instructed to skip the question (22). Although the analysis adjusts for missing data and low response rates, the surveys did not adequately differentiate between UREs and CUREs, adjust for difference in selection criteria across institutions, or control for duration (a known factor in impact), making interpretation worrisome (41, 42). Furthermore, these analyses do not establish the direction of causality since students may participate in a URE because of their desire to persist or their interest in building a relationship that could result in a letter of recommendation for graduate school, rather than persisting because of their experience in the URE.

To promote identity as a scientist, five studies augment self-report surveys about persistence with interviews (31, 43–45) or journal reflections (33). In interviews, undergraduates from groups underrepresented in science reported that research experiences increased their confidence and expanded their images of science careers by allowing them to try out the roles of research scientists (31, 45). Other undergraduates reported that the research experience gave them the opportunity to broaden their academic and professional science networks (33), the chance to learn how to act like professionals in a research setting (45), a feeling of ownership of their research project (46), and the option of determining whether the work of a scientist could align with their personal values and goals (44). Both interviews and journal writing had the added value of supporting students to connect ideas from their research experience to their views of themselves as scientists.

	Typical URE	Typical CURE
Selection criteria	Competitive, based on cumulative GPA in a declared STEM major; letters of reference; prior enrollment in a CURE Specialized, based on status as underrepresented minority or other criteria Student initiated based on faculty contact	Enrollment in course, prerequisite sometimes required
Curriculum	Apprenticeship model Observe mentor, learn data collection techniques, collect data for mentor's research question, attend lab meetings Communicate experience in poster thesis, conference	Inquiry investigation model Alternative or replacement for typical laboratory courses Guides student in explicit stages of research, culminates in paper or poster Graded assignments
Mentoring	Principal investigator, postdocs, graduate students, peers Communicate experience in poster thesis, conference	Course instructor (faculty and/or grad student), peers

Fig. 3. Characteristics of UREs and CUREs. CUREs typically provide research experiences for 30 or more students guided by a course instructor and/or graduate student, and involve classes, credits, grades, and assignments. Students typically compete for URE placements, spend time in a research laboratory, and receive one-on-one mentoring from a postdoc, graduate student, or faculty member.

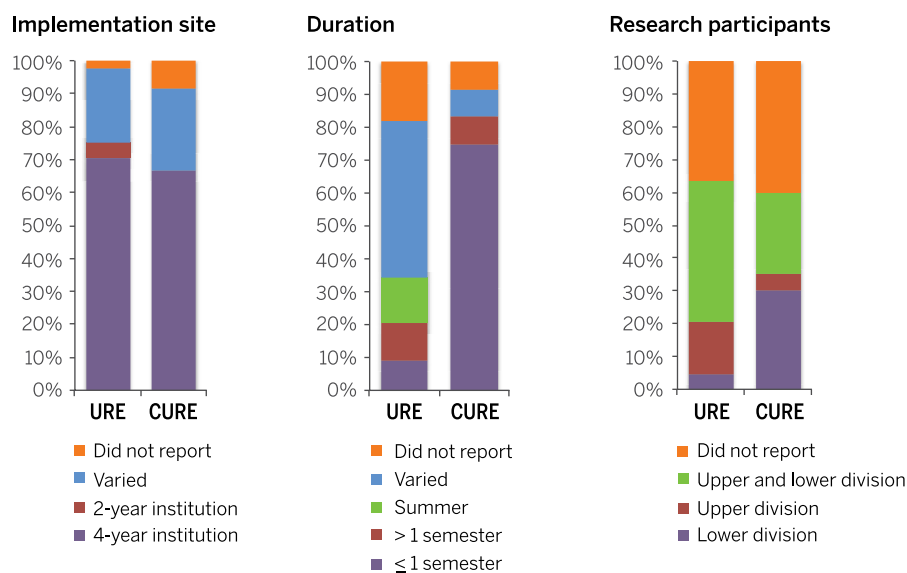


Fig. 4. Implementation site, duration, and research participants for UREs and CUREs. About 70% of the research experiences were studied at 4-year institutions. Most studies of CUREs involved lower-division students and lasted one semester or less, whereas studies of UREs involved both upper- and lower-division students whose length of participation varied within the study.

Access, duration, and selectivity of research experiences influence their impact. In the studies reviewed, students are more likely to participate in directed research with a faculty member in a small liberal arts institution (37) than in a large research university (25). Sustained participation (three or more semesters) in a URE builds identity as a scientist, whereas intermittent URE participation can be a negative experience (37) and short UREs have little to no benefit (25). Selection practices could also limit the impact of research experiences: One study found that high school preparation mattered more than research experiences for a sample of students who are from groups underrepresented in science and who begin college with high grades and aspirations (39). These findings reinforce the importance of mentoring and illustrate the complexity of designing effective research experiences.

These results raise the question of whether recruiting underrepresented students to UREs and CUREs coupled with appropriate mentoring could increase diversity in science. One program, SURE at Emory University, reports increasing diversity by bringing second-year community college students to flagship universities for UREs (41). They select students based on math preparation, experience with science, and success in overcoming challenges. Preference is given to first-generation college attendees and students from underrepresented groups. Regression analyses of transcripts revealed that SURE participants took more science courses as seniors and earned higher grades in those courses than nonparticipants. A replication with randomized assignment to SURE would strengthen the findings.

Improving research practices

Although self-report surveys show that participants believe they learned science practices such as lab techniques, ability to analyze data, and skill in oral and written presentation, the studies could be strengthened by measuring progress directly and by determining whether students have a coherent view of science practices (23, 41, 47–49). For example, students may develop data collection skills but lack ability to interpret results (25–27, 30). One study that combined surveys, interviews, and shadowing of eight undergraduates as they interacted with a research team found that students primarily set up and conducted experiments, rather than understanding the rationale for design or the interpretation of results (40).

These studies do help explain why duration affects outcomes from research experiences (23–25, 27, 37). During the first year, students, who are typically unfamiliar with the science concepts and techniques of the lab, need orientation to the specific research project and slowly acquire this knowledge. In 1 year or less, the duration of most UREs, students learn how to set up experiments specific to that lab and collect data but can rarely relate the analyses to a research question (30). Several studies found that adopting the traits, habits, and temperament (patience, perseverance, initiative) of scientific researchers only begins to emerge in the third semester of a

URE (26, 27). Some second-year students learned new methodological techniques, collected their own data, interpreted findings, and formulated new research questions. The slow enculturation into scientific practices helps explain survey results showing that 1-year UREs generate little progress in understanding science practices.

Expanding science conceptual understanding

Understanding of the underlying theories and concepts is essential for students to benefit from authentic science experiences and is more successful in CUREs than in UREs (27). CUREs offer opportunities to develop conceptual understanding by integrating lectures and readings with investigations of an important research question (50, 51). Thus, CUREs build on learning strategies that students have used in other courses.

URE placements often require conceptual understanding that is beyond the student's academic preparation, especially at research universities where students may join labs investigating questions that do not arise in undergraduate education. Although URE placements can motivate students to develop new insights, the limited evidence for gains in conceptual understanding suggests that this is rare. Typically, students need guidance to understand the rationale, research design, and contribution to the field in this new area (26, 27). Mentors may orient students to relevant literature, or students may seek resources on their own. After completing 1 year in the URE, undergraduates begin to benefit from reading literature, talking with senior scientists, and participating in lab meetings, activities likely to help them integrate their understanding of the underlying theories and concepts (30).

Studies have evaluated gains in conceptual understanding by using grade-point averages and patterns of future course selection, but these activities could result from multiple aspects of the experience (52). Promising assessments ask students to analyze new examples of primary literature, but are rarely used, probably due to the challenges of developing scoring rubrics (8, 50).

Communicating the nature of science

Both UREs and CUREs help students refine their appreciation of the process of scientific research (23, 27, 43). Students come to research experiences with inaccurate ideas about the nature of science (53, 54). For example, undergraduates expect research to be more efficient and to have fewer setbacks than they encounter. A student may describe a procedure as “finicky” or prone to errors rather than recognizing that trial and refinement are part of the nature of science (27). Students often develop conflicting ideas about the nature of science. For example, one student explained that the “scientific method” should be “stuck to like glue,” yet also reported that, “well it is alright to keep some things [the same] and change others” [(11), p. 1091].

Several studies use interviews and journals to show that students in research experiences make progress in understanding the nature of science.

In one study, undergraduates gained ability to attribute a scientific purpose to an experiment, describe theories scientifically, and recognize creativity in research and teaching (12). In another study, students shifted from viewing science as a stepwise linear progression to seeing science as messy and involving iteration (11). Examination of the interviews or journals suggests that motivating students to articulate their views about the nature of science and talk or write about their experiences helps them reflect on their experiences, consistent with the knowledge integration framework (see Fig. 2).

Conclusions

Evidence for the benefit of research experiences from the 60 reviewed studies published in the last 5 years is limited. One challenge involves documenting the differences between undergraduate research experiences and typical labs. Studies report that UREs often engage undergraduates in following experimental protocols rather than interpreting results. CUREs use lectures and readings to impart conceptual understanding about an important research question, consistent with instructional strategies in other courses (30, 50, 51, 55). While introducing new images of science, research experiences may also reinforce incomplete or inaccurate images. As expected, duration of UREs and intensity of mentoring both strengthen impacts and differentiate research experiences from typical labs (25, 36, 37).

Overall, these findings suggest the need for greater emphasis on integration of research experiences with the beliefs and expectations of undergraduates (13–17). When research experiences introduce new ideas, these ideas are often isolated and fragmented. Students need opportunities to integrate evidence from their research experiences to strengthen views of their identity as scientists, the range of science practices, ways to learn science concepts, and the nature of science. Interviews following UREs and CUREs document the value of asking students to reflect. These interviews sometimes engage undergraduates in reflecting on their experiences for the first time.

Using the knowledge integration framework to interpret the findings, we note that students need mentors who orient them to the practices and concepts of the lab so that they can fully benefit. In many UREs, it takes over a year for students to gain sufficient understanding to make sense of the science practices or concepts of the lab. The few studies that validate self-report findings with other evidence report that research experiences can expand students' images of the roles available in science (31, 45). This expanded repertoire of opportunities in science has the potential to help undergraduates find ways to self-identify as scientists. However, mentoring to incorporate these images into the students' identity is related to the amount of contact with a faculty mentor—a scarce resource in most programs. The most promising studies use interviews or journals to elicit ideas and to encourage students to distinguish among their initial ideas

and their experiences. These studies suggest that students who are encouraged to articulate their ideas and reflect on their experiences also consolidate their ideas, consistent with the emphasis in the knowledge integration framework on distinguishing ideas and reflecting. Designers could use the features of knowledge integration as criteria for reviewing and improving undergraduate research experiences (see Fig. 2).

Studies of research experiences need the same rigorous designs and assessments as other scientific research. Studies comparing promising alternative approaches to mentoring, ways to illustrate science practices, or methods for orienting participants to a URE placement would advance understanding. Following the knowledge integration framework, studies could compare journals, peer support, structured interviews, and one-on-one mentoring as ways to help students consolidate their understanding.

Comparison studies need appropriate controls to advance our understanding. Thus, comparisons of UREs and CUREs need to account for the differences among participants. For example, most students who meet the selection criteria for UREs have already decided to persist in science; those in CUREs may still be deciding.

The field needs agreed-upon criteria for undergraduate research experiences and validated, generalizable assessments for these criteria. Research to identify measures of research practices that can be used in multiple studies and criteria for evaluating mentoring interactions, as well as methods for measuring ability to locate and interpret primary literature, could advance the field. Promising measures should be tested across investigations and refined.

Disaggregating the populations targeted by undergraduate research experiences could help decision-makers allocate scarce resources. In many studies, the value of undergraduate research cannot be disentangled from precollege preparation. Using good measures of prior understanding and expectations, studies that analyze benefits for subgroups of students could also help those designing research experiences address the unique interests and aspirations of individuals and groups. Such studies could experiment with variations in the selection criteria for research experiences to determine whether current approaches are ideal. In addition, findings about successful experiences need replication and extension, particularly for students from nondominant cultures.

Research suggests a conundrum between mentor availability and mentor impact. Graduate students and postdocs generally mentor undergraduates about scientific practices and research, whereas faculty mentor undergraduates to develop an image of themselves as scientists. Mentors rarely receive guidance about how best to mentor undergraduates. The field would benefit from research that identifies mentoring practices and incorporates them into professional development for mentors, including graduate and postdoctoral researchers. Professional development can help mentors (i) identify and negotiate expectations with their mentees; (ii) explore under-

graduate assumptions about research experiences; (iii) monitor student progress; (iv) encourage reflection; and (v) support students emotionally as well as intellectually (51, 52). Methods are needed to allocate credit to faculty for mentoring students and developing effective UREs and CUREs.

Finally, the costs and benefits of research experiences for building human capital, benefiting undergraduates, improving workforce diversity, and strengthening educational outcomes need better understanding. Making the best use of extramural funds and the, often voluntary, contributions of faculty to allocate opportunities and improve undergraduate research experiences requires a strong research base.

REFERENCES AND NOTES

1. S. R. Singer, M. L. Hilton, H. A. Schweingruber, Eds., *America's Lab Report: Investigations in High School Science* (National Academies Press, Washington, DC, 2005).
2. C. Brewer, D. Smith, Eds., *Vision and Change in Undergraduate Biology Education: A Call to Action* (American Association for the Advancement of Science, Washington, DC, 2011).
3. M. J. Graham, J. Frederick, A. Byars-Winston, A. B. Hunter, J. Handelsman, Science education. Increasing persistence of college students in STEM. *Science* **341**, 1455–1456 (2013). doi: [10.1126/science.1240487](#); pmid: [24072909](#)
4. C. R. Critcher, D. Dunning, J. Pers. Soc. Psychol. **97**, 931–945 (2009).
5. T. D. Sadler, S. Burgin, L. McKinney, L. Ponjuan, Learning science through research apprenticeships: A critical review of the literature. *J. Res. Sci. Teach.* **47**, 235 (2010). doi: [10.1002/tea.20326](#)
6. A. P. Dasgupta, T. R. Anderson, N. Pelaez, Development and validation of a rubric for diagnosing students' experimental design knowledge and difficulties. *CBE Life Sci. Educ.* **13**, 265–284 (2014). doi: [10.1187/cbe.13-09-0192](#)
7. R. A. Duschl, H. A. Schweingruber, A. W. Shouse, Eds., *Taking Science to School: Learning and Teaching Science in Grades K-8* (National Academies Press, Washington, DC, 2007).
8. C. Gormally, P. Brickman, M. Lutz, Developing a Test of Scientific Literacy Skills (TOSLS): Measuring undergraduates' evaluation of scientific information and arguments. *CBE Life Sci. Educ.* **11**, 364–377 (2012). doi: [10.1187/cbe.12-03-0026](#); pmid: [23222832](#)
9. J. Osborne, Arguing to learn in science: The role of collaborative, critical discourse. *Science* **328**, 463 (2010). doi: [10.1126/science.1183944](#)
10. L. M. Stevens, S. G. Hoskins, The CREATE strategy for intensive analysis of primary literature can be used effectively by newly trained faculty to produce multiple gains in diverse students. *CBE Life Sci. Educ.* **13**, 224–242 (2014). doi: [10.1187/cbe.13-12-0239](#)
11. D. P. Cartrette, B. M. Melroe-Lehrman, describing changes in undergraduate students' preconceptions of research activities. *Res. Sci. Educ.* **42**, 1073–1100 (2012). doi: [10.1007/s11165-011-9235-4](#)
12. C. B. Russell, G. C. Weaver, A comparative study of traditional, inquiry-based, and research-based laboratory curricula: Impacts on understanding of the nature of science. *Chem. Educ. Res. Pract.* **12**, 57 (2011). doi: [10.1039/c1rp90008k](#)
13. J. D. Bransford, A. L. Brown, R. Cocking, *How People Learn: Brain, Mind, Experience, and School* (National Academy Press, Washington, DC, 1999).
14. J. W. Pellegrino, N. Chudowsky, R. Glaser, Eds., *Knowing What Students Know: The Science and Design of Educational Assessment* (National Academy Press, Washington, DC, 2001).
15. A. Wilson, S. Howitt, P. Roberts, P., G. Åkerlind, K. Wilson, Connecting expectations and experiences of students in a research-immersive degree. *Stud. High. Educ.* **38**, 1562 (2013). doi: [10.1080/03075079.2011.633163](#)
16. M. C. Linn, Designing computer learning environments for engineering and computer science: The scaffolded knowledge integration framework. *J. Sci. Educ. Technol.* **4**, 103–126 (1995). doi: [10.1007/BF02214052](#)
17. M. C. Linn, B.-S. Eylon, *Science Learning and Instruction: Taking Advantage of Technology to Promote Knowledge Integration* (Routledge, New York, 2011).
18. R. White, R. Gunstone, *Probing Understanding* (Falmer Press, New York, 1992).
19. S. E. Ainsworth, in *Current Perspectives on Cognition, Learning, and Instruction: Recent Innovations in Educational Technology That Facilitate Student Learning*, D. Robinson, G. Schraw, Eds. (Information Age Publishing, Charlotte, NC, 2008).
20. A. Collins, J. S. Brown, P. Duguid, *Educ. Res.* **18**, 32 (1989).
21. L. C. Auchincloss et al., Assessment of course-based undergraduate research experiences: A meeting report. *CBE Life Sci. Educ.* **13**, 29–40 (2014). doi: [10.1187/cbe.14-01-0004](#); pmid: [24591501](#)
22. M. K. Eagan Jr. et al., Making a difference in science education: The impact of undergraduate research programs. *Am. Educ. Res. J.* **50**, 683–713 (2013). doi: [10.3102/0002831213482038](#); pmid: [25190821](#)
23. O. A. Adedokun et al., Effect of time on perceived gains from an undergraduate research program. *CBE Life Sci. Educ.* **13**, 139–148 (2014). doi: [10.1187/cbe.13-03-0045](#); pmid: [24591512](#)
24. F. D. Carter, M. Mandell, K. I. Maton, The influence of on-campus, academic year undergraduate research on STEM PhD Outcomes: Evidence from the Meyerhoff Scholarship Program. *Educ. Eval. Policy Anal.* **31**, 441–462 (2009). doi: [10.3102/0162373709348584](#); pmid: [21785521](#)
25. M. Fecheimer, K. Webber, P. B. Kleiber, How well do undergraduate research programs promote engagement and success of students? *CBE Life Sci. Educ.* **10**, 156–163 (2011). doi: [10.1187/cbe.10-10-0130](#); pmid: [21633064](#)
26. H. Thiry, S. L. Laursen, The role of student-advisor interactions in apprenticing undergraduate researchers into a scientific community of practice. *J. Sci. Educ. Technol.* **20**, 771–784 (2011). doi: [10.1007/s10956-010-9271-2](#)
27. H. Thiry, T. J. Weston, S. L. Laursen, A. B. Hunter, The benefits of multi-year research experiences: Differences in novice and experienced students' reported gains from undergraduate research. *CBE Life Sci. Educ.* **11**, 260–272 (2012). doi: [10.1187/cbe.11-11-0098](#); pmid: [22949423](#)
28. National Academy of Sciences, National Academy of Engineering, Institute of Medicine, Adviser, Teacher, Role Model, Friend: On Being a Mentor to Students in Science and Engineering (National Academies Press, Washington, DC, 1997).
29. R. Pawson, *Mentoring Relationships: An Explanatory Review*, ESRC UK Centre for Evidence Based Policy and Practice (Working Paper 21, 2004, [www.kcl.ac.uk/sspp/departments/politicalconomy/research/cep/pubs/papers/paper-21.aspx](#)).
30. A. Feldman, K. A. Divoll, A. Rogan-Klyve, Becoming researchers: The participation of undergraduate and graduate students in scientific research groups. *Sci. Educ.* **97**, 218–243 (2013). doi: [10.1002/sce.21051](#)
31. C. Strawn, D. Livelybrooks, *J. Coll. Sci. Teach.* **41**, 47 (2012).
32. J. Schwartz, Faculty as undergraduate research mentors for students of color: Taking into account the costs. *Sci. Educ.* **96**, 527–542 (2012). doi: [10.1002/sce.21004](#)
33. O. A. Adedokun et al., *J. Coll. Sci. Teach.* **42**, 82 (2012).
34. P. R. Hernandez, W. P. Schultz, M. Estrada, A. Woodcock, R. C. Chance, Sustaining optimal motivation: A longitudinal analysis of interventions to broaden participation of underrepresented students in STEM. *J. Educ. Psychol.* **105**, 89–107 (2013). doi: [10.1037/a0029691](#)
35. A. J. Prunescu, J. Wilson, M. Walls, B. Clarke, Experiences of mentors training underrepresented undergraduates in the research laboratory. *CBE Life Sci. Educ.* **12**, 403–409 (2013). doi: [10.1187/cbe.13-02-0043](#); pmid: [24006389](#)
36. R. Taraban, E. Logue, Academic factors that affect undergraduate research experiences. *J. Educ. Psychol.* **104**, 499–514 (2012). doi: [10.1037/a0026851](#)
37. H. Thiry, S. L. Laursen, A.-B. Hunter, What experiences help students become scientists?: A comparative study of research and other sources of personal and professional gains for STEM undergraduates. *J. Higher Educ.* **82**, 357–388 (2011). doi: [10.1353/jhe.2011.0023](#)
38. B. W.-L. Packard, Mentoring and retention in college science: Reflections on the sophomore year. *J. Coll. Stud. Retention Res. Theory Pract.* **6**, 289–300 (2004-2005). doi: [10.2190/RUKP-XGVY-8LGO-75VH](#)
39. M. J. Chang, J. Sharkness, S. Hurtado, C. B. Newman, What matters in college for retaining aspiring scientists and engineers from underrepresented racial groups. *J. Res. Sci. Teach.* **51**, 555–580 (2014). doi: [10.1002/tea.21146](#)
40. L. L. Espinosa, *Harv. Educ. Rev.* **81**, 209 (2011).
41. B. Junge, C. Quiñones, J. Kakietek, D. Teodorescu, P. Marsteller, Promoting undergraduate interest, preparedness, and professional pursuit in the sciences: An outcomes evaluation of the SURE program at Emory University. *CBE Life Sci. Educ.* **9**, 119–132 (2010). doi: [10.1187/cbe.09-08-0057](#); pmid: [20516357](#)

42. P. W. Schultz *et al.*, *Educ. Eval. Policy Anal.* **33**, 95 (2011). doi: [10.3102/0162373710392371](https://doi.org/10.3102/0162373710392371)
43. M. Harrison, D. Dunbar, L. Ratmansky, K. Boyd, D. Lopatto, Classroom-based science research at the introductory level: Changes in career choices and attitude. *CBE Life Sci. Educ.* **10**, 279–286 (2011). doi: [10.1187/cbe.10-12-0151](https://doi.org/10.1187/cbe.10-12-0151); pmid: [21885824](https://pubmed.ncbi.nlm.nih.gov/21885824/)
44. M. L. Grunert, G. M. Bodner, Finding fulfillment: Women's self-efficacy beliefs and career choices in chemistry. *Chem. Educ. Res. Pract.* **12**, 420–426 (2011). doi: [10.1039/c1rp90050a](https://doi.org/10.1039/c1rp90050a)
45. S. M. Ovink, B. D. Veazey, More than "getting us through": A case study in cultural capital enrichment of underrepresented minority undergraduates. *Res. Higher Educ.* **52**, 370–394 (2011). doi: [10.1007/s11162-010-9198-8](https://doi.org/10.1007/s11162-010-9198-8)
46. D. I. Hanauer, J. Frederick, B. Fotinakes, S. A. Strobel, Linguistic analysis of project ownership for undergraduate research experiences. *CBE Life Sci. Educ.* **11**, 378–385 (2012). doi: [10.1187/cbe.12-04-0043](https://doi.org/10.1187/cbe.12-04-0043); pmid: [23222833](https://pubmed.ncbi.nlm.nih.gov/23222833/)
47. A. Khoukhi, A structured approach to honours undergraduate research course, evaluation rubrics and assessment. *J. Sci. Educ. Technol.* **22**, 630–650 (2013). doi: [10.1007/s10956-012-9419-3](https://doi.org/10.1007/s10956-012-9419-3)
48. D. Lopatto, Survey of Undergraduate Research Experiences (SURE): First findings. *Cell Biol. Educ.* **3**, 270–277 (2004). doi: [10.1187/cbe.04-07-0045](https://doi.org/10.1187/cbe.04-07-0045); pmid: [15592600](https://pubmed.ncbi.nlm.nih.gov/15592600/)
49. D. Lopatto, Undergraduate research experiences support science career decisions and active learning. *CBE Life Sci. Educ.* **6**, 297–306 (2007). doi: [10.1187/cbe.07-06-0039](https://doi.org/10.1187/cbe.07-06-0039); pmid: [18056301](https://pubmed.ncbi.nlm.nih.gov/18056301/)
50. C. D. Shaffer *et al.*, A course-based research experience: How benefits change with increased investment in instructional time. *CBE Life Sci. Educ.* **13**, 111–130 (2014). doi: [10.1187/cbe.13-08-0152](https://doi.org/10.1187/cbe.13-08-0152); pmid: [24591510](https://pubmed.ncbi.nlm.nih.gov/24591510/)
51. G. A. Szeinberg, G. C. Weaver, Participants' reflections two and three years after an introductory chemistry course-embedded research experience. *Chem. Educ. Res. Pract.* **14**, 23 (2013). doi: [10.1039/c2rp20115a](https://doi.org/10.1039/c2rp20115a)
52. S. Slovacek, J. Whittinghill, L. Flenoury, D. Wiseman, Promoting minority success in the sciences: The minority opportunities in research programs at CSULA. *J. Res. Sci. Teach.* **49**, 199–217 (2012). doi: [10.1002/tea.20451](https://doi.org/10.1002/tea.20451)
53. W. A. Sandoval, Understanding students' practical epistemologies and their influence on learning through inquiry. *Sci. Educ.* **89**, 634–656 (2005). doi: [10.1002/sce.20065](https://doi.org/10.1002/sce.20065)
54. N. G. Lederman, F. Abd-El-Khalick, R. L. Bell, R. S. Schwartz, Views of nature of science questionnaire: Toward valid and meaningful assessment of learners' conceptions of nature of science. *J. Res. Sci. Teach.* **39**, 497–521 (2002). doi: [10.1002/tea.10034](https://doi.org/10.1002/tea.10034)
55. M. Ing, W. W. Fung, D. Kisailus, *J. STEM Educ. Innovations Res.* **14**, 16 (2013).
56. E. L. Dolan, D. Johnson, Toward a holistic view of undergraduate research experiences: An exploratory study of impact on graduate/postdoctoral mentors. *J. Sci. Educ. Technol.* **18**, 487–500 (2009). doi: [10.1007/s10956-009-9165-3](https://doi.org/10.1007/s10956-009-9165-3)
57. E. L. Dolan, D. Johnson, The undergraduate-postgraduate-faculty triad: Unique functions and tensions associated with undergraduate research experiences at research universities. *CBE Life Sci. Educ.* **9**, 543–553 (2010). doi: [10.1187/cbe.10-03-0052](https://doi.org/10.1187/cbe.10-03-0052); pmid: [21123701](https://pubmed.ncbi.nlm.nih.gov/21123701/)
58. O. A. Adedokun, A. B. Bessenbacher, L. C. Parker, L. L. Kirkham, W. D. Burgess, Research skills and STEM undergraduate research students' aspirations for research careers: Mediating effects of research self-efficacy. *J. Res. Sci. Teach.* **50**, 940–951 (2013). doi: [10.1002/tea.21102](https://doi.org/10.1002/tea.21102)
59. C. Craney *et al.*, Cross-discipline perceptions of the undergraduate research experience. *J. Higher Educ.* **82**, 92–113 (2011). doi: [10.1353/jhe.2011.0000](https://doi.org/10.1353/jhe.2011.0000)
60. T. M. Edwards *et al.*, Group-Advantaged Training of Research (GATOR): A metamorphosis of mentorship. *Bioscience* **61**, 301–311 (2011). doi: [10.1525/bio.2011.61.4.10](https://doi.org/10.1525/bio.2011.61.4.10)
61. J. A. Harsh, A. V. Maltese, R. H. Tai, A perspective of gender differences in chemistry and physics undergraduate research experiences. *J. Chem. Educ.* **89**, 1364–1370 (2012). doi: [10.1021/ed200581m](https://doi.org/10.1021/ed200581m)
62. J. A. Harsh, A. V. Maltese, R. H. Tai, *J. Coll. Sci. Teach.* **41**, 84 (2011).
63. M. T. Jones, A. E. L. Barlow, M. Villarejo, Importance of undergraduate research for minority persistence and achievement in biology. *J. Higher Educ.* **81**, 82 (2010). doi: [10.1353/jhe.0.0082](https://doi.org/10.1353/jhe.0.0082)
64. J. John, J. Creighton, Researcher development: The impact of undergraduate research opportunity programmes on students in the UK. *Stud. High. Educ.* **36**, 781–797 (2011). doi: [10.1080/03075071003777708](https://doi.org/10.1080/03075071003777708)
65. L. Laursen, E. Seymour, A. Hunter, Learning, teaching and scholarship: Fundamental tensions of undergraduate research. *Change Magazine Higher Learning* **44**, 30–37 (2012). doi: [10.1080/00091383.2012.655217](https://doi.org/10.1080/00091383.2012.655217)
66. S. E. Brownell, M. J. Kloser, T. Fukami, R. Shavelson, *J. Coll. Sci. Teach.* **41**, 36 (2012).
67. J. Campisi, K. E. Finn, *J. Coll. Sci. Teach.* **40**, 38 (2011).
68. G. A. Szeinberg, *Long-Term Effects of Course-Embedded Undergraduate Research: The CASPIE Longitudinal Study* (unpublished doctoral dissertation), Purdue University, Indiana (2012).
69. C. M. Kardash, O. V. Edwards, Thinking and behaving like scientists: Perceptions of undergraduate science interns and their faculty mentors. *Instr. Sci.* **40**, 875–899 (2012). doi: [10.1007/s11251-011-9195-0](https://doi.org/10.1007/s11251-011-9195-0)
70. J. M. Burnette 3rd, S. R. Wessler, Transposing from the laboratory to the classroom to generate authentic research experiences for undergraduates. *Genetics* **193**, 367–375 (2013). doi: [10.1534/genetics.112.147355](https://doi.org/10.1534/genetics.112.147355); pmid: [23172853](https://pubmed.ncbi.nlm.nih.gov/23172853/)
71. K. M. Eagan, J. Sharkness, S. Hurtado, C. M. Mosqueda, M. J. Chang, Engaging undergraduates in science research: Not just about faculty willingness. *Res. Higher Educ.* **52**, 151–177 (2011). doi: [10.1007/s11162-010-9189-9](https://doi.org/10.1007/s11162-010-9189-9)
72. L. Behar-Horenstein, K. W. Roberts, A. C. Dix, Mentoring & tutoring. *Partnership in Learning* **18**, 269 (2010).
73. L. B. Pacifici, N. Thomson, *J. Coll. Sci. Teach.* **41**, 54 (2011a).
74. L. B. Pacifici, N. Thomson, Undergraduate science research: A comparison of influences and experiences between premed and non-premed students. *CBE Life Sci. Educ.* **10**, 199–208 (2011b). doi: [10.1187/cbe.11-01-0005](https://doi.org/10.1187/cbe.11-01-0005); pmid: [21633068](https://pubmed.ncbi.nlm.nih.gov/21633068/)

ACKNOWLEDGMENTS

This material is based upon work supported by the National Science Foundation under grant nos. DRL-1119670, DRL-0918743, and DRL-0822388. Any opinions, findings, and conclusions or recommendations expressed in this material are those of the authors and do not necessarily reflect the views of the National Science Foundation.

10.1126/science.1261757

RESEARCH ARTICLE SUMMARY

EXPRESSION PROFILING

Combinatorial labeling of single cells for gene expression cytometry

H. Christina Fan, Glenn K. Fu, Stephen P. A. Fodor*

INTRODUCTION: The measurement of specific proteins and transcripts in individual cells is critical for understanding the role of cellular diversity in development, health, and disease. Flow cytometry has become a standard technology for high-throughput detection of protein markers on single cells and has been widely adopted in basic research and clinical diagnostics. In contrast, nucleic acid measurements such as mRNA expression are typically conducted on bulk samples, obscuring the contributions from individual cells. Ideally, in order to characterize the complexity of cellular systems, it is desirable to have an affordable approach to examine the expression of a large number of genes across many thousands of cells.

RATIONALE: Here, we have developed a scalable approach that enables routine, digital gene expression profiling of thousands of single cells across an arbitrary number of genes, without using robotics or automation. The approach, termed “CytoSeq,” employs a recursive Poisson strategy. First, single cells are randomly depos-

ited into an array of picoliter wells. A combinatorial library of beads bearing cell- and transcript-barcoding capture probes is then added so that each cell is partitioned alongside a bead. The bead library has a diversity of $\sim 10^6$ so that each cell is paired with a unique cell barcode, whereas the transcript barcode diversity is $\sim 10^5$ so that each mRNA molecule within a cell becomes specifically labeled. After cell lysis, mRNAs hybridize to beads, which are pooled for reverse transcription, amplification, and sequencing. Because cDNAs from all polyadenylated transcripts of each cell are covalently archived on the bead surface, any selection of genes can be analyzed. The digital gene expression profile for each cell is reconstructed when barcoded transcripts are assigned to the cell of origin and counted.

RESULTS: We applied CytoSeq to characterize complex heterogeneous samples in the human hematopoietic system by examining thousands of cells per experiment. In addition to surface proteins that are traditional cell

type markers, we examined genes coding for cytokines, transcription factors, and intracellular proteins of various cellular functions that may not be readily accessible by flow cytometry. We demonstrated the ability to identify

ON OUR WEB SITE

Read the full article at <http://dx.doi.org/10.1126/science.1258367>

major subsets within human peripheral blood mononuclear cells (PBMCs). We compared cellular heterogeneity in resting CD3⁺ T cells versus those stimulated with antibodies to CD3 and CD28, as well as

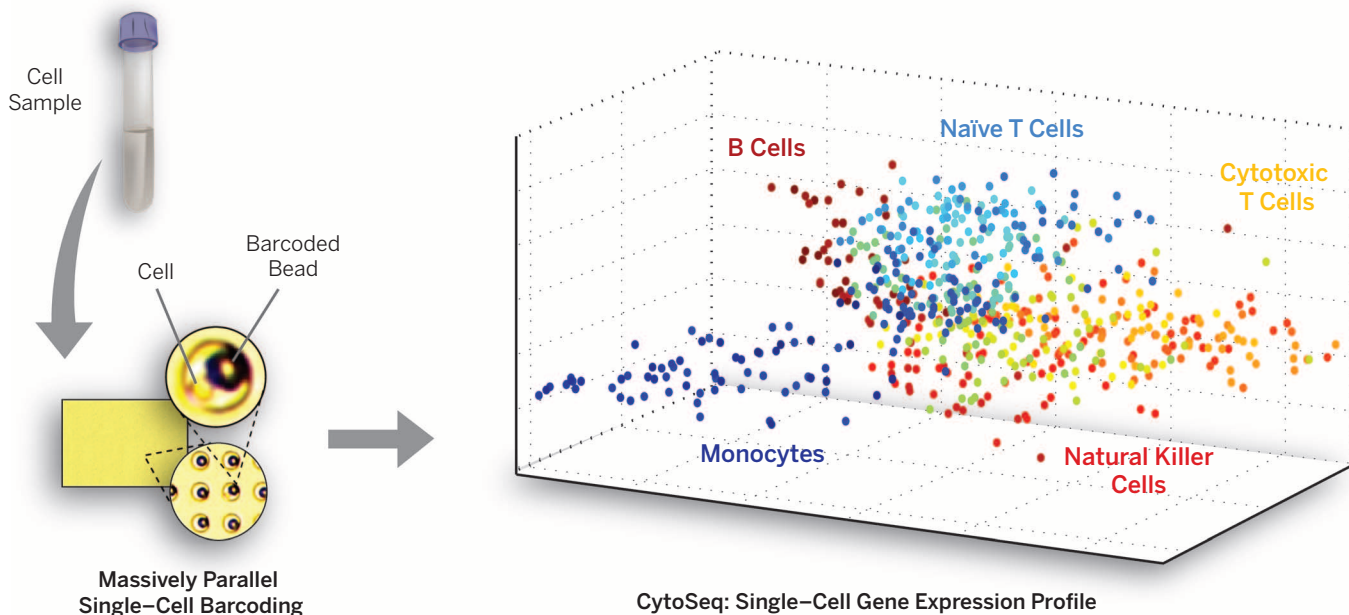
resting CD8⁺ T cells versus those stimulated with CMV peptides, and identified the rare cells that were specific to the antigen. Highlighting the specificity of large-scale single-cell analysis compared with bulk sample measurements, we found that the up-regulation of a number of genes in the stimulated samples originated from only a few cells (<0.1% of the population).

CONCLUSION: The routine availability of gene expression cytometry will help transform our understanding of cellular diversity in complex biological systems and drive novel research and clinical applications. The massively parallel single-cell barcoding strategy described here may be applied to assay other biological molecules, including other RNAs, genomic DNA, and the genome and the transcriptome together. ■

Cellular Research, Inc., 3183 Porter Drive, Palo Alto, CA 94304, USA.

*Corresponding author. E-mail: sfodor@cellular-research.com

Cite this article as H. C. Fan et al., *Science* 347, 1258367 (2015). DOI: 10.1126/science.1258367



Gene expression cytometry (CytoSeq). Massively parallel, stochastic barcoding of RNA content from single cells in a microwell bead array enables digital gene expression profiling of thousands of single cells simultaneously. Shown here is the principal component analysis for human PBMCs. Each point represents a single cell. Cells with correlated expression profiles are coded with similar colors.

RESEARCH ARTICLE

EXPRESSION PROFILING

Combinatorial labeling of single cells for gene expression cytometry

H. Christina Fan, Glenn K. Fu, Stephen P. A. Fodor*

We present a technically simple approach for gene expression cytometry combining next-generation sequencing with stochastic barcoding of single cells. A combinatorial library of beads bearing cell- and molecular-barcoding capture probes is used to uniquely label transcripts and reconstruct the digital gene expression profile of thousands of individual cells in a single experiment without the need for robotics or automation. We applied the technology to dissect the human hematopoietic system and to characterize heterogeneous response to in vitro stimulation. High sensitivity is demonstrated by detection of low-abundance transcripts and rare cells. Under current implementation, the technique can analyze a few thousand cells simultaneously and can readily scale to 10,000s or 100,000s of cells.

Understanding cellular diversity in large collections of cells requires the measurement of specific proteins or transcripts expressed by individual cells. Flow cytometry is well established as an important tool for detecting proteins in single cells. In contrast, RNA expression measurements are typically conducted on bulk samples, obscuring individual cell information. Although single-cell RNA expression measurements using microtiter plates or commercial microfluidic chips have recently been reported (1–9), these approaches require elaborate instrumentation and are expensive to implement for routine transcriptome analysis of large numbers of cells. Other methods based on nanoliter or picoliter partitioning of single cells followed by reverse transcription polymerase chain reaction (RT-PCR) (10–12) allow for the analysis of large numbers of cells but are practical for only a few genes at a time. To characterize the contributions of individual cells to a complex biological system, it is desirable to have an affordable and accessible method to couple large numbers of cells with large numbers of genes.

Here, we have developed a scalable approach that enables routine, digital gene expression profiling of thousands of single cells across an arbitrary number of genes. Microscale engineering and combinatorial techniques were used to label all mRNA molecules in a cell with a unique cellular barcode in a single massively parallel step. In addition, each transcript copy within a cell was indexed with a molecular barcode (7, 13–17), allowing PCR bias correction and absolute digital gene expression measurements. Labeled mRNA molecules from all cells were pooled, amplified, and sequenced. The digital gene expression profile of each cell was reconstructed using the cell and molecular barcodes on each sequence. This tech-

nology, which we term CytoSeq, enables the equivalent of protein flow cytometry for gene expression. We have applied the technique to multiparameter genetic classification of the hematopoietic system and demonstrated its use for characterizing cellular heterogeneity in immune response and for identifying rare cells in a population.

Results

Cell capture, labeling, and sequencing

The CytoSeq procedure is outlined in Fig. 1A. First, a cell suspension is loaded onto a microfabricated surface with up to 100,000 microwells. Each 30- μ m-diameter microwell contains a volume of ~20 picoliters. The number of cells in the suspension is adjusted so that only about 1 out of 10 wells receives a cell. Cells simply settle into wells by gravity.

Next, the bead library is loaded onto the microwell array to saturation, so that most wells become filled. The dimensions of the beads and wells have been optimized to prevent double occupancy of beads. Each 20- μ m bead has been functionalized with tens to hundreds of millions of oligonucleotide primers of the structure outlined in Fig. 1B. Oligonucleotides consist of a universal PCR priming site, followed by a combinatorial cell label, a molecular index, and an mRNA capture sequence of oligo(deoxythymidine) [oligo(dT)]. All primers on each bead share the same cell label but incorporate a diversity of molecular indices. A combinatorial split-pool synthesis method was devised to generate the bead library attaining a cell labeling diversity of close to 1 million. Because only ~1% of the total available cell label diversity is used, the probability of having two single cells tagged with the same label is low (on the order of 10^{-4}). Similarly, the diversity of the molecular labels on a single bead is on the order of 10^5 , so that the likelihood of two transcript molecules of the same gene from the same cell tagged with the same molecular index is low. Once single cells and beads are colocalized in the microwells, a lysis buffer is applied onto the surface and allowed to

diffuse inside. The high local concentration of released mRNAs (10s of nanomolar) effectively drives their hybridization onto the beads.

After mRNA capture, all beads are magnetically retrieved from the microwell array. From this point on, all reactions are carried out in a single tube. After reverse transcription, cDNA molecules synthesized on each bead become encoded with cell and molecular barcodes and serve as amplification templates (fig. S1).

Sequencing of amplification products reveals the cell label, the molecular index, and the gene identity (fig. S1). Computational analysis groups the reads based on the cell label and collapses the reads with the same molecular index and gene sequence into a single entry to correct for amplification bias, allowing the determination of absolute transcript numbers for each gene in each cell.

Identifying cell types in cell mixtures

To demonstrate the ability of CytoSeq to identify individual cells among a population of two cell types, a ~1:1 mixture of K562 (myelogenous leukemia) and Ramos (Burkitt's lymphoma) cells was loaded onto a partial array of ~25,000 microwells. A panel of 12 genes was selected and amplified from the cDNA beads and sequenced. The panel consisted of five genes specific for K562 cells, six genes specific for Ramos cells, and the common housekeeping gene *GAPDH* (table S1A). The majority of the sequencing reads (~78%) were associated with 765 unique cell labels (fig. S2).

The gene expression profile of each cell was clustered using principal component analysis (PCA) (Fig. 2A). The first principal component (PC) separated the cells into two major clusters based on cell type. The genes that contribute to the positive side of the first PC were specific to Ramos, whereas the genes that contributed to the negative side of the same PC were specific to K562. The second PC highlighted the high degree of variability in fetal hemoglobin (*HBG1*) expression within the K562 cells, which has been observed previously (15, 18).

Next, we spiked in a small number of Ramos cells into primary B cells from a healthy individual. A panel of 111 genes (table S1B) known to be involved in B cell function (19–21) was analyzed across 1198 cells. Eighteen cells (~1.5% of the population) were found to have a distinct gene expression pattern (Fig. 2B). Genes preferentially expressed by this group are known to be associated with Burkitt's lymphoma and include *MYC* and immunoglobulin M (IgM) and markers (*CD10*, *CD20*, *CD22*, and *BCL6*) associated with follicular B cells from which Burkitt's lymphoma originates (22) (Fig. 2C and fig. S3). In addition, this group of cells contained higher levels of *CCND3* and *GAPDH*, as well as an overall higher mRNA content (Fig. 2B). This finding is consistent with the fact that lymphoma cells are physically larger than primary B cells in normal individuals and that they are rapidly proliferating and transcriptionally more active.

Several methods were used to estimate the RNA capture efficiency of CytoSeq. First, *GAPDH* in 10 pg of Ramos total RNA was measured to be ~343 copies using digital RT-PCR. Additionally,

Cellular Research, Inc., 3183 Porter Drive, Palo Alto, CA 94304, USA.

*Corresponding author. E-mail: sfodor@cellular-research.com

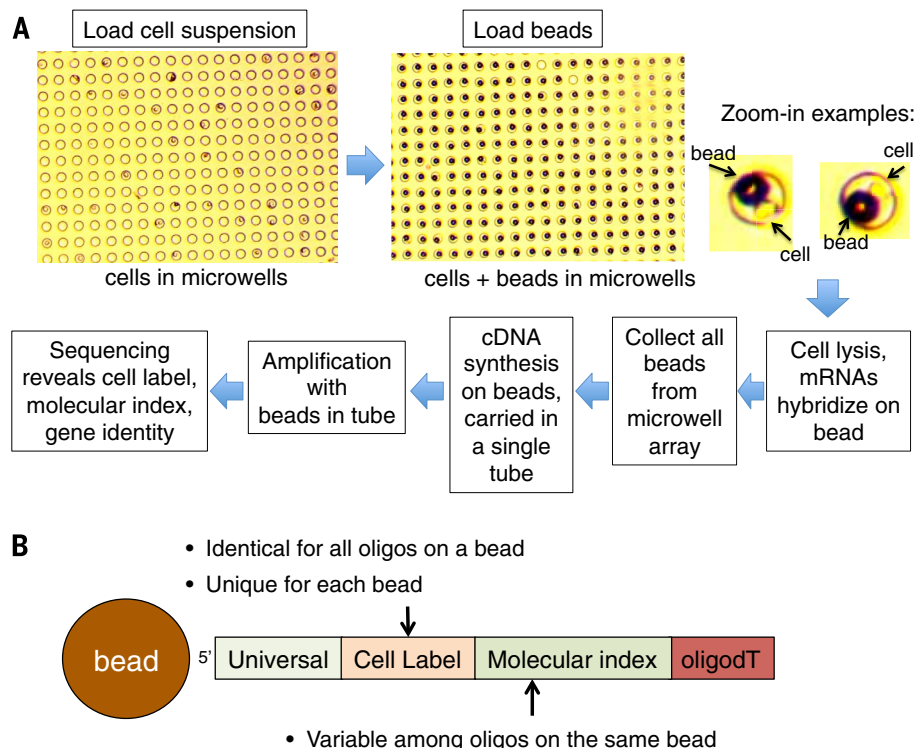


Fig. 1. Description of CytoSeq. (A) Experimental procedure for CytoSeq. (B) Structure of oligonucleotides attached to beads.

we tested individual Ramos cells using a sensitive molecular indexing technique (15) and determined an average of 214 ± 36 (SE) *GAPDH* transcripts per cell. These results were comparable to the 152 ± 10 (SE) copies yielded by CytoSeq. Further, we compared CytoSeq measurements with bulk RNA-seq data of ~20 million Ramos cells obtained from Sultan *et al.* (23). We observed a high correlation of gene expression levels ($R^2 = 0.946$) across three orders of magnitude (fig. S4).

Dissecting human PBMCs

Most biological samples, such as blood, contain diverse populations of numerous cell types and states with subtle differences in gene expression profiles. We applied CytoSeq to identify all the major cell types in human peripheral blood mononuclear cells (PBMCs), including monocytes, natural killer (NK) cells, and the different T and B cell subsets. Unlike traditional immunophenotyping that is limited mostly to surface protein markers, we included 98 genes for cytokines, transcription factors, and intracellular proteins of various cellular functions in addition to surface proteins (table S1C). We analyzed the digital gene expression profile of 632 PBMCs (Fig. 3 and fig. S5). The first PC separated monocytes and lymphocytes into two orthogonal clusters by the expression of *CD14*, *CD16a*, *SI00A12*, and *CCR2* in one cluster and lymphocyte-associated genes in the other. Subtypes of lymphocytes were located in a continuum along the second PC, with B cells [expressing immunoglobulins M and D (IgM, IgD), *TCL1A*, *CD20*, *CD24*, and *PAX5*] at one end, naïve T cells (expressing *CD4*, *CCR7*, and

CD62L) in the middle, and cytotoxic T cells (expressing *CD8A*, *CD8B*, *EOMES*, and *PRF1*) at the other end. Natural killer cells expressing killer-like immunoglobulin receptor (KIR), *CD16a*, and perforin (*PRF1*) were localized in the space between monocytes and cytotoxic T cells. We also observed that *GAPDH*, an enzyme involved in cellular metabolism, was expressed at highest levels in monocytes and lowest in B cells. Correlation analysis of gene expression profiles reiterated observations with PCA and revealed additional smaller subsets of cells within each major cell type (fig. S6). A replicate experiment with PBMCs from the same individual using 731 cells yielded similar segregation and cell type frequencies (fig. S7).

Measuring heterogeneity in activated T cells

When measurements are performed on a bulk sample, the observed gene expression levels cannot be assigned to individual cells, and large expression changes from a small number of cells cannot be distinguished from small changes in a large number of cells. The overall gene expression pattern is therefore dependent on the cell composition and the expression level of each gene in each cell type or subtype. To illustrate, we studied the variability of response of human T cells to an in vitro stimulus.

CD3⁺ T cells, isolated by negative selection from a blood donor, were stimulated with antibodies to CD28 and CD3 for 6 hours and analyzed by CytoSeq. A separate sample of unstimulated cells was also tested. Expression of a panel of 93 genes (table S1D) that included surface proteins, cytokines, and effector molecules expressed by differ-

ent T cell subsets was measured (24–26). A total of 3517 and 1478 cells were analyzed for the stimulated and unstimulated samples, respectively.

In the unstimulated sample, PCA analysis revealed two major subsets of cells. Examination of the genes enriched showed that one subset represented cytotoxic T cells with expression of *CD8A*, *CD8B*, *NKG2D*, *GZMA*, *GZMH*, *GZMK*, and *EOMES*, and the other subset represented helper T cells with expression of *CD4*, *CCR7*, and *SELL* (Fig. 4A and fig. S8).

In the stimulated sample, two branches of cells were observed on the PCA plot (Fig. 4B and fig. S9). The first principal component represented cellular response in terms of *IRF4*, gamma interferon (*IFNG*), *CD69*, tumor necrosis factor (*TNF*), and *GAPDH* expression. *CCL3*, *CCL4*, and *GZMB*, cytokines and effector molecules expressed in cytotoxic T cells, and *LAG3*, a marker associated with exhausted cells, were localized to cells in the upper branch. Expression of interleukin 2 (*IL2*), *LTA*, *CCL20*, and *CD40LG*, cytokines and surface protein associated with T helper cells (T_H1), were localized to cells in the lower branch. Additional genes, including *IL4R*, *PRDM1*, *TBX21*, *ZBED2*, *MYC*, *FOSL1*, *CSF2*, *TNFRSF9*, and *BCL2*, were expressed to various degrees in a smaller number of cells (fig. S9). Most of these cytokines, effector molecules, and transcription factors were either not expressed or were expressed at very low levels by cells in the unstimulated sample. Although most of the cells that responded within this short period of stimulation were presumably memory cells, we observed a small population of cells that produced lower levels of *IL2* and no other cytokines or effector molecules and might represent naïve cells (Fig. 4B, arrow).

To fully appreciate the heterogeneity in response, cells were clustered based on pairwise correlation coefficients. Although the two main groups of helper and cytotoxic cells were observed, there were additional smaller subsets of cells as well as considerable diversity within each subset in terms of the combination and level of activated genes expressed (fig. S10, A and B).

A few cytokines, namely *IL4*, *IL5*, *IL13*, *IL17F*, *IL22*, *LIF*, *IL3*, and *IL21*, were highly up-regulated in the stimulated sample as a whole as compared with the unstimulated sample, but were contributed only by a few cells in the sample (Fig. 4C). Subsets of these cytokines were expressed by the same cells (fig. S11). For instance, just one cell coexpressed *IL17F* and *IL22*, a signature for T_H17 cells. Another seven cells expressed various combinations of *IL4*, *IL5*, and *IL13*, signatures of T_H2 cells. The observed frequencies of T_H2 and T_H17 cells, which primarily reside in secondary lymphoid tissues and are rare in peripheral blood, agreed with those previously measured by flow cytometry (27, 28). The low frequency of specialized cells contributing to large changes in overall gene expression highlights the importance of sampling large number of single cells.

The large up-regulation of a set of genes in very few cells served as an important control to measure system cross-talk. Although any uncaptured RNA should be diluted into the vast volume

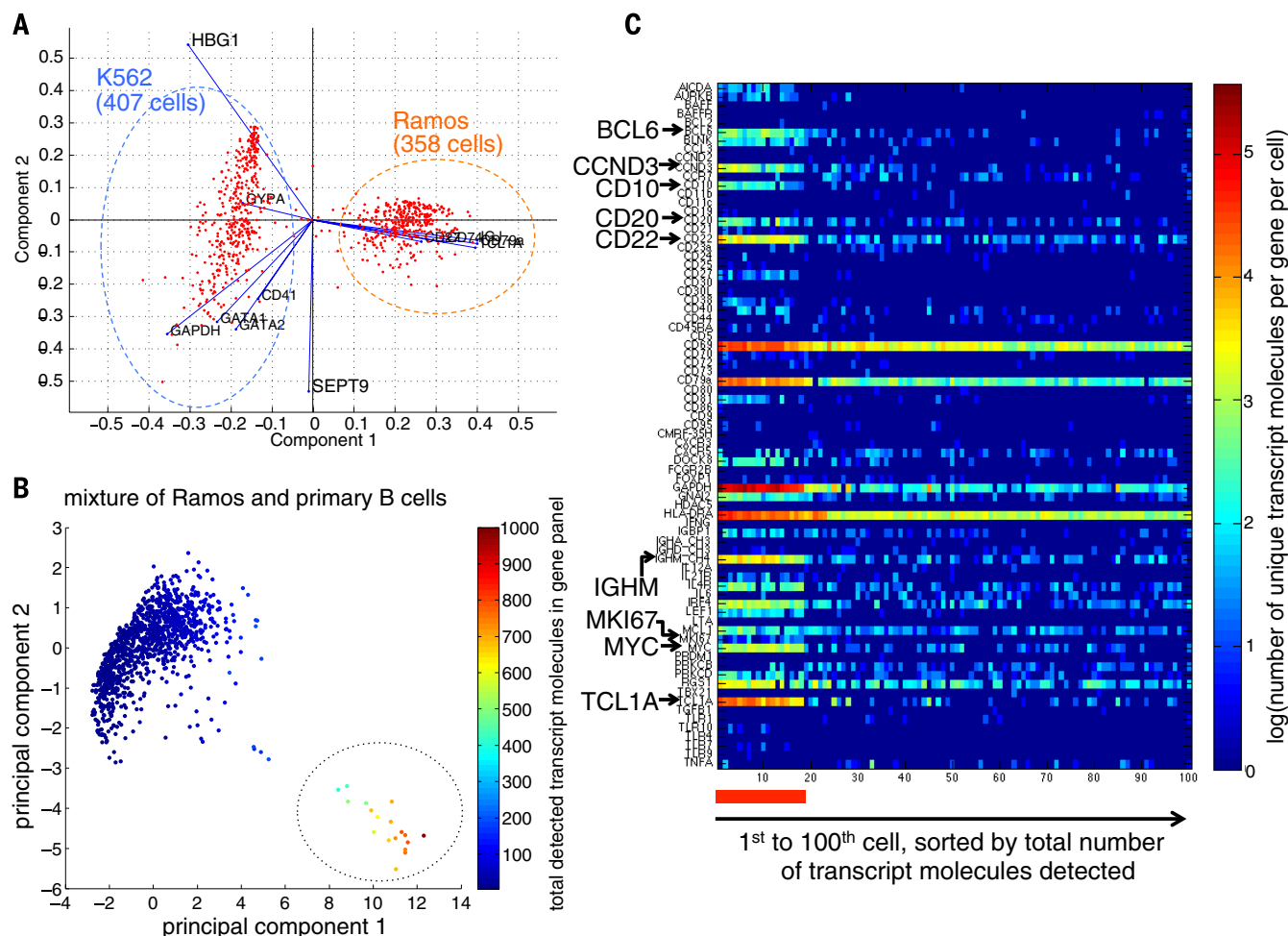


Fig. 2. Clustering of single cells in controlled mixtures containing two distinct cell types. (A) Clustering of a mixture of K562 and Ramos cells by PCA of the expression of 12 genes. The biplot shows two distinct clusters, with one cluster expressing Ramos-specific genes (*CD74*, *CD79A*, *IGJ*, *TCL1A*, *SEPT9*, and *CD27*) and the other expressing K562-specific genes (*CD41*, *GYP A*, *GATA1*, *GATA2*, and *HBG1*) separated by the first PC (horizontal). The second PC (vertical) indicates the variability in fetal hemoglobin (*HBG1*) within the K562 cells. (B) PCA of a mixture containing a small percentage of Ramos cells in a background of primary B cells from a

healthy individual using a panel of 111 genes. The color of each data point indicates the total number of unique transcript molecules detected across the entire gene panel. A set of 18 cells (circled) out of 1198 cells displays a distinct gene expression profile with much higher transcription levels. (C) Heat map showing expression level of each gene in the top 100 cells in the sample of (B), ranked by the total number of transcript molecules detected in the gene panel. The top 18 cells, indicated by the horizontal red bar, expressed preferentially a set of genes known to be associated with follicular lymphoma, as indicated by arrows.

of lysis buffer above the microwells, it is possible that a highly expressed mRNA could contaminate beads in neighboring microwells. However, high transcript counts for *IL17F* and *IL22* (~230 copies) were restricted to just one cell, with no indication of significant contamination across other beads, suggesting a low level of any cross-talk that might have occurred.

Analysis of T cells from a second blood donor (669 and 595 stimulated and unstimulated cells, respectively) also demonstrated similar partitioning of cells into the two main T cell branches (figs. S8, S9, and S10, C and D).

Identifying rare antigen-specific T cells

Fresh blood from the previous two individuals, who were seropositive for cytomegalovirus (CMV), was exposed to a CMV pp65 peptide pool. An untreated blood sample from each donor served as a control. Using negatively selected CD8⁺ T

cells, we analyzed 581 CMV-exposed cells and 253 unexposed cells for donor 1, and 2274 exposed and 2337 unexposed cells for donor 2.

Donor 1's negative control did not yield a sufficient number of cells to form well-separated clusters. The rest of the samples showed two main groups of cells (Fig. 5 and figs. S12 and S13). Cells in one group expressed naïve and central memory-associated genes (*SELL*, *CCR7*, and *CD27*), whereas cells in the other group expressed effector memory (*CCL4*, *CX3CR1*, and *CXCR3*) and effector-associated genes (*EOMES*, *GZMA*, *GZMB*, *GZMH*, *TBX21*, and *ZNF683*) (25, 26, 29). There was a small but distinct cluster of cells expressing granzyme K (*GZMK*) and another cluster expressing HLA class II histocompatibility antigen DR alpha chain (*HLA-DRA*). The differential expression of the different types of granzymes has been reported previously (30). Our results here recapitulated those observed in CyTOF experiments with CD8⁺ T cells (31).

Although a considerable proportion of cells responded to antigen exposure by expression of *CD69* and *MYC* (fig. S13A), only a few cells expressed *IFNG*, a signature cytokine for activated antigen-specific cells. The *IFNG*-expressing cells were among the most transcriptionally active and belong to the effector memory and effector cell cluster (Fig. 6 and fig. S14). We identified 5 out of 581 (0.86%) and 2 out of 2274 (0.09%) cells in donors 1 and 2, respectively, that were likely CMV-specific based on *IFNG* expression and overall transcription levels. This frequency of occurrence agrees with that observed by cytokine flow cytometry, enzyme-linked immunospot assay (ELISPOT), and tetramer assay (32). Among those cells, there was a substantial amount of heterogeneity in terms of combinations and levels of effector molecules (e.g., granzymes) and cytokines (e.g., *IFNG*, *IL2*, *CCL3*, *CCL4*, *TNF*, *CSF2*, and *IL4*) expressed (fig. S15). Interestingly, the most transcriptionally

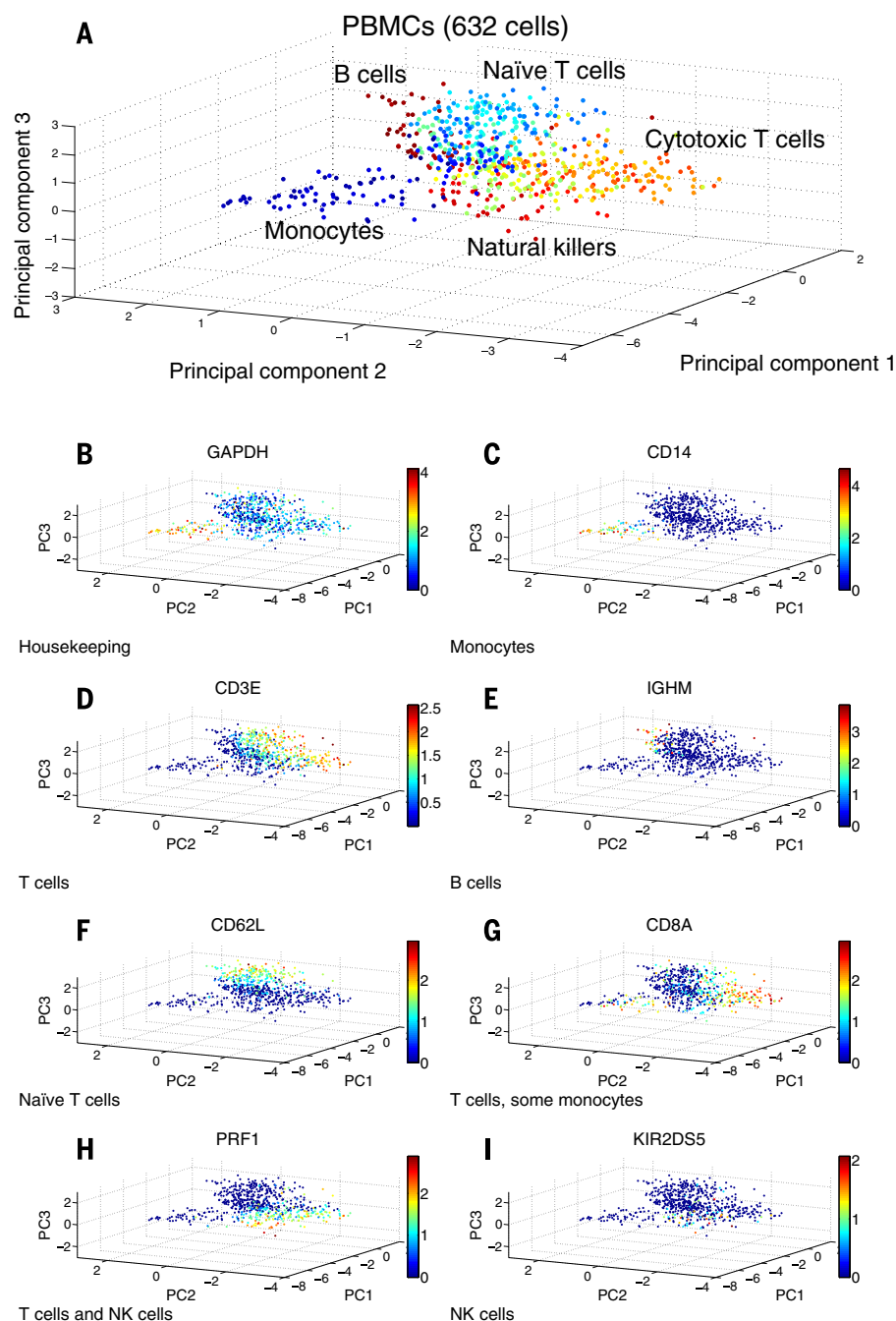


Fig. 3. Simultaneous identification of major cell types in a human PBMC sample (632 cells) by PCA analysis assayed by CytoSeq. (A) Cells with highly correlated expression profile are coded with similar color. (B to I) Expression of *GAPDH* and a representative gene of each major cell type by each cell. Color indicates natural log of the number of unique transcript molecules observed per cell. Fig. S4 shows results of 17 additional genes with clear segregation on the three-dimensional (3D) PC plot.

active cell in donor 2 did not express *IFNG* but expressed *IL6* and *IL1B*, inflammatory cytokines that are usually produced by monocytes and macrophages and might represent a unique rare subtype of CD8⁺ T cell.

Discussion

We present here highly scalable mRNA cytometry that uses a recursive Poisson strategy to isolate sin-

gle cells, uniquely barcode cellular content, and index individual molecules for quantitative analysis. We have shown the simultaneous identification and counting of transcript molecules belonging to each cell in a sample of thousands of cells. Further, this technique can be used to characterize individual cells based on their expression profiles in naturally occurring heterogeneous systems and to detect rare cells in a large background population.

CytoSeq offers advantages over existing single-cell approaches using microtiter plates or commercial microfluidic chips. Because the experimental procedure does not require expensive instrumentation, and reagent consumption per cell is low (in the nanoliter range), one can readily carry out single-cell analysis on large numbers of cells across multiple conditions. In this study, we performed single-cell gene expression measurements of ~15,000 cells across 12 experiments, which would be costly and time-consuming if attempted by existing methods. The number of cells measured by CytoSeq can be readily scaled to 10,000s or 100,000s by increasing the size of the microwell array and the library size of the barcoded beads. We calculate that the consumable cost (i.e., bar-coded beads, microwells, enzymes, and primers) required for a 10,000-cell experiment is at least two to three orders of magnitude lower (less than \$1 per cell) than current commercial microfluidics approaches. In addition, the method used for isolating single cells in CytoSeq does not impose a restriction on the uniformity of cell sizes, thus allowing direct analysis of complex samples of heterogeneous cell size and shape, such as PBMCs. Although our experiments focused on the hematopoietic system, solid samples can also be analyzed using mechanical or enzymatic tissue-dissociation methods well established for flow cytometry.

Single-cell transcriptome analysis is a powerful approach for characterizing and understanding cellular diversity. In addition, CytoSeq complements and expands the capabilities of fluorescence or mass spectrometry-based cytometry (33, 34). It increases versatility in terms of the numbers and types of gene products studied. Unlike flow cytometry, which is largely restricted to surface proteins with high-affinity antibodies, CytoSeq detects any transcribed mRNA without the limitations of antibody availability. In addition, the high sensitivity and multiparametric features of CytoSeq enable rare cell characterization on small samples with insufficient cells for traditional flow cytometry. Finally, sequencing in CytoSeq provides nucleotide precision along with quantitative gene expression information, permitting qualitative examinations of genetic structure across individual cells, such as mutations or variants, T cell receptors (35), or immunoglobulins.

Because all polyadenylated RNAs are captured and archived as covalently attached cDNAs on the beads, one can elect to study any arbitrary set of genes or repeat the analysis with other sets of genes. Whole transcriptome sampling is also possible by employing universal cDNA amplification techniques (36–39) or amplification-free single molecule DNA sequencing (40–42). However, it is important to consider the sequencing depth required for routine characterization of large number of cells across the whole transcriptome. Assuming ~200,000 transcript molecules per cell (considering only the polyadenylated portion of the transcriptome), each cell would require ~2 million reads for a 10-fold coverage. Thus, to examine 1000 cells per sample, upwards of ~2 billion reads are required—equivalent to the current

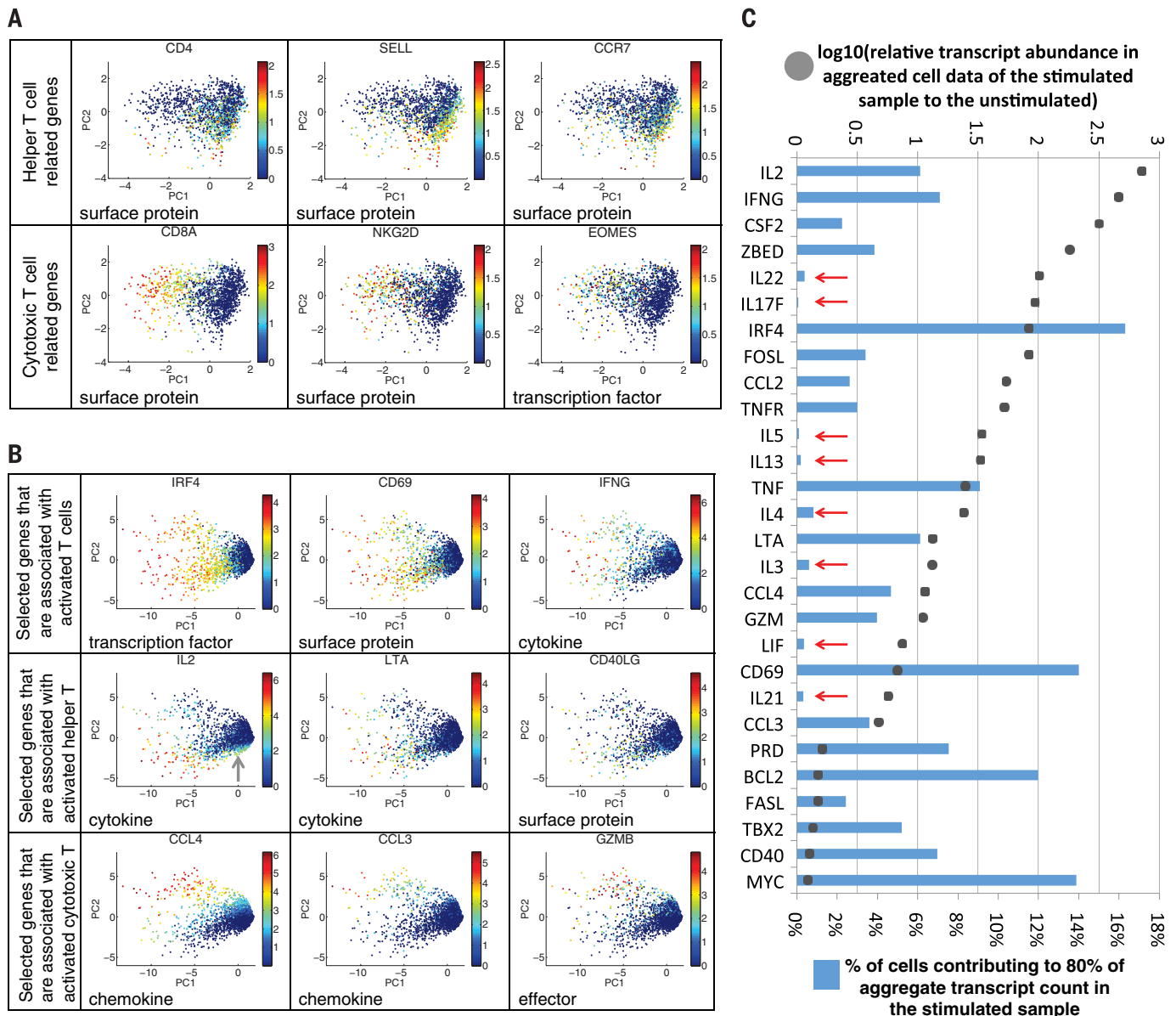


Fig. 4. Dissecting subpopulations of CD3⁺ T cells. (A) PCA of donor 1 unstimulated sample reveals two major branches of cells. The expression level (log of unique transcript molecules) of a particular gene within each cell is indicated with color. T_H cell-associated genes are enriched in cells in the lower branch, while cytotoxic T cell-associated genes are enriched in the upper branch. Shown here are representative genes. (B) PCA of donor 1 sample stimulated with antibodies to CD3 and CD28, showing enrichment of ex-

pression of indicated genes to one of the two main branches representing helper and cytotoxic T cells. These genes are present at low amounts in the unstimulated sample. (C) Number of cells that contribute to the overall expression level of genes that exhibit large relative changes when comparing stimulated over unstimulated samples in aggregate data. For several cytokines (red arrows), the contribution from only a small number of cells accounts for the large overall gene expression change in the entire population.

output of the highest-capacity next-generation sequencer (HiSeq, 2500), of which a single run can cost more than \$15,000 and requires 6 days to complete. In contrast, the same number of cells assayed across ~100 genes requires only a small sequencing run (1 to 10 million reads, less than \$1000, and a 1-day runtime). Shallow whole transcriptome sequencing (20,000 to 500,000 reads per cell), surveying several hundred to slightly over a thousand of the highly abundant genes is an alternative, as it has been shown to be sufficient to differentiate cell types in some samples (5, 43). The trade-offs of between depth of sequencing

and differential gene expression of single cells have recently been discussed (44). As sequencing costs continue to fall, whole-transcriptome implementation of CytoSeq will become more affordable to a larger number of researchers to explore larger numbers of cells and conditions.

The routine availability of gene expression cytometry will help transform our understanding of cellular diversity in complex biological systems and drive novel clinical applications, such as circulating tumor cell analysis, diagnostics of immune disorders and infectious diseases, monitoring of immunotherapy and vaccinations, and therapeutic

development. The massively parallel single-cell barcoding strategy described here may be applied to assay other biological molecules, including other RNAs, genomic DNA, and the genome and the transcriptome together.

Materials and methods

Fabrication of microwell array

Microwell arrays were fabricated using standard photolithography. An array (~35 by 15 mm) containing ~150,000 micropillars were patterned with SU-8 on a silicon wafer. Polydimethylsiloxane (PDMS) was poured onto the wafer to create

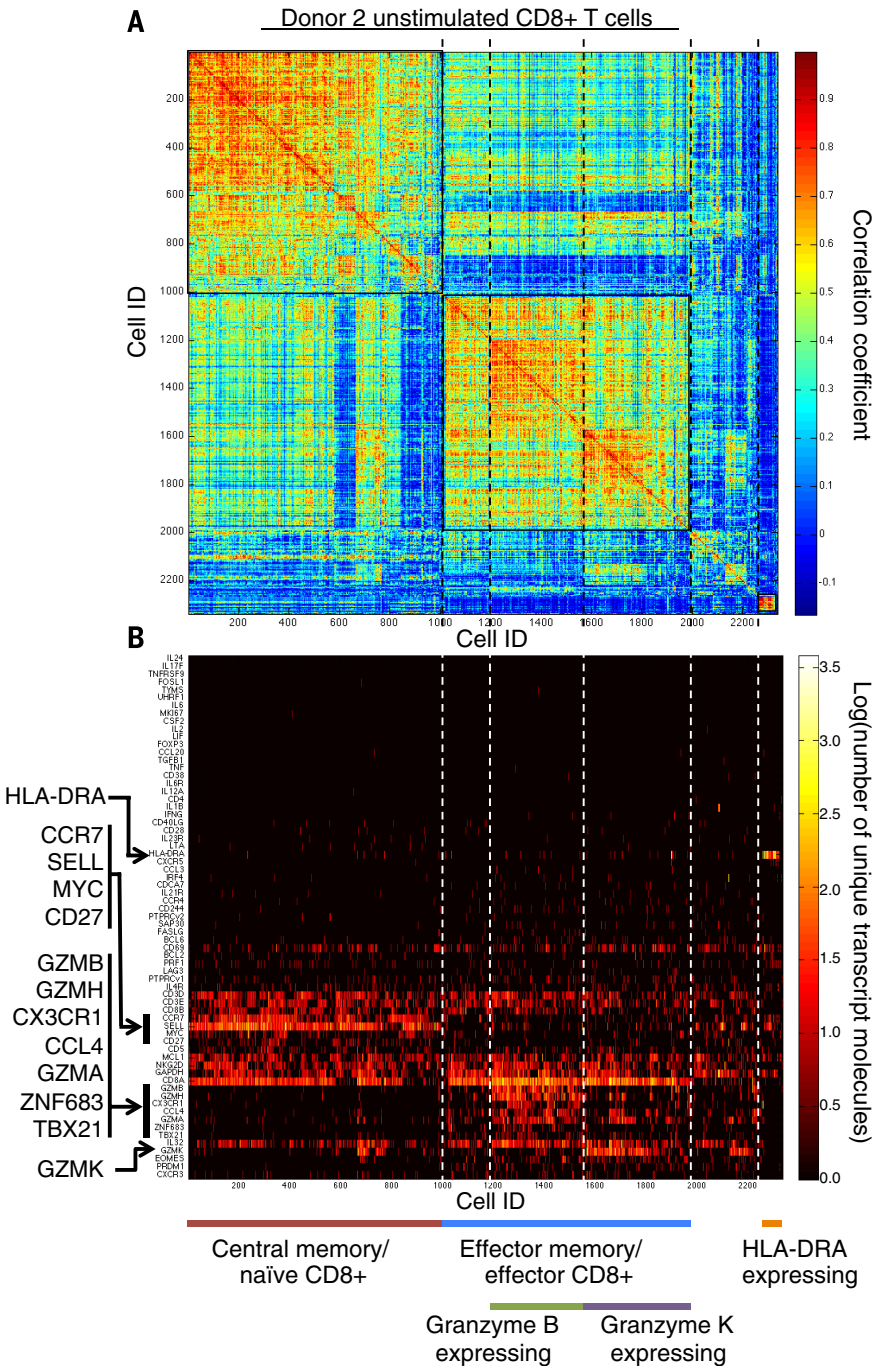


Fig. 5. Dissecting subpopulations of CD8⁺ T cells. Clustering of CytoSeq data defines two major groups of CD8⁺ cells. One group expresses genes shared by central memory/naïve cells, and the other group expresses genes shared by effector memory/effector cells. Shown here is data of donor 2's unstimulated sample. **(A)** Heat map showing correlation between each pair of cells. **(B)** Heat map showing the level of expression of each gene in each cell. Cells and genes are ordered by bidirectional hierarchical clustering.

arrays of microwells. Replicas of the wafer were made with NOA63 optical adhesive using the PDMS microwell array as template. Agarose (5%, type IX-A, Sigma) microwell arrays were cast from the NOA63 replica before each experiment. For experiments described here, a subsection of the full array was cut and used, ranging from ~25,000 to 100,000 wells (table S3). The size of the microwell array can be increased simply by

increasing the total area of the microwell array pattern on the lithography mask and fabricated with the same steps above. For instance, a 3" by 2" microscope slide can hold ~1.4 million wells, for capturing ~140,000 single cells.

Synthesis of bead library

Beads were manufactured by Cellular Research, Inc., using a split-pool combinatorial approach.

Briefly, 20- μ m-diameter magnetic beads functionalized with carboxyl groups (Spherotech) were distributed into 96 tubes. Using carbodiimide chemistry, a 5' amine modified oligonucleotide bearing a universal PCR priming sequence, a unique eight-nucleotide cell label, and a common linker were coupled to the beads in each tube. Conjugated beads from all tubes were then pooled and split into a second set of 96 tubes for annealing to template oligonucleotides bearing the complement to the common linker, another eight-nucleotide cell label, and a new common linker. After enzymatic polymerization, the beads were again pooled and split into a third set of 96 tubes for annealing to oligonucleotides bearing oligo(dA)₁₇ on the 5' end, followed by a randomly synthesized eight-nucleotide sequence that serves as the molecular index, a third eight-nucleotide cell label, and a complementary sequence to the second linker. After enzymatic polymerization, the beads were pooled to derive the final library. Each resulting bead is coated with tens to hundreds of millions of oligo-(dT) oligonucleotides of the same clonally represented cell label (884,736 or 96 \times 96 \times 96 possible barcodes) and a molecular indexing diversity of 65,536 (4⁸). The library size is increased exponentially by linearly increasing the diversity at each step of synthesis.

Sample preparation

K562 and Ramos cells were cultured in RPMI-1640 with 10% fetal bovine serum (FBS) and 1x antibiotic-antimycotic. Primary B cells from a healthy donor were purchased from Sanguine Biosciences. PBMCs from a healthy donor were isolated from fresh whole blood in sodium heparin tubes acquired from the Stanford Blood Center using Lymphoprep solution (StemCell).

T cell stimulation

Heparinized whole blood of two CMV seropositive blood donors was obtained from the Stanford Blood Center. For CMV stimulation, 1 ml of whole blood was stimulated with CMV pp65 peptide pool diluted in phosphate-buffered saline (PBS) (Milenyi Biotec) at a final concentration of 1.81 μ g/ml for 6 hours at 37°C. A separate sample of whole blood from each donor was incubated with PBS as negative controls. CD8⁺ T cells were isolated using RosetteSep cocktail (StemCell) and subsequently deposited onto microwell arrays. For stimulation with antibodies to CD3 and CD28, T cells from the same two donors were isolated from whole blood using RosetteSep T cell enrichment cocktail and resuspended in RPMI-1640 with 10% FBS and 1x antibiotic-antimycotic. One sample of cells from each donor was incubated with Dynabeads Human T-Activator CD3/CD28 (Life Technologies) at ~1:1 bead-to-cell ratio at 37°C for 6 hours. A separate sample of cells from each donor was placed in the incubator without stimulation to serve as negative controls.

Single-cell capture

Cell density was measured by hemocytometer counting (table S3) and adjusted to achieve ~1

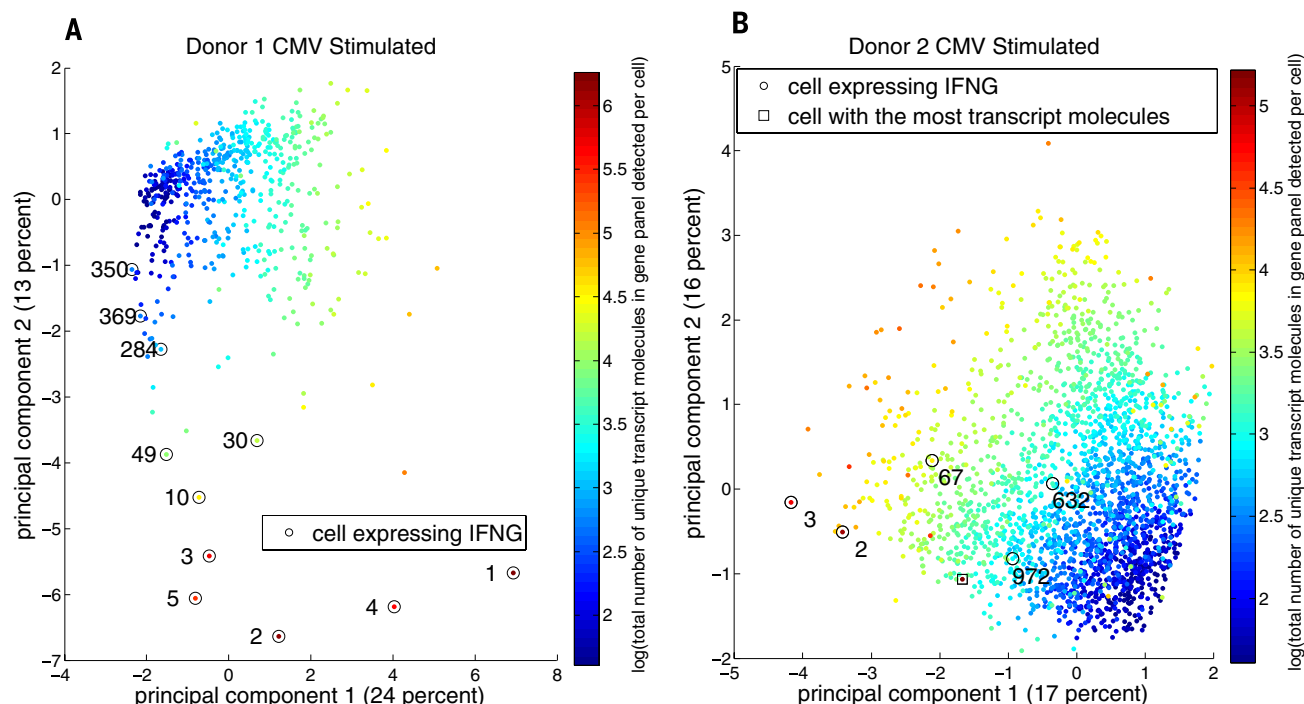


Fig. 6. Identification of rare antigen-specific T cell by expression of IFNG in CD8⁺ T cells from two donors after stimulation with CMV peptide pool.

Each cell is plotted on the 2D PC space. (A) Cells expressing IFNG (circled) are usually among those with the most total detected transcripts in the panel (indicated by the color). (B) In donor 2, the top expressing cell (square) does not produce IFNG but expresses cytokines IL6 and IL1B. Number next to each circle indicates the rank in descending order of the number of total unique transcript molecules detected for that cell.

captured cell per 10 or more microwells. The cell suspension was pipetted onto the microwell array and allowed to settle by gravity. Cell filling of microwells was confirmed by microscopy. Cells that settled on the surface in-between wells (~77% of the total surface area under current design) were removed and could be saved for future use. The bead library was then loaded at a density of ~5 beads per well to saturate all wells. Excess beads were washed away and cold lysis buffer (0.1 M Tris-HCl pH 7.5, 0.5 M LiCl, 1% LiSDS, 10 mM EDTA, and 5 mM dithiothreitol) was pipetted over the surface of the microwell array. After 10 min of incubation on a slide magnet, the lysis buffer covering the array was removed and replaced by fresh lysis buffer. Beads with captured mRNAs were retrieved by placing the magnet on top of the microwell array. Beads in solution were collected into a microcentrifuge tube by pipetting and washed twice in the tube with wash A buffer (0.1 M Tris-HCl, 0.5 M LiCl, and 1 mM EDTA) and once with wash B buffer (20 mM Tris-HCl pH 7.5, 50 mM KCl, and 3 mM MgCl₂). Under current implementation without the use of automation, this process takes up to 1.5 hours with two samples processed in parallel.

cDNA synthesis

Washed beads were resuspended in 40 μ l RT mix (Life Technologies, 1x First Strand buffer, 20 units Superscript II RNase Inhibitor, 200 units Superscript II or Superscript III, 3 mM additional MgCl₂, 1 mM dNTP, and 0.2 μ g/ μ l BSA) in a microcentrifuge tube rotated at 16 revolutions

per minute in an oven at 50°C for 50 min (when using SuperScript III for the early experiment with K562 and Ramos cells) or 42°C for 90 min (when using Superscript II for all other experiments). After cDNA synthesis, excess oligonucleotides on the beads were removed by treatment with 20 units of ExoI (NEB) in 40 μ l of 1x ExoI buffer at 37°C for 30 min and then inactivated at 80°C for 15 min.

Multiplex PCR and sequencing

Gene sequences were retrieved from RefSeq. Each marker panel consists of two sets of gene-specific primers designed using Primer3. MATLAB was used to select PCR primers with minimal 3' end complementarity within each set (table S1). The amplification scheme is shown in fig. S1. PCR was performed on the beads with the KAPA Fast Multiplex Kit, using 50 nM of each gene-specific primer in the first primer set and 400 nM universal primer in 50 μ l (for K562 and Ramos cell mixture), 100 μ l (for PBMC and B cell experiments) or 200 μ l (for T cell experiments), with the following cycling protocol: 3 min at 95°C; 15 cycles of 15 s at 95°C, 60 s at 60°C, 90 s at 72°C; and 5 min at 72°C. The increase in PCR volume was to mitigate the inhibitory effect of the iron on the magnetic beads. The beads were recovered using a magnet, and PCR products were purified with 0.7x Ampure XP (Beckman Coulter). Half of the purified products were used for the next round of nested PCR, with the second primer set using the same KAPA kit and cycling protocol. After clean-up with 0.7x Ampure XP, one-tenth

of the product was input into a final PCR reaction whereby the full-length Illumina adaptors were appended (1x KAPA HiFi Ready Mix, 200 nM of primer P5, 200 nM of primer P7; 95°C 5 min; eight cycles of 98°C 15 s, 60°C 30 s, 72°C 30 s; 72°C 5 min). Sequencing was performed on the Illumina MiSeq instrument with 150x2 base pair chemistry at a median depth of 1.6 million reads per sample (table S2).

Data analysis

The cell label, the molecular index, and the gene identity were detected on each sequenced read (fig. S1). Gene assignment for the second paired read (read 2) was performed using the alignment software "bowtie2" (45) with default settings. Cell labels and molecular indices on the first paired read (read 1) were analyzed using custom MATLAB scripts. Only reads perfectly matching the combinatorial cell barcodes were retained, but this requirement may be further relaxed since the cell barcodes were designed to enable error correction (46). Reads were grouped first by cell label, then by gene identity and molecular index. To calculate the number of unique molecules per gene per cell, the molecular indices of reads of the same gene transcript from the same cell were clustered. Edit distance greater than 1 nucleotide was considered as a unique cluster, and thus a unique transcript molecule. A table containing the digital gene expression profile of each cell was constructed for each sample; each row in the table represents a unique cell, each column represents a gene, and each entry in the table represents

the count of unique transcript molecules for that gene in any given cell. The table was filtered to remove unique molecules that were sequenced only once (i.e., redundancy = 1). For the experiment with mixture of K562 and Ramos cells, cells with 30 or more total unique molecules were retained for clustering. For the rest of the experiments, cells with a sum of 10 or more unique molecules or with coexpression of four or more genes in the panel were retained for clustering. The filtered table was then used for clustering analysis. PCA and hierarchical clustering were performed on natural log-transformed transcript count (with pseudo-count of 1 added) with built-in functions in MATLAB.

Measurement of GAPDH copy number in single Ramos cell using alternative methods

In the first method, total RNA from Ramos cells was extracted by RNeasy Mini Kit (Qiagen) and quantified by Nanodrop. Serial dilutions down to 7 pg were prepared and loaded onto the 12.765 Digital Array (Fluidigm) with 1x EXPRESS SuperScript quantitative PCR mix (Life Technologies), 1x EXPRESS SuperScript enzyme mix (Life Technologies), 1x GAPDH FAM assay (ABI), 1x Loading Reagent (Fluidigm), and 1x ROX dye. The array was analyzed on the BioMark (Fluidigm) with the following protocol: 50°C for 15 min, 95°C for 2 min, and 35 cycles of 95°C for 15 s and 60°C for 60 min. GAPDH was measured to be 34 copies per pg of total RNA. In the second method, a Ramos cell suspension was diluted in PBS to about 1 cell per 10 microliters. A microliter of suspension was pipetted into multiple 0.2-ml tubes. The presence of a single cell in a tube was confirmed by microscopy. GAPDH counts in the single cells were determined using the method outlined in Fu *et al.* (15). Measurements were obtained from eight cells. An average of 214 ± 36 (SE) copies (range 113 to 433 copies) was obtained per cell. GAPDH counts per spiked Ramos cell (18 single cells) were compared to these two methods to evaluate RNA detection efficiency.

REFERENCES AND NOTES

- S. Islam *et al.*, Characterization of the single-cell transcriptional landscape by highly multiplex RNA-seq. *Genome Res.* **21**, 1160–1167 (2011). doi: [10.1101/gr.110882.110](#); pmid: [21543516](#)
- A. K. Shalek *et al.*, Single-cell transcriptomics reveals bimodality in expression and splicing in immune cells. *Nature* **498**, 236–240 (2013). doi: [10.1038/nature12172](#); pmid: [23685454](#)
- A. R. Wu *et al.*, Quantitative assessment of single-cell RNA-sequencing methods. *Nat. Methods* **11**, 41–46 (2014). doi: [10.1038/nmeth.2694](#); pmid: [24141493](#)
- B. Treutlein *et al.*, Reconstructing lineage hierarchies of the distal lung epithelium using single-cell RNA-seq. *Nature* **509**, 371–375 (2014). doi: [10.1038/nature13173](#); pmid: [24739965](#)
- D. A. Jaitin *et al.*, Massively parallel single-cell RNA-seq for marker-free decomposition of tissues into cell types. *Science* **343**, 776–779 (2014). doi: [10.1126/science.1247651](#); pmid: [24531970](#)
- V. Sanchez-Freire, A. D. Ebert, T. Kalisky, S. R. Quake, J. C. Wu, Microfluidic single-cell real-time PCR for comparative analysis of gene expression patterns. *Nat. Protoc.* **7**, 829–838 (2012). doi: [10.1038/nprot.2012.021](#); pmid: [22481529](#)
- S. Islam *et al.*, Quantitative single-cell RNA-seq with unique molecular identifiers. *Nat. Methods* **11**, 163–166 (2014). doi: [10.1038/nmeth.2772](#); pmid: [24363023](#)
- A. K. Shalek *et al.*, Single-cell RNA-seq reveals dynamic paracrine control of cellular variation. *Nature* **510**, 363–369 (2014). pmid: [24919153](#)
- A. P. Patel *et al.*, Single-cell RNA-seq highlights intratumoral heterogeneity in primary glioblastoma. *Science* **344**, 1396–1401 (2014). doi: [10.1126/science.1254257](#); pmid: [24425914](#)
- D. J. Eastburn, A. Sciambi, A. R. Abate, Ultrahigh-throughput Mammalian single-cell reverse-transcriptase polymerase chain reaction in microfluidic drops. *Anal. Chem.* **85**, 8016–8021 (2013). doi: [10.1021/ac402057q](#); pmid: [23885761](#)
- I. K. Dimov *et al.*, Discriminating cellular heterogeneity using microwell-based RNA cytometry. *Nat. Commun.* **5**, 3451 (2014). doi: [10.1038/ncomms4451](#); pmid: [24667995](#)
- H. Zhang, G. Jenkins, Y. Zou, Z. Zhu, C. J. Yang, Massively parallel single-molecule and single-cell emulsion reverse transcription polymerase chain reaction using agarose droplet microfluidics. *Anal. Chem.* **84**, 3599–3606 (2012). doi: [10.1021/ac2033084](#); pmid: [22455457](#)
- G. K. Fu, J. Hu, P. H. Wang, S. P. Fodor, Counting individual DNA molecules by the stochastic attachment of diverse labels. *Proc. Natl. Acad. Sci. U.S.A.* **108**, 9026–9031 (2011). doi: [10.1073/pnas.1017621108](#); pmid: [21562209](#)
- T. Kivioja *et al.*, Counting absolute numbers of molecules using unique molecular identifiers. *Nat. Methods* **9**, 72–74 (2011). doi: [10.1038/nmeth.1778](#); pmid: [22101854](#)
- G. K. Fu, J. Wilhelmy, D. Stern, H. C. Fan, S. P. Fodor, Digital encoding of cellular mRNAs enabling precise and absolute gene expression measurement by single-molecule counting. *Anal. Chem.* **86**, 2867–2870 (2014). doi: [10.1021/ac500459p](#); pmid: [24579851](#)
- G. K. Fu *et al.*, Molecular indexing enables quantitative targeted RNA sequencing and reveals poor efficiencies in standard library preparations. *Proc. Natl. Acad. Sci. U.S.A.* **111**, 1891–1896 (2014). doi: [10.1073/pnas.1323732111](#); pmid: [24449890](#)
- I. Kinde, J. Wu, N. Papadopoulos, K. W. Kinzler, B. Vogelstein, Detection and quantification of rare mutations with massively parallel sequencing. *Proc. Natl. Acad. Sci. U.S.A.* **108**, 9530–9535 (2011). doi: [10.1073/pnas.1105422108](#); pmid: [21586637](#)
- R. D. Smith, J. D. Malley, A. N. Schechter, Quantitative analysis of globin gene induction in single human erythroleukemic cells. *Nucleic Acids Res.* **28**, 4998–5004 (2000). doi: [10.1093/nar/28.24.4998](#); pmid: [11121491](#)
- D. A. Kaminski, C. Wei, Y. Qian, A. F. Rosenberg, I. Sanz, Advances in human B cell phenotypic profiling. *Front. Immunol.* **3**, 302 (2012). doi: [10.3389/fimmu.2012.00302](#); pmid: [23087687](#)
- Y. Shen *et al.*, Distinct gene expression profiles in different B-cell compartments in human peripheral lymphoid organs. *BMC Immunol.* **5**, 20 (2004). doi: [10.1186/1471-2172-5-20](#); pmid: [15369600](#)
- J. A. Weinstein, X. Zeng, Y. H. Chien, S. R. Quake, Correlation of gene expression and genome mutation in single B-cells. *PLOS ONE* **8**, e67624 (2013). doi: [10.1371/journal.pone.0067624](#); pmid: [23840752](#)
- A. S. Perkins, J. W. Friedberg, *Hematology: The Education Program of the American Society of Hematology* (American Society of Hematology, Washington, DC, 2008), pp. 341–348.
- M. Sultan *et al.*, A global view of gene activity and alternative splicing by deep sequencing of the human transcriptome. *Science* **321**, 956–960 (2008). doi: [10.1126/science.1160342](#); pmid: [18599741](#)
- T. Tchanova *et al.*, Identification of T cell-restricted genes, and signatures for different T cell responses, using a comprehensive collection of microarray datasets. *J. Immunol.* **175**, 7837–7847 (2005). doi: [10.4049/jimmunol.175.12.7837](#); pmid: [16339519](#)
- T. Tchanova *et al.*, T follicular helper cells express a distinctive transcriptional profile, reflecting their role as non-Th1/Th2 effector cells that provide help for B cells. *J. Immunol.* **173**, 68–78 (2004). doi: [10.4049/jimmunol.173.1.68](#); pmid: [15210760](#)
- K. M. Hertoghs *et al.*, Molecular profiling of cytomegalovirus-induced human CD8⁺ T cell differentiation. *J. Clin. Invest.* **120**, 4077–4090 (2010). doi: [10.1172/JCI42758](#); pmid: [20921622](#)
- H. Shen, J. C. Goodall, J. S. Hill Gaston, Frequency and phenotype of peripheral blood Th17 cells in ankylosing spondylitis and rheumatoid arthritis. *Arthritis Rheum.* **60**, 1647–1656 (2009). doi: [10.1002/art.24568](#); pmid: [19479869](#)
- M. E. Truchetet, N. C. Brembilla, E. Montanari, Y. Allanoire, C. Chizzolini, Increased frequency of circulating Th22 in addition to Th17 and Th2 lymphocytes in systemic sclerosis: Association with interstitial lung disease. *Arthritis Res. Ther.* **13**, R166 (2011). doi: [10.1186/ar3486](#); pmid: [21996293](#)
- T. Willinger, T. Freeman, H. Hasegawa, A. J. McMichael, M. F. Callan, Molecular signatures distinguish human central memory from effector memory CD8 T cell subsets. *J. Immunol.* **175**, 5895–5903 (2005). doi: [10.4049/jimmunol.175.9.5895](#); pmid: [16237082](#)
- K. Bratke, M. Kuepper, B. Bade, J. C. Virchow Jr., W. Luttmann, Differential expression of human granzymes A, B, and K in natural killer cells and during CD8⁺ T cell differentiation in peripheral blood. *Eur. J. Immunol.* **35**, 2608–2616 (2005). doi: [10.1002/eji.200526122](#); pmid: [16106370](#)
- E. W. Newell, N. Sigal, S. C. Bendall, G. P. Nolan, M. M. Davis, Cytometry by time-of-flight shows combinatorial cytokine expression and virus-specific cell niches within a continuum of CD8⁺ T cell phenotypes. *Immunity* **36**, 142–152 (2012). doi: [10.1016/j.immuni.2012.01.002](#); pmid: [22265676](#)
- H. T. Maechler *et al.*, Precision and linearity targets for validation of an IFNgamma ELISPOT, cytokine flow cytometry, and tetramer assay using CMV peptides. *BMC Immunol.* **9**, 9 (2008). doi: [10.1186/1471-2172-9-9](#); pmid: [18366814](#)
- S. C. Bendall *et al.*, Single-cell mass cytometry of differential immune and drug responses across a human hematopoietic continuum. *Science* **332**, 687–696 (2011). doi: [10.1126/science.1198704](#); pmid: [21551058](#)
- S. P. Perffetto, P. K. Chattopadhyay, M. Roederer, Seventeen-colour flow cytometry: Unravelling the immune system. *Nat. Rev. Immunol.* **4**, 648–655 (2004). doi: [10.1038/nri1416](#); pmid: [15286731](#)
- A. Han, J. Glanville, L. Hansmann, M. M. Davis, Linking T-cell receptor sequence to functional phenotype at the single-cell level. *Nat. Biotechnol.* **32**, 684–692 (2014). doi: [10.1038/nbt.2938](#); pmid: [24952902](#)
- D. Ramsköld *et al.*, Full-length mRNA-Seq from single-cell levels of RNA and individual circulating tumor cells. *Nat. Biotechnol.* **30**, 777–782 (2012). doi: [10.1038/nbt.2282](#); pmid: [22820318](#)
- S. Picelli *et al.*, Smart-seq2 for sensitive full-length transcriptome profiling in single cells. *Nat. Methods* **10**, 1096–1098 (2013). doi: [10.1038/nmeth.2639](#); pmid: [24058875](#)
- Y. Sasagawa *et al.*, Quartz-Seq: A highly reproducible and sensitive single-cell RNA sequencing method, reveals non-genetic gene-expression heterogeneity. *Genome Biol.* **14**, R31 (2013). doi: [10.1186/gb-2013-14-4-r31](#); pmid: [23594475](#)
- T. Hashimshony, F. Wagner, N. Sher, I. Yanai, CEL-Seq: Single-cell RNA-Seq by multiplexed linear amplification. *Cell Reports* **2**, 666–673 (2012). doi: [10.1016/j.celrep.2012.08.003](#); pmid: [22939981](#)
- T. D. Harris *et al.*, Single-molecule DNA sequencing of a viral genome. *Science* **320**, 106–109 (2008). pmid: [18388294](#)
- J. Eid *et al.*, Real-time DNA sequencing from single polymerase molecules. *Science* **323**, 133–138 (2009). doi: [10.1126/science.1162986](#); pmid: [19023044](#)
- J. Clarke *et al.*, Continuous base identification for single-molecule nanopore DNA sequencing. *Nat. Nanotechnol.* **4**, 265–270 (2009). doi: [10.1038/nnano.2009.12](#); pmid: [19350039](#)
- A. A. Pollen *et al.*, Low-coverage single-cell mRNA sequencing reveals cellular heterogeneity and activated signaling pathways in developing cerebral cortex. *Nat. Biotechnol.* **32**, 1053–1058 (2014). doi: [10.1038/nbt.2967](#); pmid: [25086649](#)
- A. M. Streets, Y. Huang, How deep is enough in single-cell RNA-seq? *Nat. Biotechnol.* **32**, 1005–1006 (2014). doi: [10.1038/nbt.3039](#); pmid: [25299920](#)
- B. Langmead, S. L. Salzberg, Fast gapped-read alignment with Bowtie 2. *Nat. Methods* **9**, 357–359 (2012). doi: [10.1038/nmeth.1923](#); pmid: [22388286](#)
- M. Hamady, J. K. Walker, N. J. Gold, R. Knight, Error-correcting barcoded primers for pyrosequencing hundreds of samples in multiplex. *Nat. Methods* **5**, 235–237 (2008). doi: [10.1038/nmeth.1184](#); pmid: [18264105](#)

ACKNOWLEDGMENTS

We thank M. Simbirsky for primer design; F. Lee, J. Wilhelmy, and K. Cordes-Metzler for technical assistance; and M. Davis for reviewing the manuscript. G.K.F. and S.P.A.F. have been issued US Patent 8,835,358 relating to molecular counting and G.K.F., S.P.A.F., and C.F. have submitted patent applications (US61/952,036, US62/012,237, US61/871,232, US14/472,363, and PCT/US2014/053301) relating to the work described. Patents are held by Cellular Research, Inc. CytoSeq data are available in the supplementary materials. CytoSeq reagents (barcoded beads and microwell arrays) are available from Cellular Research, Inc. Raw sequence data are available at [www.cellular-research.com](#).

SUPPLEMENTARY MATERIALS

[www.sciencemag.org/content/347/6222/1258367/suppl/DC1](#)
Figs. S1 to S15
Tables S1 to S3
References
Supporting data

7 July 2014; accepted 19 December 2014
10.1126/science.1258367

REPORTS

THERMAL MEASUREMENT

Nanoscale temperature mapping in operating microelectronic devices

Matthew Mecklenburg,^{1*} William A. Hubbard,^{2,3} E. R. White,^{2,3} Rohan Dhall,⁴ Stephen B. Cronin,⁴ Shaul Aloni,⁵ B. C. Regan^{2,3*}

Modern microelectronic devices have nanoscale features that dissipate power nonuniformly, but fundamental physical limits frustrate efforts to detect the resulting temperature gradients. Contact thermometers disturb the temperature of a small system, while radiation thermometers struggle to beat the diffraction limit. Exploiting the same physics as Fahrenheit's glass-bulb thermometer, we mapped the thermal expansion of Joule-heated, 80-nanometer-thick aluminum wires by precisely measuring changes in density. With a scanning transmission electron microscope and electron energy loss spectroscopy, we quantified the local density via the energy of aluminum's bulk plasmon. Rescaling density to temperature yields maps with a statistical precision of 3 kelvin/hertz^{-1/2}, an accuracy of 10%, and nanometer-scale resolution. Many common metals and semiconductors have sufficiently sharp plasmon resonances to serve as their own thermometers.

Long before thermodynamic temperature was understood, it was defined as a measurable quantity in terms of the thermal expansion of air, red wine, alcohol, or mercury-in-glass. Now, temperature T is considered to be a statistical concept, defined by the derivative of a system's entropy S with respect to its energy E according to $T^{-1} = \partial S / \partial E$ (1). This understanding is challenged in highly localized (2) or nonequilibrium (3) systems, in which the standard statistical reasoning is difficult to apply. Small systems are also problematic from a practical standpoint. Contact thermometers (such as thermocouples) require a thermal connection that disturbs a small system's temperature (4, 5). Noncontact thermometers based on the detection of radiation—whether thermal (6), Raman (7), reflected (8), or luminescent (5, 9)—naturally have their spatial resolution limited by the wavelengths of the radiation detected (4, 5). In modern semiconductor devices, millions of transistors generate thermal gradients on length scales that are tiny compared with infrared and optical wavelengths (10). Thus, thermometric techniques with high spatial resolution are applicable to important problems ranging from the statistical foundations of thermodynamics (2, 3) to heat management in microprocessors (5, 10, 11).

High-spatial-resolution thermometry is under constant development in many arenas (5). Some approaches involve inserting local probes [even miniature expansion thermometers (12)] that can be queried remotely. For instance, luminescent nanoparticles inserted in biological systems can measure intracellular temperature gradients (9), or low-melting point metals deposited on a solid-state device can provide a binary temperature determination (13, 14). Alternatively, the thermometer can be external and mobile. Scanning probe techniques include scanning thermal microscopy (SThM), in which the tip of an atomic force microscope is equipped with a thermocouple or resistive sensor (15, 16), and near-field scanning optical microscopy, in which a fiber is used to beat the far-field diffraction limit (4, 5, 11, 17). Both of these methods can achieve resolution $\lesssim 50$ nm (16, 17). Perhaps most like the work described here, nuclear magnetic resonance (NMR) (18), electron backscatter diffraction (19), or inelastic electron scattering (20) can induce the measured system to provide its own thermometric signal. Of these three, only the NMR technique has demonstrated mapping with millimeter-scale resolution (18). Of all of the aforementioned methods, none have demonstrated detailed temperature maps with sub-10-nm spatial resolution.

Here, we describe a noncontact, thermometric technique that can measure bulk temperatures with nanometer-scale spatial resolution: plasmon energy expansion thermometry (PEET). Based on electron energy loss spectroscopy (EELS), the technique is noncontact in the sense that the measurement has a negligible effect on the measured system's temperature. Like Fahrenheit's mercury-in-glass thermometer, this thermometer derives its sensitivity and accuracy from the calibrated thermal expansion of a conve-

nient material—here, aluminum. As outlined in Fig. 1A, we applied EELS in a scanning transmission electron microscope (STEM) to measure the energy E required to excite a bulk plasmon in the metal. In the free-electron model, this energy is given by

$$E = \hbar\omega_p = \hbar\sqrt{\frac{4\pi n e^2}{m}} \quad (1)$$

where \hbar is the reduced Planck constant, ω_p is the plasmon angular frequency, and n is the number density of valence electrons with charge e and mass m . At room temperature (T_0), aluminum has $n(T_0) \approx 1.8 \times 10^{29} \text{ m}^{-3}$, which gives $E(T_0) \approx 15.8 \text{ eV}$ according to Eq. 1. This value is within 3% of the measured value of 15.2 eV (21), demonstrating the applicability of the free electron model in aluminum.

The plasmon energy is temperature-sensitive because thermal expansion changes the number density according to $n(T) \approx n(T_0)[1 - 3f(T)]$, where $f(T) \equiv \int_{T_0}^T \alpha(T') dT' \approx \alpha_1 \Delta T + \alpha_2 \Delta T^2$ and α is the coefficient of linear thermal expansion (21–23). The normalized change in the plasmon energy $R \equiv [E(T) - E(T_0)]/E(T_0)$ is thus related to the temperature change ΔT by a quadratic equation with solution

$$\Delta T \equiv T - T_0 = \frac{\alpha_1}{2\alpha_2} \left(\sqrt{1 - \frac{8R\alpha_2}{3\alpha_1^2}} - 1 \right) \quad (2)$$

In aluminum, the coefficients $\alpha_1 = 23.5 \times 10^{-6} \text{ K}^{-1}$ and $\alpha_2 = 8.9 \times 10^{-9} \text{ K}^{-2}$ approximate $f(T)$ to better than 2% over the range from 25 to 650°C (24, 25). By focusing the STEM electron beam into a nanometer-sized probe, rastering it over the sample, and analyzing the shift of the plasmon peak in the EELS spectrum according to Eq. 2, we produced a temperature map.

With a plasmon peak width $\sim 1.3 \text{ eV}$, the peak shift of roughly -0.54 meV/K (in the linear approximation) is too subtle to reliably detect by merely locating the peak maximum. However, curve-fitting improves our sensitivity to energy or temperature shifts by almost an order of magnitude (26). The shift for a large (120 K) temperature difference is shown in Fig. 1B, measured with a spectrum integration time of 26 ms. Under such imaging conditions, repeated measurements at a single point give standard deviations in the energy loss of 8 to 12 meV, which is equivalent to 15 to 21 K. For spectrum acquisition rates of 38 to 76 s⁻¹, our plasmon energy sensitivity scales like shot noise with slope $\sim 1.7 \text{ meV}/\sqrt{\text{Hz}}$, which is equivalent to 3 K/ $\sqrt{\text{Hz}}$.

To demonstrate PEET's spatial resolution, we used electron-beam lithography to fabricate a variety of serpentine aluminum devices that exhibit temperature gradients on submicrometer-length scales (Fig. 1C). Depending on the contacts used, a device can be Joule-heated locally by applying a voltage across it, or remotely by heating its neighbor (26).

Local heating gives PEET maps such as Fig. 1D. The map contains 336 by 223 pixels with an 11-nm pitch and is derived from two EELS spectrum images, one acquired at room temperature and

¹Center for Electron Microscopy and Microanalysis, University of Southern California, Los Angeles, CA 90089, USA. ²Department of Physics and Astronomy, University of California, Los Angeles, CA 90095, USA. ³California NanoSystems Institute, University of California, Los Angeles, CA 90095, USA. ⁴Department of Electrical Engineering, University of Southern California, Los Angeles, CA 90089, USA. ⁵Molecular Foundry, Lawrence Berkeley National Laboratory, Berkeley, CA 94720, USA.
*Corresponding author. E-mail: matthew.mecklenburg@usc.edu (M.M.); regan@physics.ucla.edu (B.C.R.)

the other at elevated temperature. Thus, each pixel has two associated spectra similar to those shown in Fig. 1B. Averaging over 64 pixels in the indicated square regions gives standard errors of 2 and 3 K respectively, showing a temperature difference 80 ± 4 K with a signal-to-noise ratio of 20. The highest temperatures are not found at the wire's midpoint, as would be expected for a straight and uniform one-dimensional conductor, but rather in the sections farthest from the lead connections. PEET reveals that the midpoint loses heat to the cooler end legs (only 150 nm

away) through the Si_3N_4 membrane and via near-field electromagnetic transport (17).

The PEET analysis procedure is described in more detail in Fig. 2, which shows raw maps of the plasmon energy for a device with zero (Fig. 2A) and nonzero (Fig. 2B) power applied to a remote heater. In both cases, the sensitive curve-fitting procedure reveals nanometer-scale structures in the aluminum. Most noticeable in the leads, these structures are due to grain boundaries, which show a plasmon energy decrease of $\Delta E = 13 \pm 12$ meV (figs. S1 and S2). The im-

plied density decrease of $\Delta n/n \approx 2\Delta E/E \approx 0.2\%$ is expected because of the grain boundary volume excess (27). Without correction, the grain boundary shift would give a false temperature offset of ~ 24 K. The subtraction in the normalized plasmon shift ratio $R = (B - A)/A$ (where the letters refer to the respective panels of Fig. 2) suppresses this potential systematic, leaving residuals that are barely evident in the temperature map in Fig. 2C (fig. S3).

The map in Fig. 2C shows a steady warming with distance from the lower contact, a trend

Fig. 1. Experiment overview. (A) Apparatus: a STEM, a biasing sample holder, a power source for Joule-heating the sample, and an EELS spectrometer. (B) Aluminum EELS data characteristic of 293 K (black) and 413 K (red). The vertical lines in the inset indicate the plasmon peak centers, as determined by curve-fitting, and the arrows indicate the peak maxima. (C) Scanning electron microscope image of an example device architecture. Four leads connect to three Al device geometries over an electron-transparent, Si_3N_4 membrane. (D) A false-color temperature map of a 80-nm-thick, 100-nm-wide serpentine aluminum wire Joule-heated by the application of $161 \mu\text{A}$. The histogram indicates the color scale and bins each pixel according to its temperature. The average temperatures measured in the indicated 86- by 86-nm squares are 310 ± 2 K (bottom left) and 390 ± 3 K (top right).

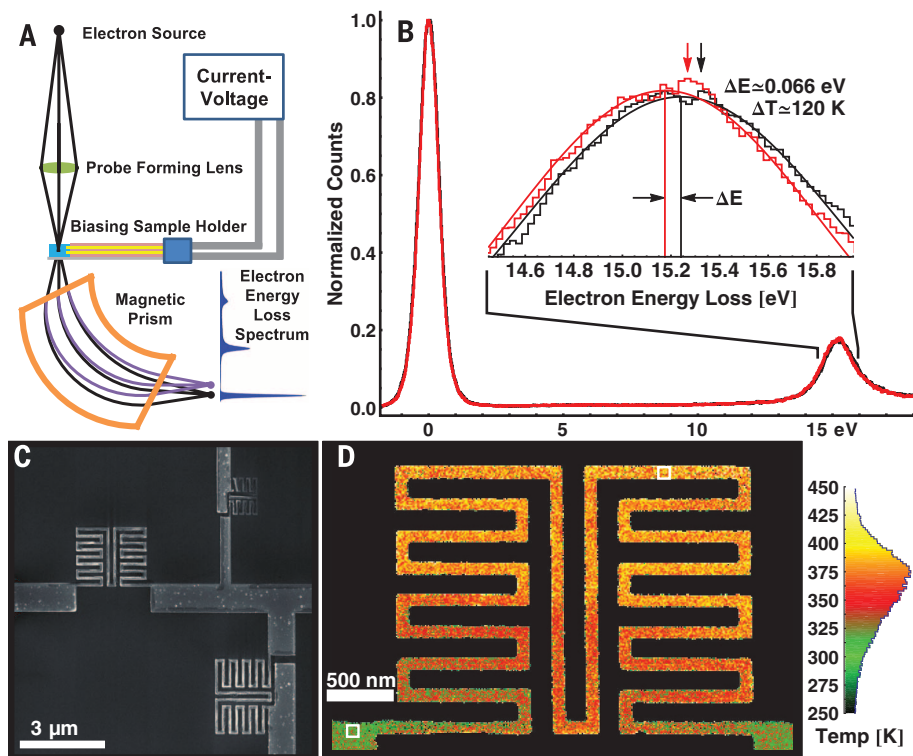
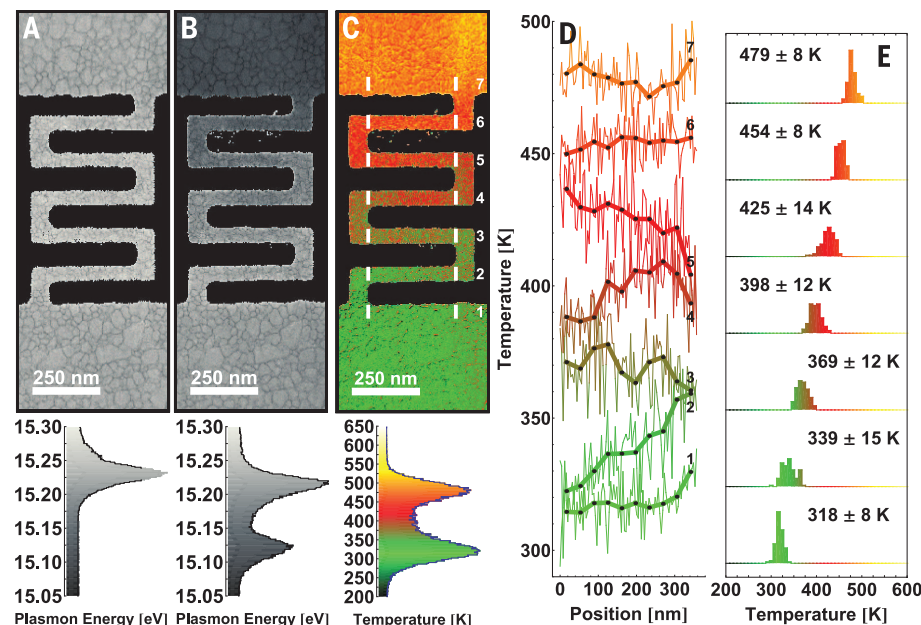


Fig. 2. Remote heating. (A and B) Plasmon energy map with 4-nm pixels of a 100-nm-thick aluminum wire (A) at room temperature and (B) with 2 mW applied to a heater outside the field of view. (C) Temperature map constructed from (A) and (B). White bars indicate the 90- by 10-pixel segments used to generate the (D) line profiles and (E) histograms. Narrow lines and histograms show data averaged over 40 nm vertically, and dots connected by thicker lines indicate data averaged over 40 nm in both directions.



easier to appreciate quantitatively in the seven line profiles in Fig. 2D. With a spectrum acquisition rate of 76 s^{-1} , each map pixel has a statistical uncertainty of 26 K. The histograms in Fig. 2E show that the mean temperature difference $\sim 30 \text{ K}$ between each horizontal leg and its neighbor is resolved. Furthermore, the topmost and bottommost profiles have standard deviations that are comparable with the expected 8 K statistical noise, whereas the other histograms are generally broadened, reflecting the substantial temperature gradients in the horizontal legs and the absence of such gradients in the contacts.

In situ thermal studies with nanoscale thermometry can use temperature control elements that are smaller and thus faster. This advantage enables rapid heating and quenching experiments and better control of systematics. For instance, annealing at elevated temperatures causes grain boundaries to reconfigure. But with a small heater over the electron-transparent window, the temperature can be cycled without pausing to wait for the thermal drift to stabilize. Thus, the T_0 reference map can be frequently refreshed, mitigating this systematic without incurring a large duty-cycle penalty.

Shown in Fig. 3 is how the temperature of an aluminum contact, here heated remotely, can be changed by hundreds of kelvins in real time, without disturbing the temperature measurement or causing the burdensome thermal drift typical of furnace-style heating sample holders. These data depict an EELS spectrum image acquisition in which the power to the remote heater

was ramped down in steps, with zero-power intervals separating each new nonzero value from the previous one (Fig. 3A). Heating effects are nearly undetectable in the annular dark field (ADF) images corresponding to zero power (Fig. 3C) and stepped power (Fig. 3D). Grain rotation induced some tiny contrast changes, and the drift was sufficiently small to be handled by the EELS data acquisition software's automated drift correction routine, which executed every two rows.

Comparison of the ADF and plasmon energy images also emphasizes the common origin of the structure evident in the zero-power (T_0) images: grains. The ADF image shows diffraction contrast varying randomly from grain to grain based on the local lattice orientation, whereas the plasmon energy image highlights the grain boundaries because of the volume excess effect discussed above (figs. S1 and S2). In the temperature map (Fig. 3G), a few grain boundaries show residuals 3 to 4 standard deviations from the mean (fig. S3), but generally, the grain boundary systematic is suppressed.

The abrupt transitions in the power-stepped plasmon energy (Fig. 3F) and temperature (Fig. 3G) maps demonstrate thermalization within a 26-ms pixel time. Although the field of view was nearly isothermal at any given instant, the effectively instantaneous temperature changes appear spatial because of the 22.5-min frame time. The mean temperature from each isothermal region is plotted in Fig. 3H as a function of the heater power. As expected for a small device in vacuum that is too cool to radiate appreciably, the temperature is linear in the applied power (6). When

working either with devices or with lamellae deployed as local thermometers, a plot such as Fig. 3G is straightforward and fast to acquire and provides a translation between power and temperature that can be ported to situations in which direct measurements of the latter are not feasible.

With careful calibration we expect sub-1 K accuracies are possible because the physics underpinning PEET is well understood on longer length scales (figs. S4 to S8) (21–23, 25). Heating by the electron beam is negligible. The temperature increment is roughly $\Delta T \approx (I_b/\epsilon\kappa)(dE/dx)$ (28), where $I_b \approx 0.5 \text{ nA}$ is the beam current and $\kappa \approx 240 \text{ W/K} \cdot \text{m}$ is aluminum's thermal conductivity. Plasmons, the dominant source of energy loss, are created by the beam in a mean free path $\ell_{\text{PL}} \sim 100 \text{ nm}$, which gives $dE/dx \sim 15 \text{ eV}/(100 \text{ nm})$. The resultant ΔT , less than 1 mK, is far below our current sensitivity. Using a furnace-style heating sample holder, we heated a sample from room temperature to 720 K, compared the PEET value with the holder's thermocouple reading, and found that they agree to within 10% (fig. S4).

For the data presented here, the rastering electron beam (probe) size was 1 to 2 nm, and the pixel spacing was as small as 2 nm (26). Is it meaningful to consider the existence of distinct temperatures at such small length scales in a solid, and can PEET measure them? Measurements of the plasmon energy do not sample distinct volumes for separations smaller than the plasmon delocalization length Λ_{pl} , which sets a resolution limit akin to the Rayleigh criterion (29). At 15.2 eV, the plasmon delocalization

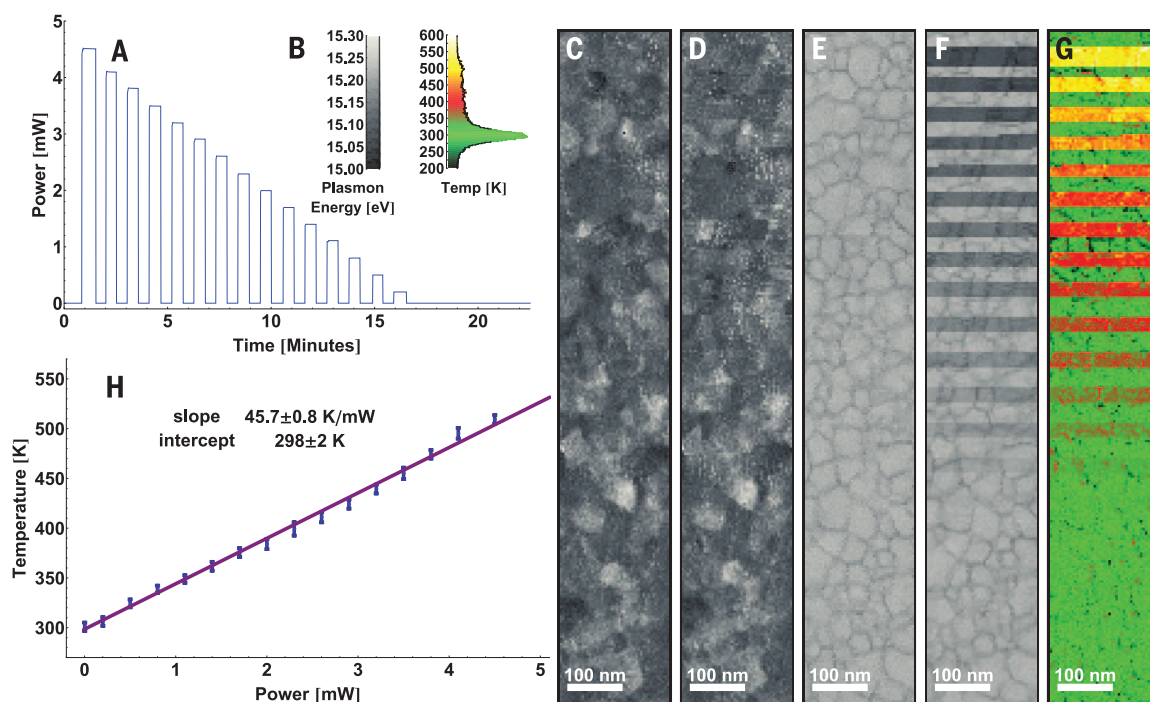


Fig. 3. Rapid linear temperature changes. (A) Remote heater power versus time. (B) Plasmon energy scale for (E) and (F), and a combination temperature scale and histogram of the pixels of (G). (C and D) ADF STEM images corresponding to zero and variable power. In these 45-by-269-pixel images the beam was rastering from left to right, with a row time of 1.2 s, and then top to bottom. (E and F) Corresponding, simultaneously acquired plasmon energy maps. (G) Temperature map constructed from the normalized subtraction of (E) from (F). (H) Temperature extracted from (G) versus heater power, along with a linear fit (purple) and the corresponding fit parameters.

is 3 nm (29), which is consistent with the grain boundary widths (which correspond to atomic-scale features) seen in our plasmon energy maps (fig. S1). However, the sample does not support a temperature gradient for separations smaller than the electron mean free path ℓ_e because electrons are ballistic over distances less than ℓ_e . Thus, ℓ_e describes the smallest thermal feature size that can exist in continuous aluminum. Similarly, because phonons generate thermal expansion, temperature cannot produce different densities at separations smaller than a phonon mean free path ℓ_{ph} . We estimate $\ell_e \leq 4$ to 15 nm and $\ell_{ph} \leq 2$ to 5 nm in our temperature range (table S1). For Λ_p smaller than ℓ_{ph} or ℓ_e , PEET achieves the maximum possible spatial resolution; temperature differences do not exist on length scales smaller than the larger mean free path.

PEET is applicable to many other technologically important metals and semiconductors. Tungsten, silver, silicon, gallium arsenide, and gallium nitride all have sufficiently sharp plasmon resonances (29). [The width of the plasmon resonance limits PEET's precision, so decreasing the zero loss peak width (30) gives only a small sensitivity improvement.] Because the product of the thermal expansion coefficient α with the melting temperature is $\alpha T_m \sim 0.02$ for many materials (31), one will generally trade high sensitivity for a large accessible temperature range, or vice versa, depending on the application. Ideally, the system to be measured serves as its own thermometer, without requiring the introduction of thermometric materials that might compromise the thermal behavior or device function.

REFERENCES AND NOTES

1. F. Reif, *Fundamentals of Statistical and Thermal Physics* (McGraw-Hill, New York, 1965).
2. M. Hartmann, G. Mahler, O. Hess, *Phys. Rev. Lett.* **93**, 080402 (2004).
3. Y. Dubi, M. Di Ventra, *Rev. Mod. Phys.* **83**, 131–155 (2011).
4. J. Christofferson *et al.*, *J. Electron. Packag.* **130**, 041101 (2008).
5. C. D. S. Brites *et al.*, *Nanoscale* **4**, 4799–4829 (2012).
6. S. B. Singer, M. Mecklenburg, E. R. White, B. C. Regan, *Phys. Rev. B* **84**, 195468 (2011).
7. V. V. Deshpande, S. Hsieh, A. W. Bushmaker, M. Bockrath, S. B. Cronin, *Phys. Rev. Lett.* **102**, 105501 (2009).
8. G. Tessier, M. Bardoux, C. Boué, C. Filloy, D. Fournier, *Appl. Phys. Lett.* **90**, 171112 (2007).
9. G. Kucsko *et al.*, *Nature* **500**, 54–58 (2013).
10. E. Pop, S. Sinha, K. E. Goodson, *Proc. IEEE* **94**, 1587–1601 (2006).
11. D. G. Cahill *et al.*, *Appl. Phys. Rev.* **1**, 011305 (2014).
12. Y. Gao, Y. Bando, *Nature* **415**, 599 (2002).
13. G. E. Begtrup *et al.*, *Phys. Rev. Lett.* **99**, 155901 (2007).
14. T. Brintlinger, Y. Qi, K. H. Baloch, D. Goldhaber-Gordon, J. Cumings, *Nano Lett.* **8**, 582–585 (2008).
15. M. Nonnenmacher, H. K. Wickramasinghe, *Appl. Phys. Lett.* **61**, 168 (1992).
16. L. Shi, S. Plyasunov, A. Bachtold, P. L. McEuen, A. Majumdar, *Appl. Phys. Lett.* **77**, 4295 (2000).
17. K. E. Goodson, M. Asheghi, *Microscale Thermophys. Eng.* **1**, 225 (1997).
18. N. N. Jarenwattananon *et al.*, *Nature* **502**, 537–540 (2013).
19. X. Wu, R. Hull, *Nanotechnology* **23**, 465707 (2012).
20. S. B. Vendelbo *et al.*, *Ultramicroscopy* **133**, 72–79 (2013).
21. H. Abe, M. Terauchi, R. Kuzuo, M. Tanaka, *J. Electron Microsc.* (Tokyo) **41**, 465 (1992).
22. G. Meyer, *Z. Phys.* **148**, 61–71 (1957).
23. P. Palanisamy, J. M. Howe, *J. Appl. Phys.* **110**, 024908 (2011).
24. Neglecting α_2 gives the simpler approximation $\Delta T = -2R/3\alpha_1$, but accounting for the temperature dependence of α is necessary because the resulting correction of $\sim 4\%$ per 100°C is larger than our sensitivity.
25. A. J. C. Wilson, *Proc. Phys. Soc.* **53**, 235–244 (1941).
26. Materials and methods are available as supplementary materials on Science Online.
27. E.-M. Steyskal *et al.*, *Phys. Rev. Lett.* **108**, 055504 (2012).
28. E. R. White, M. Mecklenburg, B. Shevitski, S. B. Singer, B. C. Regan, *Langmuir* **28**, 3695–3698 (2012).
29. R. F. Egerton, *Rep. Prog. Phys.* **72**, 016502 (2009).
30. O. L. Krivanek *et al.*, *Nature* **514**, 209–212 (2014).
31. K. A. Gschneidner, *Solid State Physics*, Frederick Seitz, David Turnbull, Eds. (Academic Press, 1964), vol. 16, pp. 275–426.

ACKNOWLEDGMENTS

This work has been supported by National Science Foundation award DMR-1206849 and in part by Function Accelerated nanoMaterial Engineering (FAME), one of six centers of Semiconductor Technology Advanced Research network (STARnet), a Semiconductor Research Corporation program

sponsored by the Microelectronics Advanced Research Corporation and Defense Advanced Research Projects Agency. Data presented in this article were acquired at the Center for Electron Microscopy and Microanalysis at the University of Southern California. Work at the Molecular Foundry was supported by the Office of Science, Office of Basic Energy Sciences, of the U.S. Department of Energy under contract DE-AC02-05CH11231.

SUPPLEMENTARY MATERIALS

www.sciencemag.org/content/347/6222/629/suppl/DC1
Materials and Methods
Table S1
Figs. S1 to S8
References (32, 33)
6 November 2014; accepted 12 January 2015
10.1126/science.aaa2433

EXOPLANET DYNAMICS

Asynchronous rotation of Earth-mass planets in the habitable zone of lower-mass stars

Jérémy Leconte,^{1,2,3*} Hanbo Wu,^{1,4} Kristen Menou,^{2,5} Norman Murray^{1,4}

Planets in the habitable zone of lower-mass stars are often assumed to be in a state of tidally synchronized rotation, which would considerably affect their putative habitability. Although thermal tides cause Venus to rotate retrogradely, simple scaling arguments tend to attribute this peculiarity to the massive Venusian atmosphere. Using a global climate model, we show that even a relatively thin atmosphere can drive terrestrial planets' rotation away from synchronicity. We derive a more realistic atmospheric tide model that predicts four asynchronous equilibrium spin states, two being stable, when the amplitude of the thermal tide exceeds a threshold that is met for habitable Earth-like planets with a 1-bar atmosphere around stars more massive than ~ 0.5 to 0.7 solar mass. Thus, many recently discovered terrestrial planets could exhibit asynchronous spin-orbit rotation, even with a thin atmosphere.

As we experience in our everyday life, atmospheric temperatures oscillate following the diurnal insolation cycle. This in turn creates periodic large-scale mass redistribution inside the atmosphere—the so-called thermal atmospheric tides. But as we all also have experienced, the hottest moment of the day is actually not when the Sun is directly overhead, but a few hours later. This is due to the thermal inertia of the ground and atmosphere that creates a delay between the solar heating and thermal response (driving mass redistribution), causing the whole atmospheric response to lag behind the Sun (1).

Because of this asymmetry in the atmospheric mass redistribution with respect to the subsolar

point, the gravitational pull exerted by the Sun on the atmosphere has a nonzero net torque that tends to accelerate or decelerate its rotation, depending on the direction of the solar motion (2, 3). Because the atmosphere and the surface are usually well coupled by friction in the atmospheric boundary layer, the angular momentum transferred from the orbit to the atmosphere is then transferred to the bulk of the planet, modifying its spin (4).

On Earth, this effect is negligible because we are too far away from the Sun, but the atmospheric torque due to thermal tides can be very powerful, as seen on Venus. Indeed, although tidal friction inside the planet is continuously trying to spin it down to a state of synchronous rotation, thermal tides are strong enough to drive the planet out of synchronicity and to force the slow retrograde rotation that we see today (2–6). Very simple scaling arguments predict that the amplitude of the thermal tide is proportional to the ratio of the atmospheric mean surface pressure over its scale height (1). Everything else being equal, one would thus expect the thermal tide to be ~ 50 times weaker if Venus had a less massive, cooler Earth-like atmosphere. Whether this scaling really holds and how massive the atmosphere

¹Canadian Institute for Theoretical Astrophysics, 60 St George Street, University of Toronto, Toronto, ON M5S3H8, Canada. ²Center for Planetary Sciences, Department of Physical and Environmental Sciences, University of Toronto Scarborough, Toronto, ON M1C 1A4, Canada. ³Laboratoire de Météorologie Dynamique, Institut Pierre Simon Laplace, 4 Place Jussieu, BP 99, 75252 Paris, France. ⁴Department of Physics, University of Toronto, 60 St George Street, Toronto, ON M5S 1A7, Canada. ⁵Department of Astronomy and Astrophysics, University of Toronto, Toronto, ON M5S 3H8, Canada.

*Corresponding author. E-mail: jleconte@cita.utoronto.ca

must be to affect the planetary rotation has not yet been determined.

These issues are of utmost importance as we now find many terrestrial planets in a situation similar to Venus. Because the habitable zone—the zone around a star inside which a planet can sustain surface liquid water—is closer around

lower-mass stars, planets in this region are often expected to be tidally synchronized with the orbit (7–15). This seems to create additional difficulties for keeping a habitable environment over the lifetime of the planet. In particular, the permanent night side can be an efficient cold-trap for water (13, 14), strongly destabilize the carbonate-silicate cycle (10, 11), and even cause atmospheric collapse in extreme cases (9, 15).

Here, we investigate whether or not thermal tides can drive terrestrial planets in the habitable zone out of synchronous rotation if a relatively thin atmosphere is present. Previous studies on Venus (2–6), and for exoplanets (16, 17), have shown that this reduces to the search for equilibrium rotation states for which the bodily torque (T_g) and the atmospheric torque (T_a) cancel each other and provide a restoring force against deviations from this equilibrium. In the circular case with zero obliquity, these torques are given by

$$T_a = -\frac{3}{2}K_a b_a(2\omega - 2n)$$

and

$$T_g = -\frac{3}{2}K_g b_g(2\omega - 2n) \quad (1)$$

where $K_a \equiv (3M_* R_p^3)/(5\bar{\rho} a^3)$; $K_g \equiv GM_*^2 R_p^5/a^6$; G is the universal gravitational constant; M_* is the mass of the star; R_p , ω , and $\bar{\rho}$ are the planet's radius, rotation rate, and mean density, respectively; and a and n are its orbital semimajor axis and mean motion, respectively (5, 6). $b_g(\sigma)$ characterizes the frequency-(σ)-dependent response of the body of the planet (its rheology), and $b_a(\sigma)$ characterizes that of the atmosphere. Unlike trapping in asynchronous spin-orbit resonances (for example, Mercury) (18), thermal tides do not need any eccentricity to drive a planet out of synchronous rotation. Although some general conclusions can be reached without a precise knowledge of these responses (5, 6, 16, 17), the biggest limitation in predicting the properties of equilibrium spin states lies in the uncertainties on the shape and amplitude of the atmospheric response [$b_a(\sigma)$]. In particular, the relation between the mass of the atmosphere and the strength of the thermal tide is key in quantifying whether asynchronicity is ubiquitous and remains unknown.

To tackle this issue, we use a generic global climate model (14, 19, 20), commonly used to model planets in the habitable zone of low-mass stars, to

empirically quantify the amplitude of torque induced by thermal tides for planets with various atmospheric masses (characterized by the surface pressure, p_s), compositions, and incoming stellar fluxes (F). Once p_s and F are chosen, we run the atmospheric model for several diurnal frequencies, $\sigma \equiv \omega - n$. Because of the thermal forcing, a surface pressure pattern lagging behind the substellar point forms (fig. S1). Once mean thermal equilibrium is reached, we compute the complex amplitude of the quadrupolar thermal tide (\tilde{q}_a) (21), as shown in Fig. 1, and the value of the torque is given by

$$\text{Eq. 1, where } b_a(2\omega - 2n) = -\sqrt{\frac{10}{3\pi}} \text{Im}[\tilde{q}_a(\omega - n)]$$

To test our framework, we applied our model to Earth and Venus, where our results meet existing constraints (fig. S2) (21). However—rather counterintuitively—for the same forcing frequency, the amplitude of the thermal tide in an Earth-like atmosphere of 1 bar is almost an order of magnitude stronger than on Venus (Fig. 1B). This difference is the result of the sunlight being almost completely scattered or absorbed before it reaches Venus's surface (21).

As discussed earlier, the lag and amplitude of thermal tides are closely related to the thermal inertia of the system. In fact, a careful analysis of the result of the climate model shows that the frequency dependence of the atmospheric response shown in Fig. 1 is fairly analogous to the thermal response of a radiating slab with a finite thermal inertia that is periodically heated. Therefore, to a very good approximation, we can write

$$\tilde{q}_a(\sigma) = -\frac{q_0}{1 + i\sigma/\omega_0}$$

where $i^2 = -1$, ω_0 is the inverse of the time scale needed for the system to reach thermal equilibrium, and q_0 is the amplitude of the quadrupole term of the pressure field at zero frequency (21). In theory, ω_0 can be estimated if the heat capacity of the system is known (21), but in practice, both ω_0 and q_0 are computed from the numerical model for a given atmosphere and are shown in Table 1 for limit cases. In the circular case with zero obliquity, the torque is expressed as

$$T_a(\omega - n, p_s, F) = \frac{3}{2}K_a q_0(p_s, F) \times \frac{(\omega - n)/\omega_0(p_s, F)}{1 + [(\omega - n)/\omega_0(p_s, F)]^2}$$

Although governed by different physics, the atmospheric torque follows the same law as the body torque for a viscoelastic sphere (with the opposite sign).

A first qualitative difference with previous works (3–5, 16, 17) is that we derive a very different functional form for the atmospheric torque. In particular, the function $f(\sigma) \equiv b_a(2\sigma)/b_g(2\sigma)$ (5) is not monotonic around potential equilibria when a realistic rheology is used. As seen in Fig. 2, for a constant- Q or an Andrade rheology, this results in the possible existence of up to five equilibria in the circular case, two of them being

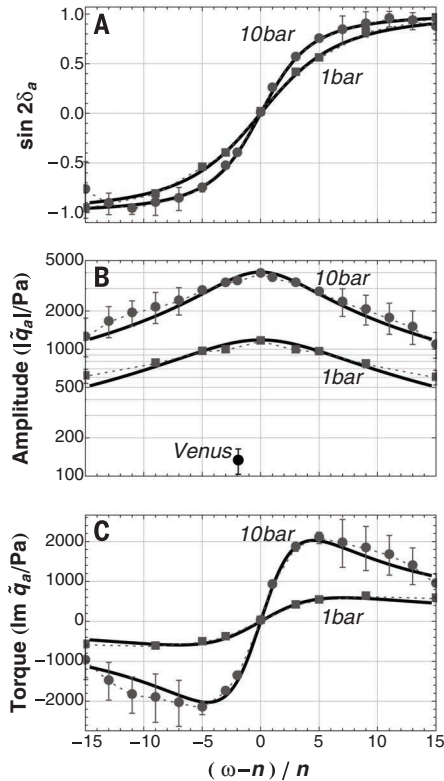


Fig. 1. Frequency dependence of the torque. (A) Sin of the lag angle ($\sin 2\delta_a$), (B) amplitude of the pressure bulge ($|\tilde{q}_a|$), and (C) torque [$\text{Im}(\tilde{q}_a)$] as a function of the forcing frequency [$(\omega - n)/n$] computed from the numerical atmospheric model (gray data points) and given by our analytical model (black curve). Results are shown for two pressures (squares, 1 bar; circles, 10 bar) in the 1366 W/m^2 case with an orbital period of 225 days. The error bars show the internal variability ($\pm 1\sigma$). The Venusian tide amplitude is shown in (B). Despite its simplicity, the analytical model fairly captures the frequency dependence of the thermal tide response.

Table 1. Characteristics of the thermal tide for various types of atmospheres. Numerical values of the amplitude of the atmospheric quadrupole (q_0) and intrinsic thermal frequency of the atmosphere (ω_0) derived from the global climate model.

Sets of simulations	Model output				
	$F(\text{W.m}^{-2})$	$p_s(\text{bar})$	$q_0(\text{Pa})$	$\omega_0(\text{s}^{-1})$	$2\pi/\omega_0(\text{days})$
Venus	2610	92	201	3.77×10^{-7}	193
Inner habitable zone	1366	1	1180	2.30×10^{-6}	32
		10	4050	1.46×10^{-6}	50
Outer habitable zone (N_2)	450	1	890	1.18×10^{-6}	62
		10	2960	7.17×10^{-7}	101
Outer habitable zone (CO_2)	450	10	2590	9.7×10^{-7}	70

unstable (21). The diversity of equilibria might be even richer in eccentric systems where these numbers could change (16, 17). The synchronous spin state is stable. Knowing that Venus, despite such a

rheology, did not end up synchronized tells us that a planet can avoid being trapped in such a stable synchronous state and constrains the history of the Venusian atmosphere (21).

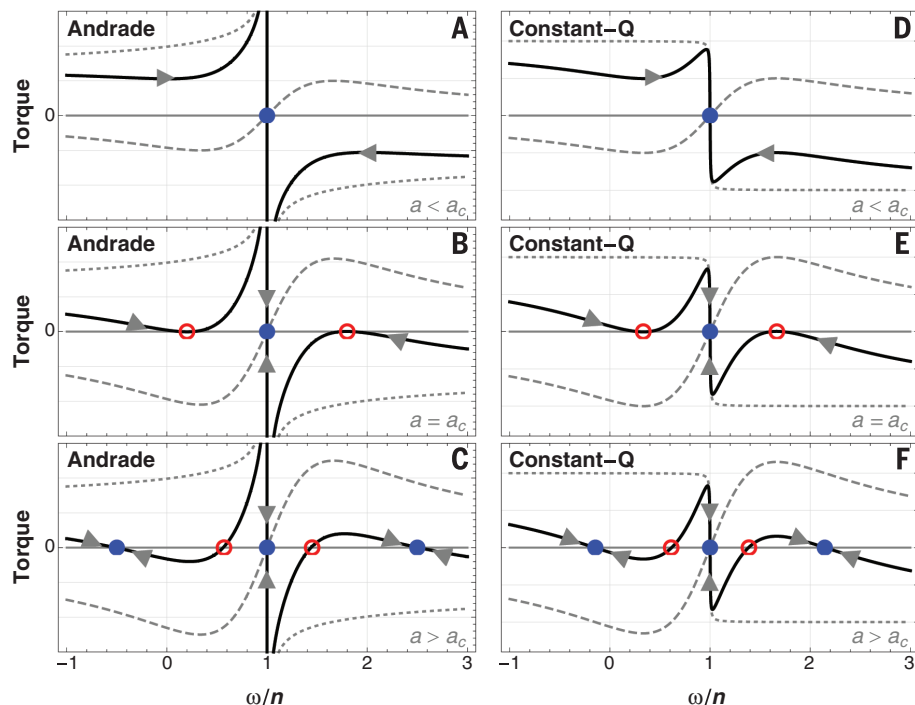
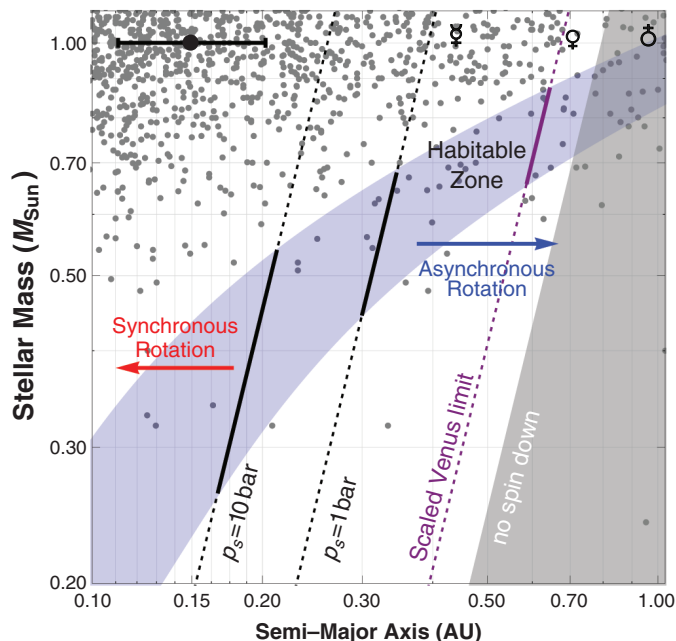


Fig. 2. Equilibrium spin states of the planet. Atmospheric (dashed), gravitational (dotted), and total (solid) torque as a function of spin rate for two tidal models, (A to C) Andrade and (D to F) Constant-Q. Arrows show the sense of spin evolution. (A) and (D) show weak atmospheric torque, only one equilibrium, and synchronous spin state exists (blue circle). (B) and (E) show the bifurcation point ($a = a_c$). In (C) and (F), the atmospheric torque is strong enough to generate four asynchronous equilibrium spin states, two being unstable (red open circles) and two being stable (blue circles; one is retrograde in the case shown). The synchronous spin state remains stable. The figure is to be compared with figure 6 of (24).

Fig. 3. Spin state of planets in the habitable zone.

The blue region depicts the habitable zone (14, 25), and gray dots are detected and candidate exoplanets. Each solid black line marks the critical orbital distance (a_c) (Eq. 2) separating synchronous (left, red arrow) from asynchronous planets (right, blue arrow) for $p_s = 1$ and 10 bar (the extrapolation outside the habitable zone is shown with dotted lines). Objects in the gray area are not spun down by tides. The error bar illustrates how limits would shift when varying the dissipation inside the planet ($Q \sim 100$) (21) within an order of magnitude.



In addition, the number and location of equilibria undergo a bifurcation because asynchronous spin states exist only when the amplitude of the thermal tide reaches a threshold. Thus, our results reveal the existence of a critical distance a_c beyond which the planet can be asynchronous, which, using a constant- Q rheology, reads

$$a_c = \left(\frac{10\pi}{3}\right)^{1/6} \left(GM_* \bar{\rho} R_p^2 \frac{k_2}{q_0 Q}\right)^{1/3} \quad (2)$$

where k_2 is the Love number and Q is the tidal quality factor (21). Both a_c (Fig. 3) and the equilibrium asynchronicity $|\omega - n| = \omega_0[(a/a_c)^3 + \sqrt{(a/a_c)^6 - 1}]$ (fig. S3) can be computed for various cases by using Table 1. The corollary is that even without any spin-orbit trapping due to a permanent asymmetry of the mantle (triaxiality), planets on circular orbits for which atmospheric tides are too weak should be in exact spin-orbit resonance.

Our results provide a robust framework for the quantitative assessment of the efficiency of thermal tides for different atmospheric masses without having to rely on scaling arguments calibrated on Venus. This is crucial because Venus thermal tides turn out to be relatively weak (Fig. 1B). As can be seen in Fig. 3, Earth-like planets with a 1-bar atmosphere are expected to have a nonsynchronous rotation if they are in the habitable zone of stars more massive than ~ 0.5 to $0.7M_\odot$ (depending on their location in the habitable zone). This lower limit decreases to $\leq 0.3M_\odot$ for a 10-bar atmosphere. These limits are much less restrictive than the one obtained from our Venus model (Fig. 3, purple line). This realization required full atmospheric modeling.

Atmospheres as massive as 1 bar are a reasonable expectation value given existing models and solar system examples. This is especially true in the outer habitable zone, where planets are expected to build massive atmospheres with several bars of CO_2 (7). So, our results demonstrate that asynchronism mediated by thermal tides should affect an important fraction of planets in the habitable zone of lower-mass stars.

This has many implications. On one hand, the difficulties in sustaining a habitable climate far from the star due to the presence of a permanent cold, night side (9–15) may not be as severe as usually thought. On the other hand, the habitable zone has been recently shown to be more extended near the star for synchronous planets (12). For these objects, if the atmosphere is thick enough, the nonsynchronous rotation that should ensue may thus come to limit the extent of the habitable zone around lower-mass stars.

The thermal tide mechanism presented here does not only affect habitable-zone planets, so many other terrestrial bodies with substantial atmospheres could potentially have asynchronous rotations, depending on their orbital location (Fig. 3). With that in mind, observational methods

that can constrain the rotation rate of exoplanets (22, 23) become more valuable and could even be used to constrain their atmospheres.

REFERENCES AND NOTES

- S. Chapman, R. Lindzen, *Atmospheric Tides, Thermal and Gravitational* (Reidel, Dordrecht, 1970).
- T. Gold, S. Soter, *Icarus* **11**, 356–366 (1969).
- A. P. Ingersoll, A. R. Dobrovolskis, *Nature* **275**, 37–38 (1978).
- A. R. Dobrovolskis, A. P. Ingersoll, *Icarus* **41**, 1–17 (1980).
- A. C. Correia, J. Laskar, *Nature* **411**, 767–770 (2001).
- A. C. Correia, J. Laskar, *J. Geophys. Res. Planets* **108** (E11), 5123 (2003).
- J. F. Kasting, D. P. Whitmire, R. T. Reynolds, *Icarus* **101**, 108–128 (1993).
- R. Heller, J. Leconte, R. Barnes, *Astron. Astrophys.* **528**, A27 (2011).
- M. M. Joshi, R. M. Haberle, T. T. Reynolds, *Icarus* **101**, 108–128 (1993).
- E. S. Kite, E. Gaidos, M. Manga, *Astrophys. J.* **743**, 41 (2011).
- A. R. Edson, J. F. Kasting, D. Pollard, S. Lee, P. R. Bannon, *Astrobiology* **12**, 562–571 (2012).
- J. Yang, N. B. Cowan, D. S. Abbot, *Astrophys. J.* **771**, L45 (2013).
- K. Menou, *Astrophys. J.* **774**, 51 (2013).
- J. Leconte et al., *Astron. Astrophys.* **554**, A69 (2013).
- K. Heng, P. Kopparla, *Astrophys. J.* **754**, 60 (2013).
- A. C. Correia, B. Levrard, J. Laskar, *Astron. Astrophys.* **488**, L63–L66 (2008).
- D. Cunha, A. C. Correia, J. Laskar, Spin evolution of Earth-sized exoplanets, including atmospheric tides and core-mantle friction. *Int. J. Astrobiol.*, 10.1017/S1473550414000226 (2014).
- V. V. Makarov, C. Bergea, M. Efroimsky, *Astrophys. J.* **761**, 83 (2012).
- F. Forget et al., *Icarus* **222**, 81–99 (2013).
- J. Leconte, F. Forget, B. Charnay, R. Wordsworth, A. Pottier, *Nature* **504**, 268–271 (2013).
- Materials and methods are available as supplementary materials on Science Online.
- F. Selsis et al., *Astron. Astrophys.* **555**, A51 (2013).
- I. A. G. Snellen et al., *Nature* **509**, 63–65 (2014).
- A. C. M. Correia, J. Laskar, O. N. de Sury, *Icarus* **163**, 1–23 (2003).
- R. K. Kopparapu et al., *Astrophys. J.* **765**, 131 (2013).

ACKNOWLEDGMENTS

J.L. thanks S. Lebonnois for providing the numerical outputs of the Venus model. The authors thank three anonymous referees for their insightful comments that substantially enhanced the manuscript. N.M. is supported in part by the Canada Research Chair program. This work was supported by grants from the Natural Sciences and Engineering Research Council of Canada to K.M. and N.M. J.L. is a Banting Fellow.

SUPPLEMENTARY MATERIAL

www.sciencemag.org/content/347/6222/632/suppl/DC1
Materials and Methods
Supplementary Text
Figs. S1 to S5
References (26–35)

14 July 2014; accepted 19 December 2014
10.1126/science.1258686

METALLURGY

Origin of dramatic oxygen solute strengthening effect in titanium

Qian Yu,^{1,2*} Liang Qi,^{1,3†} Tomohito Tsuru,³ Rachel Traylor,¹ David Rugg,⁴ J. W. Morris Jr.,¹ Mark Asta,¹ D. C. Chrzan,¹ Andrew M. Minor^{1,2§}

Structural alloys are often strengthened through the addition of solute atoms. However, given that solute atoms interact weakly with the elastic fields of screw dislocations, it has long been accepted that solution hardening is only marginally effective in materials with mobile screw dislocations. By using transmission electron microscopy and nanomechanical characterization, we report that the intense hardening effect of dilute oxygen solutes in pure α -Ti is due to the interaction between oxygen and the core of screw dislocations that mainly glide on prismatic planes. First-principles calculations reveal that distortion of the interstitial sites at the screw dislocation core creates a very strong but short-range repulsion for oxygen that is consistent with experimental observations. These results establish a highly effective mechanism for strengthening by interstitial solutes.

Solute atoms are intentionally added to pure metals so as to engineer their mechanical properties but may also be present because they are incorporated naturally during processing or service. The strengthening effect of such solutes ordinarily is due to their resistance to dislocation motion, which is conventionally attributed to the elastic interaction between the respective lattice strains of the solute atoms and the dislocations. In isotropic elasticity theory, however, a perfect screw dislocation results in only a shear stress field and does not interact with a solute atom that creates an isotropic vol-

ume change (1, 2). The interaction remains relatively weak even when anisotropic elasticity, anisotropic solute strain, and the “modulus effect” of the solute are taken into account. It follows that solution hardening is not ordinarily expected to be an effective hardening mechanism in metals with mobile screw dislocations.

First-principles calculations suggest that under appropriate conditions, there may be a strong, specific structural interaction between solute atoms and the dislocation core that is not captured by the continuum elastic field (3, 4). This raises the possibility that solution hardening may be effective when mobile screw dislocations are present.

The present work addresses solution hardening by small oxygen additions to hexagonally close-packed (HCP) α -Ti. This is a particularly attractive system for such studies both because of its technological importance and because of the dramatic hardening effect of small oxygen additions (5–9). We exploit recent advances in aberration-corrected transmission electron mi-

croscopy (TEM), in situ small-scale mechanical testing, three-dimensional (3D) dislocation analysis, and first-principles computational modeling to clarify solution-hardening in this system. The experimental evidence discussed below documents strong solution-hardening by oxygen, shows substantial solute pinning of screw dislocations, reveals the incorporation of oxygen atoms in the dislocation core, and illustrates interesting features of dislocation motion and reconfiguration in the presence of oxygen. The parallel first-principles calculations clarify the crystallographic source of the oxygen interaction with the screw dislocation core. The distortion of the interstitial sites at the dislocation core creates a very strong but short-range repulsion for oxygen atoms. As a result, dislocations can only move via a “mechanical shuffle” of the oxygen interstitial or by a local cross slip that creates immobile dislocation segments. Both mechanisms effectively pin the dislocation near the oxygen interstitial.

The experimental samples include nominally pure α -Ti with 0.1, 0.2, and 0.3 weight percent (wt %) O additions. All of the materials are solid solutions (their chemical compositions are shown in table S1), although a few precipitates were observed in the Ti-0.3 wt % O sample. Details of the sample preparation are provided in the supplementary materials. In hexagonal α -Ti, the primary mobile dislocations are believed to be $\langle a \rangle$ -type dislocations on the prismatic plane (1, 10), although perpendicular screw dislocations are also active. To characterize dislocations and image the oxygen in their immediate neighborhood, we used the Transmission Electron Aberration-Corrected Microscope (TEAM) 0.5 microscope, a double-aberration-corrected (scanning) TEM capable of producing images with 50-pm resolution (11). The types of the dislocations were first determined at low magnification by using standard $g \cdot b$ analysis. We found that a majority of the “near-edge” dislocations were not pure $\langle a \rangle$ -type; they demonstrated weak contrast under the [0002] reflection, indicating $\langle c \rangle$ components.

¹Department of Materials Science and Engineering, University of California, Berkeley, CA, USA. ²National Center for Electron Microscopy, Molecular Foundry, Lawrence Berkeley National Laboratory, Berkeley, CA, USA. ³Nuclear Science and Engineering Directorate, Japan Atomic Energy, Tokai-mura, Ibaraki, Japan. ⁴Rolls Royce, Derby DE24 8BJ, UK.

*These authors contributed equally to this work. †Present Address: Department of Materials Science and Engineering, Zhejiang University, China. ‡Present Address: Department of Materials Science and Engineering, University of Michigan, Ann Arbor, MI, USA.

§Corresponding author. E-mail: aminor@berkeley.edu

This mixed character was also confirmed through further high-resolution STEM (HR-STEM) studies. Shown in Fig. 1A are typical dark-field and bright-field STEM images of a “near-edge” dislocation core, in which the Burgers circuit in green shows both $\langle a \rangle$ and $\langle c \rangle$ components. The segregation of oxygen atoms at the HCP octahedral sites was observed on the tension side of the edge dislocation core. The atomic structure of edge dislocation cores was similar for both the Ti-0.1 wt % O and Ti-0.3 wt % O samples.

In contrast, the core structures of screw dislocations changed substantially as the oxygen content increased, as illustrated in Fig. 1B. Focusing on screw dislocations with Burgers vector $1/3[11\bar{2}0]$, we plotted the in-plane core atom displacement vectors for the screw dislocation in both Ti-0.1 wt % and Ti-0.3 wt % O samples. We found that the projected view of the screw dislocation core has an extended in-plane displacement field in the Ti-0.1 wt % O sample. However, the screw dislocation core is smaller

in projection for the Ti-0.3 wt % O sample, with a narrow displacement field averaging ~ 0.5 nm in width. Oxygen interstitials are more frequently observed near the core of screw dislocations in the Ti-0.3 wt % O samples, where they occupy octahedral sites, and the displacements are tightly confined to the core, as suggested by the first-principles calculations described in the supplementary materials. The high-resolution TEM observations seem to establish a direct interaction between oxygen interstitials and screw dislocation cores that becomes more apparent as the oxygen concentration increases.

To quantify the impact of such oxygen-dislocation interactions on the mechanical properties, we performed in situ TEM nanocompression tests in which the real-time mechanical response and the evolution of the deformation microstructure were monitored simultaneously. Nanopillars oriented along $\langle 01\bar{1}0 \rangle$ were prepared from Ti-0.1, Ti-0.2, and Ti-0.3 wt % O bulk polycrystalline samples, respectively, by using focused ion beam milling and Ar^+ cleaning. The pillars were ~ 150 nm in diameter. Potential Ga damage in the fabrication of the nanopillars was studied (a HR-STEM image of the edge of a nanopillar is shown in fig. S1) and is considered as negligible. These tests isolate the solid solution strengthening effect from any competing influence of precipitation hardening. The dimensions of the pillars are less than the average spacing between oxide precipitates, and the samples were observed to be free of such precipitates. Quantitative nanocompression tests were performed in a JEOL 3010 TEM by using a Hysitron (Eden Prairie, MN) picoindenter in displacement-control mode. The load was applied along the $\langle 01\bar{1}0 \rangle$ direction. Prismatic slip should be the primary deformation mode in this orientation. The size, orientation, and initial microstructure of the pillars, as well as the structure of the edge dislocation cores, were quite similar across the different samples. Thus, the observed differences in the mechanical properties and deformation microstructure with

Fig. 1. Imaging of oxygen interstitials and their effect on the dislocation cores in Ti.

(A) High-angle annular dark-field scanning (HAADF)-STEM image of an edge dislocation core in a Ti-0.1 wt % O sample. Zone axis is $[2\bar{1}10]$. At right are shown higher-magnification HAADF-STEM (top) and the corresponding bright-field STEM image (bottom) of the same edge dislocation core. Oxygen atoms can be seen at the interstitial positions and segregated to the tension side of the dislocation core. (B) HAADF-STEM image of a screw dislocation core in Ti-0.1 wt % O (left) and Ti-0.3 wt % O (right). Beam direction is $[11\bar{2}0]$. The in-plane displacement vectors are plotted where each blue vector represents the actual physical displacement of Ti atoms, and the presence of an arrowhead without a tail indicates that the vector is less than or equal to the length of the arrowhead. The blue arrowheads point to the ideal position of the atoms. (Right) The black arrows point to the oxygen atom columns around the screw dislocation core.

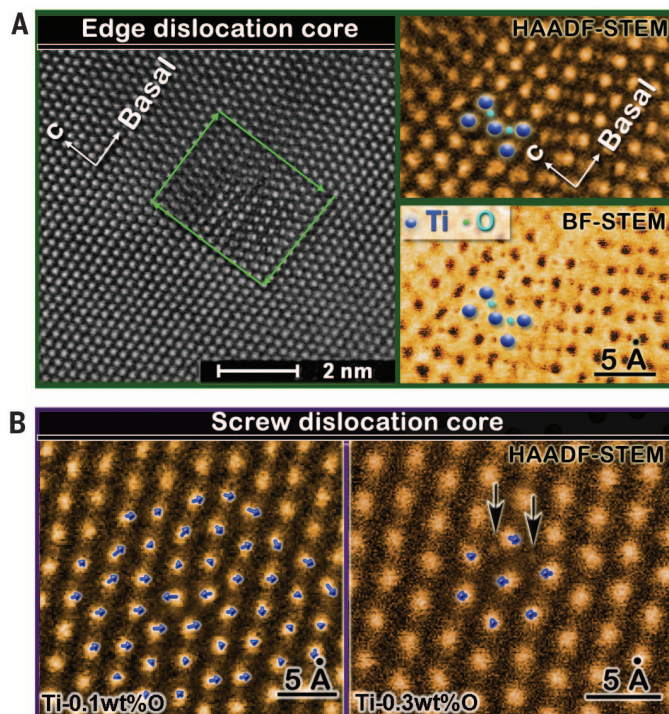
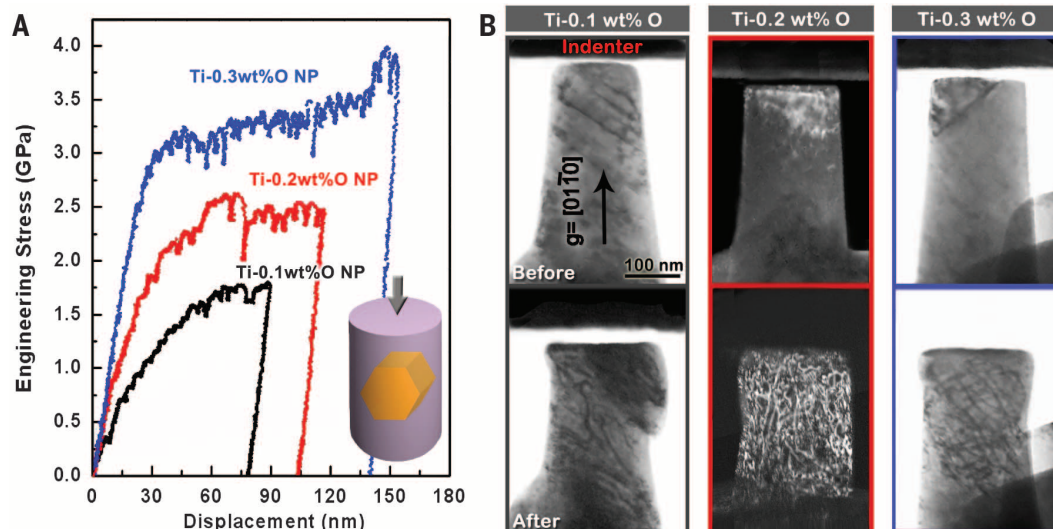


Fig. 2. In situ TEM nanocompression tests of Ti with 0.1, 0.2, and 0.3 wt % O, respectively. (A) The engineering-displacement curves of pillar compression tests at different oxygen concentrations. A schematic of the sample and crystallographic orientation is shown bottom right, where the loading direction is along $[01\bar{1}0]$. (B) Corresponding TEM images of the pillars before and after compression. g vector is along $[01\bar{1}0]$. The Ti-0.1 wt % O and Ti-0.3 wt % O samples were tested under bright-field TEM mode, whereas this Ti-0.2 wt % O sample was tested under dark-field TEM mode.



increasing oxygen content are expected to be mainly due to the enhanced interaction between the solute atoms and screw dislocations as the concentration increases.

Shown in Fig. 2A are typical engineering stress-displacement curves from nanocompression tests of pillars of varying oxygen concentrations. It is observed that the Ti-0.1 wt % O pillars exhibited the lowest strength, but with substantial work hardening upon yielding. The average yield strength of the Ti-0.3 wt % O pillars was ~2.5 GPa, which is almost 8 times greater than the average yield strength of Ti-0.1 wt % O pillars (~320 MPa). The yield strength of Ti-0.2 wt % O pillars was intermediate between these two samples, as expected. However, the increase in yield strength was not linear with the increase of oxygen concentration. For comparison, bulk compression tests were also performed on these same three alloys at the millimeter scale, with details described in the supplementary materials (fig. S3). It is observed that the oxygen strengthening effect in the nanopillars is stronger than that in bulk samples in which the collective deformation mechanisms are more complex.

As shown in Fig. 2, there were changes in the microstructural deformation pattern as the oxygen content increased. Shown in Fig. 2B are before and after images corresponding to the tests documented in Fig. 2A. As shown in Fig. 2B, most of the pillars contained few preexisting <a>-type screw dislocations. After compression,

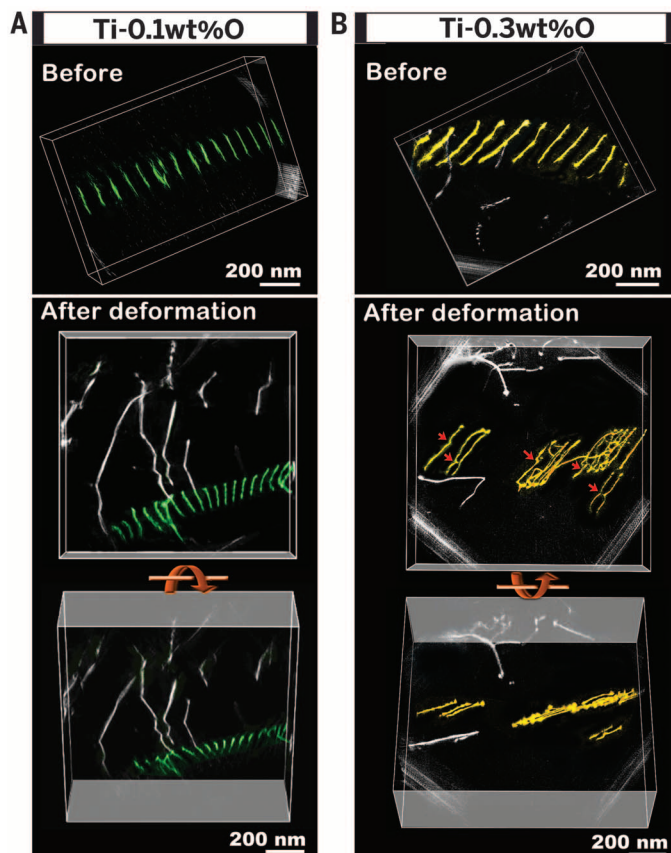
localized primary shear was commonly observed in Ti-0.1 wt % O pillars. Because the pillars were loaded along $\langle 01\bar{1}0 \rangle$, the shear traces can be considered to be associated with prismatic slip. However, as the oxygen concentration increased to 0.2 wt %, localized shear was not typically observed. In the Ti-0.3 wt % O pillars, the plastic deformation was almost homogenous; the pillars eventually deformed into “mushroom” shapes, with no obvious shear localization.

We then matched the in situ TEM movies to the real-time mechanical response of the samples. The results showed that dislocation activity in the Ti-0.1 wt % O pillar shown in Fig. 2B originated from the top of the pillar at about 300 MPa. Localized shear began at ~750 MPa on a prismatic plane that contained one visible preexisting dislocation and continued along this prismatic plane, indicating that the dislocation generation and glide on this plane dominated the deformation. In contrast, pillars with higher oxygen concentrations yielded with a “burst” of dislocations. In the Ti-0.3 wt % O pillar that is shown in Fig. 2B, the stress for the “dislocation-burst” event was ~2.5 GPa, indicating that strong barriers opposed dislocation motion. Moreover, these dislocations were quickly repinned. Eventually, a complex dislocation network developed and filled the volume of the pillar, producing a much more homogenous deformation. These observations are attributable to the increasing oxygen-screw dislocation interaction as the oxygen content was raised.

The results from the pillar tests demonstrate that oxygen interstitials act as extraordinarily strong obstacles for the activation of dislocation glide, with the consequence that an addition of only 0.1 wt % O increases the yield stress several times. In addition, the strong pinning effect of oxygen on screw dislocations is reflected in the 3D development of the dislocation deformation microstructure. To investigate the latter phenomenon in more detail, we used a combination of electron tomography and **g·b** analysis to characterize the evolution of screw dislocation arrays. The technique involves the recording of a series of 2D projections of a sample volume at regular intervals over a large angular range, to produce a 3D reconstruction of the sample state. We compared the evolution of screw dislocation arrays that had similar initial configurations and Burgers vectors of $b = \pm[10\bar{1}2]$ in 0.1 and 0.3 wt % O pillars. The tilt series were collected using $g = [10\bar{1}1]$, as detailed in the supplementary materials. Both the Ti-0.1 and Ti-0.3 wt % O samples were then loaded in tension by using a Gatan straining holder ex situ. The samples were loaded to similar displacements, which given the similar sample geometries generates a comparable level of strain. The tilt series were then collected again in the deformed samples, and the changes of the 3D structure of the same dislocation arrays were recorded. Shown in Fig. 3, A and B, are the tomograms of the dislocation arrays before and after strain. After strain, the same location is imaged, and the dislocation arrays found at this location demonstrate that the basic structure of the screw dislocation array was maintained in the Ti-0.1 wt % O samples, whereas some other dislocations, with kinked structures, glided into the nearby region. A tilted view of the original dislocation array shows that the dislocations remained on the same crystal plane. In contrast, the structure of the screw dislocation array (in terms of the average spacing between dislocations and the arrangement of dislocations) was substantially changed during deformation in the Ti-0.3 wt % O samples. In this case, the dislocation array broke up into groups, each containing several dislocation lines with defined pinning points. From the tilted view, it is clear that some groups had slipped onto other crystal planes, promoting the development of a more homogenous deformation pattern. Together, the nanopillar and dislocation tomography experiments demonstrate strong interactions between oxygen interstitials and screw dislocations.

Turning to the theoretical analysis, we began from the observation that solute-dislocation interactions arise from two primary mechanisms: elastic interactions mediated by the long-ranged strain fields produced by a dislocation, and shorter-ranged interactions with the dislocation core that are generally referred to as “chemical” interactions (4, 6). The former are generally weak (on the scale of ~0.1 eV per solute atom); in fact, symmetry constraints have the consequence that there should be no linear elastic interaction at all between oxygen interstitials at octahedral sites and a straight <a> screw dislocation in the hcp

Fig. 3. Tomograms shown the 3D evolution of screw dislocation arrays in Ti-0.1 and Ti-0.3 wt % O, respectively. (A) The structure of the dislocation array is similar before and after deformation in Ti-0.1 wt % O. **(B)** The dislocation array has become tangled and moved to different planes after deformation in Ti-0.3 wt % O.



structure (details are provided in fig. S6, and the corresponding analysis is in the supplementary materials). On the other hand, short-range interactions can change the dislocation core structure and influence dislocation mobility by changing the restoring force due to lattice slip. This effect can be described indirectly in terms of the generalized stacking fault (GSF) energy (12–14)—the energy as a function of the relative displacement of two half crystals parallel to a slip plane—and can be found directly by computing the energetics of the dislocation core structure. Consequently, we used first-principles density functional theory (DFT) calculations (15) to find the effects of oxygen interstitial atoms on the GSF energy for slip along the $[1\bar{1}20]$ direction on the Ti prismatic plane and on the core structure of an $\langle a \rangle$ screw dislocation in the Ti lattice.

The calculated results for GSF energy as a function of slip distance are shown in Fig. 4A. Two features of the results are immediately apparent. First, if the O interstitial is located at an octahedral site on the slip plane (“path I”), the calculated GSF energy is much higher than that for pure Ti. Second, as shown in Fig. 4B, the original octahedral site on the slip plane gradually disappears during slip and transforms to a tetrahedral site with much lower interstitial volume when slip is close to $0.5a$. At the same time, a new octahedral site is formed on the basal plane of the Ti structure. Transfer of the O atom from the original octahedral site to this newly formed interstitial site reduces the energy by as much as 1.6 eV (fig. S4) (16). The GSF energy also can be computed with O at the basal-plane interstitial site (“path II”). As shown in Fig. 4A, this path leads to lower energies than path I once the slip displacement is larger than approximately $a/4$. The barrier for oxygen to shuffle (hop) from the original site in path I to the new site in path II varies from between 0.42 to 0.95 eV, depending on the magnitude of the slip displacement, which is consistent with the large diffusion barrier for oxygen in the bulk hcp Ti structure (17). Within the classical Peierls-Nabarro model (18), variations in the restoring force on the GSF surface can change the Peierls stress (the minimum stress required to move a straight dislocation at zero temperature) exponentially. The large increase in the GSF energy, coupled with the large barrier (at least 16 times the thermal energy at room temperature) for oxygen shuffle due to lattice slip, qualitatively explains the strong strengthening effects observed in the in situ experiments.

The large changes in GSF energy associated with the presence of oxygen on the slip plane can be correlated with the changes in interstitial volume induced by the slip displacements. These changes are also observed in direct simulations of the core structures of $\langle a \rangle$ screw dislocations in α -Ti, as shown in Fig. 4C. In the bulk hcp structure of Ti, the octahedral site has the largest interstitial volume. Near a screw dislocation core, the interstitial volumes of these octahedral sites decrease by approximately 50% at the geometric center of the dislocation core. On the other hand, a new interstitial site is formed on the basal plane

near the core. These changes agree with the change of atomic structure found from the GSF calculations. In addition, the most pronounced changes in the volumes of the interstitial sites are observed on one prismatic plane, on which the core structure of $\langle a \rangle$ screw dislocations in Ti is spread [the spreading of screw dislocation cores on prismatic planes found here is consistent with previous theoretical studies (19)].

We also calculated the interaction energies between oxygen interstitial atoms and the dislocation core using DFT. In these calculations, oxygen is inserted into every octahedral site near the dislocation core (details are provided in the supplementary materials), and for each site, the change in energy with respect to placing oxygen far from the dislocation is computed. The results show that the interaction energies are very weak (0.06 eV or smaller) as long as the oxygen is on a prismatic plane other than the one including the dislocation core, or as long as the oxygen is at a distance larger than $c/2$ from the center of the core on the same prismatic plane. The relatively small magnitude of the interaction energies for sites away from the core is consistent with the predictions of the linear theory described above. On the other hand, if oxygen is inserted into the small core region on the same prismatic plane as the dislocation, there is a strong repulsive interaction, which is associated with the small interstitial volume shown in Fig. 4C. In the calculations, this interaction is so strong that the dislocation core is observed to displace from its original position, partially cross slipping onto an adjacent prismatic

plane (fig. S5) during the atomic relaxations. In contrast, if the oxygen is inserted into the interstitial site on the Ti basal planes within the core, there is only a small repulsive energy (~ 0.05 eV), which is consistent with GSF calculations.

The computational results summarized above suggest two effects associated with the interaction of a screw dislocation and oxygen interstitial. First, interstitial oxygen atoms may be forced to move away from their original sites to nearby Ti basal planes because the shear dramatically decreases the volume of the octahedral site. Consistent with this expectation, we have observed by means of HR-STEM oxygen interstitials located on basal planes in some lightly deformed samples (fig. S2); these observations suggest that after the passage of a dislocation, oxygen atoms may become “stuck” in the basal-plane sites rather than hop back to the lower-energy bulk octahedral positions. Second, as shown in Fig. 4D, the presence of oxygen interstitials near the core may force part of the dislocation line to cross-slip to the nearest neighboring prismatic plane. This has the effect of producing two short dislocation edge segments that connect the screw dislocation segments on the two neighboring prismatic planes. These segments can only glide on the basal planes perpendicular to the prismatic planes, and they should thus have very low mobility owing to the larger GSF energy on basal planes (20). Additionally, the resolved shear stress for the edge segments is zero under stress conditions that cause motion of the $\langle a \rangle$ screw dislocation along the $\langle c \rangle$ direction on the prismatic

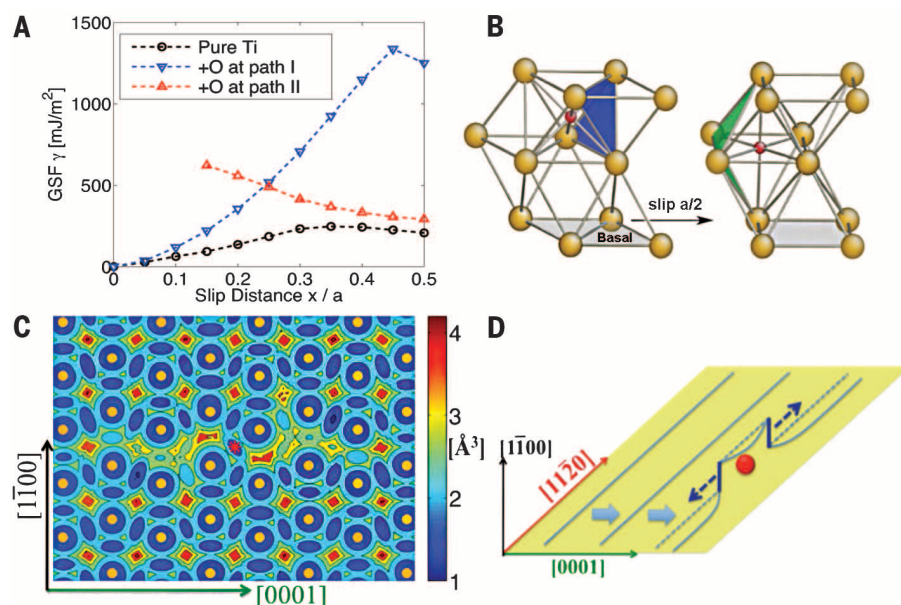


Fig. 4. Simulation results showing the crystallographic source of the oxygen interaction with the screw dislocation core. (A) GSF curves for $[1\bar{1}20](1\bar{1}00)$ slip system in $(2a \times 1c)$ supercell in Ti with oxygen at different interstitial sites on the slip interface. (B) In path I, oxygen is near the original octahedral site in the perfect lattice as the left part figure; in path II, oxygen is at the new octahedral site on Ti basal plane when lattice slip is close to $0.5a$ (right part). (C) Distribution of interstitial volume near $\langle a \rangle$ screw dislocation core. Yellow dots stand for the position of Ti atoms, and the red asterisk in the center is the geometric center of dislocation core. The interstitial volume is defined as $1/6 \times \pi \times d^3$, where d is the distance between one point to its nearest Ti atom. (D) A schematic of local dislocation cross slip when $\langle a \rangle$ screw dislocation encounters oxygen interstitials.

plane. The net result is expected to be a pinning of the dislocation core near the oxygen interstitials as shown in Fig. 1B, resulting in strong strengthening effects. The local cross-slipping due to oxygen interstitials is consistent with the tomograms of the dislocation arrays in Ti-0.3 wt % O samples in Fig. 3B. The classical solid solution strengthening model that neglects these two effects may not provide an accurate description of oxygen strengthening in α -Ti (details are provided in the supplementary materials).

The present work establishes a direct connection between the pronounced strengthening effect of oxygen in hcp-structured α -Ti and the strong interactions between these solute atoms with screw dislocation cores. The strongly repulsive solute-dislocation interaction energies, the large barriers for the “mechanical shuffle” of oxygen atoms in the core, and the local cross-slip induced by oxygen interstitials combine to result in a strong pinning effect on screw dislocations. We suggest that these results provide a well-documented, prototypic example of solid solution strengthening by solute interaction with screw dislocations. This type of crystallographically induced strengthening mechanism

should also exist for other types of dislocations, depending on the corresponding dislocation core structures and the mobility of solid solute atoms.

REFERENCES AND NOTES

1. J. P. Hirth, J. Lothe, *Theory of Dislocations* (McGraw-Hill, New York, 1982).
2. H. Neuhäuser, *Phys. Scr.* **T49B**, 412–419 (1993).
3. G. P. M. Leyson, W. A. Curtin, L. G. Hector Jr., C. F. Woodward, *Nat. Mater.* **9**, 750–755 (2010).
4. J. A. Yasi, L. G. Hector Jr., D. R. Trinkle, *Acta Mater.* **58**, 5704–5713 (2010).
5. *Metals Handbook* (ASM International, Metals Park, OH, ed. 10, 1990), vol. 2.
6. H. Conrad, *Prog. Mater. Sci.* **26**, 123–403 (1981).
7. G. Lutjering, J. C. Williams, *Titanium* (Springer-Verlag, Berlin, ed. 2, 2007).
8. W. R. Tyson, *Scr. Metall.* **3**, 917–921 (1969).
9. M. L. Wasz, F. R. Brotzen, R. B. McLellan, A. J. Griffin, *Int. Mater. Rev.* **41**, 1–12 (1996).
10. F. D. Rosi, C. A. Dube, B. H. Alexander, *Trans. Am. Inst. Mining Metall. Eng.* **197**, 257 (1953).
11. C. Kisielowski et al., *Microsc. Microanal.* **14**, 469–477 (2008).
12. S. Kibey, J. B. Liu, M. J. Curtis, D. D. Johnson, H. Sehitoglu, *Acta Mater.* **54**, 2991–3001 (2006).
13. G. Lu, N. Kioussis, V. Bulatov, E. Kaxiras, *Phys. Rev. B* **62**, 3099–3108 (2000).
14. V. Vitek, *Philos. Mag.* **18**, 773–786 (1968).
15. G. Kresse, J. Furthmüller, *Phys. Rev. B Condens. Matter* **54**, 11169–11186 (1996).
16. M. Ghazisaeidi, D. R. Trinkle, *Acta Mater.* **76**, 82–86 (2014).
17. H. H. Wu, D. R. Trinkle, *Phys. Rev. Lett.* **107**, 045504 (2011).
18. B. Joós, M. S. Duesbery, *Phys. Rev. Lett.* **78**, 266–269 (1997).
19. M. Ghazisaeidi, D. R. Trinkle, *Acta Mater.* **60**, 1287–1292 (2012).
20. X. Z. Wu, R. Wang, S. F. Wang, *Appl. Surf. Sci.* **256**, 3409–3412 (2010).

ACKNOWLEDGMENTS

We gratefully acknowledge funding from the U.S. Office of Naval Research under grant N00014-12-1-0413. Work at the Molecular Foundry was supported by the Office of Science, Office of Basic Energy Sciences, of the U.S. Department of Energy under contract DE-AC02-05CH11231. T.T. acknowledges the financial support of the Japanese Ministry of Education, Culture, Sports, Science and Technology (MEXT), Grant-in-Aid for Scientific Research in Innovative Areas “Bulk Nanostructured Materials.” We thank J. Kacher for dislocation tomography training and Timet (Exton, PA) for the production of the high-purity model alloys used in this study.

SUPPLEMENTARY MATERIALS

www.sciencemag.org/content/347/6222/639/suppl/DC1
Materials and Methods
Supplementary Text
Figs. S1 to S6
Tables S1
References (21–39)
Movies S1 to S7

27 August 2014; accepted 8 January 2015
10.1126/science.1260485

DNA NANOTECHNOLOGY

Programming colloidal phase transitions with DNA strand displacement

W. Benjamin Rogers¹ and Vinodhan N. Manoharan^{1,2,*}

DNA-grafted nanoparticles have been called “programmable atom-equivalents”: Like atoms, they form three-dimensional crystals, but unlike atoms, the particles themselves carry information (the sequences of the grafted strands) that can be used to “program” the equilibrium crystal structures. We show that the programmability of these colloids can be generalized to the full temperature-dependent phase diagram, not just the crystal structures themselves. We add information to the buffer in the form of soluble DNA strands designed to compete with the grafted strands through strand displacement. Using only two displacement reactions, we program phase behavior not found in atomic systems or other DNA-grafted colloids, including arbitrarily wide gas-solid coexistence, reentrant melting, and even reversible transitions between distinct crystal phases.

Like atoms, colloidal particles suspended in a fluid can form bulk phases such as gases and crystals. These particles can also be directed to form new states of matter (1) through careful tuning of their interparticle interactions—for example, by grafting DNA strands onto the particles to create specific attractions (2, 3). Such DNA-grafted particles have been called “programmable atom-equivalents” (4), a moniker that highlights the experimenter’s ability to dictate, or “program,” the self-assembled structures through the DNA sequences. The implied analogy to computer programming is a

useful way to conceptualize how information in the sequences is translated to structure: Much as one can program a computer to perform complex tasks by writing statements that are compiled to machine code, one can “program” a colloid to form a complex structure by designing nucleotide sequences (statements) that are “compiled” into specific interparticle interactions (machine code). Recent advances in our understanding of this compilation process, in the form of design rules (5) or mean-field models (6–8) relating the effective interactions directly to the nucleotide sequences (9), have enabled the assembly of crystal phases not found in ordinary colloids (5, 10–13) and could be extended, in principle, to the assembly of prescribed nonperiodic structures (14, 15).

Structure, however, is just one aspect of self-assembly; more generally, self-assembly describes a phase transition between a disordered and an ordered state, or a pathway on a phase diagram. Thus far, only a subset of the full colloidal phase diagram has been programmed: the equilibrium structure of the ordered state as a function of density and composition. Programmatic control over the phase behavior in the orthogonal thermodynamic dimension—the temperature—remains elusive. Typically, the attraction between two DNA-grafted particles decreases steeply and monotonically with increasing temperature (16, 17). As a result, the suspension displays phase behavior resembling that of simple atoms rather than programmable ones: It is fluid at high temperature and solid at low temperature (Fig. 1A). Our goal here is to develop a comprehensive approach to programming the full phase diagram of colloidal suspensions: We seek to design a set of interaction “primitives” that can be combined to program both the structure of equilibrium phases and their temperature-dependent transitions. In other words, we aim to program the equilibrium self-assembly pathways, not just their end points.

We achieve this goal by adding information to the buffer in the form of free DNA strands. We refer to these as displacing strands because their sequences are designed to be complementary to subunits of the grafted strands; they can therefore react with a double-stranded bridge, displacing one of the grafted strands and forming a nonbridging duplex (Fig. 1B). This hybridization reaction, known as toehold exchange or strand displacement, is widely used in the DNA nanotechnology field to construct dynamic assemblies and devices (18, 19). Strand displacement has

¹School of Engineering and Applied Sciences, Harvard University, Cambridge, MA 02138, USA. ²Department of Physics, Harvard University, Cambridge, MA 02138, USA.
*Corresponding author. E-mail: vnm@seas.harvard.edu

also been used to melt or change the lattice constants of nanoparticle-based materials (20–23). Here, rather than modifying the structure of an already assembled material, we use strand-displacement reactions to control the equilibrium assembly process. The additional degrees of freedom that we introduce allow us to design temperature-dependent interaction potentials with tunable shape, steepness, and specificity (Fig. 1, B and C). Returning to the computer programming analogy, the free DNA sequences act as the language for programming the transitions between phases, much as the grafted sequences program the structure of the phases. Because we separate the functions of the grafted and free strands, the two mechanisms can be controlled independently.

To understand how displacing strands affect the interparticle potential, consider the hybridization reactions shown in Fig. 1. Given that hybridization of complementary strands happens on time scales much shorter than that of particle motion, we can assume that interacting DNA strands are in chemical equilibrium (6–8). More precisely, the DNA-induced colloidal attraction is determined by the spatially varying hybridization yield of DNA bridges, whose temperature dependence comes from the free energy change $\Delta G/RT$ [for details, see (7, 24, 25)]. In the absence of displacement, the free energy change of the hybridization reaction $A + B \rightleftharpoons AB$, given by $\Delta G/RT = \Delta H_{AB}/RT - \Delta S_{AB}/R$, is monotonic with a steepness set by ΔH_{AB} , because the enthalpy change ΔH_{AB} and entropy change ΔS_{AB} are largely independent of temperature (Fig. 1A).

With displacing strands, the free energy difference between bridged and unbridged states can be modified owing to the additional reaction pathways $AB + D_1 \rightleftharpoons AD_1 + B$ and $AB + D_2 \rightleftharpoons A + BD_2$. Because the enthalpic changes of displacement reactions can be tuned through the base sequences of the displacing strands, the free energy change $\Delta G/RT$ can be designed to have various nonlinear dependences on temperature (figs. S1 and S2). Furthermore, the entropic changes of the displacement reactions can be adjusted by changing the molar concentrations of the displacing strands, providing a way to tune the magnitude of $\Delta G/RT$ independently of its dependence on temperature.

A single displacement reaction (Fig. 2A) allows precise control over the thermodynamics of the fluid-solid transition. We control the temperature dependence of the free energy change $\Delta G/RT$, and thus of the interaction potential, by changing the displacing strand sequence. Using the nearest-neighbor model, which relates DNA sequences to hybridization free energies (9), we predict the enthalpic changes of displacement and bridge formation. If we choose the appropriate sequences such that these enthalpic changes are the same ($\Delta H_{AB} = \Delta H_{AD_1}$), we can eliminate the temperature dependence entirely over a range of temperatures (fig. S1). We thereby establish a dynamic equilibrium in which the bridging and nonbridging duplexes exchange freely by toehold-exchange hybridization, without an enthalpic barrier.

This single-displacement scheme, where $\Delta H_{AB} = \Delta H_{AD_1}$, eliminates the boundary between the coexistence region and the solid phase, resulting in coexistence between fluid and solid that persists even at low temperatures (Fig. 2B). In the absence of the displacing strand, we find a single, steep melting curve with an approximate width of 1°C, consistent with earlier reports (16). The melting transition softens with increasing concentration of the free strand (Fig. 2C), widening by 10°C or more. Furthermore, the singlet fraction remains nonzero and constant down to room temperature. Because the entropy of the free strands can be adjusted by changing their molar concentration, the singlet fraction, and thus the interaction strength, can still be tuned.

This single-displacement scheme solves a long-standing problem in DNA-directed self-assembly: the steep dependence of the interparticle attraction on temperature (17), which frustrates equilibrium self-assembly. Previous experiments and simulations have shown that crystal nucleation and growth occur over a range of interaction strengths only 1 to 2 $k_B T$ wide, corresponding to a temperature window roughly 1°C wide (6, 26). In contrast, with a single displacement reaction, we find that nucleation and growth of binary crystals occurs over a range of temperatures wider than 10°C—an improvement of at least an

order of magnitude relative to displacement-free schemes. Expanding the temperature window of equilibrium assembly makes it easier to grow crystals and obviates the need for precision temperature control, temperature gradients, or complex annealing schemes (10, 11, 13).

Our model of DNA-mediated attractions in the presence of strand displacement quantitatively reproduces these measurements (Fig. 2C). Taking the grafting density, free-strand concentration, ionic strength, and DNA sequences as inputs, we reproduce the measured singlet fractions to within the inherent uncertainty associated with the nearest-neighbor model (25). This level of agreement supports our physical picture—that the changes in the temperature dependence result directly from molecular-scale displacement reactions—and demonstrates that the emergent phase behavior can be predicted and therefore programmed.

With two-displacement reactions (Fig. 3A), we can make the free energy not only a nonlinear function of temperature but also a nonmonotonic one, with interesting consequences for the phase behavior: The resulting suspensions display multiple fluid-solid transitions and inverted phase behavior, in which the stable, low-temperature phase is a fluid that freezes upon heating before melting again at higher temperatures. Such

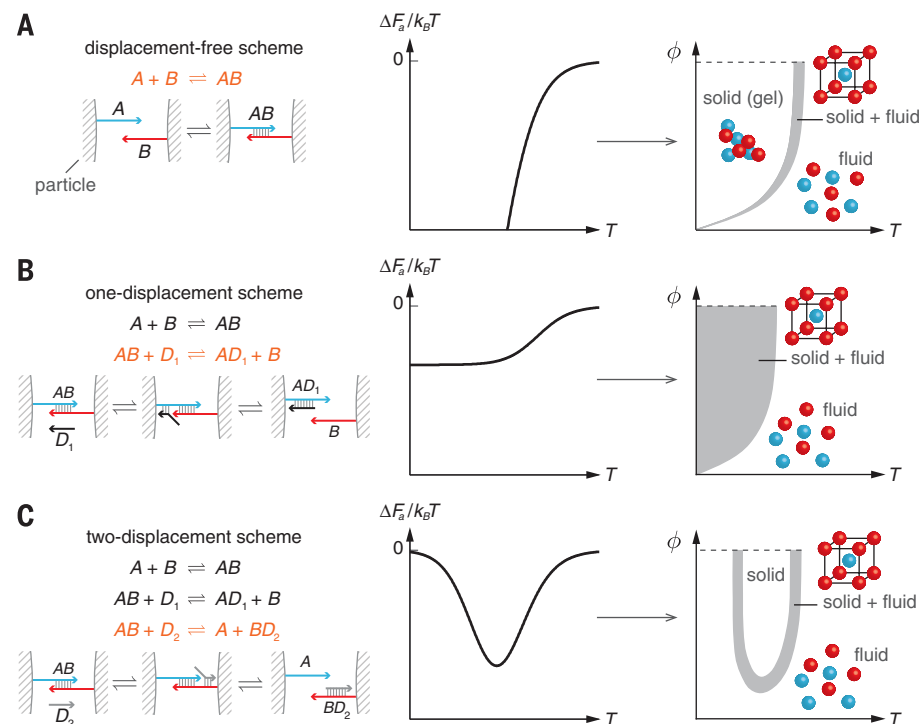


Fig. 1. Strand-displacement reactions program phase behavior by modifying the local chemical equilibrium between DNA-grafted particles. (A) In the absence of displacing strands, the strength of the DNA-induced attraction (ΔF_a) decreases monotonically with increasing temperature T , resulting in simple phase behavior in the ϕ - T space, where ϕ is the particle volume fraction. The fluid-solid coexistence region is shown in gray. (B) A single displacement reaction eliminates the temperature dependence of $\Delta F_a/k_B T$ over a range of temperatures, thereby widening the fluid-solid coexistence region. (C) Adding a second strand-displacement reaction allows $\Delta F_a/k_B T$ to vary nonmonotonically with T , inverting the colloidal phase behavior and creating a reentrant fluid phase. The elementary reaction steps in orange are drawn schematically.

reentrant behavior results from a competition between entropy and enthalpy. The low-temperature fluid is stabilized enthalpically: Because each bridge can be replaced by two nonbridging duplexes of the same length, the most favorable state contains few or no bridges between particles, thus maximizing the total number of base pairs. At higher temperatures, entropy favors the solid phase, because formation of a single bridge liberates two displacing strands. At even higher temperatures, the solid phase melts again, owing to thermal dissociation of DNA bridges.

Our experiments (Fig. 3B) show that the resulting reentrant melting transition is tunable and can be programmed independently of the solid-phase symmetry. By adjusting the concentrations of the displacing strands, we control the temperature window in which the solid phase is stable (Fig. 3C). Higher concentrations of displacing strands shift the local chemical equilibrium toward nonbridging duplexes, leading to a narrower window (Fig. 3D). Strand concentrations exceeding a critical limit prevent freezing entirely. The crystals that we assemble have the expected cesium chloride (CsCl) symmetry (fig. S3).

Because energetic arguments suggest that intraspecies attractions as weak as $\sim 1 k_B T$ would lead to formation of Cu-Au crystals instead of the observed CsCl crystals (13, 27), we conclude that our approach does not result in undesired cross-talk between intra- and interspecies attractions.

Of course, the principal feature of DNA-grafted particles is the ability to create multiple particle species that interact with each other in specific ways. Strand displacement allows us to modify each interaction and thereby program pathways between different self-assembled structures. To demonstrate this feature of our approach, we combine the displacement-free and two-displacement schemes to program a reversible pathway between two compositionally distinct equilibrium ordered phases. Specifically, we design a system containing three different particle species with a temperature-dependent interaction matrix, implemented through six DNA sequences (table S5), four of which are grafted to particles and two of which are displacing strands that modulate interactions between species 2 (green in Fig. 4A) and the other two species. At low temperatures, the interaction matrix favors cocrystallization of species 2 and 3, as confirmed

by confocal fluorescence microscopy (Fig. 4B). At high temperatures, it favors cocrystallization of species 1 and 2. At intermediate temperatures, we program an intervening fluid phase by tuning the displacing strand concentrations, which allows us to easily nucleate and grow either crystal by lowering or raising the temperature. Because the system is in equilibrium at each temperature, the observed phase transitions are completely reversible.

These last experiments demonstrate that the specificity afforded by Watson-Crick base pairing, which is used to program the structure of equilibrium self-assembled phases, can itself be programmed to depend on temperature, enabling reconfigurable materials in which particles change their interactions and reconfigure their structure in response to temperature. The approach is limited only by the freezing and boiling points of the buffer: Because the transition illustrated in Fig. 4 is roughly 10°C wide, one could conceivably design transitions between at least 10 distinct solid phases in the 0° to 100°C temperature range, which could each be directed to self-assemble independently and on cue simply by changing the temperature. Moreover, incorporation of thermally driven solid-solid transitions could also enable the sequential self-assembly of other crystal phases not accessible by direct nucleation from the fluid, but which have the lowest free energy at a given temperature (13). These systems represent an additional direction in self-assembly, in which information supplied to the buffer can program equilibrium pathways between many different target structures within a closed system.

The zero-, one-, and two-displacement reaction schemes constitute a set of primitives that can be combined to further program thermal pathways to self-assembly. We have demonstrated one such combination—a zero-displacement reaction combined with a two-displacement reaction—but many others are possible, owing to the specificity of DNA hybridization. A key feature of our approach is that it separates the functions of the grafted strands, which encode the interaction matrix, and the free displacing strands, which control the temperature dependence of the interaction matrix. Other competitive binding schemes have been proposed (28–30), but none results in independent control of the temperature-dependent phase transitions and the symmetry of the equilibrium phases. This independent control, which is crucial to fully program self-assembly, could make it possible to assemble complex materials in multiple stages. For example, particles might first self-assemble into a scaffold that would disassemble after helping the final, prescribed structure to assemble. Similar strategies are used in biological systems such as bacteriophages (31) and could prove to be more robust than current one-step approaches to assembly. More generally, our demonstration that strand displacement alters the local chemical equilibrium between DNA-grafted particles opens the door to the inclusion of more complex strand displacement-based devices into colloidal assembly. For example,

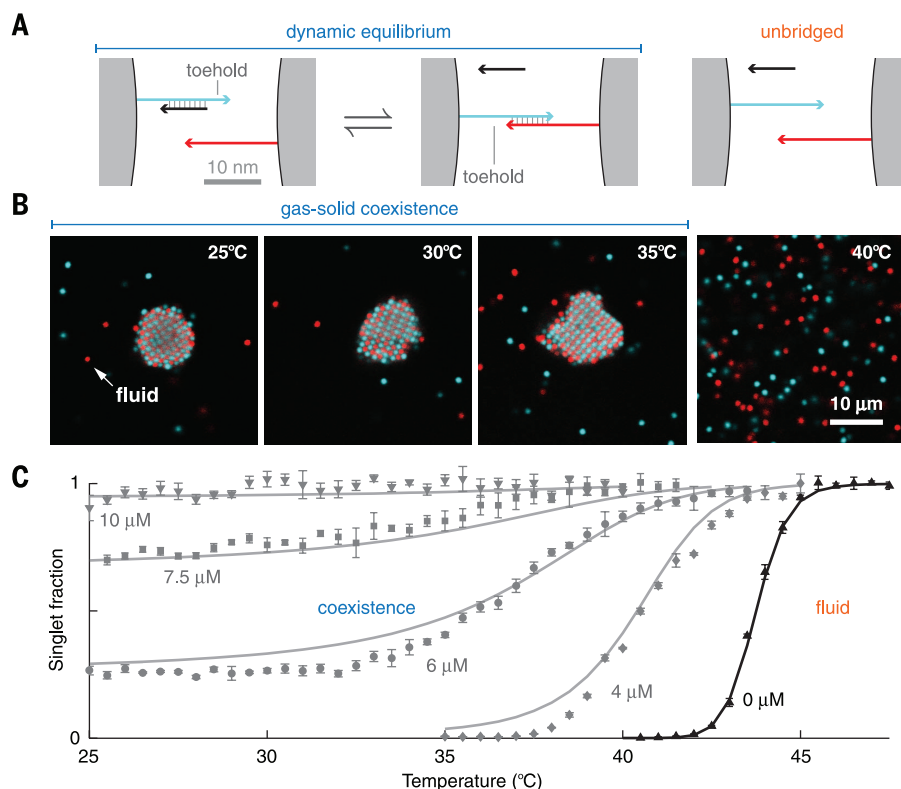


Fig. 2. A single displacement reaction eliminates the temperature dependence of binding. (A) Competition between bridge formation and strand displacement results in stable coexistence between fluid and solid phases that persists over a wide range of temperatures. (B) Representative confocal fluorescence micrographs of a binary suspension of DNA-grafted particles at various temperatures. (C) Experimentally measured particle singlet fraction (symbols) shows the broadening of the melting transition with increasing concentration of free strand D_1 (indicated on plot) (25). Error bars denote SD of three measurements. A model based on local chemical equilibrium (curves), together with a separate model of the singlet fraction (16), reproduces our results to within the inherent uncertainty of the nearest-neighbor model (9, 25, 32). DNA sequences and predicted free energies are given in tables S1 and S2.

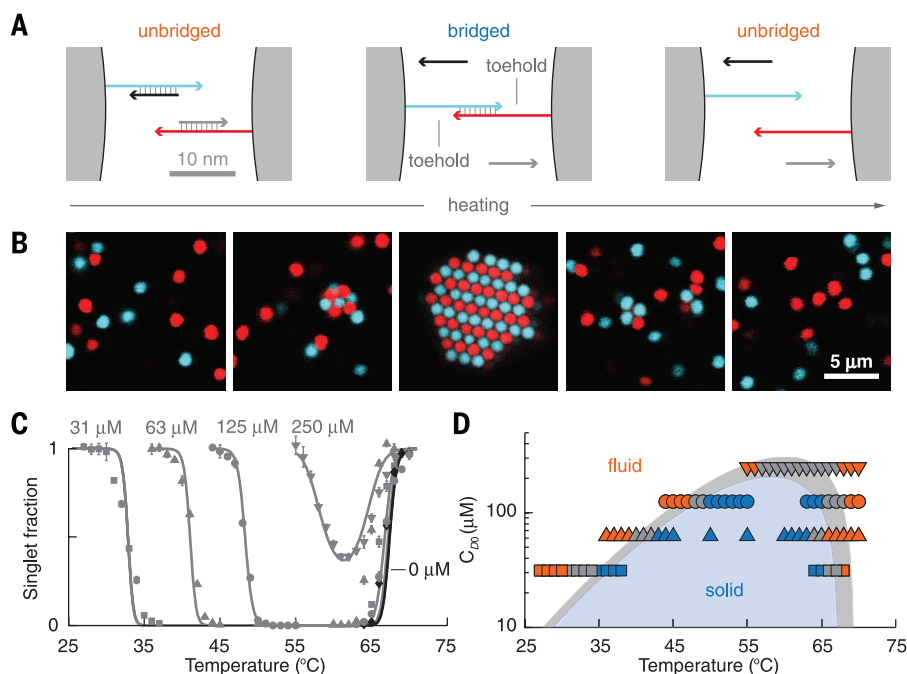


Fig. 3. Two strand-displacement reactions program a tunable reentrant melting transition. (A) Hybridization of free displacing strands induces a second melting transition. (B) Representative confocal fluorescence micrographs show reentrant melting of a binary suspension of DNA-grafted particles. (C) Singlet fraction f measurements (symbols) show that the reentrant melting transition can be tuned by changing the displacing strand concentrations C_{D0} for equimolar mixtures of D_1 and D_2 (indicated on plot) (25). Error bars denote SD of three measurements. Our local chemical equilibrium model (curves) reproduces our results to within the inherent uncertainty of nearest-neighbor predictions (9, 25, 32). (D) The displacing strand concentration–temperature coexistence envelope is delimited by the temperature and C_{D0} where $0.15 < f < 0.85$ (gray). Symbols show experimental data: orange for $f > 0.85$, blue for $f < 0.15$. We achieve coexistence over roughly 10°C when $C_{D0} = 250 \mu\text{M}$. DNA sequences and hybridization free energies are shown in tables S3 and S4.

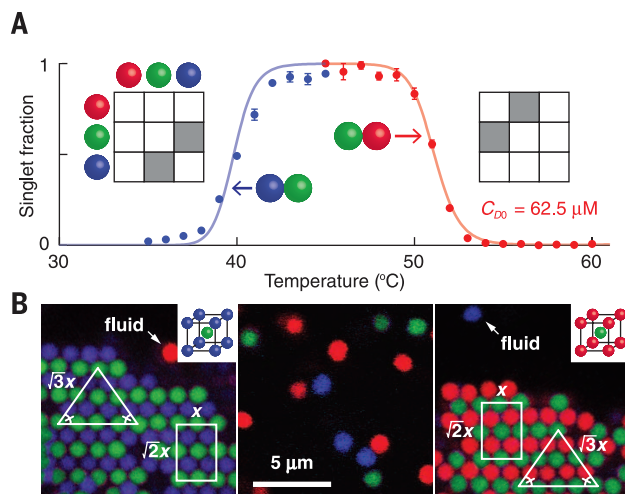


Fig. 4. The zero- and two-displacement reaction schemes are combined to program a pathway between two colloidal crystals. (A) Strand displacement yields a temperature-dependent specificity matrix defining favorable (gray) and unfavorable (white) interactions in a ternary suspension. Measured pair interactions (symbols) in this experimental system agree quantitatively with our model calculations (curves). Error bars denote SD of three measurements. (B) Confocal fluorescence experiments (25) show CsCl binary crystals of species 2 (green) and 3 (blue) in coexistence with a fluid of species 1 (red) at low temperature (left), and CsCl crystals of species 1 (red) and 2 (green) in coexistence with a fluid of species 3 (blue) at high temperature (right), separated by a homogeneous fluid phase of all three species at intermediate temperature (middle), as predicted. The two crystals have the same symmetry, as determined by the lattice distance $x = [4/\sqrt{3}]D$ in the $\{110\}$ plane, but different compositions; D is the particle diameter. Hybridization free energies are shown in table S6.

incorporation of DNA-based logic gates, cascaded circuits, or catalytic amplifiers (19) could make it possible to program nonequilibrium self-assembly pathways in colloidal matter.

REFERENCES AND NOTES

1. D. Frenkel, *Science* **296**, 65–66 (2002).
2. C. A. Mirkin, R. L. Letsinger, R. C. Mucic, J. J. Storhoff, *Nature* **382**, 607–609 (1996).
3. A. P. Alivisatos *et al.*, *Nature* **382**, 609–611 (1996).
4. R. J. Macfarlane, M. N. O'Brien, S. H. Petrosko, C. A. Mirkin, *Angew. Chem. Int. Ed.* **52**, 5688–5698 (2013).
5. R. J. Macfarlane *et al.*, *Science* **334**, 204–208 (2011).
6. P. L. Biancianiello, A. J. Kim, J. C. Crocker, *Phys. Rev. Lett.* **94**, 058302 (2005).
7. W. B. Rogers, J. C. Crocker, *Proc. Natl. Acad. Sci. U.S.A.* **108**, 15687–15692 (2011).
8. P. Varilly, S. Angioletti-Uberti, B. M. Mognetti, D. Frenkel, *J. Chem. Phys.* **137**, 094108 (2012).
9. J. SantaLucia Jr., *Proc. Natl. Acad. Sci. U.S.A.* **95**, 1460–1465 (1998).
10. D. Nykypanchuk, M. M. Maye, D. van der Lielie, O. Gang, *Nature* **451**, 549–552 (2008).
11. S. Y. Park *et al.*, *Nature* **451**, 553–556 (2008).
12. R. J. Macfarlane, M. R. Jones, B. Lee, E. Auyeung, C. A. Mirkin, *Science* **341**, 1222–1225 (2013).
13. M. T. Casey *et al.*, *Nat. Commun.* **3**, 1209 (2012).
14. J. D. Halverson, A. V. Tkachenko, *Phys. Rev. E* **87**, 062310 (2013).
15. Z. Zeravcic, V. N. Manoharan, M. P. Brenner, *Proc. Natl. Acad. Sci. U.S.A.* **111**, 15918–15923 (2014).
16. R. Dreyfus *et al.*, *Phys. Rev. Lett.* **102**, 048301 (2009).
17. L. Di Michele, E. Eiser, *Phys. Chem. Chem. Phys.* **15**, 3115–3129 (2013).
18. B. Yurke, A. J. Turberfield, A. P. Mills Jr., F. C. Simmel, J. L. Neumann, *Nature* **406**, 605–608 (2000).
19. D. Y. Zhang, G. Seelig, *Nat. Chem.* **3**, 103–113 (2011).
20. C. K. Tison, V. T. Milam, *Langmuir* **23**, 9728–9736 (2007).
21. M. M. Maye, M. T. Kumara, D. Nykypanchuk, W. B. Sherman, O. Gang, *Nat. Nanotechnol.* **5**, 116–120 (2010).
22. J. T. McGinley, I. Jenkins, T. Sinno, J. C. Crocker, *Soft Matter* **9**, 9119 (2013).
23. B. A. Baker, G. Mahmoudabadi, V. T. Milam, *Soft Matter* **9**, 11160 (2013).
24. W. B. Rogers, J. C. Crocker, *Proc. Natl. Acad. Sci. U.S.A.* **109**, E380 (2012).
25. See supplementary materials on Science Online.
26. T. I. Li, R. Sknepnek, M. Olvera de la Cruz, *J. Am. Chem. Soc.* **135**, 8535–8541 (2013).
27. R. Scarlett, M. Ung, J. Crocker, T. Sinno, *Soft Matter* **7**, 1912 (2011).
28. S. Angioletti-Uberti, B. M. Mognetti, D. Frenkel, *Nat. Mater.* **11**, 518–522 (2012).
29. B. Mognetti, M. Leunissen, D. Frenkel, *Soft Matter* **8**, 2213 (2012).
30. S. Roldán-Vargas, F. Smallegange, W. Kob, F. Sciortino, *Sci. Rep.* **3**, 2451 (2013).
31. J. King, S. Casjens, *Nature* **251**, 112–119 (1974).
32. J. N. Zadeh *et al.*, *J. Comput. Chem.* **32**, 170–173 (2011).

ACKNOWLEDGMENTS

We thank S. Magkiriadou, J. Collins, Z. Zeravcic, and M. Brenner for helpful discussions. Supported by the Harvard MRSEC through NSF grant DMR-0820484, NSF grant DMR-1435964, and an Alfred P. Sloan Research Fellowship. See the supplementary materials for additional data.

SUPPLEMENTARY MATERIALS

www.sciencemag.org/content/347/6222/639/suppl/DC1
Materials and Methods
Figs. S1 to S3
Tables S1 to S6
References (33–40)

7 August 2014; accepted 29 December 2014
10.1126/science.1259762

CARBON RADICALS

Direct observation and kinetics of a hydroperoxyalkyl radical (QOOH)

John D. Savee,* Ewa Papajak,* Brandon Rotavera, Haifeng Huang, Arkke J. Eskola, Oliver Welz,† Leonid Sheps, Craig A. Taatjes, Judit Zádor, David L. Osborn‡

Oxidation of organic compounds in combustion and in Earth's troposphere is mediated by reactive species formed by the addition of molecular oxygen (O_2) to organic radicals. Among the most crucial and elusive of these intermediates are hydroperoxyalkyl radicals, often denoted "QOOH." These species and their reactions with O_2 are responsible for the radical chain branching that sustains autoignition and are implicated in tropospheric autoxidation that can form low-volatility, highly oxygenated organic aerosol precursors. We report direct observation and kinetics measurements of a QOOH intermediate in the oxidation of 1,3-cycloheptadiene, a molecule that offers insight into both resonance-stabilized and nonstabilized radical intermediates. The results establish that resonance stabilization dramatically changes QOOH reactivity and, hence, that oxidation of unsaturated organics can produce exceptionally long-lived QOOH intermediates.

Oxidation of organic compounds in such disparate processes as secondary organic aerosol (SOA) formation in Earth's troposphere (1–3) and fuel autoignition in internal combustion engines (4) is governed by a surprisingly similar set of reactive intermediates. At the heart of low-temperature oxidation are chain reactions initiated by peroxy radicals, ROO (4, 5). These oxygen-centered radicals are formed when O_2 adds to an organic radical, R, initially formed

by either hydrogen abstraction from RH or addition of radicals (primarily OH) to π bonds between carbon atoms. It is well established that isomerization of ROO to a carbon-centered hydroperoxyalkyl radical (typically denoted as QOOH) can occur via intramolecular hydrogen abstraction, and in many cases this isomerization step profoundly influences the rate and effect of the oxidation reaction (4, 6–8).

Unimolecular decomposition of QOOH can produce a reactive OH radical and therefore plays an important role in radical chain propagation. More important, reaction of QOOH with O_2 can form OOQOOH intermediates that may subsequently decompose, yielding two OH radicals. This mechanism is regarded as the most important radical

chain-branching step in hydrocarbon oxidation below ~ 900 K (4). In combustion, understanding low-temperature chain branching is critical for improving efficiency through new engine designs in which ignition is controlled by fuel oxidation chemistry (autoignition) (9). In the tropospheric context, recent studies suggest that facile isomerization of ROO to QOOH in the oxidation of isoprene (2, 10–12) and other biogenic hydrocarbons (13–15) may participate both in the generation of low-volatility SOA precursors (1, 8, 16) and in HO_x regeneration over remote (low- NO_x) areas (11, 17–20).

Despite this awareness of the importance of QOOH intermediates, they have eluded direct experimental detection. With one exception (21) studies of QOOH reactivity rely on measurements that necessarily involve complex assumptions about the reaction mechanism. Routine theoretical calculations of QOOH + O_2 kinetics are hindered by the large size of these systems and the absence of a saddle point separating QOOH + O_2 from OOQOOH, necessitating extensive and computationally demanding sampling of the potential energy surface (PES). Theoretical predictions of QOOH + O_2 rate coefficients are thus scarce (21–24), and direct experimental measurements combined with theory and modeling are critical for a detailed understanding of this class of chemical reactions.

The PESs for hydrocarbon oxidation reactions illustrate why direct observation of QOOH is fundamentally difficult. For reactions governing alkane oxidation, exemplified by the 2-butyl + O_2 reaction shown in Fig. 1 (red path), QOOH intermediates generally lie higher in energy than ROO, with equilibrium heavily favoring the latter (25). Here, barriers to unimolecular decomposition of QOOH generally lie at or even below

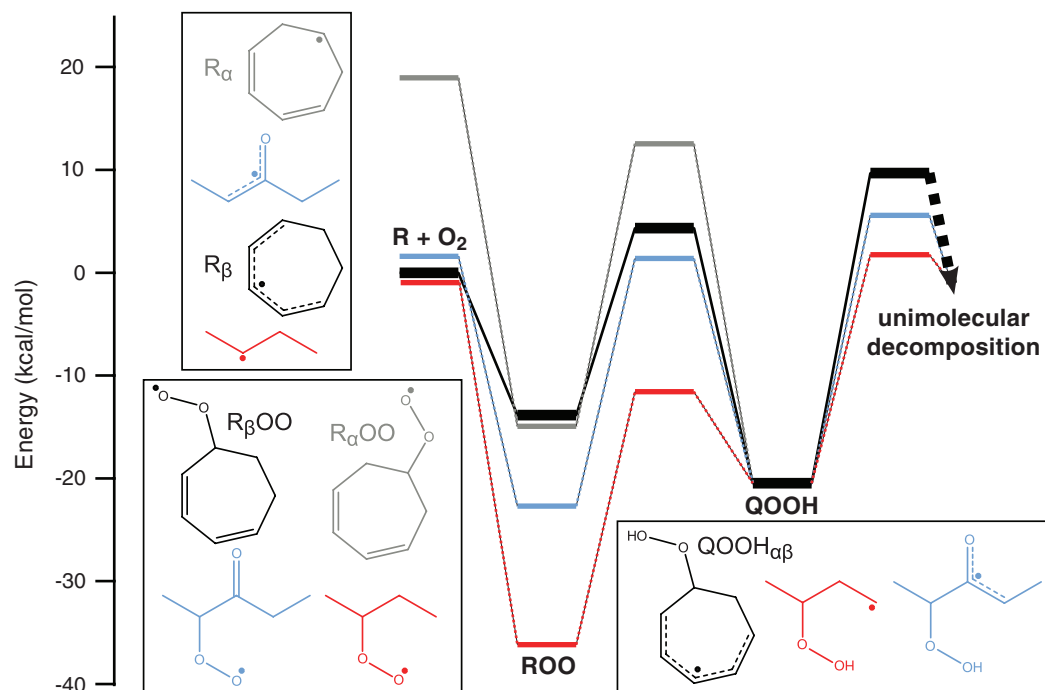


Fig. 1. Energy landscape for QOOH formation. Computed 0 K stationary point energies relevant to the production of QOOH from $R + O_2$ for $R = 2$ -butyl (red, derived from n -butane) (25), 3-oxopent-2-yl (blue, derived from 3-pentanone) (27), and 3,5-cycloheptadienyl (gray, R_α) and 2,4-cycloheptadienyl (black, R_β) (both derived from c -hpd and calculated in the present work). The different PESs are offset to match at the energy of QOOH. For clarity, slight barriers that may exist in $R + O_2$ entrance channels are not shown.

Combustion Research Facility, Mail Stop 9055, Sandia National Laboratories, Livermore, CA 94551-0969, USA. *These authors contributed equally to this work. †Present address: Institute for Combustion and Gas Dynamics, University of Duisburg-Essen, Duisburg, Germany. ‡Corresponding author. E-mail: dlosbor@sandia.gov

the reactant ($R + O_2$) energy. At atmospheric conditions (i.e., 300 K and 1 atm), much of the flux from $R + O_2$ is stabilized in the deep ROO well. In the low-temperature oxidation regime in combustion (i.e., 500 to 900 K), isomerization of ROO becomes rapid, resulting in substantial flux through QOOH. However, rapid decomposition, isomerization, and reaction with O_2 typically remove QOOH faster than it is formed.

Molecular structure can substantially affect QOOH reactivity. In particular, pathways in which R and/or QOOH exhibit resonance stabilization are common in oxidation of carbonyl-containing molecules and unsaturated hydrocarbons (8, 11, 26). For example, for 3-pentanone, a model system for autoxidation in the troposphere (8) and a potential biofuel (27), vinoxylic resonance stabilization in R has two significant effects on the $R + O_2$ PES (Fig. 1, blue path) when compared with alkyl + O_2 systems. First, resonance stabilization in R results in a smaller well depth for ROO, which cannot be resonance stabilized. Second, resonance stabilization of QOOH makes it nearly isoenergetic with ROO and increases barrier heights for unimolecular decomposition.

Here, we report direct detection of a resonance-stabilized QOOH intermediate formed during oxidation of the cyclic unsaturated hydrocarbon 1,3-cycloheptadiene ($c\text{-C}_7\text{H}_{10}$, $c\text{-hpd}$). As shown in Fig. 2, abstraction of one of the allylic (α) or allylic (β) H atoms from $c\text{-hpd}$ leads to two starting points on the $R + O_2$ ($c\text{-C}_7\text{H}_9 + O_2$) PES: the non-resonance stabilized R_α or the doubly allylic resonance-stabilized R_β radicals. Although numerous pathways are possible from these two entry points [figs. S14 and S15], electronic structure calculations suggest that the kinetically most favored pathways from both entrance channels lead to the same doubly allylic, resonance-stabilized QOOH intermediate (2-hydroperoxy-4,6-cycloheptadienyl, $QOOH_{\alpha\beta}$), as shown in Fig. 1 (black and gray paths). The double resonance stabilization of $QOOH_{\alpha\beta}$ lowers its energy below that of $R_\alpha\text{OO}$ and $R_\beta\text{OO}$. Our experiments produce both R_α and R_β , enabling investigation of both nonstabilized and resonance-stabilized R in this system.

We characterized $QOOH_{\alpha\beta}$ spectroscopically and performed direct kinetics measurements of its reaction with O_2 at 400 K and 10 Torr using photoionization mass spectrometry with synchrotron-generated tunable vacuum ultraviolet ionizing radiation. This method, described in the supplementary materials (SM), provides simultaneous kinetic and spectroscopic identification of multiple species in a reacting gas mixture. The experiments are complemented by kinetic modeling using quantum chemical calculations and time-dependent master equation rate coefficient calculations. In experiments, R_α and R_β were generated in roughly similar yields, based on predictions from structure-activity relationships [see (28) and the SM], via abstraction of H atoms from $c\text{-hpd}$ by Cl radicals. The reactions are initiated by pulsed 351-nm laser photolysis of a gas mixture containing $c\text{-hpd}$, Cl_2 , varying amounts of O_2 (in sufficient excess to ensure pseudo-first-order

conditions), and He as a buffer gas. In the presence of O_2 , we observed a transient reaction product at mass-to-charge ratio (m/z) = 125.06, corresponding to the sum formula $C_7H_9O_2$, consistent with ROO and/or QOOH (Fig. 3 inset and SM).

Different $C_7H_9O_2$ isomers (e.g., ROO and QOOH) could be identified by their characteristic photoionization spectra. A photoionization spectrum of $C_7H_9O_2$ (Fig. 3) shows a clear onset near 7.2 eV. This value is consistent with the calculated adiabatic ionization energy (AIE) of $QOOH_{\alpha\beta}$ (7.21 eV) but not with the calculated AIEs for the $R_\alpha\text{OO}$ and $R_\beta\text{OO}$ isomers (8.70 and 8.78 eV, respectively). Photoionization spectra obtained at a variety of $[O_2]$, temperatures, and time intervals after photolysis have identical shapes in the 7.1- to 8.5-eV range, evidence that signal in this spectral region arises solely from $QOOH_{\alpha\beta}$ (SM). The

scaled photoionization spectrum for $C_7H_9O_2$ at a late reaction time (Fig. 3) shows increased ion signal above ~8.5 eV, consistent with contributions from ROO species, which are less reactive than QOOH and therefore persist to longer times. Other $C_7H_9O_2$ isomers exhibit considerable barriers to their formation or have AIEs inconsistent with the observed $C_7H_9O_2$ signal onset. Quantum chemical calculations suggest that contributions from dissociative ionization of likely $QOOH_{\alpha\beta} + O_2$ products can also be excluded.

We also probed the time dependence of $QOOH_{\alpha\beta}$ as a function of oxygen concentration ($[O_2] = 1.9 \times 10^{16}$ to $1.5 \times 10^{17} \text{ cm}^{-3}$) at a photoionization energy of 8.3 eV. Time-dependent $QOOH_{\alpha\beta}$ signals (Fig. 4A and fig. S17) are well fit by a double exponential kinetic model, yielding time constants for both

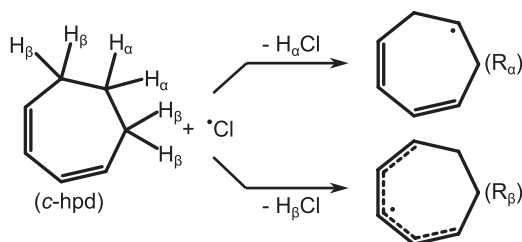


Fig. 2. Initial $c\text{-C}_7\text{H}_9$ radicals (R_α , R_β) formed by H-abstraction from $c\text{-hpd}$.

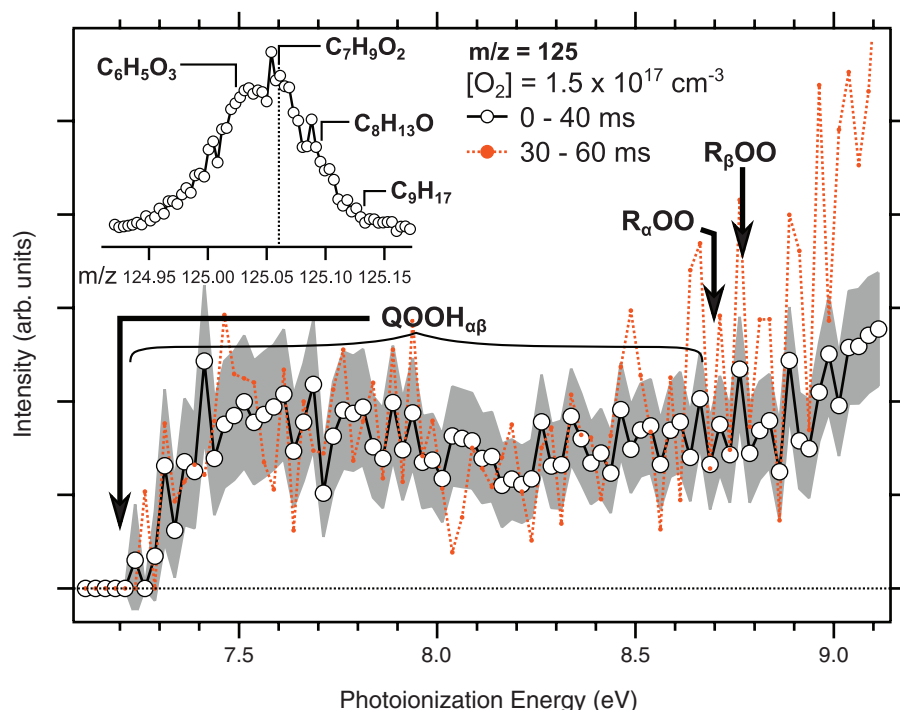


Fig. 3. Mass and photoionization spectra of $C_7H_9O_2$. The inset shows a $c\text{-hpd}$ oxidation mass spectrum near $m/z = 125$, indicating the sum formula $C_7H_9O_2$. The main figure presents superimposed photoionization spectra for $C_7H_9O_2$ over two different time intervals, with 2-SD uncertainties derived from Poisson counting statistics for the 0- to 40-ms interval shown in gray. Above 8.5 eV, the spectrum depends on its observation time interval, suggesting the presence of at least two isomers consistent with $QOOH_{\alpha\beta}$ (AIE = 7.21 eV) and $R_\alpha\text{OO}$ (8.70 eV) and/or $R_\beta\text{OO}$ (8.78 eV). Calculated AIEs are marked by arrows.

the rise (τ_{rise}) and decay (τ_{decay}) that decrease with increasing $[\text{O}_2]$. Oxygen-centered ROO radicals are not expected to react with O_2 , and the presence of two time constants that depend on $[\text{O}_2]$ provides further evidence that $\text{C}_7\text{H}_9\text{O}_2$ signal probed at 8.3 eV arises from the carbon-centered $\text{QOOH}_{\alpha\beta}$ radical. The observed linear dependence of $1/\tau_{\text{rise}}$ and $1/\tau_{\text{decay}}$ on $[\text{O}_2]$ (Fig. 4B) yields second-order rate coefficients at 10 Torr and 400 K of $k_{\text{rise}} = (2.9 \pm 1.0) \times 10^{-15} \text{ cm}^3 \text{ s}^{-1}$ and $k_{\text{decay}} = (3.2 \pm 0.5) \times 10^{-16} \text{ cm}^3 \text{ s}^{-1}$ (uncertainties 2 SD precision). The y intercepts likely result from reactions with Cl_2 molecules and do not affect rate coefficient determinations.

However, detecting the intermediate species in sequential kinetic schemes is insufficient to assign the measured time constants (τ_{rise} or τ_{decay}) to formation and depletion. To this end, in separate experiments at a radical concentration lower by a factor of 50, designed to minimize self- and cross-reactions of R_α and R_β , we measured loss of $c\text{-C}_7\text{H}_9$ as a function of $[\text{O}_2]$ and independently extracted the rate coefficient for reaction of R_β with O_2 , $k(\text{R}_\beta + \text{O}_2) = (3.3 \pm 0.5) \times 10^{-16} \text{ cm}^3 \text{ s}^{-1}$. The equivalence of this value with k_{decay} obtained from the $\text{QOOH}_{\alpha\beta}$ time profile is experimental evidence that k_{decay} is the rate coefficient for $\text{QOOH}_{\alpha\beta}$ formation (predominantly via $\text{R}_\beta + \text{O}_2$ reactions); therefore, k_{rise} describes $\text{QOOH}_{\alpha\beta}$ consumption via the reaction $\text{QOOH}_{\alpha\beta} + \text{O}_2 \rightarrow \text{products}$.

Examining the underlying $\text{C}_7\text{H}_9\text{O}_2$ PES and comparing experimental results to a kinetic model

of this reaction system (SM) confirms this interpretation and affords additional mechanistic details. This model combines master-equation calculated rate coefficients of reactions on the $\text{C}_7\text{H}_9\text{O}_2$ PES with kinetic parameters for $\text{R} + \text{R}$, $\text{RH} + \text{Cl}$, $\text{R} + \text{Cl}_2$, and others taken from literature measurements of analogous reactions. Because the experiment provides time profiles and photoionization spectra for many species, comparison with the detailed model is a rigorous test of the experimental reaction system. Although we observe several $[\text{O}_2]$ -dependent signals that likely reflect products formed from $\text{QOOH}_{\alpha\beta}$ consumption, they cannot be definitively assigned.

The $\text{R} + \text{O}_2$ PES shown in Fig. 1 and master equation rate coefficients reported in table S3 provide the necessary framework for understanding the observed $\text{QOOH}_{\alpha\beta}$ kinetics. Although the $\text{R}_\alpha + \text{O}_2 \rightleftharpoons \text{R}_\alpha\text{OO}$ addition step is barrierless and the $\text{R}_\alpha\text{OO} \rightleftharpoons \text{QOOH}_{\alpha\beta}$ isomerization barrier is lower in energy than $\text{R}_\alpha + \text{O}_2$, kinetic modeling suggests that pathways from the more stable R_β radical are the major source of $\text{QOOH}_{\alpha\beta}$ production (see fig. S21). The R_αOO potential well is rather deep ($-33.9 \text{ kcal mol}^{-1}$ relative to $\text{R}_\alpha + \text{O}_2$) so that thermal equilibrium at 400 K strongly favors the stabilized R_αOO species ($[\text{R}_\alpha]/[\text{R}_\alpha\text{OO}] \sim 10^{-9}$ at $[\text{O}_2] \sim 10^{17} \text{ cm}^{-3}$ and 400 K) and effectively traps almost all R_α as R_αOO . The kinetic model (SM) predicts that $\text{R}_\alpha + \text{O}_2$ generates only 5% of all $\text{QOOH}_{\alpha\beta}$, with equal contributions from the chemically activated pathway $\text{R}_\alpha + \text{O}_2 \rightarrow \text{QOOH}_{\alpha\beta}$ (i.e., without stabilization in the R_αOO

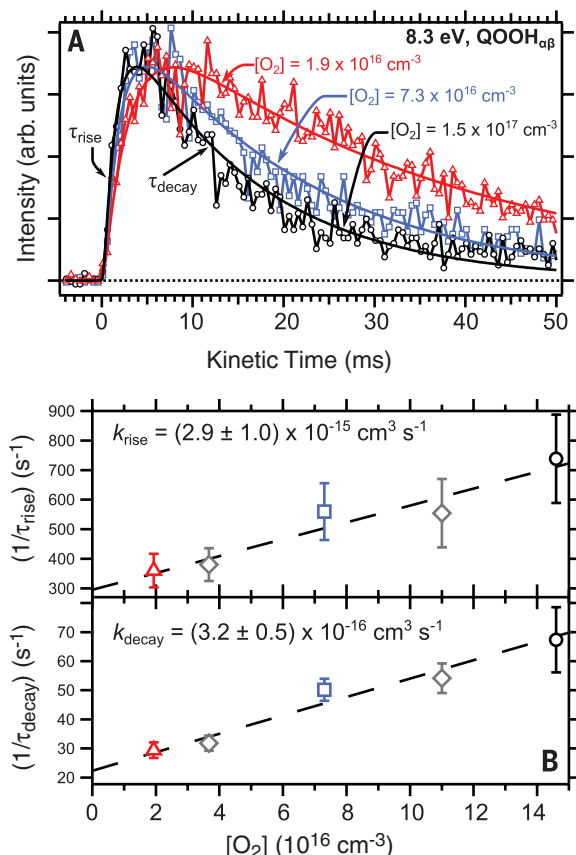
well) and from slow, tunneling-mediated isomerization of $\text{R}_\alpha\text{OO} \rightarrow \text{QOOH}_{\alpha\beta}$. Under our conditions, $\text{R}_\alpha + \text{O}_2 \rightarrow \text{R}_\alpha\text{OO}$ reaches equilibrium in $<1 \text{ ms}$ and does not affect measurement of the slower R_β reactions.

By contrast, a small barrier ($+1.4 \text{ kcal mol}^{-1}$, not shown in Fig. 1) separates the resonance-stabilized R_β radical from the shallow R_βOO well ($-13.9 \text{ kcal mol}^{-1}$ relative to $\text{R}_\beta + \text{O}_2$), and equilibrium favors $\text{R}_\beta + \text{O}_2$ under our conditions ($[\text{R}_\beta]/[\text{R}_\beta\text{OO}] \sim 10^2$ at $[\text{O}_2] \sim 10^{17} \text{ cm}^{-3}$ and 400 K). Moreover, the $\text{R}_\beta\text{OO} \rightleftharpoons \text{QOOH}_{\alpha\beta}$ isomerization barrier is higher in energy than $\text{R}_\beta + \text{O}_2$. Nevertheless, the model predicts that R_β pathways account for 95% of total $\text{QOOH}_{\alpha\beta}$ formation, primarily through two tunneling-mediated processes: isomerization of R_βOO (66%) and chemically activated reaction directly from $\text{R}_\beta + \text{O}_2$ (29%). Based on master equation predictions for $\text{R}_\beta + \text{O}_2$ (table S3) and the large size of the $\text{QOOH}_{\alpha\beta} + \text{O}_2$ system, we anticipate that the present conditions (400 K and 10 Torr) probe kinetics near the high-pressure limit.

Only one direct experimental rate coefficient for any $\text{QOOH} + \text{O}_2$ reaction exists in the literature (21), along with a few calculated rate coefficients (21–24, 29), in all cases for saturated parent hydrocarbons. These rate coefficients are $\sim 10^{-11}$ to $\sim 10^{-12} \text{ cm}^3 \text{ s}^{-1}$ near 400 K and in the high pressure limit (21–23, 29), three to four orders of magnitude larger than the $(2.9 \pm 1.0) \times 10^{-15} \text{ cm}^3 \text{ s}^{-1}$ value determined here for $\text{QOOH}_{\alpha\beta} + \text{O}_2$. This dramatic reduction is likely due to the doubly allylic resonance stabilization of $\text{QOOH}_{\alpha\beta}$. Comparing $\text{R} + \text{O}_2$ rate coefficients for saturated hydrocarbon radicals to analogous systems where R has doubly allylic resonance stabilization (e.g., cyclohexyl versus 2,4-cyclohexadienyl and neopentyl versus 2,4-pentadienyl; see table S1) suggests that a decrease of $\sim 10^3$ in the rate coefficient for reaction with O_2 is reasonable. Resonance-stabilized QOOH intermediates will occur in many important systems, such as the oxidation of biogenically derived hydrocarbons [e.g., isoprene (11, 12) and α/β -pinene (13, 14)]. This small rate coefficient for reaction with O_2 implies a long lifetime of the resonance-stabilized $\text{QOOH}_{\alpha\beta}$, suggesting that QOOH photochemistry and bimolecular reactions with minor species such as HO_x and NO_x may need to be considered. In the general case, both R and QOOH are carbon-centered radicals, and it is often assumed that these species exhibit similar reactivity toward O_2 (30). However, we find that the rate coefficient for $\text{QOOH}_{\alpha\beta} + \text{O}_2$ is ~ 10 times as large as in the analogous $\text{R}_\beta + \text{O}_2$ reaction. This finding suggests reexamination of assumed equivalences between rate coefficients for $\text{R} + \text{O}_2$ and $\text{QOOH} + \text{O}_2$ reactions used in many organic oxidation models (31, 32).

In addition to a tunneling-mediated $\text{ROO} \rightarrow \text{QOOH}$ pathway (12), we have revealed a chemically activated mechanism as an important source of QOOH production in $c\text{-hpd}$ oxidation with resonance-stabilized R and QOOH species. Although chemical activation is more prominent at low pressure, there is evidence for this type of

Fig. 4. QOOH kinetics. (A) Time dependence of $m/z = 125.06$ signal obtained at 8.3 eV (i.e., probing only $\text{QOOH}_{\alpha\beta}$) at several $[\text{O}_2]$ (open symbols) and the corresponding double exponential fits (solid lines). (B) Second-order plots showing the linearity of $1/\tau_{\text{rise}}$ and $1/\tau_{\text{decay}}$ versus $[\text{O}_2]$ (open symbols) and accompanying linear fits [symbols and colors correspond to (A)]. Their slopes determine k_{rise} and k_{decay} , respectively, which we assign as rate coefficients for $\text{QOOH}_{\alpha\beta} + \text{O}_2 \rightarrow \text{products}$ and $\text{R}_\beta + \text{O}_2 \rightarrow \text{QOOH}_{\alpha\beta}$ reactions, respectively.



mechanism in the troposphere (33). Current tropospheric models underpredict HO_x regeneration by isoprene oxidation in pristine environments (18), and a recently proposed mechanism suggests that ROO ⇌ QOOH isomerization pathways are a substantial source of this missing HO_x (11, 12). Like the *c*-hpd system investigated here, oxidation of isoprene proceeds through resonance-stabilized initial radicals (isoprene-OH adducts) that undergo peroxy chemistry, with the lowest-energy pathways leading to resonance-stabilized QOOH intermediates. The direct detection and kinetic determination provided here give experimental benchmarks for reactivity of resonance-stabilized QOOH and suggest that such radicals, including those proposed in formation of SOA precursors (8), may be relatively long-lived in the troposphere and in combustion systems.

REFERENCES AND NOTES

- M. Ehn *et al.*, *Nature* **506**, 476–479 (2014).
- F. Paulot *et al.*, *Science* **325**, 730–733 (2009).
- M. Claeys *et al.*, *Science* **303**, 1173–1176 (2004).
- J. Zádor, C. A. Taatjes, R. X. Fernandes, *Prog. Energy Combust. Sci.* **37**, 371–421 (2011).
- J. J. Orlando, G. S. Tyndall, *Chem. Soc. Rev.* **41**, 6294–6317 (2012).
- O. Perrin, A. Heiss, K. Sahetchian, L. Kerhoas, J. Einhorn, *Int. J. Chem. Kinet.* **30**, 875–887 (1998).
- L. Vereecken, J. S. Francisco, *Chem. Soc. Rev.* **41**, 6259–6293 (2012).
- J. D. Crounse, L. B. Nielsen, S. Jørgensen, H. G. Kjaergaard, P. O. Wennberg, *J. Phys. Chem. Lett.* **4**, 3513–3520 (2013).
- J. E. Dec, *Proc. Combust. Inst.* **32**, 2727–2742 (2009).
- J. D. Crounse, F. Paulot, H. G. Kjaergaard, P. O. Wennberg, *Phys. Chem. Chem. Phys.* **13**, 13607–13613 (2011).
- J. Peeters, T. L. Nguyen, L. Vereecken, *Phys. Chem. Chem. Phys.* **11**, 5935–5939 (2009).
- J. Peeters, J. F. Müller, T. Stavrou, V. S. Nguyen, *J. Phys. Chem. A* **118**, 8625–8643 (2014).
- L. Vereecken, J. F. Müller, J. Peeters, *Phys. Chem. Chem. Phys.* **9**, 5241–5248 (2007).
- L. Vereecken, J. Peeters, *Phys. Chem. Chem. Phys.* **14**, 3802–3815 (2012).
- R. Asatryan, G. da Silva, J. W. Bozzelli, *J. Phys. Chem. A* **114**, 8302–8311 (2010).
- A. J. Kalafut-Pettibone, J. P. Klems, D. R. Burgess Jr., W. S. McGivern, *J. Phys. Chem. A* **117**, 14141–14150 (2013).
- P. Tunved *et al.*, *Science* **312**, 261–263 (2006).
- J. Lelieveld *et al.*, *Nature* **452**, 737–740 (2008).
- P. M. Edwards *et al.*, *Atmos. Chem. Phys.* **13**, 9497–9514 (2013).
- A. T. Archibald *et al.*, *Geophys. Res. Lett.* **38**, L05804 (2011).
- J. Zádor *et al.*, *Phys. Chem. Chem. Phys.* **15**, 10753–10760 (2013).
- C. F. Goldsmith, W. H. Green, S. J. Klippenstein, *J. Phys. Chem. A* **116**, 3325–3346 (2012).
- A. Andersen, E. A. Carter, *Mol. Phys.* **106**, 367–396 (2008).
- R. Asatryan, J. W. Bozzelli, *J. Phys. Chem. A* **114**, 7693–7708 (2010).
- J. D. DeSain, C. A. Taatjes, J. A. Miller, S. J. Klippenstein, D. K. Hahn, *Faraday Discuss.* **119**, 101–120 (2001).
- F. Zhang, T. S. Dibble, *J. Phys. Chem. A* **115**, 655–663 (2011).
- A. M. Scheer, O. Welz, J. Zádor, D. L. Osborn, C. A. Taatjes, *Phys. Chem. Chem. Phys.* **16**, 13027–13040 (2014).
- M. J. Ezell, W. Wang, A. A. Ezell, G. Soskin, B. J. Finlayson-Pitts, *Phys. Chem. Chem. Phys.* **4**, 5813–5820 (2002).
- R. X. Fernandes, J. Zádor, L. E. Jusinski, J. A. Miller, C. A. Taatjes, *Phys. Chem. Chem. Phys.* **11**, 1320–1327 (2009).
- B. Husson *et al.*, *Combust. Flame* **159**, 1399–1416 (2012).
- F. Battin-Leclerc, *Prog. Energy Combust. Sci.* **34**, 440–498 (2008).
- O. Herbinet, W. J. Pitz, C. K. Westbrook, *Combust. Flame* **157**, 893–908 (2010).
- D. R. Glowacki *et al.*, *Science* **337**, 1066–1069 (2012).

ACKNOWLEDGMENTS

Additional details of the experiments, calculations, and kinetic model are available in the supplementary materials. We thank H. Johnsen and the staff at the Chemical Dynamics Beamline of the Advanced Light Source (ALS) for technical support. This material is based on work supported by the U.S. Department of Energy (DOE), Office of Science, Office of Basic Energy Sciences (BES). Sandia is a multiprogram laboratory operated by Sandia Corporation, a Lockheed Martin Company, for the National Nuclear Security Administration under contract DE-AC04-94AL85000. This research used resources of the ALS, which is a DOE Office of Science User Facility. The ALS is supported by the Director, Office of Science, BES/DOE, under contract DE-AC02-05CH11231 between Lawrence Berkeley National Laboratory and the DOE.

SUPPLEMENTARY MATERIALS

www.sciencemag.org/content/347/6222/643/suppl/DC1
Materials and Methods
Supplementary Text
Figs. S1 to S21
Tables S1 to S4
References (34–51)

23 October 2014; accepted 8 January 2015
10.1126/science.aaa1495

NONCOVALENT ASSEMBLY

A rational strategy for the realization of chain-growth supramolecular polymerization

Jiheong Kang,^{1,2} Daigo Miyajima,^{1*} Tadashi Mori,³ Yoshihisa Inoue,³ Yoshimitsu Itoh,² Takuzo Aida^{1,2*}

Over the past decade, major progress in supramolecular polymerization has had a substantial effect on the design of functional soft materials. However, despite recent advances, most studies are still based on a preconceived notion that supramolecular polymerization follows a step-growth mechanism, which precludes control over chain length, sequence, and stereochemical structure. Here we report the realization of chain-growth polymerization by designing metastable monomers with a shape-promoted intramolecular hydrogen-bonding network. The monomers are conformationally restricted from spontaneous polymerization at ambient temperatures but begin to polymerize with characteristics typical of a living mechanism upon mixing with tailored initiators. The chain growth occurs stereoselectively and therefore enables optical resolution of a racemic monomer.

Since Staudinger experimentally proved the existence of covalent macromolecular chains in the late 1920s, after a long debate on the controversial concept of colloidal aggregates (1), numerous essential achievements in the field of polymer science have precipitated major innovations in everyday life (2–4). In the late 1980s, alongside substantial progress in the field of non-covalent chemistry (5, 6), research groups led by Lehn (7–9) and Meijer (10, 11) breathed life into

the controversial concept of colloidal aggregates (1). These authors demonstrated that linear aggregates (i.e., supramolecular polymers) of small molecules that are tailored by complementary hydrogen-bonding (H-bonding) interactions are sufficiently stable, even in dilute solution, to behave like covalent linear polymers under appropriate conditions (10, 12). With a view to reduce the dynamic nature of supramolecular polymerization, Wang *et al.* reported in 2007 a strategy of

using crystallizable monomers upon self-assembly and successfully obtained well-defined block copolymers (13). This achievement, together with some related works reported later (14–16), indicated new possibilities of supramolecular polymerization in the context of precision macromolecular engineering. However, because of the preconceived notion that supramolecular polymerization follows a step-growth mechanism (Fig. 1A, upper), the prospect of realizing noncovalent chain-growth polymerization has received little attention until recently. Encouraging reports to this end used thermally cleaved supramolecular polymers as seeds for noncovalently polymerizing the associated monomers, where elongation of polymer chains with incubation time was observed by atomic force microscopy (AFM) and/or transmission electron microscopy (13, 14, 16). Nevertheless, even at this stage, no strategic rationale has been proposed for achieving chain-growth supramolecular polymerization (Fig. 1A, lower). In contrast with step-growth polymerization, chain-growth polymerization uses monomers that do not polymerize spontaneously without initiators (11, 17). In this context, we noticed that a particular compound in our separate work (18) serves as a metastable monomer that is

¹RIKEN Center for Emergent Matter Science, 2-1 Hirosawa, Wako, Saitama 351-0198, Japan. ²Department of Chemistry and Biotechnology, School of Engineering, The University of Tokyo, 7-3-1 Hongo, Bunkyo-ku, Tokyo 113-8656, Japan. ³Department of Applied Chemistry, Graduate School of Engineering, Osaka University, 2-1 Yamada-oka, Suita, Osaka 565-0871, Japan.

*Corresponding author. E-mail: daigo.miyajima@riken.jp (D.M.); aida@macro.t.u-tokyo.ac.jp (T.A.)

temporarily disabled for spontaneous polymerization in the absence of initiators.

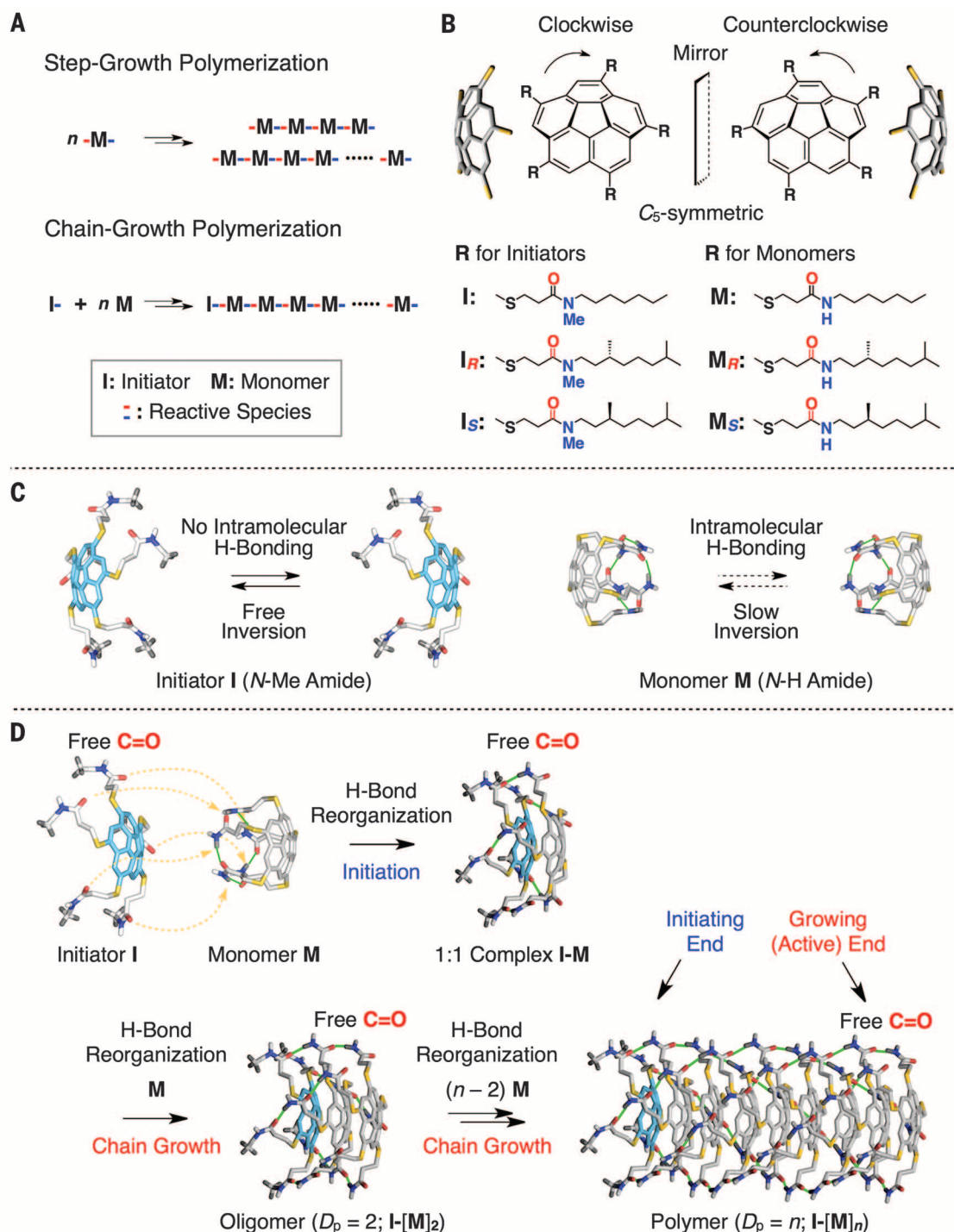
Here we report the realization of chain-growth supramolecular polymerization involving defined initiation and propagation steps. Figure 1B illustrates the metastable monomers and tail-

ored initiators used for the present study, all of which carry a corannulene core with five amide-appended thioalkyl side chains (18–20). Although these corannulene derivatives are chiral because of their C_5 -symmetric nonplanar bowl shape, bowl-to-bowl inversion, leading to racemization, can

occur thermally even at 25°C. Recently, we reported that compound **M** (Fig. 1B) adopts a cagelike closed conformation (Fig. 1C, right) in low-polarity media such as methylcyclohexane (MCHex), because the bowl-shaped core orients the side-chain amide units to facilitate their intramolecular

Fig. 1. A monomer-initiator system for supramolecular chain-growth polymerization.

(A) Schematic representations of step-growth (upper) and chain-growth (lower) polymerizations. In step-growth polymerization, propagation involves coupling of multiple combinations of monomers and oligomers of varying lengths. Chain-growth polymerization requires an initiator that reacts with a monomer to produce a dimer carrying a reactive terminus; subsequently, polymer chains grow exclusively by sequential monomer addition to these termini. The growth of a polymer occurs only at its reactive terminus with the monomer. (B) Chemical structures of C_5 -symmetric corannulene-based chiral initiators and monomers carrying amide-appended thioalkyl side chains and a schematic representation for the bowl-to-bowl corannulene inversion. The arc-shaped arrows represent tentative definitions of the clockwise and counterclockwise $H \rightarrow R$ substituent arrays along the corannulene periphery. (C) Schematic representations of the conformational and configurational aspects of the initiator and monomer families. The corannulene core of the monomer family adopts a cagelike closed conformation with a small activity for the bowl-to-bowl inversion due to an intramolecularly H-bonded amide network. By contrast, the initiator family adopts an open conformation with a large activity for the bowl-to-bowl inversion at the corannulene core because its side-chain amide groups are N-methylated and cannot form such an intramolecular, cyclic H-bonded network. (D) Schematic representation of the chain-growth supramolecular polymerization of monomer **M** initiated with **I**, where the chain growth is accompanied by the H-bond reorganization of **M**. The growing polymer carries an initiator unit at one end (the initiating end), whereas the other end [the growing (active) end] adopts a structure analogous to **I**, with free amide C=O groups. This structural feature prevents bimolecular coupling of the propagating ends.



H-bonding interactions (18). Consequently, unlike disk-shaped triphenylene analogs (17), monomer **M** does not self-assemble (polymerize) in solution. However, during the course of this study, we found that **M** spontaneously polymerizes into a one-dimensional polymeric assembly upon heating in MCHex. Unexpectedly, even without further heating, this polymer continued to grow when a fresh feed of **M** was provided.

From these observations, we hypothesized that **M** is metastable and temporarily restricted from spontaneously polymerizing but possesses the capacity to undergo chain-growth polymerization (Fig. 1A, lower). As highlighted in this paper, we discovered that compound **I** (Fig. 1B), an N-methylated derivative of **M**, can initiate the polymerization of **M** (Fig. 1D) in MCHex at 25°C. The polymerization proceeds with characteristics typical of a living process (17). Initiator **I** lacks the capacity for intramolecular H-bonding (Fig. 1C, left) and does not self-assemble but serves as a proton acceptor for H-bonding interactions.

As a typical example of the polymerization, 10 μ l of a solution **I** (1.0 mM in MCHex) were added

to 500 equivalents of **M** (5 ml of a 1.0 mM solution in MCHex), and the mixture was allowed to stand at 25°C for 6 hours, during which **M** gradually transformed into a supramolecular polymer with a small polydispersity index (PDI). As observed by dynamic light scattering (DLS), the average hydrodynamic diameter of the polymer increased continuously whenever a fresh feed of **M** was added to the system after a certain interval (Fig. 2A). Diffusion-ordered spectroscopy (DOSY) nuclear magnetic resonance (NMR) measurements in deuterated MCHex indicated that the diffusion coefficient (D) of the polymer decreases nonlinearly upon increment of the total monomer-to-initiator mole ratio ($[\mathbf{M}]_{\text{total}}/[\mathbf{I}]_0$) (Fig. 2B and fig. S10). According to a diffusion theory of polymers (21), a cube root of the molecular weight of a polymer is proportional to D^{-1} using **M** as a reference. As shown in Fig. 2B, the D_p values thus estimated are in good agreement with the ratios of $[\mathbf{M}]_{\text{total}}/[\mathbf{I}]_0$. Figure 2C exemplifies tapping-mode AFM images on silicon wafers of air-dried polymerization mixtures formed at $[\mathbf{M}]_0/[\mathbf{I}]_0 = 1000$ and 2000. Their height profiles (0.9 nm)

confirm that the polymer molecules thus visualized are unimolecularly dispersed. In accord with the results of DLS and DOSY NMR measurements, the polymer chains formed at $[\mathbf{M}]_0/[\mathbf{I}]_0 = 2000$ (Fig. 2C, bottom) are clearly longer than those at $[\mathbf{M}]_0/[\mathbf{I}]_0 = 1000$ (Fig. 2C, top). As shown by the histogram in Fig. 2D, the contour lengths of polymers formed at $[\mathbf{M}]_{\text{total}}/[\mathbf{I}]_0 = 250, 500, 1000$, and 2000 were successfully evaluated by measuring the lengths of 100 randomly selected polymer chains at individual $[\mathbf{M}]_{\text{total}}/[\mathbf{I}]_0$ ratios (fig. S11). We confirmed that their average chain lengths are proportional to the ratios of $[\mathbf{M}]_{\text{total}}/[\mathbf{I}]_0$ employed (Fig. 2D, inset). Because the overall noncovalent interaction, operative in a single polymer chain, is rather strong (see below), the polymerization can be traced by size-exclusion chromatography (SEC) on a polystyrene gel column under optimized conditions at 4°C using MCHex/CHCl₃ (1/1 v/v) as an eluent. Figure 2E shows that, as the $[\mathbf{M}]_{\text{total}}/[\mathbf{I}]_0$ ratio increased, the elution peak of the produced polymer, though exhibiting a little broadening, shifted stepwise toward a region of higher molecular

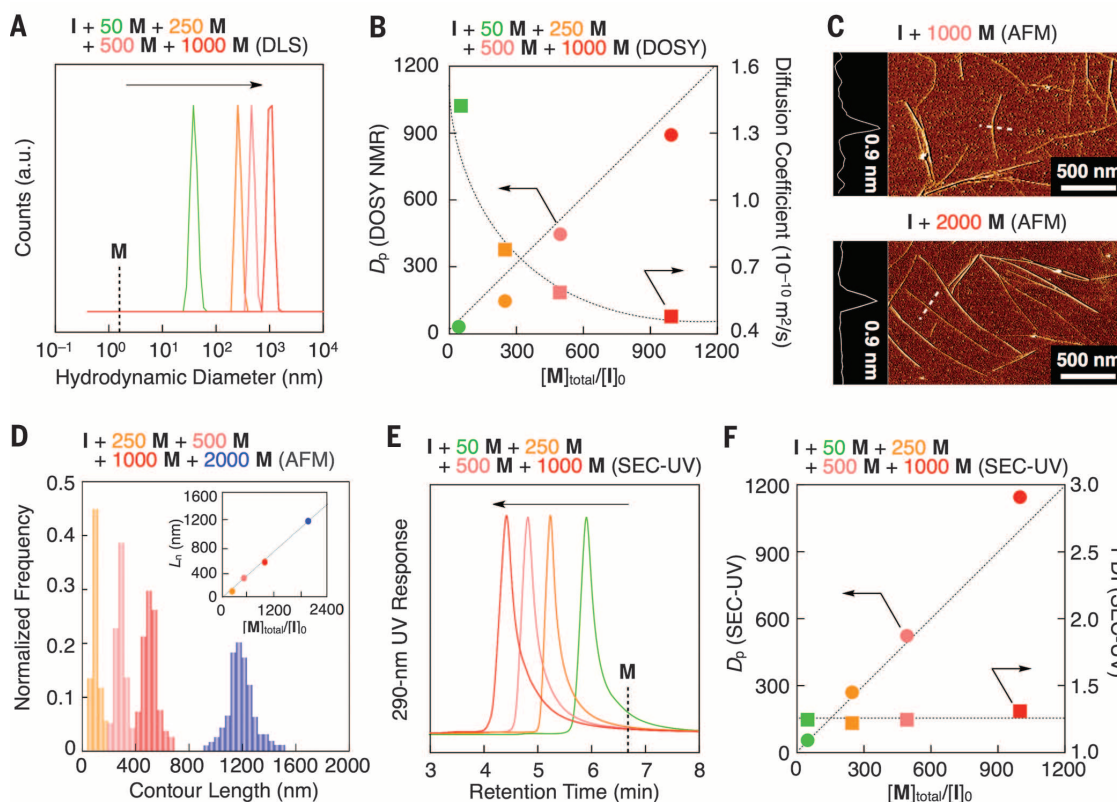


Fig. 2. Multistage chain-growth supramolecular polymerization of monomer **M with initiator **I** in MCHex at 25°C.** Reactions were conducted by stepwise addition of fresh feeds of **M**, after a certain interval, to a 10 μ l initiator solution ($[\mathbf{I}]_0 = 1.0$ mM) at varying $[\mathbf{M}]_{\text{total}}/[\mathbf{I}]_0$ ratios. (A) DLS profiles in MCHex at 25°C of polymers formed at $[\mathbf{M}]_{\text{total}}/[\mathbf{I}]_0 = 50$ (green), 250 (orange), 500 (pink), and 1000 (red). The vertical dashed line represents the peak-top position of **M**. a.u., arbitrary units. (B) Plots of the diffusion coefficients D of polymers formed at $[\mathbf{M}]_{\text{total}}/[\mathbf{I}]_0 = 50$ (green), 250 (orange), 500 (pink), and 1000 (red), evaluated with DOSY NMR in deuterated MCHex at 20°C, and their degrees of polymerization D_p theoretically calculated using

the D value of **M** as a reference. (C) Tapping-mode AFM images on a silicon substrate with height profiles of air-dried polymers formed at $[\mathbf{M}]_{\text{total}}/[\mathbf{I}]_0 = 1000$ and 2000. (D) AFM-based histogram of the counter lengths of randomly selected 100-polymer chains formed at $[\mathbf{M}]_{\text{total}}/[\mathbf{I}]_0 = 250$ (orange), 500 (pink), 1000 (red), and 2000 (blue). (Inset) Average polymer chain lengths (L_n). (E) SEC traces of polymers formed at $[\mathbf{M}]_{\text{total}}/[\mathbf{I}]_0 = 50$ (green), 250 (orange), 500 (pink), and 1000 (red), monitored using an UV detector at 290 nm. The vertical dashed line represents the peak-top position of **M**. (F) Plots of the D_p and PDI versus $[\mathbf{M}]_{\text{total}}/[\mathbf{I}]_0$, as estimated from the SEC-UV traces using polystyrene standards for calibration.

weight (22). The average D_p values of the polymers formed at individual stages, as estimated using polystyrene standards for calibration, scaled linearly over a wide range with $[M]_{\text{total}}/[I]_0$ (Fig. 2F, circles). Equally important, the PDI values of the polymers were all determined to lie

in a range of 1.2 to 1.3 (Fig. 2F, squares), which is much smaller than that of a polymer formed upon heating without initiator **I** (fig. S12).

We posit that the monomer units in the polymer chain are intermolecularly H-bonded at their side-chain amide groups. Infrared spectroscopy

(fig. S13) demonstrates that the polymerization is accompanied by a shift of an H-bonded amide C=O vibration from 1650 to 1642 cm^{-1} . Simultaneously, the amide NH groups that are H-bonded to C=O shifted from 3331 to 3326 cm^{-1} . Thus, the H-bonds formed intermolecularly in the polymer chain are more robust than those oriented intramolecularly in the monomer state. As expected from the non-self-assembling behavior of **I** (the N-methylated derivative of **M**) in MCHex, corannulene derivatives without H-bonding side-chain motifs hardly stack, even in the solid state (23). Considering also that the electronic absorption spectrum of the polymer is substantially the same as that of **M** (fig. S14), the van der Waals contributions, including a π -electronic interaction, between the constituent monomer units are rather weak in this solvent (11). MCHex is an excellent solvent for the supramolecular polymerization of **M**. In this low-polarity medium, the H-bonds in the polymer chain are stable at ambient temperatures and, even upon 10-fold dilution ($[M] = 0.1 \text{ mM}$), the polymer obtained upon initiation by **I** did not exhibit any substantial change in its SEC profile (fig. S15). However, when the MCHex solution was annealed at 100°C for 1 hour, the polymer underwent quick depolymerization. As expected, the heated mixture underwent repolymerization when it was allowed to cool to 25°C. In this case, particularly when the cooling rate was as small as 1.0°C min^{-1} , the elution profile of the resultant mixture in SEC became more complicated than that before the thermal treatment (fig. S16), indicating that the polymerization of **M** with **I** is driven kinetically and is pathway-dependent (16, 24). In sharp contrast, in polar media (including moderately polar CHCl_3 , in which H-bonding interactions are destabilized), the polymer, once formed in MCHex, dissociated within a few minutes, even without heating (fig. S17). Accordingly, **M** did not polymerize.

The extraordinary stability of the polymer in MCHex is essential for achieving the living character of polymerization. Equally important to consider is an end-capped structure of the polymer. As described, initiator **I** was derived from **M** by N-methylation of the side-chain amide groups (Fig. 1B). Owing to the initiation mechanism illustrated in Fig. 1D, the produced polymer should be end-capped with initiator **I** at the initiating end. This capped initiating end lacks the capacity for H-bonding interactions because the C=O groups at its N-methylated amide units are H-bonded with the amide NHs of its neighboring monomer unit. Hence, this capped end neither interacts with incoming **M** nor recombines with the other polymer terminus, although bimolecular recombination often occurs in conventional supramolecular polymerization and enlarges the PDI (22). To support the importance of this end-capped structure, we cleaved the polymer chain using sonication in MCHex to generate terminally uncapped, short polymer chains (fig. S18, A and B) and then allowed the resultant mixture to stand at 25°C. SEC showed that these short polymer chains recombined spontaneously (fig. S18C), whereas no

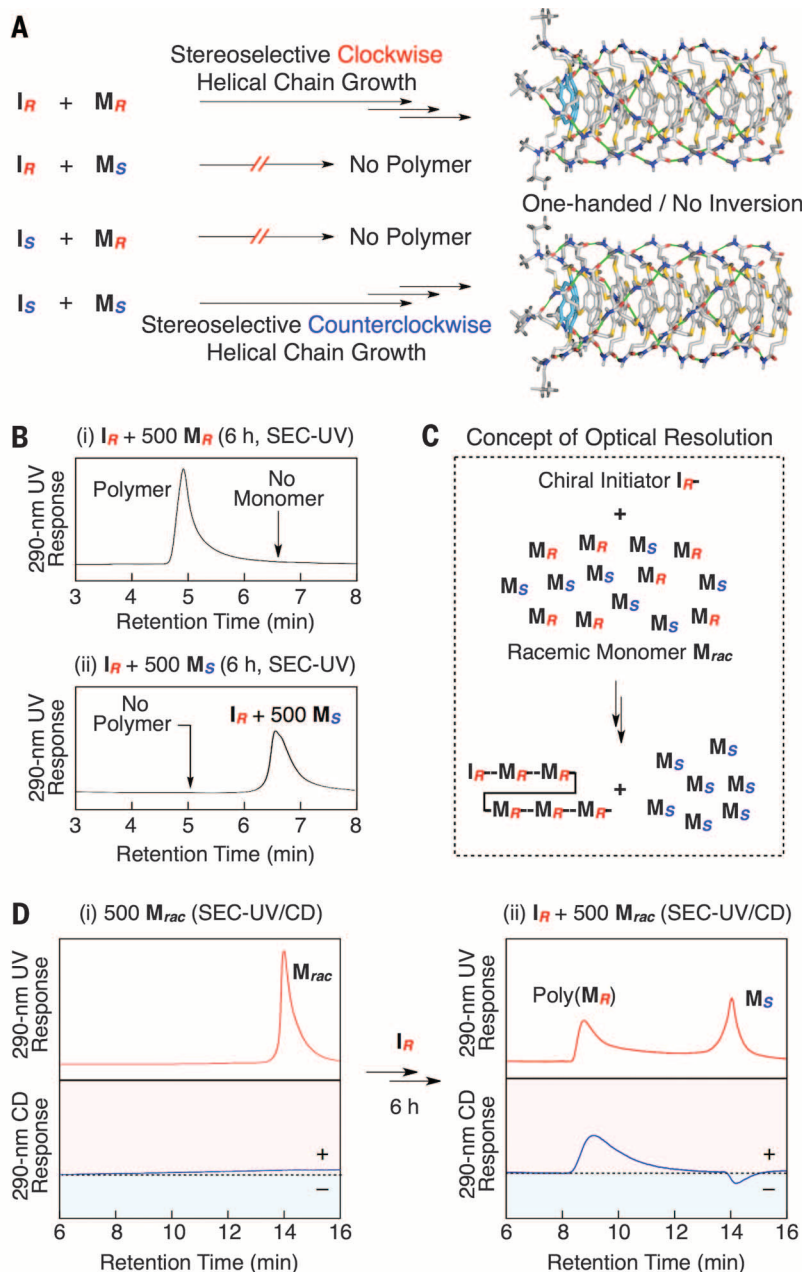


Fig. 3. Stereoselective chain growth polymerization of chiral monomers. (A) Schematic representation of the stereoselective chain-growth supramolecular polymerization of monomers **M_R** and **M_S** with initiators **I_R** and **I_S** (Fig. 1B), respectively, where the monomers and initiators both carry chiral side chains. The polymerization proceeds only when the absolute configurations of their side-chain stereogenic centers are identical to one another. (B) SEC-UV traces at 290 nm of the supramolecular polymerization of **M_R** (i) and **M_S** (ii) using **I_R** as the initiator at the initial monomer-to-initiator mole ratio of 500 in MCHex at 25°C for 6 hours. (C) Schematic representation of the optical resolution of racemic monomer **M_{rac}** by stereoselective polymerization initiated with **I_R**. (D) SEC-UV and SEC-CD traces at 290 nm of **M_{rac}** (i) and its polymerized mixture initiated with **I_R** at $[M_{rac}]_0/[I_R]_0 = 500$ in MCHex at 25°C for 6 hours (ii). The flow rate of the eluent for SEC was set at 0.5 ml min^{-1} except for the case of Fig. 3D, for which the flow rate was 0.2 ml min^{-1} (23).

recombination took place when initiator **I**, capable of end-capping, was immediately added to the sonicated mixture at $[\mathbf{I}]/[\mathbf{M}]_{\text{total}} = 1/5$ (fig. S18, D and E). Therefore, we conclude that our design strategy for chain-growth supramolecular polymerization operates as intended.

We next explored the possibility of stereoselective polymerization using chiral initiators (25). Unlike **M**, compounds **M_R** and **M_S**, together with their respective N-methylated derivatives **I_R** and **I_S** (Fig. 1B), carry chiral side chains, and each chain has a stereogenic center in proximity to the H-bonding amide unit. We found that **M_R** and **M_S** polymerize in a precise stereoselective manner using **I_R** and **I_S**, respectively, as chiral initiators (Fig. 3A and figs. S19 to S21). For example, when **I_R** was added at 25°C to a MCHex solution of **M_R** at $[\mathbf{M}_R]_0/[\mathbf{I}_R]_0 = 500$, **M_R** polymerized in the same way as **M**, thereby yielding a polymer with a small PDI in 6 hours (Fig. 3B, i). In stark contrast, the opposite enantiomer **M_S** did not polymerize with **I_R** (Fig. 3B, ii), even with a prolonged reaction time, whereas it polymerized readily upon mixing with initiator **I_S** (fig. S22). Namely, the polymerization occurs only when the stereogenic centers of the monomer and initiator in their chiral side chains are matched in configuration. Such precise enantioselection of chiral monomers **M_R** and **M_S** indicates a large energetic penalty for stereochemical mismatching in the polymer sequence (26).

In relation to the stereoselective nature of polymerization described above, we also investigated

the polymerization of **M** using chiral initiators **I_R** and **I_S** (Fig. 4A). As described previously, monomer **M**, identical to **M_R** and **M_S**, carries an asymmetric center at the C₅-symmetric corannulene core, but it is devoid of chiral side chains and therefore exists as a racemic mixture (Fig. 1B). The main interest here is whether **I_R** and **I_S** can differentiate the enantiomeric forms of **M** in the polymerization (25, 27). Thus, a solution of a mixture of **M** and **I_R** and at $[\mathbf{M}]_0/[\mathbf{I}_R]_0 = 500$ in MCHex ($[\mathbf{M}] = 1.0$ mM) was incubated at 25°C, wherein **M** was completely consumed in 6 hours, as observed by SEC, to yield a polymer in a manner analogous to the case of using **I** as the initiator. As expected, the results were the same when **I_S** was used as the initiator instead of **I_R** under conditions otherwise identical to those described above. In a SEC trace monitored with a circular dichroism (CD) detector at 290 nm (SEC-CD) (Fig. 4B), the resultant polymers exhibited positive (red) and negative (blue) chiroptical responses when **I_R** and **I_S** were used as the initiators, respectively. As shown in Fig. 4C (right), the vibrational circular dichroism (VCD) spectroscopy displayed a positive or negative band at ~ 1000 cm⁻¹ due to the corannulene skeleton of polymeric **M**. Figure 4D shows that the polymers are also CD-active, displaying mirror image spectra of one another. Furthermore, the CD spectra intensified with time monotonically at the initial stage and then fell off gradually to reach a plateau in 5 hours. Although the time to reach such a plateau region became shorter when $[\mathbf{M}]_0/[\mathbf{I}_R]_0$ was reduced from 500

to 250 and then 50, at a constant $[\mathbf{M}]_0$ of 1.0 mM the CD intensities finally attained were substantially the same as one another (Fig. 4E). Note that the CD spectral pattern is almost identical to that of monomeric **M_R** or **M_S** (fig. S23). Together with the VCD spectral profile in Fig. 4C (right), the CD spectra in Fig. 4D most likely reflect the genuine chiroptical feature of the corannulene skeleton rather than of the intermolecular exciton couples (28). By applying the molar ellipticity of the enantiomerically pure C₅-symmetric corannulene skeleton (18), the enantiomeric excess of **M** in the polymer chain was estimated as close to 100% in MCHex at 25°C (tables S2 and S3).

In accord with the posited mechanism in Fig. 1D, initiator **I_R** or **I_S** attaches to the initiating end of polymeric **M** and serves as a chiral auxiliary to stereochemically bias the polymerization (Fig. 4A). How does this chiral auxiliary at a polymer terminus enable such strong geometrical control over the entire polymer chain? In relation to this question, we noticed that not only the corannulene skeleton but also the H-bonded amide C=O at 1642 cm⁻¹ is VCD-active (Fig. 4C, left), thus indicating that the polymer adopts either a clockwise or counterclockwise helical geometry (Fig. 4A) (29). This helical structure is stabilized by the intermolecular H-bonded amide network. Hence, no racemization resulted when the polymer chain end-capped with **I_R** or **I_S** was cleaved by sonication to transform into uncapped, short polymer chains (fig. S24). We consider that this highly stable helical geometry most likely

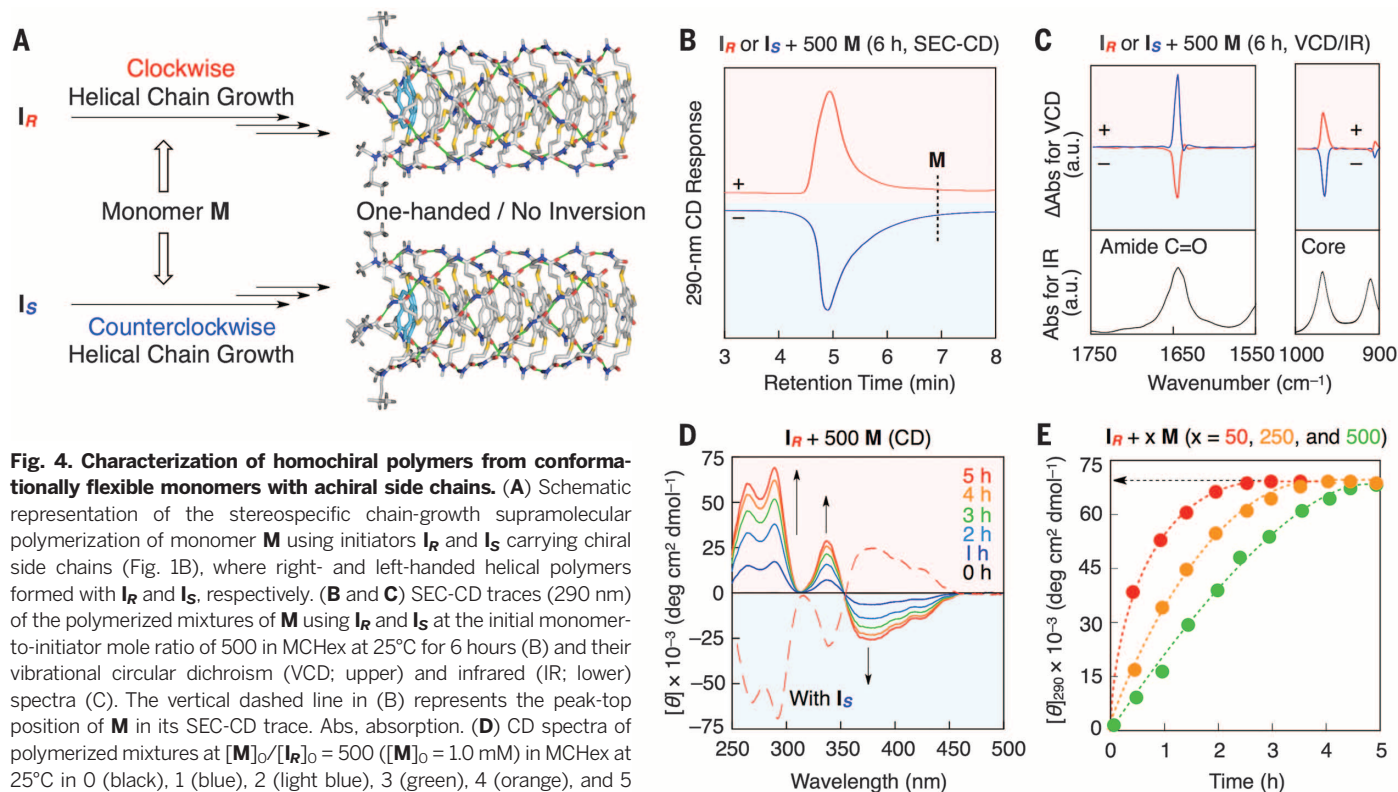


Fig. 4. Characterization of homochiral polymers from conformationally flexible monomers with achiral side chains. (A) Schematic representation of the stereospecific chain-growth supramolecular polymerization of monomer **M** using initiators **I_R** and **I_S** carrying chiral side chains (Fig. 1B), where right- and left-handed helical polymers formed with **I_R** and **I_S**, respectively. (B and C) SEC-CD traces (290 nm) of the polymerized mixtures of **M** using **I_R** and **I_S** at the initial monomer-to-initiator mole ratio of 500 in MCHex at 25°C for 6 hours (B) and their vibrational circular dichroism (VCD; upper) and infrared (IR; lower) spectra (C). The vertical dashed line in (B) represents the peak-top position of **M** in its SEC-CD trace. Abs, absorption. (D) CD spectra of polymerized mixtures at $[\mathbf{M}]_0/[\mathbf{I}_R]_0 = 500$ ($[\mathbf{M}]_0 = 1.0$ mM) in MCHex at 25°C in 0 (black), 1 (blue), 2 (light blue), 3 (green), 4 (orange), and 5 (red) hours. The dashed curve represents the CD spectrum of a polymerized mixture of **M** using **I_S** under conditions otherwise identical to those described above. (E) Plots of molar ellipticity at 290 nm ($[\theta]_{290}$) against incubation time in the polymerization of **M** with **I_R** at $[\mathbf{M}]_0/[\mathbf{I}_R]_0 = 50$ (red), 250 (orange), and 500 (green) ($[\mathbf{M}]_0 = 1.0$ mM) in MCHex at 25°C.

accounts for the near 100% stereochemical bias of the C_5 -symmetric corannulene core of **M** in the polymer chain. After observing the notable stereoselectivity of the polymerization in Fig. 3A, we were motivated to investigate whether **M_{rac}**, a racemic mixture of **M_R** and **M_S**, could be optically resolved by the polymerization using **I_R** or **I_S** as the initiator (Fig. 3C). Thus, **I_R** was added at 25°C to a solution of **M_{rac}** (1.0 mM) in MCHex at $[\text{M}_{\text{rac}}]_0/[\text{I}_{\text{R}}]_0 = 500$, where in 6 hours the SEC-ultraviolet (UV) profile demonstrated the appearance of a polymeric fraction along with the monomer (Fig. 3D, ii, red). By means of SEC-CD, the polymeric fraction was revealed to possess a positive CD sign at 290 nm, whereas the unassembled monomer fraction possessed a negative CD sign (Fig. 3D, ii, blue). Even upon prolonged reaction for 14 days, the residual monomer observed in 6 hours remained without further consumption (fig. S25A).

For the purpose of quantitatively analyzing the SEC-CD profile in Fig. 3D, we prepared two reference samples, a MCHex solution of non-polymerized **M_S** ($[\text{M}_{\text{S}}] = 0.5$ mM) and its polymerized version using **I_R** as the initiator at $[\text{M}_{\text{R}}]_0/[\text{I}_{\text{R}}]_0 = 250$ ($[\text{M}_{\text{S}}] = 0.5$ mM). As shown in fig. S25B, the SEC-CD (ii, blue) and SEC-UV (ii, red) traces in Fig. 3D were perfectly reproduced when the corresponding SEC traces of the above reference samples were superimposed. We thus succeeded in optically resolving **M_S** and **M_R**, using initiator **I_R** to polymerize only **M_R** and vice versa stereoselectively, thus leaving **M_S** or **M_R** unpolymerized (Fig. 3C). This notable stereochemical selection results from the homochiral nature of the polymer with respect to both the chiral side chains and stacked corannulene units. So far, some chiral monomers are known to self-assemble only homochirally. However, this process yields a racemic mixture of right- and left-hand helical polymers (26) because the conventional mechanism does not allow for selection of one enantiomer of the monomer for polymerization. Even for thoroughly studied covalent chain-growth polymerizations, such a high level of optical resolution has been rarely reported (30).

In differential scanning calorimetry (DSC), **M** unavoidably polymerizes during the heating process. Upon first heating in DSC (fig. S26, blue), monomeric **M** exhibited an exotherm (20 J g^{-1}) at 82°C and an endotherm at 175°C (27 J g^{-1}). By reference to the DSC profile of polymeric **M** separately prepared (endothermic peak at 177°C, 27 J g^{-1}) (fig. S26, red), the exotherm and endotherm in fig. S26 (blue) are assigned to the thermal polymerization of **M** and dissociation of the resulting polymer, respectively. These DSC profiles corroborate the H-bond stability of **M**, as suggested by comparing its infrared spectrum with that of polymeric **M**. Although the exotherm in the DSC trace indicates that the polymerization is enthalpically driven, the monomer **M** does not spontaneously polymerize without initiator **I** at ambient temperatures because **M** is metastable with a sufficiently large energetic barrier for the self-opening of its intramolecularly H-bonded cage. We presume that

the chain growth proceeds through an H-bond-assisted transition state (Fig. 1D), where **M** is preorganized with the growing end of the polymer as well as initiator **I** (both having free amide C=O groups) and transforms its H-bonding mode from intramolecular to intermolecular. This transition state is energetically less demanding than the self-cleavage of the H-bonded amide network in the monomer state. Although the concave structure of the monomer is critical for the present work, further conceptual diversification of metastable monomers for chain-growth supramolecular polymerization may give rise to a paradigm shift in precision macromolecular engineering.

REFERENCES AND NOTES

1. B. Ranby, in *Macromolecular Concept and Strategy for Humanity in Science, Technology and Industry* (Springer, Berlin, 1996), pp. 3–13.
2. H. Staudinger, *Ber. Deut. Chem. Ges.* **53**, 1073–1085 (1920).
3. P. J. Flory, *Principles of Polymer Chemistry* (Cornell Univ. Press, Ithaca, NY, 1969).
4. R. Mülhaupt, *Angew. Chem. Int. Ed.* **43**, 1054–1063 (2004).
5. H. Rehage, H. Hoffmann, *J. Phys. Chem.* **92**, 4712–4719 (1988).
6. N. Zimmerman, J. S. Moore, S. C. Zimmerman, *Chem. Ind.* **1998**, 604–610 (1998).
7. J.-M. Lehn, *Macromol. Chem. Macromol. Symp.* **69**, 1 (1993).
8. J.-M. Lehn, *Supramolecular Chemistry-Concepts and Perspectives* (Wiley-VCH, Weinheim, Germany, ed. 1, 1995).
9. J.-M. Lehn, *Polym. Int.* **51**, 825–839 (2002).
10. R. P. Sijbesma *et al.*, *Science* **278**, 1601–1604 (1997).
11. T. F. A. De Greef *et al.*, *Chem. Rev.* **109**, 5687–5754 (2009).
12. C. Fouquey, J.-M. Lehn, A.-M. Levelut, *Adv. Mater.* **2**, 254–257 (1990).
13. X. Wang *et al.*, *Science* **317**, 644–647 (2007).
14. J. B. Gilroy *et al.*, *Nat. Chem.* **2**, 566–570 (2010).
15. W. Zhang *et al.*, *Science* **334**, 340–343 (2011).
16. S. Ogi, K. Sugiyasu, S. Manna, S. Samitsu, M. Takeuchi, *Nat. Chem.* **6**, 188–195 (2014).
17. G. Odian, *Principles of Polymerization* (Wiley-VCH, New York, ed. 4, 2004).
18. J. Kang *et al.*, *J. Am. Chem. Soc.* **136**, 10640–10644 (2014).
19. Y. T. Wu, J. S. Siegel, *Chem. Rev.* **106**, 4843–4867 (2006).
20. V. M. Tsefnikas, L. T. Scott, *Chem. Rev.* **106**, 4868–4884 (2006).
21. R. Schmidt, M. Stoltz, M. Grüne, F. Würthner, *Macromolecules* **44**, 3766–3776 (2011).
22. Y. Ishida, T. Aida, *J. Am. Chem. Soc.* **124**, 14017–14019 (2002).
23. D. Miyajima *et al.*, *J. Am. Chem. Soc.* **131**, 44–45 (2009).
24. P. A. Korevaar *et al.*, *Nature* **481**, 492–496 (2012).
25. M.-I. Childers, J. M. Longo, N. J. Van Zee, A. M. LaPointe, G. W. Coates, *Chem. Rev.* **114**, 8129–8152 (2014).
26. F. Helmich, M. M. J. Smulders, C. C. Lee, A. P. H. J. Schenning, E. W. Meijer, *J. Am. Chem. Soc.* **133**, 12238–12246 (2011).
27. Y. Okamoto, T. Nakano, *Chem. Rev.* **94**, 349–372 (1994).
28. N. Berova, K. Nakanishi, R. W. Woody, *Circular Dichroism: Principles and Applications* (Wiley-VCH, New York, ed. 2, 2000).
29. M. M. J. Smulders *et al.*, *Chirality* **20**, 1016–1022 (2008).
30. W. Hirahata, R. M. Thomas, E. B. Lobkovsky, G. W. Coates, *J. Am. Chem. Soc.* **130**, 17658–17659 (2008).

ACKNOWLEDGMENTS

This work was financially supported by a Grant-in-Aid for Specially Promoted Research (25000005) on “Physically Perturbed Assembly for Tailoring High-Performance Soft Materials with Controlled Macroscopic Structural Anisotropy” for T.A. and a Grant-in-Aid for Research Activity Startup (2588024) for D.M.

SUPPLEMENTARY MATERIALS

www.sciencemag.org/content/347/6222/646/suppl/DC1
Materials and Methods
Supplementary Text
Figs. S1 to S27
Tables S1 to S3
References (31–34)

4 December 2014; accepted 12 January 2015
10.1126/science.aaa4249

ECOLOGICAL FEEDBACKS

Termite mounds can increase the robustness of dryland ecosystems to climatic change

Juan A. Bonachela,^{1,*} Robert M. Pringle,^{1,2} Efrat Sheffer,¹ Tyler C. Coverdale,¹ Jennifer A. Guyton,¹ Kelly K. Caylor,^{2,3} Simon A. Levin,¹ Corina E. Tarnita^{1,2,†}

Self-organized spatial vegetation patterning is widespread and has been described using models of scale-dependent feedback between plants and water on homogeneous substrates. As rainfall decreases, these models yield a characteristic sequence of patterns with increasingly sparse vegetation, followed by sudden collapse to desert. Thus, the final, spot-like pattern may provide early warning for such catastrophic shifts. In many arid ecosystems, however, termite nests impart substrate heterogeneity by altering soil properties, thereby enhancing plant growth. We show that termite-induced heterogeneity interacts with scale-dependent feedbacks to produce vegetation patterns at different spatial grains. Although the coarse-grained patterning resembles that created by scale-dependent feedback alone, it does not indicate imminent desertification. Rather, mound-field landscapes are more robust to aridity, suggesting that termites may help stabilize ecosystems under global change.

Over the past decade, many studies have documented large-scale, spatially periodic clusters of vegetation and other sessile organisms, typically in resource-limited environments (1–4). Such patterns, found at many levels of biological organization (5),

can be described by models of scale-dependent feedback (SDF) coupling short-range activation with long-range inhibition (3–9). For example, in arid and semi-arid savannas and grasslands (“drylands”), plants facilitate neighbors by increasing water infiltration while competing for

water with distant individuals (10). In these models, reducing rainfall generates a predictable sequence of patterns with decreasing overall plant biomass: overdispersed gaps, labyrinths, spots, and finally, barren desert. This last transition is known as a “catastrophic shift,” or sudden collapse to an unvegetated state (11, 12).

¹Department of Ecology and Evolutionary Biology, Princeton University, Princeton, NJ 08544, USA. ²Mpala Research Centre, Post Office Box 555, Nanyuki, Kenya. ³Department of Civil and Environmental Engineering, Princeton University, Princeton, NJ 08544, USA.

*Present address: Marine Alliance for Science and Technology Scotland (MASTS) Marine Population Modelling Group, Department of Mathematics and Statistics, University of Strathclyde, 26 Richmond Street, Glasgow G1 1XH, Scotland, UK. †Corresponding author. E-mail: ctarnita@princeton.edu

The robustness [sensu (13), also called resilience (14)] of drylands to such catastrophic shifts is an urgent concern given the importance of these systems to human livelihoods [drylands cover >40% of Earth's land surface and are home to >38% of the populace (15)] and the increased frequency/intensity of drought expected under climate change (16). Scientists have therefore proposed using spotted vegetation patterns, readily identifiable in aerial imagery, as “early-warning signals” of imminent catastrophic shifts (11, 12). However, operationalizing an early-warning system requires mechanistic understanding of both the cause of spotted patterns and the linkage between patterns and robustness; otherwise, “false alarms” could lead to costly resource misallocation (17).

Prior SDF models assume soil homogeneity, but most real ecosystems feature heterogeneous substrates. One globally widespread source of heterogeneity is ecosystem engineering by soil-dwelling macrofauna such as termites, ants, and earthworms. Termites are particularly important in savannas of Africa, Australasia, and South America, and their nest structures (“mounds”) shape many environmental properties; analogous structures built by ants and burrowing mammals are similarly influential worldwide (18). Mound soils differ from surrounding “matrix” soils in physical and chemical composition, which enhances vegetation growth (19, 20), creating “islands of fertility” (Fig. 1) (20–22). Moreover, mounds are frequently spatially overdispersed

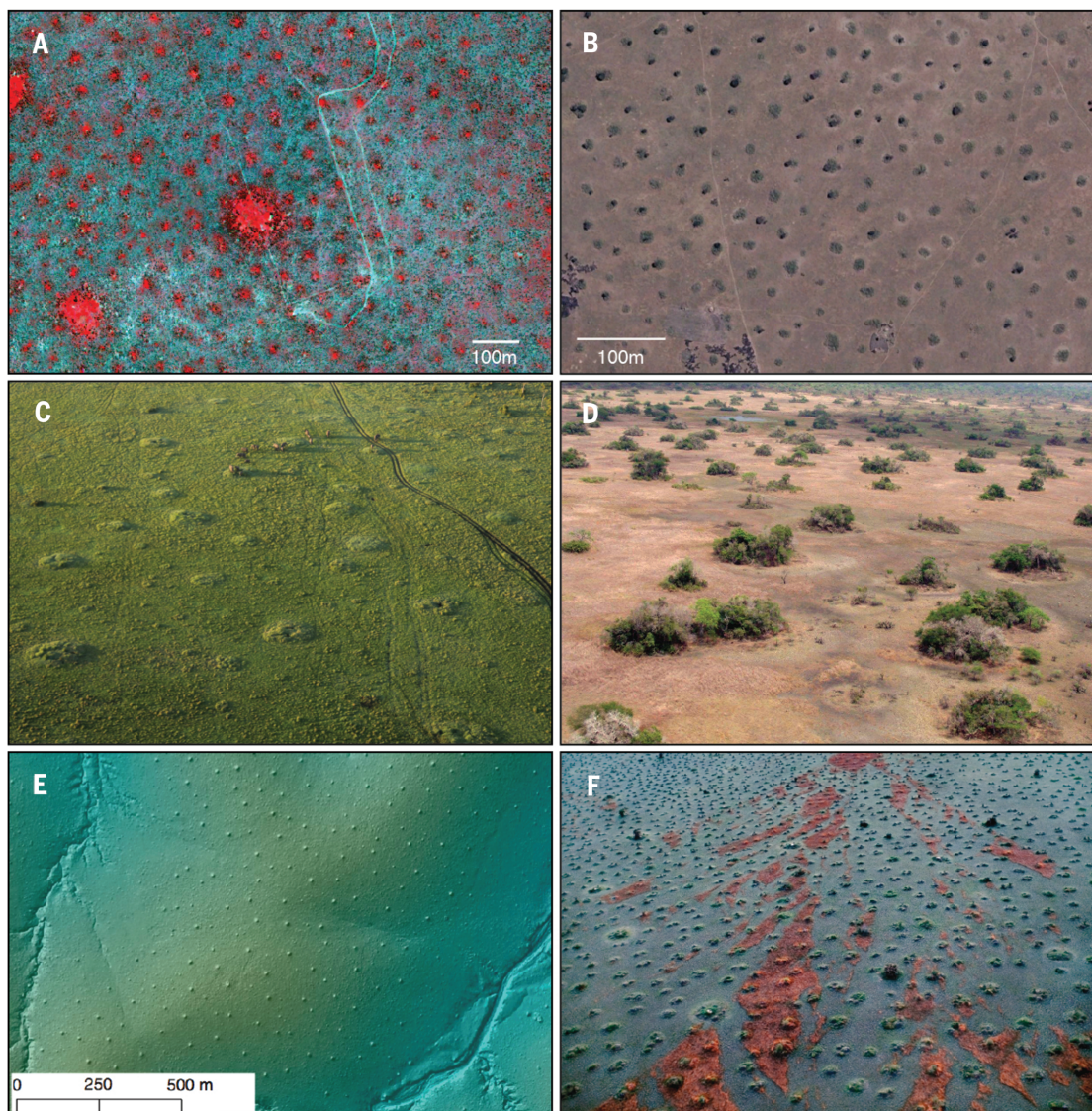


Fig. 1. Patterned termite mounds in real ecosystems. (A) False-color infrared Quickbird satellite image (2.4-m resolution) of termite mounds at MRC; mounds appear as small red spots, indicating high primary productivity (larger red patches are abandoned cattle corrals). (B) Presumed termite mounds in northwestern Tanzania (−1.29158 latitude, 34.37146 longitude) identified by using Google Earth (2006 image copyright DigitalGlobe). Barren halos are visible around many mounds, as pre-

dicted by our model. (C) Grass-dominated mounds in Kenya's Masai Mara, taken from hot-air balloon; elephants in the photo provide scale. (D) Tree-dominated mounds in Sofala, Mozambique, taken from helicopter (image courtesy of Marc Stalmans). (E) Light detection and ranging (LIDAR) hillshade image of termite mounds in South Africa's Kruger National Park, from (25). (F) Termite mounds on Bangweulu floodplain, Zambia (image courtesy of Frans Lanting).

owing to competition among neighboring colonies (20–25), which creates spotted vegetation patterns (Fig. 1). The resemblance of these patterns to those predicted by SDF has been noted (4, 10) but not formally analyzed. These two patterning mechanisms are not mutually exclusive and may co-occur.

We modeled SDF on a template of overdispersed termite mounds and tested results against

imagery from semi-arid savanna at Kenya's Mpala Research Centre (MRC). Mounds in this system—lenticular humps with belowground chambers and passages (21)—are built by fungus-cultivating termites (Macrotermitinae: *Odontotermes*), which are common throughout the Paleotropics. However, our results are applicable to mounds of diverse species and architectures, provided nutrient and/or water availability is elevated either

on the mound-proper or in the annular zone around the mound.

We adapt a well-studied three-variable SDF model (10) that describes the spatiotemporal dynamics of aboveground vegetation biomass as a function of rainfall (partitioned into runoff and soil water) (10, 23). In traditional two-component SDF models, short-distance enhancement leading to pattern formation usually arises from

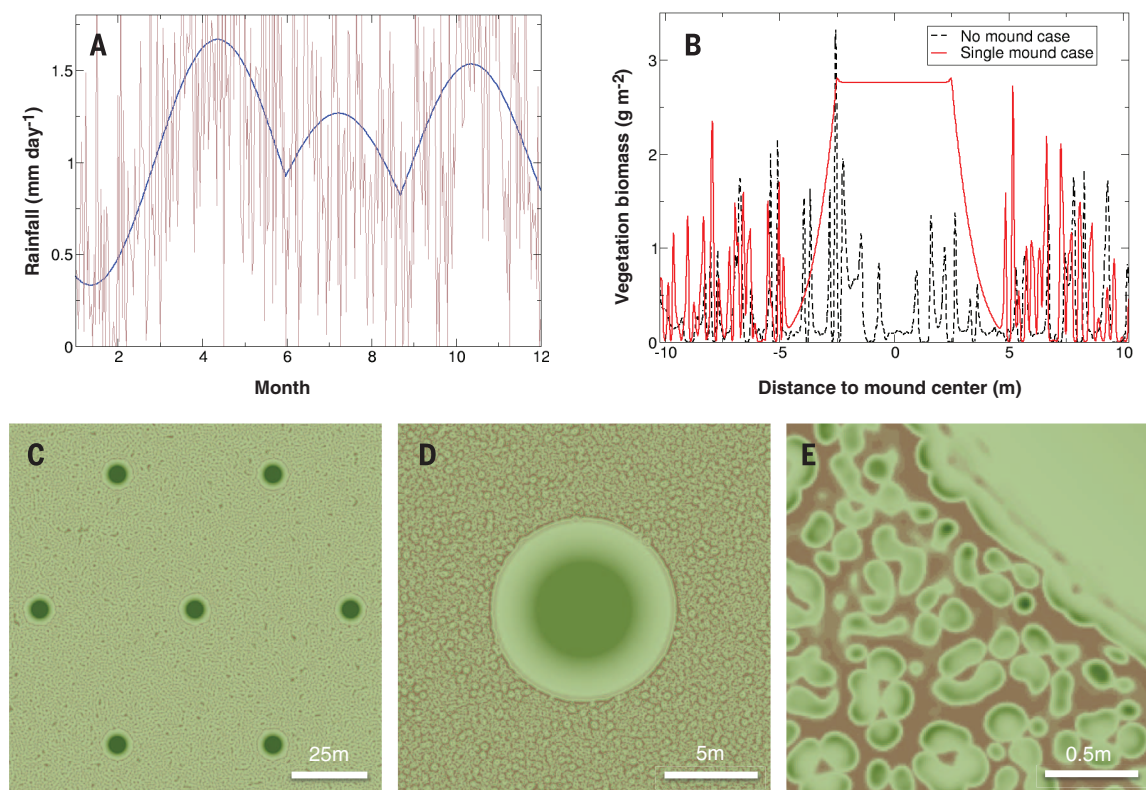


Fig. 2. Vegetation patterns obtained with stochastic rainfall and termite-induced heterogeneity. (A) Stochastic rainfall (brown curve) based on observed mean-monthly rainfall (blue curve) at MRC, 1999–2013. (B) Transect of predicted vegetation biomass density through a mound (solid curve) and in the absence of mounds (dashed curve). (C to E) Model outputs showing (C) 123- by 123-m region encompassing seven hexagonal

mounds; (D) 20.5- by 20.5-m region with only one mound, showcasing halo effect (for comparison, Fig. 1, B and D); and (E) 2- by 2-m region showing patchy off-mound vegetation and homogeneous on-mound vegetation. Green represents vegetation; brown represents soil. Darker green regions have higher biomass. Parameterization is provided in table S1.

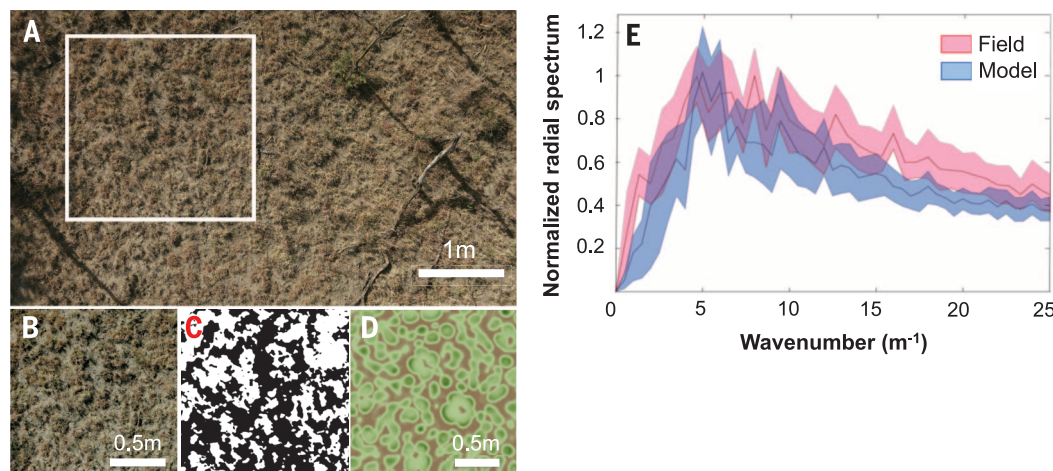


Fig. 3. Correspondence of predicted and observed vegetation patterns. (A) Photograph of 3.5- by 6-m region of matrix vegetation taken from 10 m height. (B) 1.5- by 1.5-m section used in the analysis, from white square in (A). (C) Binary transformation of (B) (white represents vegetation, black represents soil). (D) Model output used for comparison, with parameterization as in Fig. 2. (E) Normalized radial spectrum of real images ($n = 14$ samples) and model simulations ($n = 192$ samples), as a function of wave number.

autocatalysis (positive-feedback) in an “activator” species (8, 9). When more than two components interact, as in the model used here, enhancement can arise indirectly through autocatalytic feedback loops (here, plants–soil water), generating similar pattern morphologies (26). We include termite-mound effects in the model by modifying just two parameters. One is the conversion factor c , the efficiency with which plants convert water into biomass (“water-use efficiency”), which we assume is mediated by elevated nutrient availability on mounds (19, 27). The other is the half-saturation constant of water infiltration, k_2 , which we modify to account for termites’ creation of macropores and alteration of soil texture (19, 28). We leave all other parameters unchanged (table S1) to enable comparison with prior work.

We assume that both nutrient-mediated water-use efficiency and infiltration are elevated on mounds (fig. S1), which is consistent with prior research; specifically, we explore a likely range of on- versus off-mound increases of 0 to 67% for infiltration and 0 to 50% for water-use efficiency (20, 23, 29). We further assume that termites’ effects on water-use efficiency (but not infiltration) are zero-sum: Termites concentrate nutrients on mounds (27) but do not increase net nutrient content of the system [this is conservative in terms of finding beneficial effects of termites, and we analyze alternative scenarios in (23)]. To assess the effects of rainfall variability, we incorporate seasonality and stochasticity in rainfall based on MRC rainfall records (Fig. 2A).

This modified model yields greater on- than off-mound vegetation biomass (Fig. 2B). Two types of pattern can be identified. One is a coarse-grained lattice of overdispersed vegetation hotspots, reflecting the underlying distribution of termite mounds (27), which is exogenous to our model, in conjunction with mounds’ positive effects on plant biomass, which is predicted by our model and confirmed with field data from MRC (Fig. 2C) (23). The other comprises fine-grained regularity of mound and matrix vegetation resulting from SDF (Fig. 2, D and E). The wavelengths of the fine-grained pattern, both on and off mounds, are determined by local dispersal of plants and diffusion of soil and surface water (30) and depend on the values of water-use efficiency and infiltration: Greater values increase vegetation homogeneity; lower values yield regular gaps, labyrinths, and spots, as found in prior SDF models. Thus, the greater the termite-induced improvements in water-use efficiency and infiltration, the more divergent the on- versus off-mound patterning (Fig. 2D and fig. S6). These fine-grained patterns are insensitive to mound distribution (we find equivalent patterns for a single mound and square or hexagonal arrangements), and off-mound patterning is largely insensitive to mound proximity (fig. S3). Our model also produces a “halo” of barren soil at mound edges, resulting from the highly vegetated mound acting as a sink for nearby water, matching observations from various African savannas (Fig. 1, B and D).

To evaluate model predictions of fine-grained patterning, we used Fourier transforms to analyze low-altitude (10 m) aerial photographs of matrix vegetation from MRC (Fig. 3, A to C) (23). Off-mound, we find spotted patterns with ~20-cm wavelength, which closely matches the simulated pattern (Fig. 3, D and E). Moreover, as predicted, mound vegetation is both denser (23) and more evenly distributed than matrix vegetation (fig. S8). Thus, incorporating termite-induced soil heterogeneity in the SDF framework gives a realistic description of observed patterning. Exact quantitative correspondence is not expected because our analysis uses generic parameter values from prior work (10). This model could be further extended to include interactions among plant types (such as trees versus grasses) and/or herbivore impacts, and its predictions could be tested via rain-out/watering experiments.

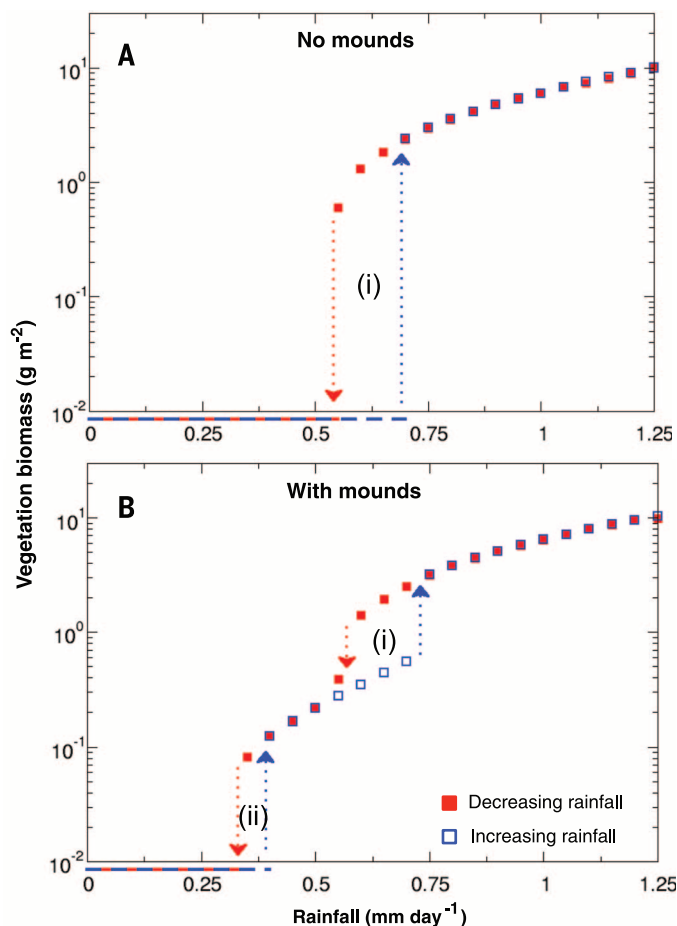
We next used the modified model to analyze the system’s robustness (13) to precipitation changes. We consider two components of robustness: “resistance” to perturbation and “recovery” from an undesirable stable state. We find that termite mounds increase ecosystem robustness in three ways (Fig. 4). They enhance resistance, enabling vegetation to persist under substantially reduced rainfall; they reduce the rainfall threshold required for recovery from desert; and they make desertification more gradual (less cat-

astrophic) and thus easier to anticipate and ameliorate. These changes occur because improved infiltration and water-use efficiency on and around mounds enable plants to persist and to repopulate after extirpation, under more arid conditions: Mounds act as refugia for vegetation after the matrix has collapsed to desert.

Sufficient improvement of either water-use efficiency or infiltration can independently increase robustness. As rainfall decreases, two sudden drops in biomass occur (Fig. 4B and figs. S4 and S5). The first (Fig. 4B, i) represents loss of matrix vegetation only and corresponds to total desertification in the system without mounds (Fig. 4A, i). The second (Fig. 4B, ii) represents loss of vegetation from mounds (and hence the entire system) and occurs at lower rainfall, indicating enhanced resistance. As rainfall increases from zero, two sudden jumps in biomass occur (Fig. 4B and figs. S4 and S5): Revegetation of mounds occurs first, at lower rainfall, followed by revegetation of the matrix, indicating enhanced recovery. Insufficient termite-induced improvements yield only one shift, as occurs in the absence of mounds (10), and do not enhance ecosystem robustness (fig. S5); in this case, on- and off-mound trajectories are similar. Improving either parameter yields comparable effects, but for our parameter regions, water-use efficiency contributes more to robustness than does infiltration (fig. S5).

Fig. 4. Termite mounds increase ecosystem robustness. (A and B)

Semilogarithmic phase diagrams under increasing (blue) and decreasing (red) rainfall for (A) model with no termite mounds and (B) the modified model with 50% on- versus off-mound improvement in both growth rate and infiltration efficiency. (A) Without mounds, one hysteresis cycle occurs (i), corresponding to sudden transitions to and from desertification. (B) Adding mounds generates two hysteresis cycles, corresponding to loss/recovery of matrix vegetation (i) and desertification/revegetation (ii). For both (A) and (B), we used fixed rainfall rates and parameters as described in table S1 and fig. S5.



This model describes annual-to-decadal temporal scales, over which precipitation influences the dynamics of vegetation, but not the mounds (23). Thus, the model captures pattern evolution and sudden transitions in response to climate-change-induced pulses of drought and rainfall but may not apply if sustained (>50-year) reductions in baseline precipitation cause termite extinction and subsequent homogenization of mound structures. Future theoretical and empirical work is needed to elucidate longer-term dynamic feedbacks between vegetation and mound construction, distribution, and decay.

Our analysis shows that when SDF occurs on a template of overdispersed mounds created by ecosystem engineers, two distinct types of regular patterning coexist at different scales. The fine-grained SDF-generated patterns documented here may be common, but previously unreported because (i) they cannot be observed in available satellite imagery; (ii) even at lower altitudes, grass canopies obscure patterns with centimeter-scale wavelengths; and (iii) stochastic rainfall decreases apparent regularity (compare Fig. 2 and movies S1 and S2 with fig. S3, which assumes constant rainfall). The simplest SDF scenarios typically produce patterns with a single characteristic wavelength (3), whereas models combining multiple mechanisms can show complex patterns (31, 32). Thus, co-occurrence of patterns with distinct wavelengths may be a general indicator that multiple mechanisms are operating simultaneously. The mound-SDF interaction is one such route to pattern coexistence and is likely common worldwide because it does not depend on specific mound attributes. Appropriately modified models might therefore inform ongoing debates in which SDF and soil macrofauna are considered alternative hypotheses for particular large-scale patterns, such as Namibian “fairy circles” (33, 34) and various “mima-like mounds” worldwide (35).

We further conclude that termites, by creating refugia for plants and nuclei for revegetation, can enhance drylands’ resistance to and recovery from drought. These islands of fertility (20) appear spot-like in remotely sensed imagery (Fig. 1), but unlike SDF-generated spots, they indicate robustness rather than vulnerability to collapse. These findings confirm the critical links between remotely sensed patterns and ecosystem dynamics but qualify the use of remotely sensed patterning to predict catastrophic shifts. Similar phenomena may occur in other systems in which vegetation patterning is governed by mechanisms that generate apparent SDF dynamics, such as banded vegetation arising from runoff induced by biological crusts on arid hillslopes (4, 36). By such engineering of soil, termites and other ecosystem engineers may buffer the effects of anthropogenic global change in some of the world’s most environmentally and socioeconomically sensitive regions.

REFERENCES AND NOTES

- C. A. Klausmeier, *Science* **284**, 1826–1828 (1999).
- J. van de Koppel *et al.*, *Science* **322**, 739–742 (2008).
- M. Rietkerk, J. van de Koppel, *Trends Ecol. Evol.* **23**, 169–175 (2008).
- V. Deblauwe, P. Couteron, O. Lejeune, J. Bogaert, N. Barbier, *Ecography* **34**, 990–1001 (2011).
- H. Meinhardt, *Nature* **376**, 722–723 (1995).
- S. A. Levin, L. A. Segel, *SIAM Rev.* **27**, 45–67 (1985).
- E. Meron, *Math. Model. Nat. Phenom.* **6**, 163–187 (2011).
- A. Gierer, H. Meinhardt, *Kybernetik* **12**, 30–39 (1972).
- P. K. Maini, K. J. Painter, H. Nguyen Phong Chau, *Faraday Trans.* **93**, 3601–3610 (1997).
- M. Rietkerk *et al.*, *Am. Nat.* **160**, 524–530 (2002).
- M. Scheffer *et al.*, *Nature* **461**, 53–59 (2009).
- M. Rietkerk, S. C. Dekker, P. C. de Ruiter, J. van de Koppel, *Science* **305**, 1926–1929 (2004).
- S. A. Levin, J. Lubchenco, *Bioscience* **58**, 27 (2008).
- C. S. Holling, *Annu. Rev. Ecol. Syst.* **4**, 1–23 (1973).
- J. F. Reynolds *et al.*, *Science* **316**, 847–851 (2007).
- N. S. Diffenbaugh, C. B. Field, *Science* **341**, 486–492 (2013).
- V. Dakos, S. Kéfi, M. Rietkerk, E. H. van Nes, M. Scheffer, *Am. Nat.* **177**, E153–E166 (2011).
- C. Alba-Lynn, J. K. Detling, *Oecologia* **157**, 269–278 (2008).
- P. Jouquet, S. Traoré, C. Chosai, C. Hartmann, D. Bignell, *Eur. J. Soil Biol.* **47**, 215–222 (2011).
- G. W. Sileshi, M. A. Arshad, S. Konaté, P. O. Nkunika, *J. Veg. Sci.* **21**, 923–937 (2010).
- R. M. Pringle, D. F. Doak, A. K. Brody, R. J. Jock, T. M. Palmer, *PLOS Biol.* **8**, e1000377 (2010).
- A. B. Davies *et al.*, *Ecography* **37**, 852–862 (2014).
- Materials and methods are available as supplementary materials on Science Online.
- J. Korb, K. E. Linsenmair, *Oecologia* **127**, 324–333 (2001).
- S. R. Levick *et al.*, *Nat. Commun.* **1**, 1–7 (2010).
- R. A. Satnoianu, M. Menzinger, P. K. Maini, *J. Math. Biol.* **41**, 493–512 (2000).
- C. L. Seymour *et al.*, *Soil Biol. Biochem.* **68**, 95–105 (2014).
- N. Bottinelli *et al.*, *Soil Tillage Res.* **2014**, 1–7 (2014).
- A. Mando, L. Stroosnijder, L. Brussaer, *Geoderma* **74**, 107–113 (1996).
- E. Sheffer, J. von Hardenberg, H. Yizhak, M. Shachak, E. Meron, *Ecol. Lett.* **16**, 127–139 (2013).
- K. M. Page, P. K. Maini, N. A. Monk, *Physica D* **202**, 95–115 (2005).
- Q.-X. Liu *et al.*, *Nat. Commun.* **5**, 5234 (2014).
- N. Juergens, *Science* **339**, 1618–1621 (2013).
- S. Getzin *et al.*, *Ecography* **37**, 1–11 (2014).
- M. D. Cramer, N. N. Barger, *Palaeogeogr. Palaeoclimatol.* **409**, 72–83 (2014).
- O. Malam Issa, J. Trichet, C. Défarge, A. Couté, C. Valentin, *Catena* **37**, 175–196 (1999).

ACKNOWLEDGMENTS

The data are located on the Dryad Digital Repository. This work is a product of U.S. National Science Foundation grant DEB-1355122 to C.E.T., R.M.P., and D. F. Doak. Additional support was provided by the Princeton Environmental Institute (Grand Challenges grant to R.M.P. and C.E.T.), the National Geographic Society (9291 to R.M.P.), the National Science Foundation (EAR-0847368 and DEB-0816453 to K.K.C.), the Andrew W. Mellon Foundation (“Dynamics of South African Vegetation” to S.A.L.), and the John Templeton Foundation (Foundational Questions in Evolutionary Biology RFP-12-14 to C.E.T. and S.A.L.). We thank the Government of Kenya for permission to conduct research; I. Cuesta, D. F. Doak, L. Hedin, R. Martinez-Garcia, J. D. Murray, J. van de Koppel, and T. P. Young for helpful discussions; three anonymous referees for insightful suggestions; K. Grabowski and M. Mohamed for field assistance; and T. P. Young, C. Riginos, and K. Veblen for access to the Kenya Long-term Exclosure Experiment (KLEE), funded by NSF LTREB 12-56034. C.E.T. conceived the study; C.E.T., R.M.P., and J.A.B. developed the theory; J.A.B. analyzed the model; E.S. performed the analysis of pattern in imagery and its comparison with simulation results; R.M.P., T.C.C., and J.A.G. collected field data; S.A.L., K.K.C., and E.S. contributed to discussions of the modeling and analysis; C.E.T., R.M.P., and J.A.B. wrote the first draft of the manuscript; and all authors contributed revisions.

SUPPLEMENTARY MATERIALS

www.sciencemag.org/content/347/6222/651/suppl/DC1
Supplementary Text

Figs. S1 to S8
Table S1

References (37–84)
Movies S1 and S2

19 September 2014; accepted 16 December 2014
10.1126/science.1261487

PLANT DEVELOPMENT

Genetic control of distal stem cell fate within root and embryonic meristems

Brian C. W. Crawford,¹ Jared Sewell,² Greg Golembeski,¹ Carmel Roshan,¹ Jeff A. Long,^{2*} Martin F. Yanofsky^{1*}

The root meristem consists of populations of distal and proximal stem cells and an organizing center known as the quiescent center. During embryogenesis, initiation of the root meristem occurs when an asymmetric cell division of the hypophysis forms the distal stem cells and quiescent center. We have identified *NO TRANSMITTING TRACT (NTT)* and two closely related paralogs as being required for the initiation of the root meristem. All three genes are expressed in the hypophysis, and their expression is dependent on the auxin-signaling pathway. Expression of these genes is necessary for distal stem cell fate within the root meristem, whereas misexpression is sufficient to transform other stem cell populations to a distal stem cell fate in both the embryo and mature roots.

Development of plant roots depends on regulation of stem cell function in the root apical meristem, where the quiescent center separates two populations of stem cells into proximal and distal domains (Fig. 1A) (1, 2). The cells in the quiescent center rarely divide themselves but signal to surrounding stem cells to remain undifferentiated. The quiescent center is formed during embryo development when the

uppermost cell of the suspensor, known as the hypophysis, divides asymmetrically to initiate the root meristem. Here we analyze the signals

¹Division of Biological Sciences, University of California San Diego, La Jolla, CA 92093, USA. ²Department of Molecular, Cell and Developmental Biology, University of California Los Angeles, Los Angeles, CA 90095, USA.

*Corresponding author. E-mail: marty@ucsd.edu (M.F.Y.); jeffalong@ucla.edu (J.A.L.)

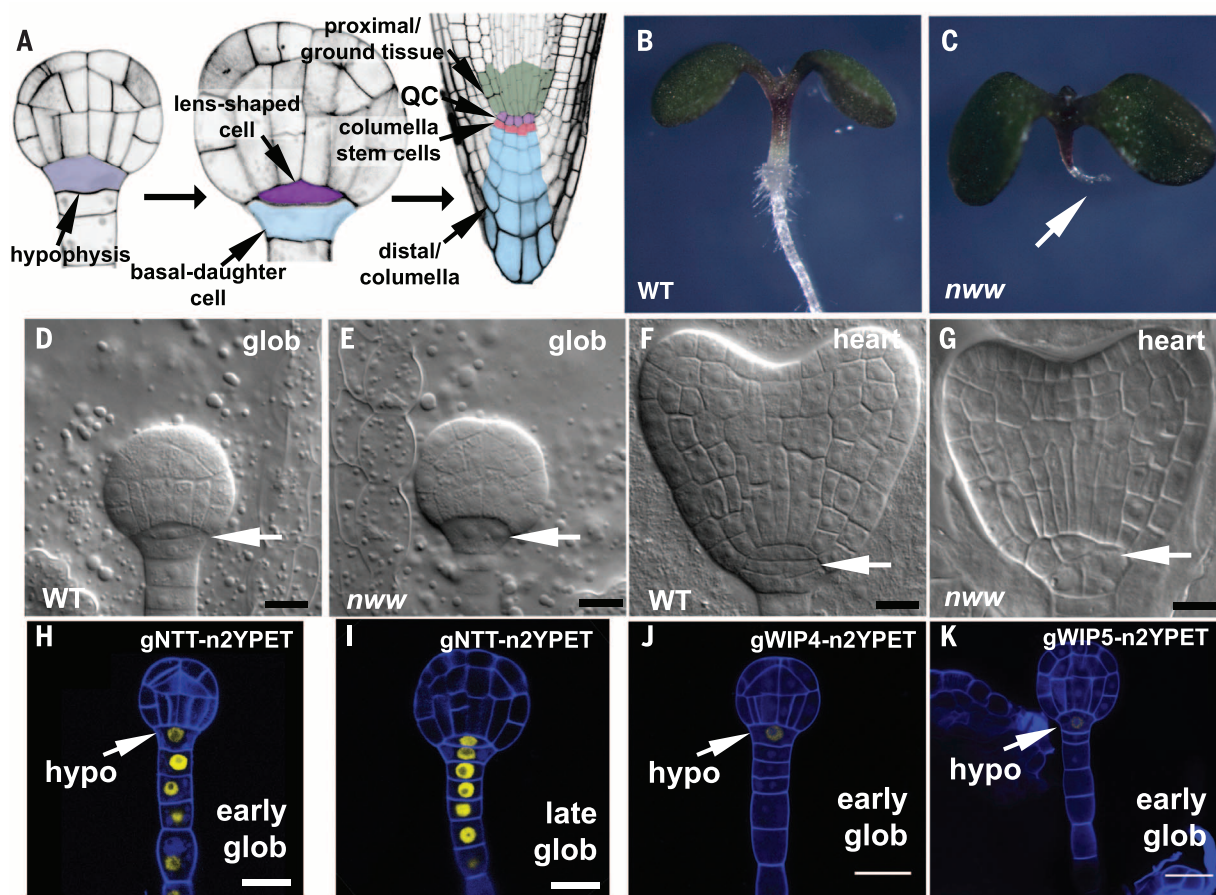


Fig. 1. Phenotype of the *nww* mutant and expression of *NWW* genes in embryos. (A) Stages in root meristem development, from an early globular-stage embryo to a mature root meristem with different regions of the meristem labeled and colored. QC, quiescent center. (B and C) Seedling phenotype of the wild type (B) and *nww* mutant (C). The arrow in (C) indicates the absence of the root. (D to G) Arrows indicate root meristem initiation in globular (glob) and heart-stage embryos of the wild type [(D) and (F)] and *nww* mutant [(E) and (G)]. (H to K) Recombineered NTT [(H) and (I)], WIP4 (J), and WIP5 (K) reporters in a 32-cell or early globular stage before root meristem initiation [arrows in (H), (J), and (K)] and a late globular stage (I). Arrows point to hypophysis (hypo) cell in (H), (J), and (K). Scale bars, 20 μ m in (D) to (K).

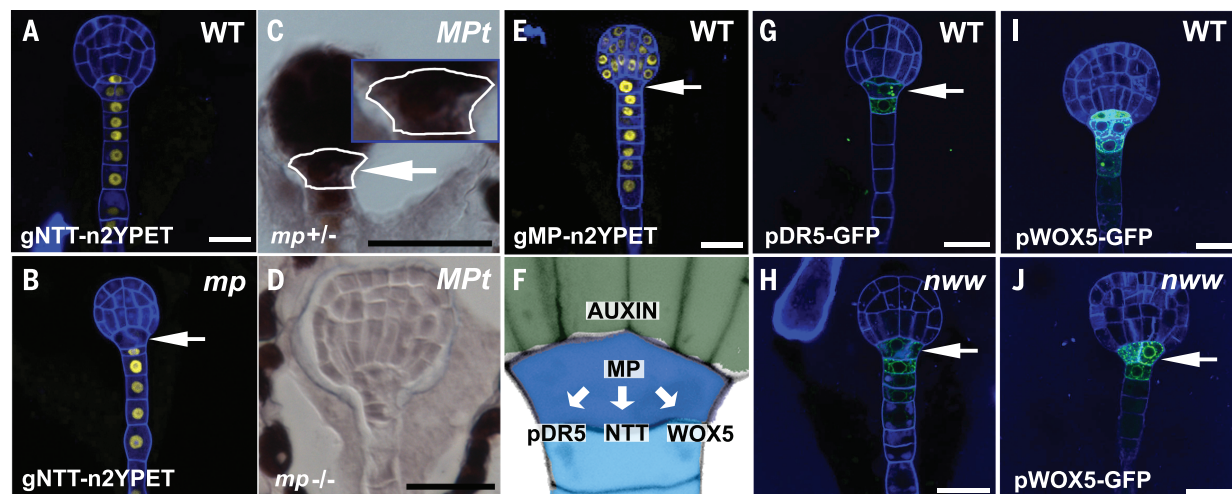


Fig. 2. Expression analysis in WT and mutant embryos. (A and B) Arrows indicate gNTT-n2YPET accumulation in divided hypophysis of WT (A) and *mp* mutant (B) globular-stage embryos. (C and D) In situ hybridization of MP in globular-stage embryos. To ensure that we were not detecting background signal, we used a segregating *mp* mutant population along with an in situ probe that only detected WT MP transcript. Arrows show expression in outlined hypophysis (C) of early globular-stage embryo, but no expression in

a phenotypically *mp* mutant (D) late globular-stage embryo. (E) Accumulation of recombineered gMP-n2YPET throughout an early globular embryo. The arrow indicates accumulation within the hypophysis. (F) Diagram of the genetic pathway to promote root initiation. (G and H) Normal initiation of pDR5-GFP expression is indicated by arrows in the wild type (G) and *nww* mutant (H). (I and J) Normal initiation of pWOX5-GFP expression indicated by arrows in the wild type (I) and *nww* mutant (J). Scale bars, 20 μ m in (A) to (E) and (G) to (J).

that first establish the quiescent center and distal stem cell populations.

The *NO TRANSMITTING TRACT* (*NTT*) gene encodes a putative zinc finger transcription factor that is required in developing carpels for transmitting tract formation (3, 4). *NTT* is also expressed in root meristems, although *ntt* homozygous mutant roots are normal. To determine if *NTT* acts redundantly with other genes, we combined mutations in *NTT* with mutations in *WIP DOMAIN PROTEIN 4* (*WIP4*) and *WIP5*, the two genes most closely related to *NTT* (5) (see supplementary materials and methods). Although plants lacking one or two of these genes had normal roots, plants lacking all three genes—*ntt*, *wip4*, and *wip5* (hereafter referred to as *nww*)—had no roots (Fig. 1, B and C, and fig. S1). Thus, the *NWW* function is required for root formation, and these three genes can each individually fulfill that function.

Development of wild-type (WT) and *nww* mutant embryos diverges at the 32-cell (early globular) stage, when the hypophysis normally divides asymmetrically to form the lens-shaped cell that goes on to generate the quiescent center (Fig. 1A). In *nww* mutants, this asymmetric cell division

fails to occur, and the lens-shaped cell does not form (Fig. 1 and fig. S1). Because activity of the root meristem is dependent on the quiescent center, loss of the lens-shaped cell likely explains the absence of roots in the *nww* mutant.

As WT embryos continue to develop, the root meristem becomes more distinct. In *nww* mutant embryos, this region is highly disorganized, lacking a recognizable root meristem (Fig. 1 and fig. S1). In *nww* mutant embryos, cell divisions above the hypophysis appear normal at the globular stage, but after failure of that key asymmetric cell division, they become progressively more abnormal. These cell division defects may be a result of the loss of the quiescent center, which normally sends a signal to the proximal stem cells, and these defects are reflected postembryonically by the lack of vasculature tissue in the hypocotyl of the *nww* mutant (fig. S2).

To determine if the pattern of expression and protein accumulation for *NTT* correlated with the observed mutant phenotypes, we created a recombinant construct expressing 2YYPET fused to *NTT* under the control of the entire *NTT* locus, gNTT-n2YYPET (6, 7). This construct was capable

of complementing the *ntt* single- and *nww* triple-mutant phenotypes. The expression pattern was indistinguishable from in situ hybridization patterns (fig. S3). *NTT* was expressed in the hypophysis cell in globular-staged embryos (Fig. 1H) and was maintained as the hypophysis gave rise to the apical and basal daughter cells (Fig. 1I). *WIP4* and *WIP5* were similarly expressed in the hypophysis but, in contrast with *NTT*, not in the suspensor (Fig. 1, H to K). Thus, the *NWW* genes are all expressed in the hypophysis, where they act redundantly to promote root meristem initiation.

The rootless phenotype of the *nww* triple mutant resembles mutants in the auxin response factor *MONOPTEROS* (*MP/ARF5*) (8). We therefore examined accumulation of *NTT* in *mp* mutants to determine if *NTT* accumulation was dependent on MP. Whereas gNTT-n2YYPET accumulation was observed in the hypophysis of WT embryos (Fig. 2A), little or no accumulation in the hypophysis was detected in *mp* mutants (Fig. 2B and fig. S4). This suggests that *NTT* acts downstream of MP in promoting root meristem initiation.

To better understand the relationship between MP and *NTT*, we examined *MP* expression within

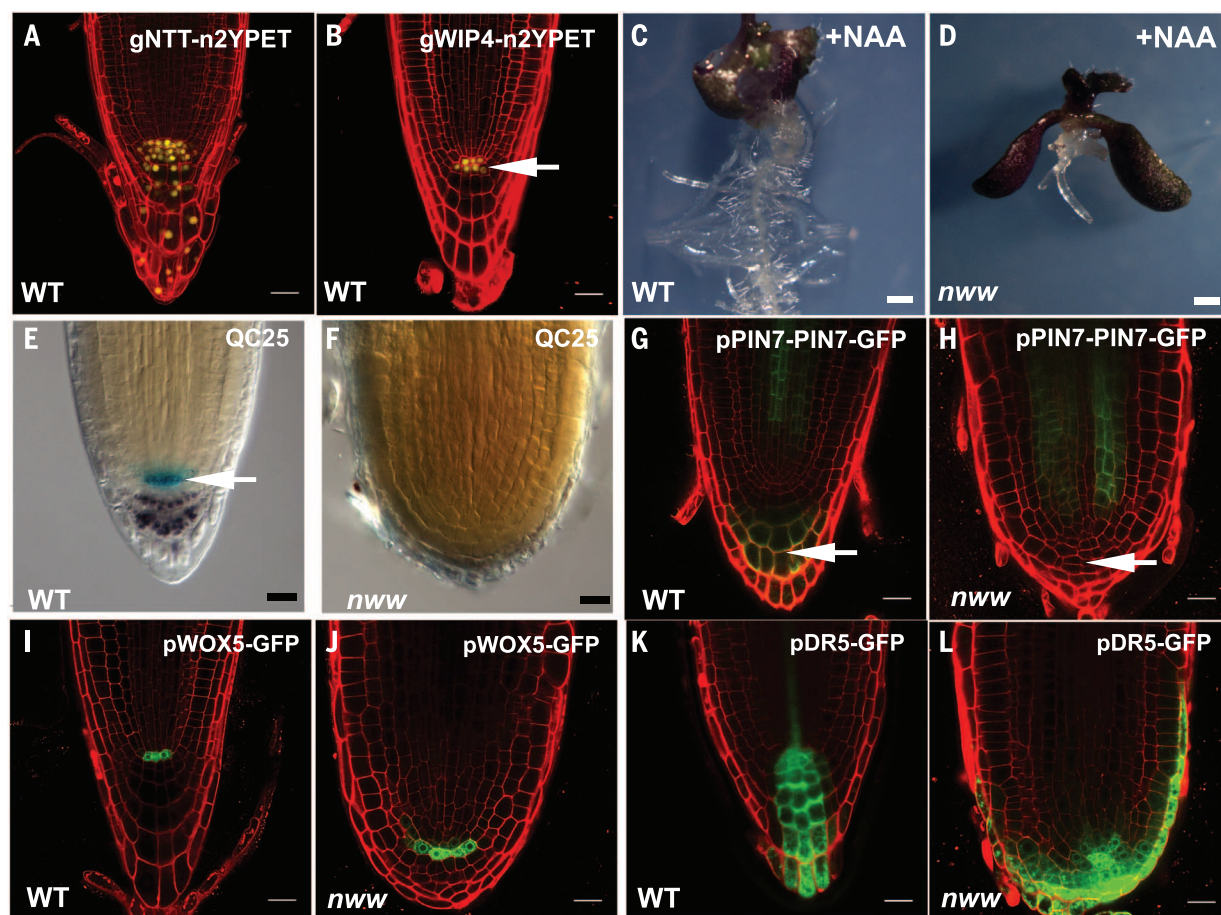


Fig. 3. Control of distal meristem fate within the root. (A and B) Accumulation of *NTT* (A) and *WIP4* (B) in the quiescent center and columella initials (arrow) of the root meristem. (C and D) Rescued root phenotype of the wild type (C) and *nww* mutant (D) after auxin treatment and 2 days after transfer to MS media. (E to L) Phenotype of the wild type [(E), (G), (I), and (K)] and *nww* mutant [(F), (H), (J), and (L)]. The QC25

marker is indicated by an arrow in the wild type (E) and is absent in *nww* mutant (F). pPIN7-PIN7-GFP marker, with distal expression indicated by an arrow in the wild type (G) and absent in the *nww* mutant (H). pWOX5-GFP [(I) and (J)] and pDR5-GFP [(K) and (L)] markers in the wild type [(I) and (K)] and *nww* mutant [(J) and (L)]. Scale bars, 20 μ m in (A), (B), and (E) to (L); 1 mm in (C) and (D).

the embryo. A recombinered *MP* 2XYPET reporter, gMP-n2YPET, accumulated broadly in the embryo, including all of the suspensor region that includes the hypophysis (Fig. 2E and fig. S5). Similarly, in situ data and the pMP-MP-green fluorescent protein (GFP) reporter showed expression in the hypophysis (fig. S5, D to G). We detected *MP* expression in WT embryos but not in the *mp* mutant embryos (Fig. 2, C and D). RNA-seq data confirm expression of *MP* in the suspensor region (<http://seedgenenetwork.net>) (fig. S5H). We conclude that *MP* is expressed in the hypophysis, where it promotes root meristem initiation by activating the *NWW* genes. To provide further support for the idea that NTT functions downstream of MP, we used a chromatin immunoprecipitation assay and found that MP binds in vivo to a conserved AuxRE binding site within the *NTT* intron (fig. S4F). Similar AuxRE sites are conserved in the introns of both *WIP4* and *WIP5*, and these AuxRE sites are also found in orthologs of the *NWW* genes in other Brassicaceae species (fig. S4G). These data are consistent with NTT functioning downstream of MP and suggest that MP directly binds to *NTT* regulatory sequences to promote expression.

To provide further insights into the nature of the defects seen in the *nww* triple mutant, we analyzed the expression of several relevant markers. We first looked at the expression of the pDR5-GFP marker that contains several AuxRE sites and reflects auxin signaling (9–11). In WT embryos, pDR5-GFP expression was observed in the hypophysis, and the loss of this expression in *mp* mutants has been linked to the absence of root meristem initiation (12). We found that the initial expression of the pDR5-GFP marker was similar in both WT and *nww* mutant embryos at the globular stage (Fig. 2, G and H, and fig. S6, A and B). Thus, in contrast to *MP*, our data show that the *NWW* genes are not required for the initial activation of the pDR5-GFP marker, consistent with the *NWW* genes functioning downstream of *MP*. At later stages of embryo development, expression of pDR5-GFP was much reduced in the *nww* mutant as compared with the wild type, presumably a consequence of the failure of the root meristem to form (fig. S6).

We next examined the expression of *WUSCHEL-RELATED HOMEODOMAIN* 5 (*WOX5*), a gene that is expressed in the quiescent center and is required for columella stem cell maintenance (13). During root meristem initiation, pWOX5-GFP is first detected in the hypophysis and is absent in *mp* mutants (13), which suggests that, similar to pDR5-GFP, pWOX5-GFP is also dependent on MP expression. In contrast, we found that the initial expression of pWOX5-GFP was normal in the *nww* mutant (Fig. 2, I and J), although later expression was diffuse and mislocalized apically within the *nww* mutant embryo (fig. S6). Thus, *NWW* genes are not required for the initial activation of *WOX5* but are required for maintenance of the *WOX5* expression pattern within the root meristem. Thus, even though the *MP* and *NWW* genes are normally required for root initiation, other MP-dependent targets are still activated independently of *NWW* genes (Fig. 2F).

Expression of the three *NWW* genes persists in the root meristem during postembryonic root development. We detected gNTT-n2YPET expression within the mature root meristem in the quiescent center, columella stem cells (also referred to as columella initials), and columella cells (Fig. 3A). We similarly found that gWIP4-n2YPET and gWIP5-n2YPET were expressed in the mature root meristem, although their expression was restricted to the quiescent center and columella initial cells (Fig. 3B and fig. S3J). Thus, the *NWW* genes may be needed to maintain meristem integrity in the developing root.

The plant hormone auxin can promote root initiation in tissue culture. Despite the requirement for MP for root initiation in the embryo, phenotypically WT roots can be induced if *mp* mutants are treated with auxin (14). We found that exogenous application of auxin could similarly rescue root formation in *nww* mutants (Fig. 3, C and D, and fig. S7). However, in contrast to *mp* mutants, the rescued roots of *nww* mutants are highly abnormal. The *nww*-rescued roots were larger than WT roots and failed to form amyloplasts, a marker for distal stem cell fate (Fig. 3, E and F). As a result, these rescued roots

lack a gravitropic response. Our data indicate that the *NWW* genes are required to pattern distal stem cells within the root meristem. To further test this idea, we analyzed the PINFORMED 7 marker (pPIN7-PIN7-GFP), which is normally expressed in cells derived from both the proximal and distal regions of the root meristem (Fig. 3, G and H). Consistent with our hypothesis, we found that PIN7 expression was not detected in the distal region of the *nww* mutant root meristem yet was still present in the proximal region.

Because the stereotypical pattern of cell divisions within the root meristem is dependent on signals from the quiescent center (15), the increased size and disorganization of the *nww* mutant roots suggest that the quiescent center may be abnormal. We examined the expression of two quiescent center markers, QC25 and *WOX5*. We found that the QC25 marker was not detected in the rescued roots of the *nww* mutant (Fig. 3, E and F), consistent with the idea that the quiescent center is not normal. As different quiescent center markers depend on different stem cell regulators (13), we also analyzed the expression of *WOX5*. In WT roots, pWOX5-GFP expression was detected

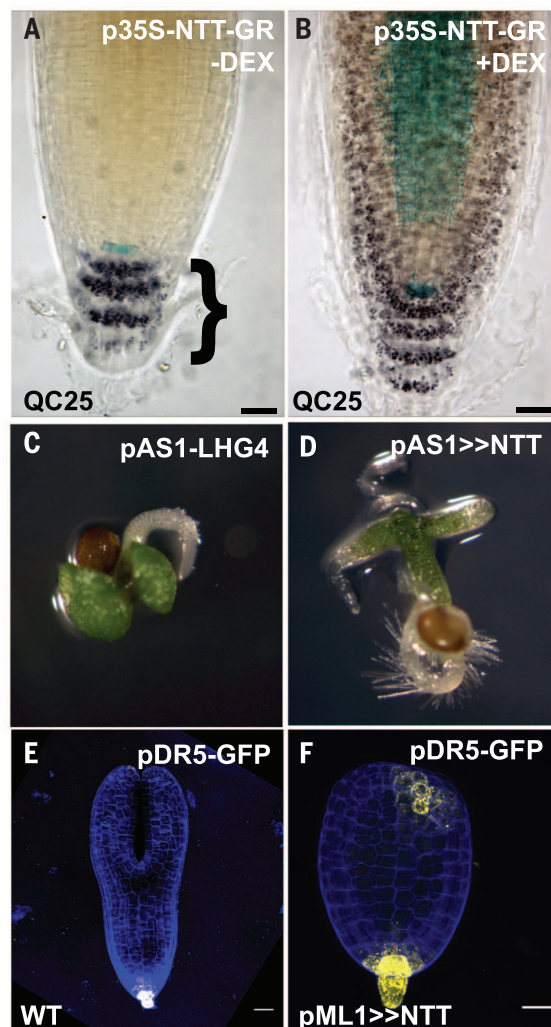


Fig. 4. QOOH kinetics. (A) Time dependence of $m/z = 125.06$ signal obtained at 8.3 eV (i.e., probing only $\text{QOOH}_{\alpha\beta}$) at several $[\text{O}_2]$ (open symbols) and the corresponding double exponential fits (solid lines). (B) Second-order plots showing the linearity of $1/\tau_{\text{rise}}$ and $1/\tau_{\text{decay}}$ versus $[\text{O}_2]$ and accompanying linear fits [symbols and colors correspond to (A)]. Their slopes determine k_{rise} and k_{decay} , respectively, which we assign as rate coefficients for $\text{QOOH}_{\alpha\beta} + \text{O}_2 \rightarrow \text{products}$ and $\text{R}_{\beta} + \text{O}_2 \rightarrow \text{QOOH}_{\alpha\beta}$ reactions, respectively.

only within the four cells of the quiescent center, whereas expression in the *nww* mutant expanded to include a larger number of cells (Fig. 3, I and J).

Because *WOX5* has been shown to be downstream of auxin signaling, we also analyzed pDR5-GFP expression to determine whether auxin signaling is altered in the *nww* mutant root (Fig. 3, K and L, and fig. S7). In WT roots, pDR5-GFP was observed in only the quiescent center and columella cells. In the rescued roots of the *nww* mutant, pDR5-GFP was misexpressed throughout the presumptive root cap. Although auxin signaling still occurs in the *nww* mutant, the altered pDR5-GFP expression pattern suggests that the roots are unable to respond to auxin in an appropriate manner. Thus, the *NWW* genes are required for appropriate development of the quiescent center and the distal root meristem.

Misexpression of *NTT* might be sufficient to transform other stem cells within the root meristem into a distal fate. To test this prediction, we created an inducible line by fusing *NTT* to the glucocorticoid receptor (p35S-NTT-GR) (16). In the wild type, columella cells are restricted to the distal region within the root meristem. In contrast, induction of *NTT* activity within mature root meristems caused ectopic production of columella cells (Fig. 4, A and B). The QC25 marker, normally expressed only in the quiescent center, was ectopically expressed in the proximal region when *NTT* activity was induced. Thus, *NTT* is both necessary and sufficient to pattern distal stem cell identity within the root meristem. The p35S-NTT-GR line can also mimic the root-inducing effects of exogenous auxin application. When WT seedlings were transferred to normal media after germinating on 10- μ M 1-naphthaleneacetic acid (NAA), extra roots were produced. Similarly, extra roots formed after p35S-NTT-GR seeds were germinated in the presence of the dexamethasone inducer and then transferred to normal media (fig. S8). This is consistent with a role of the *NWW* genes in mediating an auxin signal for root initiation.

NTT misexpression can also change stem cell fate within the embryo. In WT embryos, the apical region gives rise to the shoot apical meristem and two groups of primordial cells known as the cotyledon initials. The *ASI* gene is strongly expressed in the cotyledon initials in transition-stage embryos (17). Misexpression of *NTT* under the control of the *ASI* promoter caused roots to form instead of cotyledons in the resultant seedlings (Fig. 4, C and D, and fig. S8, E to G). This suggests that *NTT* expression is sufficient to transform cotyledon primordia to a root meristem fate within the apical region of the embryo.

More widespread *NTT* misexpression in the protodermal layer of the apical cells of early globular-stage embryos using the AtML1 promoter (pML1>>NTT) (18) resulted in embryos with asymmetrical structure, losing both the cotyledons and the shoot apical meristem (Fig. 4, E and F, and fig. S8). Taken together, these studies support a model in which *NTT* misexpression is sufficient to pattern basal stem cell identity within the embryo and distal stem cell identity in the root meristem (fig. S8K).

There is tremendous interest in identifying the major pathways that specify stem cells in both animal and plant systems. Identification of the *NWW* genes will help to explain the formation of stem cells and may ultimately allow for the manipulation of the root to enhance agricultural yield. Additionally, although many regulators have been found to pattern plant meristems, it is likely that additional intrinsic factors remain undiscovered due to genetic redundancy, as is the case with the *NWW* genes.

REFERENCES AND NOTES

1. T. Bennett, B. Scheres, in *Plant Development*, M. C. P. Timmermans, Ed. (Academic Press, San Diego, CA, 2010), pp. 67–102.
2. B. Scheres, P. Benfey, L. Dolan, in *The Arabidopsis Book*, C. R. Somerville, E. M. Meyerowitz, Eds. (American Society of Plant Biologists, Rockville, MD, 2002), pp. 1–18.
3. B. C. Crawford, M. F. Yanofsky, *Curr. Biol.* **18**, R972–R978 (2008).
4. B. C. Crawford, G. Ditta, M. F. Yanofsky, *Curr. Biol.* **17**, 1101–1108 (2007).
5. M. Sagasser, G. H. Lu, K. Hahlbrock, B. Weisshaar, *Genes Dev.* **16**, 138–149 (2002).
6. S. Warming, N. Costantino, D. L. Court, N. A. Jenkins, N. G. Copeland, *Nucleic Acids Res.* **33**, e36 (2005).
7. Y. G. Liu et al., *Proc. Natl. Acad. Sci. U.S.A.* **96**, 6535–6540 (1999).

8. C. S. Hardtke, T. Berleth, *EMBO J.* **17**, 1405–1411 (1998).
9. J. Friml et al., *Nature* **426**, 147–153 (2003).
10. J. Friml et al., *Cell* **108**, 661–673 (2002).
11. D. Weijers et al., *Plant Cell* **17**, 2517–2526 (2005).
12. D. Weijers et al., *Dev. Cell* **10**, 265–270 (2006).
13. A. K. Sarkar et al., *Nature* **446**, 811–814 (2007).
14. T. Berleth, G. Jurgens, *Development* **118**, 575–587 (1993).
15. C. van den Berg, V. Willemsen, G. Hendriks, P. Weisbeek, B. Scheres, *Nature* **390**, 287–289 (1997).
16. T. Aoyama, N. H. Chua, *Plant J.* **11**, 605–612 (1997).
17. M. E. Byrne et al., *Nature* **408**, 967–971 (2000).
18. A. Sessions, D. Weigel, M. F. Yanofsky, *Plant J.* **20**, 259–263 (1999).

ACKNOWLEDGMENTS

We thank A. Gallavotti and B. Bargmann for their critical comments and M. Estelle and Y. Zhang for use and help with the confocal microscope. This work was funded by the NSF (grants IOS-0817544 and IOS-1121055 to M.F.Y. and IOS-0822411 to J.A.L.) and the NIH (NIH/NIGMS grant 5 R01 GM072764 to J.A.L.). The supplementary materials contain additional data.

SUPPLEMENTARY MATERIALS

www.sciencemag.org/content/347/6222/655/suppl/DC1

Materials and Methods

Figs. S1 to S8

Table S1

References (19–29)

8 October 2014; accepted 9 January 2015

Published online 22 January 2015;

10.1126/science.aaa0196

ADDICTION THERAPY

Refining deep brain stimulation to emulate optogenetic treatment of synaptic pathology

Meaghan Creed,¹ Vincent Jean Pascoli,¹ Christian Lüscher^{1,2*}

Circuit remodeling driven by pathological forms of synaptic plasticity underlies several psychiatric diseases, including addiction. Deep brain stimulation (DBS) has been applied to treat a number of neurological and psychiatric conditions, although its effects are transient and mediated by largely unknown mechanisms. Recently, optogenetic protocols that restore normal transmission at identified synapses in mice have provided proof of the idea that cocaine-adaptive behavior can be reversed in vivo. The most efficient protocol relies on the activation of metabotropic glutamate receptors, mGluRs, which depotentiate excitatory synaptic inputs onto dopamine D1 receptor medium-sized spiny neurons and normalizes drug-adaptive behavior. We discovered that acute low-frequency DBS, refined by selective blockade of dopamine D1 receptors, mimics optogenetic mGluR-dependent normalization of synaptic transmission. Consequently, there was a long-lasting abolishment of behavioral sensitization.

Deep brain stimulation (DBS) consists of passing electric current, typically in excess of 100 Hz, through electrodes surgically implanted into subcortical nuclei of the brain. DBS is currently an FDA-approved treatment for Parkinson's disease, dystonia, and essential tremor (1, 2). Additional indications,

such as depression, obsessive-compulsive disorders, and addiction have been considered (3). The mechanisms by which DBS produces its therapeutic effects remain largely unknown (4, 5), although recent studies suggest that it may have widespread effects on brain network activity (6, 7). In the context of addictive disorders, altered activity in areas projecting to the nucleus accumbens (NAc), such as the medial prefrontal cortex (mPFC), has been implicated in the effects of DBS (8). The effects of classical high-frequency DBS are transient. Symptoms

¹Department of Basic Neurosciences, University of Geneva, Geneva, Switzerland. ²Service of Neurology, Department of Clinical Neurosciences, University Hospital of Geneva, Geneva, Switzerland.

*Corresponding author. E-mail: christian.luscher@unige.ch

typically reappear once stimulation is stopped, requiring lifelong continuous stimulation (9). Because pathological synaptic plasticity drives circuit dysfunction in many neurological and psychiatric disorders (10, 11), tailoring DBS to restore normal transmission may have long-lasting effects and thus represent a major therapeutic advance.

Addiction may be a condition ideally suited to test the potential of DBS to correct pathological synaptic function, because the disease is associated with behavioral changes (12) that are caused by drug-evoked synaptic plasticity of glutamatergic transmission in the mesolimbic dopamine system (13, 14). Specifically, in the NAc, cocaine exposure increases the strength of excitatory afferents onto dopamine D1 receptor-expressing medium-sized spiny neurons (D1R MSNs) (15, 16). This plasticity

underlies behavioral changes associated with drugs of abuse, such as psychomotor sensitization (15, 17). Low-frequency optogenetic stimulation of the excitatory projections to the NAc is able to reverse cocaine-evoked plasticity and erase drug-adaptive behaviors (15, 18).

Locomotor sensitization is a straightforward behavioral paradigm used to model drug-adaptive behavior (19, 20). In rodents, repeated cocaine exposure induces progressively enhanced locomotor activation in response to a cocaine injection; after five injections, the locomotor response is typically fully sensitized, a state that persists for months after cocaine withdrawal (21). Locomotor sensitization is thus thought to underlie important aspects of vulnerability to drug addiction and relapse, specifically drug craving (19, 21, 22). The expression of locomotor sensitization is medi-

ated by enhanced glutamatergic transmission in the NAc (23–25). After repeated cocaine exposure, glutamate projections selectively onto D1R MSNs of the NAc are strengthened (15, 26), which is driven by the insertion of AMPA receptors (27–29).

As expected, sequential injections of cocaine in mice [20 mg per kilogram of body weight (mg/kg), intraperitoneally (i.p.)] progressively enhanced the locomotor response, which plateaued after five sequential injections and was still elevated during the cocaine challenge test, given after 10 days of withdrawal (Fig. 1A). Classical high-frequency DBS (130 Hz, 90 μ s) applied to the shell of the NAc (Fig. 1B and fig. S1) during the cocaine challenge suppressed the sensitization, but had no effect on the acute locomotor response to cocaine in saline controls (Fig. 1C). When DBS was applied to the NAc shell for 60 min leading up to the cocaine

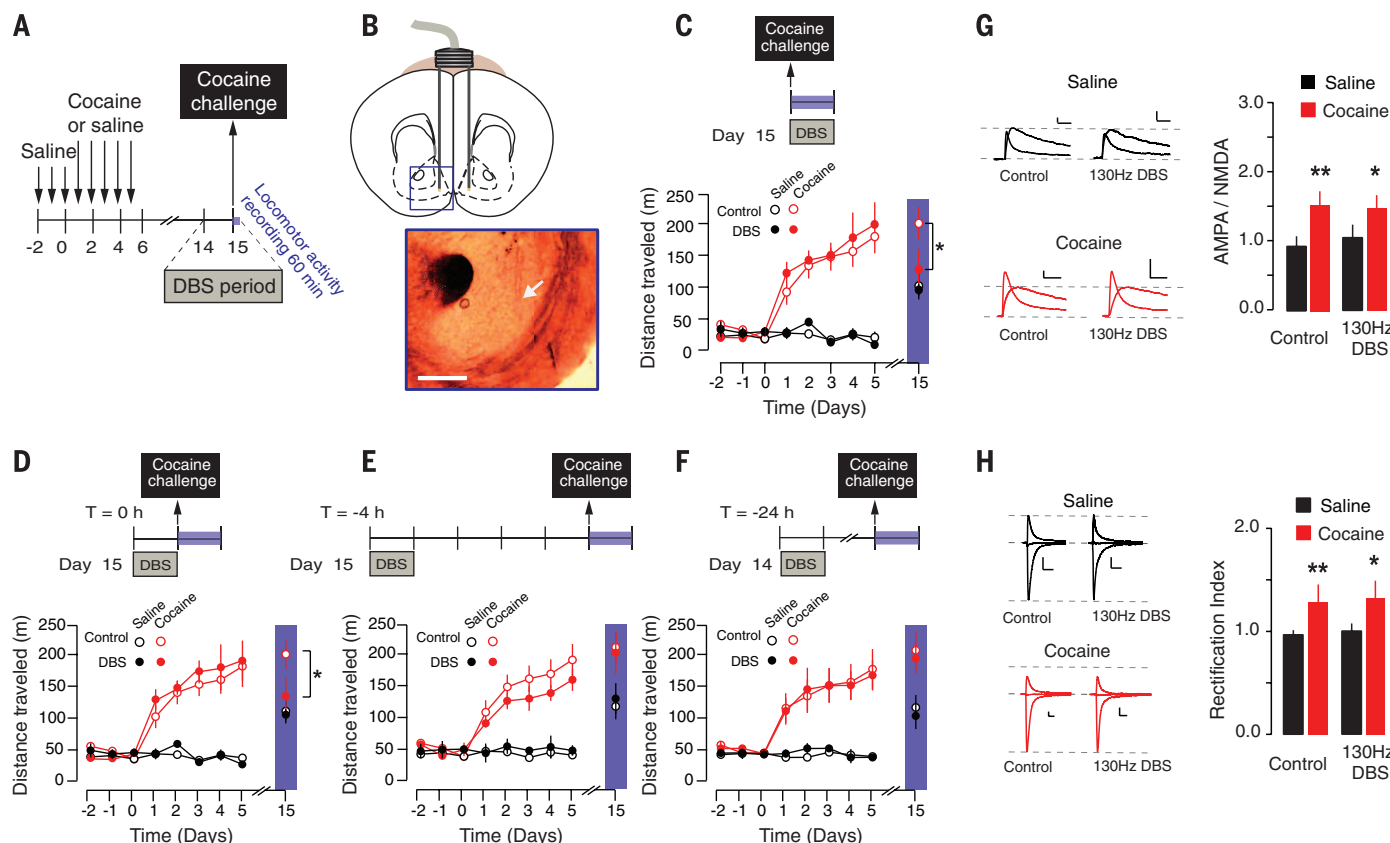


Fig. 1. Classical DBS transiently suppresses locomotor sensitization to cocaine and fails to depotentiate excitatory transmission onto D1R MSNs.

(A) Schematic of experiment: Cocaine locomotor activity is monitored for 60 min, immediately after the injection of cocaine or saline. (B) Coronal section depicting bilateral electrode placement in the anterior portion of the NAc shell. Scale bar, 250 μ m. (C) After five daily cocaine injections, a robust locomotor sensitization is observed that persists for 10 days after withdrawal; 130-Hz DBS applied during the cocaine challenge on day 15 reduced the locomotor sensitized response [controls: saline/cocaine = 10/10; 130-Hz DBS: saline/cocaine = 8/8. Repeated measures analysis of variance (ANOVA) with post-hoc *t* test; cocaine control versus cocaine 130-Hz DBS, *t* = 2.27, *P* = 0.035]. (D) 130-Hz DBS applied immediately before cocaine challenge [time (T) = 0 hours] also suppressed the sensitized response to cocaine (controls: saline/cocaine = 9/14, T = 0 hours; 130-Hz DBS: saline/cocaine = 5/9. Repeated measures ANOVA with post-hoc *t* test; cocaine control versus cocaine 130-Hz DBS, *t* = 2.19, *P* = 0.041). (E) 130-Hz DBS

did not have an effect on the sensitized response to cocaine when applied 4 hours (T = 4 hours, 130-Hz DBS: saline/cocaine = 6/8) and (F) 24 hours (T = 24 hours, 130-Hz DBS: saline/cocaine = 5/8) before cocaine challenge. (G) Cocaine treatment significantly increased the AMPA/NMDA ratio (controls: saline/cocaine = 8/7; 130-Hz DBS: saline/cocaine = 7/7. Two-way ANOVA with post-hoc *t* test, saline versus cocaine control, *t* = 2.34, *P* = 0.036, saline 130-Hz DBS versus cocaine 130-Hz DBS, *t* = 2.23, *P* = 0.049). (H) Cocaine treatment also significantly increased the rectification index (controls: saline/cocaine = 7/6; 130-Hz DBS: saline/cocaine = 7/7. Two-way ANOVA with post-hoc *t* test, saline versus cocaine control, *t* = 2.39, *P* = 0.034; saline 130-Hz DBS versus cocaine 130-Hz DBS, *t* = 2.21, *P* = 0.050) measured in D1R MSNs; 130-Hz DBS had no effect on either parameter. Representative traces of control animals (left) and animals treated with 130-Hz DBS (right) are shown. Saline-treated animals are shown in black and cocaine-treated animals in red. Scale bars are 20 pA and 20 ms. All plots are means with SEM, **P* < 0.05, ***P* < 0.01.

challenge, locomotor sensitization was still suppressed (Fig. 1D and fig. S2, A and B). This suppression was not observed when DBS was applied to the mPFC (fig. S2C) or the core of the NAc (fig. S2D). However, when the interval between DBS offset and cocaine challenge was extended to 4 hours (Fig. 1E) or 24 hours (Fig. 1F), the sensitized response was not reduced, relative to unstimulated controls. High-frequency DBS had no effect on general ambulatory activity, as measured by an open-field task (fig. S3A). Classical high-frequency DBS thus has only a transient effect on behavioral sensitization, probably because this manipulation does not affect cocaine-evoked synaptic plasticity.

As in previous studies (15), cocaine led to a long-lasting strengthening of excitatory transmission onto D1R MSNs (Fig. 1G), which were identified by using BAC transgenic mice expressing a reporter protein (td-Tomato) under the control of a *drd1a* promoter. This potentiation was determined by measuring an increase of the ratio of AMPA receptor (AMPA) excitatory postsynaptic potentials (EPSCs) over *N*-methyl-D-aspartate receptor (NMDAR) EPSCs (the AMPA/NMDA ratio). In addition, we observed an inward rectification of AMPAR currents (Fig. 1H).

This inward rectification is indicative of GluA2-lacking AMPARs. Their insertion also contributes to increases in synaptic strength (30–32). Viral insertion of GluA2-lacking AMPARs into the NAc is indeed sufficient to induce sensitization (33). Neither of these indices of cocaine-evoked plasticity was affected by the 130-Hz DBS applied 24 hours before the ex vivo recordings (Fig. 1, G and H).

Why was high-frequency DBS unable to restore normal synaptic transmission in the NAc? To reverse cocaine-evoked potentiation, one would have to apply a depotentiation or long-term depression (LTD) protocol. Stimulation frequencies at very high frequencies (>100 Hz) are unlikely to induce a LTD [previous studies have actually shown an induction of long-term potentiation (LTP) (34, 35)] of excitatory transmission. However, in the NAc, low-frequency (10 to 15 Hz) stimulation elicits a LTD that depends on mGluRs and also efficiently removes GluA2-lacking AMPARs (36). We therefore directly compared the magnitude of synaptic depression induced by optogenetic and electrical stimulation delivered at 12 Hz in slices obtained from cocaine-treated *drd1a*-td-tomato mice (Fig. 2, A and B).

For these proof-of-concept experiments, we used one injection of cocaine 7 days before the electrophysiological recordings or the cocaine challenge, a protocol that efficiently potentiates D1R MSN afferents and induces sensitization (15). We injected ChR2 tagged with enhanced yellow fluorescent protein (eYFP) into the mPFC of *drd1a*-td-tomato mice (fig. S4A) and cut slices of the NAc after 5 to 8 weeks of expression (see the supplementary materials). Ex vivo, 473-nm light stimulation at 12 Hz induced a robust LTD of excitatory transmission onto D1R MSNs (Fig. 2C), whereas this same protocol applied with electrical stimulation failed to do so (Fig. 2D, open circles). Because previous studies have indicated that blockade of D1Rs is necessary to unmask the mGluR-dependent LTD in D1R MSNs (37), we repeated the electrical stimulation in the presence of the D1R antagonists SCH23390 (10 μ M) or SCH39166 (10 μ M). In the presence of either compound, we observed an LTD comparable to that observed with optogenetic stimulation (Fig. 2D and fig. S5A).

Using the insight gained from these ex vivo LTD experiments, we sought to design a rational DBS protocol for use in vivo. Using a two-injection

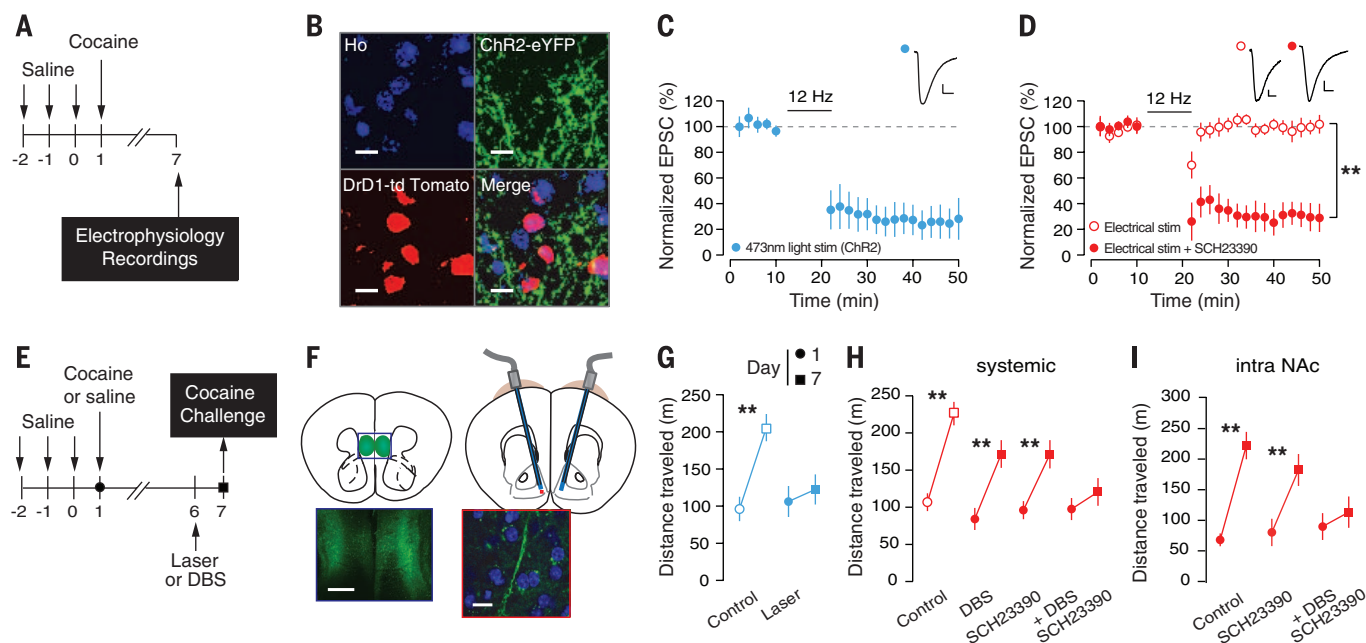


Fig. 2. Optogenetically inspired DBS reverses locomotor sensitization to cocaine and induces LTD in vitro, in the presence of a D1 antagonist. (A) Schematic of the experiment. (B) Confocal image with DAPI staining of ChR2 fibers tagged with eYFP in the NAc shell in a D1R-td-tomato mouse (scale bar, 20 μ m). (C) A robust (–61.2%) LTD of EPSC was induced by 12-Hz laser stimulation in D1R MSNs ($n = 10$, t test with paired samples, mean baseline versus mean post-HFS, $t = 4.68$, $P < 0.001$). Inset: Representative trace at baseline (black) and after 12-Hz stimulation (blue); scale bar, 5 ms, 10 pA. Symbols represent the average of 12 trials. (D) LTD of EPSC measured in D1R MSNs was not induced by 12-Hz electrical stimulation in control conditions (open circles) but was unmasked in the presence of SCH23390 (–65.17%, solid circles). Inset: Representative traces in the absence (left) and presence (right) of SCH23390 at baseline (black) and after 12-Hz stimulation (red); scale bar, 5 ms, 10 pA; left, control; right, SCH23390 (control/SCH23390 = 6/7, repeated measures ANOVA, $T \times$ SCH23390, $F = 8.50$, $P < 0.001$). (E)

Schematic of in vivo experiments. (F) Diagram of channelrhodopsin infection site (mPFC; scale bar, 200 μ m) with optic fibers implanted in the NAc shell (scale bar, 20 μ m). (G) Sensitization was abolished by 12-Hz optogenetic stimulation in vivo (control $n = 9$, laser $n = 9$; $t = 2.73$, $P = 0.015$). (H) Sensitization was significantly reduced by 12-Hz DBS in combination with SCH23390, but not by either intervention alone (control $n = 11$, SCH23390 $n = 9$, 12-Hz DBS $n = 12$, DBS + SCH23390 $n = 12$, ANOVA with t test: control versus SCH23390 + 12-Hz DBS, $t = 2.98$, $P = 0.007$, SCH23390 versus SCH23390 + 12-Hz DBS, $t = 2.63$, $P = 0.016$, 12-Hz DBS versus SCH23390 + 12-Hz DBS, $t = 2.23$, $P = 0.034$). (I) Sensitization was significantly reduced when SCH23390 was infused into the NAc shell in combination with 12-Hz DBS (control = 11, SCH23390 intraNAc + 12-Hz DBS = 12, $t = 3.00$, $P = 0.007$), but not by infusion of SCH23390 alone ($n = 12$, control versus SCH23390 intraNAc, $t = 0.93$, $P = 0.363$). All plots are means with SEM, * $P < 0.05$, ** $P < 0.01$.

sensitization paradigm, we determined that 12-Hz *in vivo* optogenetic stimulation (Fig. 2, E and F, and fig. S4B) applied bilaterally to the NAc 24 hours before the cocaine challenge abolished the sensitized locomotor response (Fig. 2G). Neither 12-Hz DBS alone nor SCH23390 (0.3 mg/kg, *i.p.*) administered alone affected sensitization,

but when given in combination, sensitization was abolished when challenged 24 hours later (Fig. 2H). To confirm that local blockade of D1Rs is necessary for the effects of 12-Hz DBS, we infused SCH23390 (0.15 μ g in 300 nl) bilaterally into the NAc shell. This infusion, in combination with 12-Hz DBS, was sufficient to abolish sensitization,

confirming the important role of the antagonism of D1R specifically in the NAc (Fig. 2I). None of the above interventions affected spontaneous locomotor activity (fig. S3, B and C).

To establish a causal link between cocaine-evoked synaptic plasticity and the abolition of fully established locomotor sensitization, we evaluated

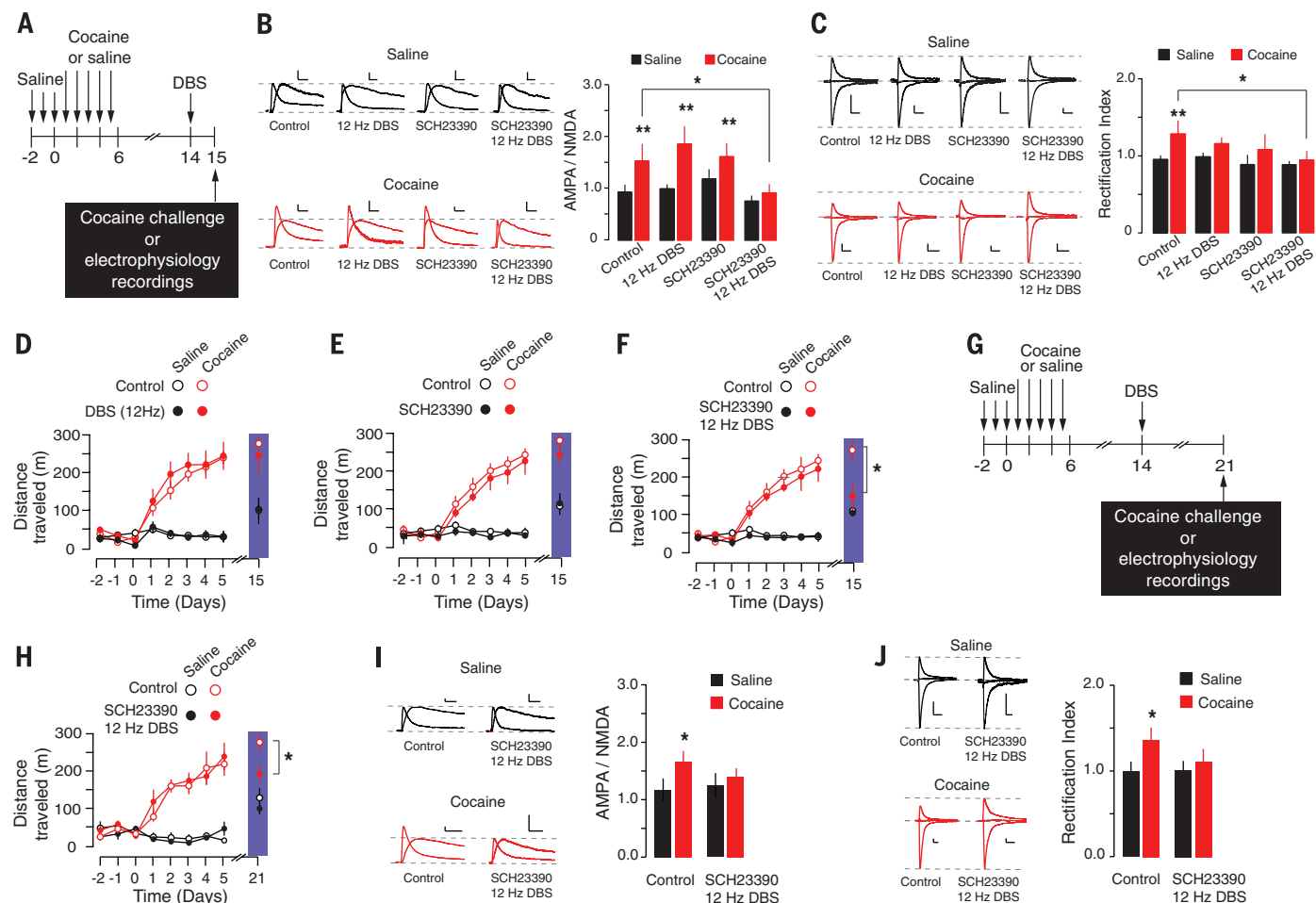


Fig. 3. Optogenetically inspired DBS reverses locomotor sensitization to cocaine and cocaine-evoked plasticity in D1R MSNs. (A) Schematic of experiment. (B) Representative traces and summary plot of AMPA/NMDA ($n = 6$ to 8 cells per condition). There was a significant effect of cocaine (ANOVA, cocaine effect $F_1 = 10.76$, $P = 0.002$) and a significant interaction between DBS and SCH23390 treatment ($F_1 = 5.74$, $P = 0.020$) on the AMPA/NMDA ratio. AMPA/NMDA in cocaine-treated animals treated with DBS was reduced to the level of that in saline-treated controls (cocaine control versus cocaine + DBS, $t = 2.39$, $P = 0.029$). Sample traces are of AMPA and NMDA EPSCs at +40 mV from saline- (black) and cocaine-treated (red) animals. (C) Representative traces and summary plot of rectification index ($n = 6$ to 8 cells per condition). There was a significant effect of cocaine on RI (ANOVA, cocaine effect $F_1 = 6.04$, $P = 0.018$); cocaine-treated animals that had undergone DBS were not different from saline-treated controls (cocaine control versus cocaine + DBS, $t = 2.16$, $P = 0.046$). Sample traces are of AMPAR EPSCs at -70, 0, and +40 mV from saline- (black) and cocaine-treated (red) animals. (D) 12-Hz DBS alone (controls: saline/cocaine = 9/10, 12-Hz DBS: saline/cocaine = 6/8) or (E) SCH23390 alone (controls: saline/cocaine = 9/9; SCH23390: saline/cocaine = 5/7) did not affect sensitization to cocaine. (F) 12-Hz DBS in combination with SCH23390 reduced the sensitized locomotor response to cocaine (controls: saline/cocaine = 9/10;

DBS: saline/cocaine = 11/8, post-hoc t test on cocaine challenge: cocaine control versus cocaine 12-Hz DBS, $t = 2.98$, $P = 0.008$); there was a significant effect of cocaine (repeated measures ANOVA, $F_1 = 30.72$, $P < 0.001$) and interaction between time and DBS ($F_5 = 17.48$, $P < 0.001$) and interaction between cocaine and treatment ($F_5 = 2.707$, $P = 0.022$, post-hoc t test on cocaine challenge: cocaine control versus cocaine DBS, $t = 2.98$, $P = 0.008$). (G) Experimental protocol. (H) Locomotor response to cocaine was suppressed 7 days after DBS with SCH23390 (controls: saline/cocaine = 4/6; DBS + SCH23390: saline/cocaine = 6/10, cocaine control versus cocaine + SCH23390 and DBS, $t = 2.59$, $P = 0.021$). (I) Representative traces and summary plot of AMPA/NMDA in cocaine-treated animals treated with DBS was reduced to the level of saline-treated controls (cocaine control versus cocaine + SCH23390 DBS, $t = 2.35$, $P = 0.029$). Sample traces are of AMPA and NMDA EPSCs at +40 mV from saline- (black) and cocaine-treated (red) animals. (J) Representative traces and summary plot of rectification index ($n = 6$ to 9 cells per condition). Cocaine-treated animals that had undergone DBS were not different from saline-treated controls (cocaine control versus cocaine + DBS, $t = 2.02$, $P = 0.062$). Sample traces are of AMPAR EPSCs at -70, 0, and +40 mV from saline- (black) and cocaine-treated (red) animals. Scale bars, 20 pA and 20 ms. * $P < 0.05$, ** $P < 0.01$.

the effects of LTD on synaptic transmission by returning to the five-injection sensitization protocol. Mice underwent 5 days of cocaine treatment, and electrophysiological recordings were performed after 10 days of withdrawal (Fig. 3A and fig. S5B). In control animals, cocaine treatment led to an increase in the AMPA/NMDA ratio and rectification index (Fig. 3, B and C, and fig. S4C). 12-Hz DBS, when applied in combination with the D1R antagonist, normalized these parameters, but 12-Hz DBS or D1R antagonist applied separately failed to do so (Fig. 3, B and C, and fig. S5, C and D). Accordingly, in the five-injection sensitization protocol, 12-Hz DBS alone (Fig. 3D) or SCH23390 alone (Fig. 3E) had no effect on sensitization, whereas SCH23390 or SCH39166 in combination with DBS significantly reduced the sensitization, without affecting the acute response to cocaine (Fig. 3F and fig. S5E). There was a trend toward a decrease in the RI with SCH23390, which could be due to an endogenous activation of mGluR signaling. In the case of 12-Hz DBS alone, the strong mGluR activation may partially overcome inhibi-

tion by D1R signaling. However, these effects were not significant, and there was no effect of either intervention on locomotor sensitization.

These results were comparable in magnitude to the effects of 12-Hz optogenetic stimulation on the sensitized response to cocaine and cocaine-evoked plasticity in the same five-injection protocol (fig. S6, A to D). Furthermore, we confirmed that the sensitized locomotor response to cocaine was still present 2 weeks after cocaine exposure (Fig. 3G), and we demonstrated that the sensitized locomotor response was still suppressed when DBS in combination with SCH23390 was given 1 week before the challenge. Cocaine-evoked plasticity was also still normalized at this time point (Fig. 3, I and J). These results strengthen the observation that the acute intervention has long-lasting effects on both cocaine-evoked plasticity and consequent locomotor sensitization.

There are two general classes of LTD available in MSNs of the NAc. mGluR-dependent LTD is induced at frequencies between 10 and 15 Hz,

whereas a second form depends on NMDAR activation and is induced by stimulation at lower frequencies (~1 Hz) (38–40). Given that DBS was delivered at 12 Hz, a mGluR-dependent mechanism seems likely. In a final series of experiments, we confirmed the crucial role of mGluR1 in the effects of DBS in combination with SCH23390. Mice pretreated with the selective mGluR1 antagonist A-841720 (0.1 mg/kg, i.p.) were not sensitive to the effects of SCH23390 in combination with 12-Hz DBS, in reversing both locomotor sensitization (Fig. 4A) and cocaine-evoked plasticity (Fig. 4B). Conversely, pretreatment with NMDAR antagonist MK-801 (0.2 mg/kg, i.p.) had no effect on the efficacy of SCH23390 in combination with 12-Hz DBS (Fig. 4, C and D). Again, no intervention tested affected acute locomotor activity (fig. S2D). To further highlight the crucial role of the mGluR1 receptor in the depotentiation mechanism induced by DBS, we first showed that the activation of mGluR1 by dihydroxyphenylglycine (DHPG) in presence of the mGluR5 antagonist MPEP (see

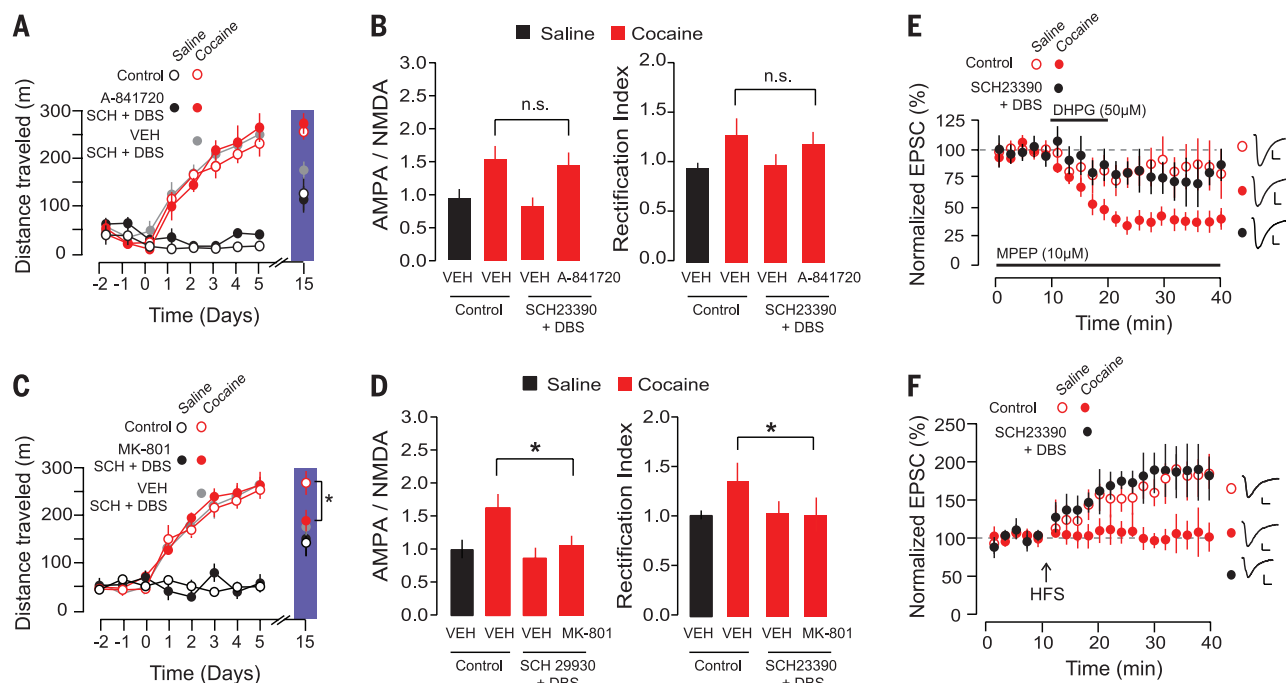


Fig. 4. Optogenetically inspired DBS exerts its effects via an mGluR-dependent mechanism. (A) Pretreatment with the mGluR1 antagonist A-841720 prevented the reversal of sensitized locomotor response (controls: saline/cocaine = 7/12; A-841720 with SCH23390 + 12-Hz DBS: saline/cocaine = 4/6) and (B) reversal of increased AMPA/NMDA and rectification index (AMPA/NMDA: controls: saline/cocaine = 8/7; cocaine with SCH23390 + 12-Hz DBS with/without A-841720 pretreatment = 11/12. Rectification index: controls: saline/cocaine = 6/7; cocaine with O_iDBS with/without A-841720 pretreatment = 8/11) induced by SCH23390 + 12-Hz DBS in cocaine-treated animals. (C) MK-801 did not alter the ability of SCH23390 + 12-Hz DBS to reverse locomotor sensitization (controls: saline/cocaine = 7/6; A-841720 with SCH23390 + 12-Hz DBS: saline/cocaine = 5/5) or (D) cocaine-evoked increases in the AMPA/NMDA (left) or rectification index (right). (E) A slight LTD of EPSCs in D1R MSNs was induced by DHPG (50 μM) in saline-treated animals (−22.67% ± 18.74), which was greater in cocaine-treated animals (−68.26%, ± 16.14), after incubation with MPEP. This DHPG-induced LTD was occluded in cocaine-treated animals that underwent

SCH23390 + 12-Hz DBS (−19.65% ± 15.52. Controls: saline/cocaine = 9/12; cocaine with SCH23390 + 12-Hz DBS = 8. Repeated measures ANOVA, treatment effect $F_2 = 5.92$, $P = 0.008$; Bonferroni post-hoc test, saline versus cocaine $P = 0.006$, saline versus cocaine and SCH23390 + 12-Hz DBS, $P = 0.939$). Inset: Representative traces at baseline (black) and 20 min after protocol (red) in saline-treated mice (top), cocaine-treated mice (center), and cocaine-treated mice that underwent SCH23390 + 12-Hz DBS 24 hours before being killed (bottom). Scale bar = 10 pA, 50 ms. (F) HFS induced an LTP of EPSCs in D1R MSNs in saline-treated animals (89.37%, ± 21.31), but was occluded in cocaine-treated animals (−76.4%, ± 15.132) (controls: saline/cocaine = 9/7, repeated measures ANOVA, effect of treatment $F_2 = 9.016$, $P = 0.002$; Bonferroni post-hoc test, saline versus cocaine, $P = 0.987$). LTP in cocaine-treated mice was rescued by treatment with SCH23390 + 12-Hz DBS (110.49%, ± 29.87; $n = 6$, $P = 0.004$). Inset: Representative traces at baseline (black) and 20 min after protocol (red), in saline-treated mice (top), cocaine-treated mice (center), and cocaine-treated mice that underwent SCH23390 + 12-Hz DBS (bottom). Scale bars, 10 pA, 50 ms.

methods) induced a LTD of excitatory transmission onto D1R MSNs (Fig. 4E). Consistent with previous studies, the magnitude of this LTD was enhanced in cocaine-treated as compared to saline-treated animals (41, 42). However, in cocaine-treated animals that underwent SCH23390 exposure in combination with 12-Hz DBS 24 hours before being killed, this enhanced mGluR1 LTD was occluded, suggesting a shared mechanism between DBS and DHPG-induced LTD. Finally, cocaine exposure occludes the ability of high-frequency stimulation (HFS) to induce a LTP in D1R MSNs (15). SCH23390 in combination with 12-Hz DBS rescued HFS LTP in cocaine treated animals, further suggesting that DBS induces a depotentiation in vivo (Fig. 4F).

We used insight obtained from optogenetic in vivo manipulations to propose a novel DBS protocol, which efficiently abolishes behavioral sensitization to cocaine through the reversal of cocaine-evoked potentiation of excitatory transmission onto D1R MSNs. Classical high-frequency DBS does not alter cocaine-evoked plasticity and has only transient effects on locomotor sensitization; its behavioral effects are mediated through a mechanism that remains elusive. Low-frequency DBS applied on its own fails to affect drug-evoked plasticity, most likely because it causes release from dopamine terminals, due to the nonspecific nature of electrical stimulation. Only the combination of acute low-frequency DBS with a D1R antagonist (optogenetically inspired DBS) then enables the induction of the mGluR1 LTD necessary for the depotentiation of synapses on D1R MSNs, most likely formed by the projections from the mPFC (18), and abolishment of the drug-adaptive behavior. Given that SCH23390 is a U.S. Food and Drug Administration-approved D1R antagonist (43), translational studies in humans may be feasible.

Our results demonstrate the potential of novel DBS protocols inspired by optogenetic manipulations of synaptic pathology. Using DBS to correct synaptic pathology and restore normal behavior may have applications in other neuropsychiatric disorders. Given the obstacles to the rapid translation of optogenetic interventions to humans (44), these findings may lead to a full realization of the potential of novel DBS protocols.

REFERENCES AND NOTES

1. A. L. Benabid et al., *Lancet* **337**, 403–406 (1991).
2. S. Miocinovic, S. Somayajula, S. Chitnis, J. L. Vitek, *J. Am. Med. Assoc. Neurol.* **70**, 163–171 (2013).
3. N. R. Williams, M. S. Okun, *J. Clin. Invest.* **123**, 4546–4556 (2013).
4. H. J. Heinze et al., *Front. Hum. Neurosci.* **3**, 22 (2009).
5. U. J. Müller et al., *Ann. N. Y. Acad. Sci.* **1282**, 119–128 (2013).
6. P. J. Hahn, C. C. McIntyre, *J. Comput. Neurosci.* **28**, 425–441 (2010).
7. M. S. Okun, *N. Engl. J. Med.* **28**, 425–441 (2010).
8. F. M. Vassoler et al., *J. Neurosci.* **33**, 14446–14454 (2013).
9. K. A. Follett, *Annu. Rev. Med.* **51**, 135–147 (2000).
10. A. F. Arnsten, K. Rubia, *J. Am. Acad. Child Adolesc. Psychiatry* **51**, 356–367 (2012).
11. K. Deisseroth, *Nature* **505**, 309–317 (2014).
12. G. F. Koob, N. D. Volkow, *Neuropsychopharmacology* **35**, 217–238 (2010).
13. M. C. Creed, C. Lüscher, *Curr. Opin. Neurobiol.* **23**, 553–558 (2013).
14. C. Lüscher, R. C. Malenka, *Neuron* **69**, 650–663 (2011).
15. V. Pascoli, M. Turiault, C. Lüscher, *Nature* **481**, 71–75 (2011).
16. A. F. MacAskill, J. M. Cassel, A. G. Carter, *Nat. Neurosci.* **17**, 1198–1207 (2014).
17. G. Di Chiara, V. Bassareo, *Curr. Opin. Pharmacol.* **7**, 69–76 (2007).
18. V. Pascoli et al., *Nature* **509**, 459–464 (2014).
19. T. E. Robinson, K. C. Berridge, *Addiction* **96**, 103–114 (2001).
20. E. Valjent et al., *Neuropsychopharmacology* **35**, 401–415 (2010).
21. T. E. Robinson, K. C. Berridge, *Brain Res. Brain Res. Rev.* **18**, 247–291 (1993).
22. J. D. Stokette, P. W. Kalivas, *Pharmacol. Rev.* **63**, 348–365 (2011).
23. M. S. Reid, S. P. Berger, *Neuroreport* **7**, 1325–1329 (1996).
24. Y. Li, M. E. Wolf, F. J. White, *Behav. Brain Res.* **104**, 119–125 (1999).
25. P. W. Kalivas, B. Weber, *J. Pharmacol. Exp. Ther.* **245**, 1095–1102 (1988).
26. J. P. Britt et al., *Neuron* **76**, 790–803 (2012).
27. A. C. Boudreau, M. E. Wolf, *J. Neurosci.* **25**, 9144–9151 (2005).
28. K. L. Conrad et al., *Nature* **454**, 118–121 (2008).
29. L. J. Vanderschuren, P. W. Kalivas, *Psychopharmacology (Berlin)* **151**, 99–120 (2000).
30. E. S. Guire, M. C. Oh, T. R. Soderling, V. A. Derkach, *J. Neurosci.* **28**, 6000–6009 (2008).
31. S. Q. Liu, S. G. Cull-Candy, *Nature* **405**, 454–458 (2000).
32. K. Plant et al., *Nat. Neurosci.* **9**, 602–604 (2006).
33. W. A. Carlezon Jr. et al., *Science* **282**, 2272–2275 (1998).
34. S. M. Schotanus, K. Chergui, *Eur. J. Neurosci.* **27**, 1957–1964 (2008).
35. E. Cahill et al., *Mol. Psychiatry* **19**, 1295–1304 (2014).
36. C. C. Huang et al., *J. Neurosci.* **31**, 4194–4203 (2011).
37. W. Shen, M. Flajolet, P. Greengard, D. J. Surmeier, *Science* **321**, 848–851 (2008).
38. S. Thomas et al., *Philos. Trans. R. Soc. London Ser. B* **358**, 815–819 (2003).
39. D. Robbe, M. Kopf, A. Remaury, J. Bockaert, O. J. Manzoni, *Proc. Natl. Acad. Sci. U.S.A.* **99**, 8384–8388 (2002).
40. C. Lüscher, R. C. Malenka, *Cold Spring Harb. Perspect. Biol.* **4**, 1–15 (2012).
41. J. E. McCutcheon et al., *J. Neurosci.* **31**, 14536–14541 (2011).
42. M. E. Wolf, K. Y. Tseng, *Front. Mol. Neurosci.* **5**, 72 (2012).
43. R. C. Pierce, C. P. O'Brien, P. J. Kenny, L. J. Vanderschuren, *Cold Spring Harb. Perspect. Med.* **2**, 1–8 (2012).
44. B. Y. Chow, E. S. Boyden, *Sci. Transl. Med.* **5**, 177ps5 (2013).

ACKNOWLEDGMENTS

Funding was provided by the Swiss National Science Foundation, the National Competence Center for Research Synapsy, the European Brain Council (Advanced grant MeSSI), the Carigest Foundation, the Academic Society of Geneva, and the Fondation Divisa Foundation. We thank P. Pollak, D. Jabaudon, E. O'Connor, and A. Holtmaat for feedback on the manuscript and members of the Lüscher lab for stimulating discussions. Data sets presented in this study are available at the University of Geneva open access data archive (www.archive-ouverte.unige.ch) with accession number 18515.

SUPPLEMENTARY MATERIALS

www.sciencemag.org/content/347/6222/659/suppl/DC1
Materials and Methods
Figs. S1 to S6
Table S1
References (45–49)

3 September 2014; accepted 8 January 2015
10.1126/science.1260776

GENOMIC VARIATION

Impact of regulatory variation from RNA to protein

Alexis Battle,^{1,2,*} Zia Khan,^{3,†} Sidney H. Wang,^{3,‡} Amy Mitrano,³ Michael J. Ford,⁴ Jonathan K. Pritchard,^{1,2,§} Yoav Gilad^{3,§}

The phenotypic consequences of expression quantitative trait loci (eQTLs) are presumably due to their effects on protein expression levels. Yet the impact of genetic variation, including eQTLs, on protein levels remains poorly understood. To address this, we mapped genetic variants that are associated with eQTLs, ribosome occupancy (rQTLs), or protein abundance (pQTLs). We found that most QTLs are associated with transcript expression levels, with consequent effects on ribosome and protein levels. However, eQTLs tend to have significantly reduced effect sizes on protein levels, which suggests that their potential impact on downstream phenotypes is often attenuated or buffered. Additionally, we identified a class of cis QTLs that affect protein abundance with little or no effect on messenger RNA or ribosome levels, which suggests that they may arise from differences in posttranslational regulation.

To understand the links between genetic and phenotypic variation, it may be essential to first understand how genetic variation impacts the regulation of gene expression. Previous studies have evaluated the association between variation and transcript expression in humans (1–3). Yet protein abundances are more direct determinants of cellular functions (4), and the impact of genetic differences on the multistage process of gene expression through transcription and translation to steady-state protein levels has not been fully characterized. Studies in model organisms have shown that var-

iations in mRNA and protein expression levels are often uncorrelated (5–8). Comparative studies (9–13) have suggested that protein expression evolves under greater evolutionary constraint than transcript levels (14) and have provided evidence consistent with buffering of protein expression with respect to variation introduced at the transcript level. Yet, in contrast to comparative work, there are few reports of quantitative trait loci (QTLs) associated with protein levels (pQTLs) in humans (15–17).

Here, we present a unified analysis of the association of genetic variation with transcript

expression, ribosome profiling (18), and steady-state protein levels in a set of HapMap Yoruba (Ibadan, Nigeria) lymphoblastoid cell lines (LCLs). We collected ribosome profiling data for 72 Yoruba LCLs and quantified protein abundance in 62 of these lines. Genome-wide genotypes and RNA-sequencing (RNAseq) data were available for all lines (29).

Ribosome profiling is an effective way to measure changes in translational regulation by using sequencing (18). We obtained a median coverage of 12 million mapped reads per sample, and as expected, the ribosome profiling reads are highly concentrated within coding regions and show an enrichment of a 3-base pair (bp) periodicity, which reflects the progression of a translating ribosome (figs. S1 to S3 and table S1).

We collected relative protein expression measurements using a SILAC internal standard sample

(20) and quantitative protein mass spectrometry (fig. S4). To confirm the quality of the proteomics data (tables S2 and S3), we evaluated the agreement between measurements of distinct groups of peptides from the same protein. Differences between these measurements can reflect true biological variation (e.g., splicing) or experimental noise. The high correlations (Spearman's rho 0.7 to 0.9; R^2 of 0.3 to 0.7; depending on the sample) confirmed that we are able to precisely quantify interindividual variation in protein levels (fig. S5). We also analyzed quantifications of peptides that overlapped nonsynonymous SNPs that were heterozygous in either the analyzed or the internal standard sample (fig. S6). The median ratios measured from these peptides matched the expected values closely, indicating that our protein measurements were likely not subject to ratio compression (figs. S7 and S8).

As a final quality check, we considered variation in expression levels within and between genes. We found that transcript and protein

expression levels—which are the furthest removed processes studied here—are the least correlated (figs. S9 and S10). Our observations are in agreement with most high-throughput studies that considered large number of samples, although smaller studies have often observed higher correlations (18, 21, 22).

We mapped genetic associations with regulatory phenotypes. First, we evaluated QTLs for each phenotype independently by testing for association between the phenotype and all genetic variants with minor allele frequency >10% in a 20-kb window around the corresponding gene. We used a shared standardization, normalization, regression, and permutation pipeline for all three phenotypes. At a false discovery rate (FDR) of 10%, we detected 2355 eQTLs, 939 rQTLs, and 278 pQTLs (Table 1 and fig. S11).

There is substantial overlap among detected QTLs (fig. S12). Among the 4322 genes quantified for all three phenotypes, 54% of the genes with pQTLs also have a significant rQTL and/or eQTL. Given the incomplete statistical power

¹Department of Genetics, Stanford University, Stanford, CA 94305, USA. ²Howard Hughes Medical Institute, Stanford University, Stanford, CA 94305, USA. ³Department of Human Genetics, University of Chicago, Chicago, IL 60637, USA. ⁴MS Bioworks, LLC, 3950 Varsity Drive, Ann Arbor, MI 48108, USA. ⁵Department of Biology, Stanford University, Stanford, CA 94305, USA.
*Present address: Department of Computer Science, Johns Hopkins University, Baltimore, MD 21218, USA. †Present address: Department of Computer Science, University of Maryland, College Park, MD 20742, USA. ‡These authors contributed equally to this work. §Corresponding author. E-mail: pritch@stanford.edu (J.K.P.); gilad@uchicago.edu (Y.G.)

Table 1. Number of cis-QTLs identified at FDR of 10%.

Measurement	Genes tested	No. of cell lines	cis-QTLs
Protein abundance	4,381	62	278
Ribosome occupancy	15,059	72	939
mRNA expression	16,614	75	2,355

A shared-QTL: SLFN5, rs11080327

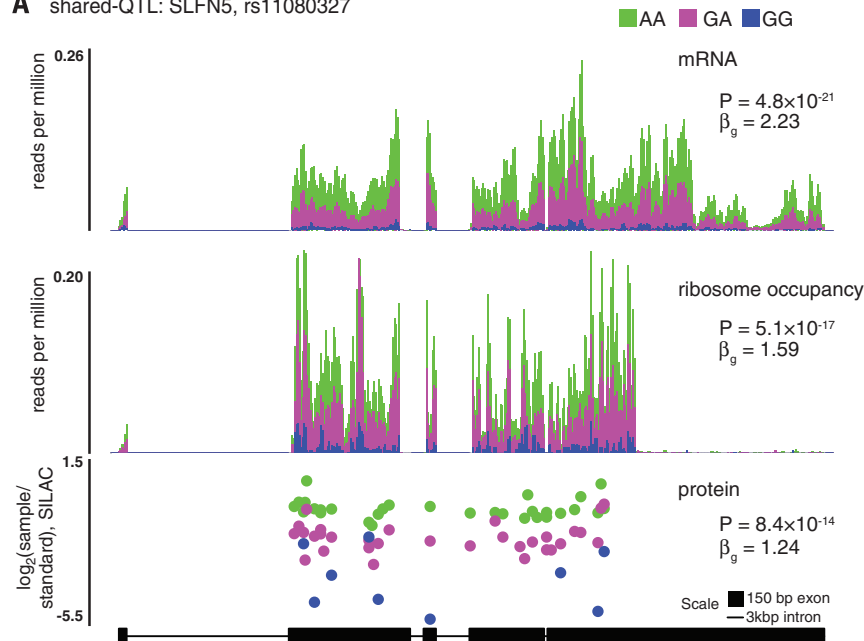


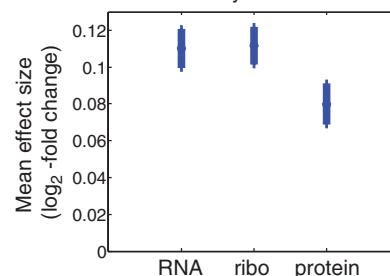
Fig. 1. Comparisons of QTLs at three levels of gene regulation. (A) Many QTLs exhibit shared effects across mRNA, ribosome occupancy, and protein. This example illustrates a shared QTL for the schlafen family member 5 (*SLFN5*) gene (24). (Top two panels) Mean sequence depth (per bp) for mRNA and ribosome occupancy, averaged among individuals with each genotype at the QTL SNP. (Bottom) Median \log_2 SILAC ratios at each detected peptide, relative to the shared internal standard. **(B)** Replication rates between independently tested cis-QTLs for each phenotype pair, at FDR = 10%. QTLs

B replication rates of cis-QTLs across phenotypes

		Replication pheno		
Discovery pheno		RNA	ribo	prot
	RNA N=902	1	0.66	0.35
	ribo N=520	0.88	1	0.51
	prot N=277	0.67	0.75	1

*FDR 0.1

C effect size of eQTLs ascertained from the GEUVADIS study



detected for the phenotype labeled on each row were tested in the phenotype listed for each column, considering only the 4322 genes quantified in all three phenotypes. **(C)** On average, eQTLs exhibit attenuated effects on protein abundance but not on ribosome occupancy. We used eQTLs detected by the GEUVADIS study to avoid ascertainment bias, and we polarized the alleles according to the direction of effect in GEUVADIS. Mean effect sizes and standard errors of the means, measured as expected fold-change per allele copy on a \log_2 scale.

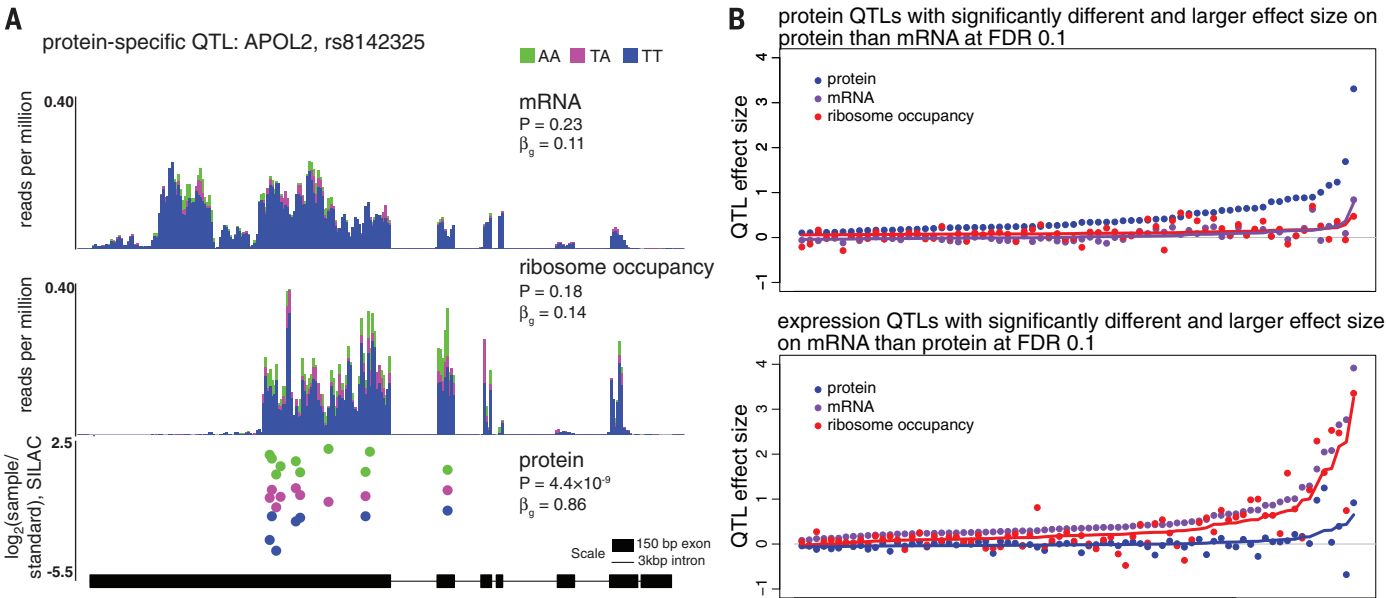


Fig. 2. Protein-specific and RNA-specific QTLs. (A) An example of a protein-specific QTL, for the apolipoprotein L 2 (*APOL2*) gene, detected by both the interaction model and the conditional models, indicating both larger effect (LRT, $P = 3.3 \times 10^{-6}$, interaction model; $P = 5.1 \times 10^{-13}$, conditional model) in protein than mRNA and that the effect on protein is not mediated by either mRNA or ribosome occupancy (LRT, $P = 2.1 \times 10^{-12}$, conditional model). Plotting details as in Fig. 1A. Although the causal variant underlying this pQTL is unknown, several linked variants near the 3' end of *APOL2* are all strongly associated with protein levels, including rs8142325

shown here and missense variant rs7285167 [linear model coefficient $\beta_g = 0.83$, $P = 9.8 \times 10^{-9}$; LRT, $P = 2.1 \times 10^{-5}$, interaction model; $P = 5.5 \times 10^{-13}$, conditional model]. (B) Effect sizes for ribosome occupancy tend to track with RNA—not protein. (Top) effect sizes in all three phenotypes are shown for psQTLs. Effect sizes were estimated using linear regression in each of the phenotypes independently. The signs of the effects were set to be positive in protein. Solid lines reflect predicted effects based on a linear model. (Bottom) Similarly, effect sizes in all three phenotypes for esQTLs. Here, signs of the effects were set to be positive in RNA.

Table 2. Enrichment of genomic annotations among esQTLs and psQTLs. Enrichments were evaluated by a continuous test using QTL results from the conditional model (see supplementary materials). Columns (from left to right) describe the annotation being considered, the number of SNPs matching this annotation, the set of SNPs used as background for the corresponding test, and the enrichment P values for psQTLs and esQTLs, respectively.

Annotation	No. of SNPs	Background	Protein	RNA
Exonic	12,568	Intergenic	2.8×10^{-14}	2.3×10^{-21}
5' UTR	6,488	Intergenic	3.2×10^{-5}	5.9×10^{-19}
3' UTR	15,139	Intergenic	2.0×10^{-6}	1.7×10^{-16}
Intronic	628,591	Intergenic	7.1×10^{-3}	$2.9 \times 10^{-38*}$
Nonsynonymous	2,099	Exonic	5.7×10^{-3}	9.7×10^{-2}
Ribo SNitch	414	Exonic	5.2×10^{-2}	2.5×10^{-2}
Acetylation site	22	Nonsynonymous	3.2×10^{-2}	0.62

*Depletion relative to background.

to detect QTLs in each dataset independently, we performed replication testing across data sets, using the specific single-nucleotide polymorphism (SNP)–gene pairs underlying each class of QTLs. This analysis is less sensitive to power limitations than genome-wide testing. The results confirm that many QTLs are shared across all three phenotypes (example in Fig. 1A). In particular, most (90%) genetic variants associated with ribosome occupancy are also associated with transcript levels (fig. S13). In contrast, eQTLs showed the lowest overlap with pQTLs (35%), as expected (Fig. 1B).

Our observation that many SNPs identified as eQTLs are not associated with differences in protein levels is consistent with the notion that, across species, protein levels diverge less

than transcript levels (12–17). Yet some QTLs may not replicate at the protein level simply because of incomplete mapping power. To address this and to avoid overestimation of effect sizes due to ascertainment bias at significant QTLs, we focused on eQTLs detected previously in European samples by the GEUVADIS study (2). We then attempted to replicate the GEUVADIS eQTLs using our transcript, ribosome profiling, and protein data and considered the mean QTL effect size in each data type. Mean effect sizes calculated in this way are expected to be unbiased with respect to either technical or biological variance.

Using this approach, we observed a reduced mean effect size for the GEUVADIS eQTLs in the protein data compared with either the RNAseq

data (t test $P = 6.7 \times 10^{-3}$) or ribosome data ($P = 5.6 \times 10^{-3}$) (Fig. 1C). In contrast, the average effect sizes observed for the RNAseq and ribosome data are not significantly different from each other, and their effect sizes are highly correlated across the tested eQTLs (Pearson $c = 0.79$, $P < 10^{-96}$) (fig. S14). The reduction in effect size observed in protein data is robust with respect to potential technical confounders, including intensity-based absolute quantification intensity level and transcript model complexity (fig. S15). We thus conclude that the majority of genetic variants affecting transcript levels also alter ribosomal occupancy, typically with a similar magnitude of effect. Yet both QTL mapping and effect-size analyses indicate that many eQTLs have attenuated (or absent) effects on steady-state protein levels (fig. S16).

In addition to the observation of generally attenuated effect sizes in pQTLs compared with eQTLs, we identified a subset of variants that appear to affect levels of proteins but not mRNA and, hence, are candidates to affect posttranscriptional gene regulation. To evaluate evidence for these, we tested each SNP for association with one regulatory phenotype, while treating one or both of the other phenotypes as covariates (conditional model). Considering protein levels, with RNA levels as a covariate, we identified 146 protein-specific QTLs (psQTLs) at FDR = 10% (Fig. 2A). The identification of psQTLs is generally robust to the choice of technology used to characterize transcript expression (fig. S17).

Using an alternative approach, an interaction model, we identified 68 psQTLs with significantly larger effects in protein than mRNA [according to a likelihood ratio test (LRT)] (FDR = 10%). We also used the interaction model to identify 76 expression-specific QTLs (esQTLs, interaction model, LRT; FDR = 10%). We then considered the ribosomal data. We found that the effect sizes for ribosomal occupancy are similar to the esQTL effect sizes (Fig. 2B). Yet, for psQTLs, low ribosome effect sizes are observed. Thus, for QTLs with discordant effects between transcript and protein, the ribosome data usually tracked with levels of RNA. Put together, these results allow us to identify loci where genetic variants have specific impacts on protein levels that are not fully mediated by regulation of either transcription or translation and hence may affect rates of protein degradation.

Finally, we performed enrichment analysis in which we considered each tested gene-SNP pair separately and evaluated the full distribution of *P* values from the conditional model (rather than choosing a significance threshold) for different genomic and functional annotations. SNPs within transcribed regions [exonic and in the untranslated region (UTR)] are enriched for more significant psQTL effects, compared with intergenic or intronic SNPs, even within the narrow 20-kb windows tested (figs. S18 to S20). In addition, psQTLs are further enriched for nonsynonymous sites (compared with all exonic SNPs) (Table 2).

Investigating additional annotations (Table 2 and fig. S21), we found that nonsynonymous SNPs near acetylation sites showed nominal enrichment for psQTLs. This possibly reflects the functional role of lysine acetylation in modulating protein degradation (23). Overall, the enrichment results suggest that genetic variants involved in posttranscriptional regulation are functionally distinct from genetic variants that primarily affect transcription—they are more likely to fall within translated regions of the gene and more likely to occur at nonsynonymous sites.

In summary, we have shown that, although a substantial fraction of regulatory genetic variants influence gene expression at all levels from mRNA to steady-state protein abundance, there are also a number of effects with specific impact on particular expression phenotypes. QTLs affecting mRNA levels are, on average, attenuated or buffered at the protein level, as has been observed between species (14). Our analysis indicates that this attenuation is not evident at the stage of translation. Although the overall phenotypic similarity between ribosome occupancy and protein abundance is high, cis-regulatory genetic effects on ribosome occupancy appear to be more strongly shared with mRNA than with protein. These observations, along with the phenotype-specific QTL analysis, indicate a scarcity of translation-specific QTLs and minimal attenuation of genetic impact between mRNA and ribosome phenotypes.

REFERENCES AND NOTES

1. A. Battle *et al.*, *Genome Res.* **24**, 14–24 (2014).
2. T. Lappalainen *et al.*, *Nature* **501**, 506–511 (2013).

3. E. Grundberg *et al.*, *Nat. Genet.* **44**, 1084–1089 (2012).
4. C. Vogel, E. M. Marcotte, *Nat. Rev. Genet.* **13**, 227–232 (2012).
5. A. Ghazalpour *et al.*, *PLOS Genet.* **7**, e1001393 (2011).
6. E. J. Foss *et al.*, *Nat. Genet.* **39**, 1369–1375 (2007).
7. P. Picotti *et al.*, *Nature* **494**, 266–270 (2013).
8. F. W. Albert, S. Treusch, A. H. Shockley, J. S. Bloom, L. Kruglyak, *Nature* **506**, 494–497 (2014).
9. J. M. Laurent *et al.*, *Proteomics* **10**, 4209–4212 (2010).
10. S. P. Schrimpf *et al.*, *PLOS Biol.* **7**, e48 (2009).
11. M. Stadler, A. Fire, *PLOS Genet.* **9**, e1003739 (2013).
12. C. G. Artieri, H. B. Fraser, *Genome Res.* **24**, 411–421 (2014).
13. C. J. McManus, G. E. May, P. Spealman, A. Shteyman, *Genome Res.* **24**, 422–430 (2014).
14. Z. Khan *et al.*, *Science* **342**, 1100–1104 (2013).
15. L. Wu *et al.*, *Nature* **499**, 79–82 (2013).
16. R. J. Hause *et al.*, *Am. J. Hum. Genet.* **95**, 194–208 (2014).
17. N. Garge *et al.*, *Mol. Cell. Proteomics* **9**, 1383–1399 (2010).
18. N. T. Ingolia, S. Ghaemmaghami, J. R. Newman, J. S. Weissman, *Science* **324**, 218–223 (2009).
19. J. K. Pickrell *et al.*, *Nature* **464**, 768–772 (2010).
20. S. E. Ong *et al.*, *Mol. Cell. Proteomics* **1**, 376–386 (2002).
21. M. Wilhelm *et al.*, *Nature* **509**, 582–587 (2014).
22. B. Schwahnhauser *et al.*, *Nature* **473**, 337–342 (2011).

23. X. J. Yang, E. Seto, *Mol. Cell* **31**, 449–461 (2008).
24. M. N. Lee *et al.*, *Science* **343**, 1246980 (2014).

ACKNOWLEDGMENTS

We thank M. Stephens, T. Flutre, and members of the Pritchard and Gilad labs for helpful discussions. This work was supported by NIH grants GM077959, HG007036, and MH084703. A.B. and J.K.P. were supported by the Howard Hughes Medical Institute. Z.K. was supported by F32HG006972. The proteomics data are available at ProteomeXchange (accession PXD001406). The ribosome profiling data are available at GEO (accession GSE61742). J.K.P. is on the Senior Advisory Board for 23andMe and DNAnexus and holds stock in both. A.B. holds stock in Google, Inc.

SUPPLEMENTARY MATERIALS

www.sciencemag.org/content/347/6222/664/suppl/DC1
Materials and Methods

Figs. S1 to S21

Tables S1 to S3

References (25–43)

Data Tables S1 to S4

3 September 2014; accepted 9 December 2014

Published online 18 December 2014;

10.1126/science.1260793

HOST RESPONSE

Inflammation-induced disruption of SCS macrophages impairs B cell responses to secondary infection

Mauro Gaya,^{1*} Angelo Castello,^{1*} Beatriz Montaner,¹ Neil Rogers,² Caetano Reis e Sousa,² Andreas Bruckbauer,¹ Facundo D. Batista^{1†}

The layer of macrophages at the subcapsular sinus (SCS) captures pathogens entering the lymph node, preventing their global dissemination and triggering an immune response. However, how infection affects SCS macrophages remains largely unexplored. Here we show that infection and inflammation disrupt the organization of SCS macrophages in a manner that involves the migration of mature dendritic cells to the lymph node. This disrupted organization reduces the capacity of SCS macrophages to retain and present antigen in a subsequent secondary infection, resulting in diminished B cell responses. Thus, the SCS macrophage layer may act as a sensor or valve during infection to temporarily shut down the lymph node to further antigenic challenge. This shutdown may increase an organism's susceptibility to secondary infections.

The highly organized architecture of the lymph node (LN) is critical for mounting effective immune responses against pathogens. One particular facet of this organization is the layer of CD169⁺ macrophages at the subcapsular sinus (SCS) floor; strategically positioned at the lymph-tissue interface to capture pathogens as they enter the LN (1). This prevents

systemic dissemination of pathogens (2–5) and allows presentation of intact antigen in the form of immune complexes, viruses, and bacteria to cognate B cells for the initiation of humoral immune responses (2, 6–8).

Infection causes a remodeling of the global architecture of the LN (9, 10). However, how this process affects the organization of the SCS macrophage layer is not well defined. To address this, we visualized the distribution of SCS macrophages in draining LNs of C57BL/6 mice after ear skin infection with *Staphylococcus aureus*, the most common etiological organism of skin and soft tissue infection. Cryosections of superficial cervical LNs were immunostained and examined 7 days after infection by confocal microscopy. The

¹Lymphocyte Interaction Laboratory, London Research Institute, Cancer Research UK, 44 Lincoln's Inn Fields, London WC2A 3LY, UK. ²Immunobiology Laboratory, London Research Institute, Cancer Research UK, 44 Lincoln's Inn Fields, London WC2A 3LY, UK.

*These authors contributed equally to this work. †Corresponding author. E-mail: facundo.batista@cancer.org.uk

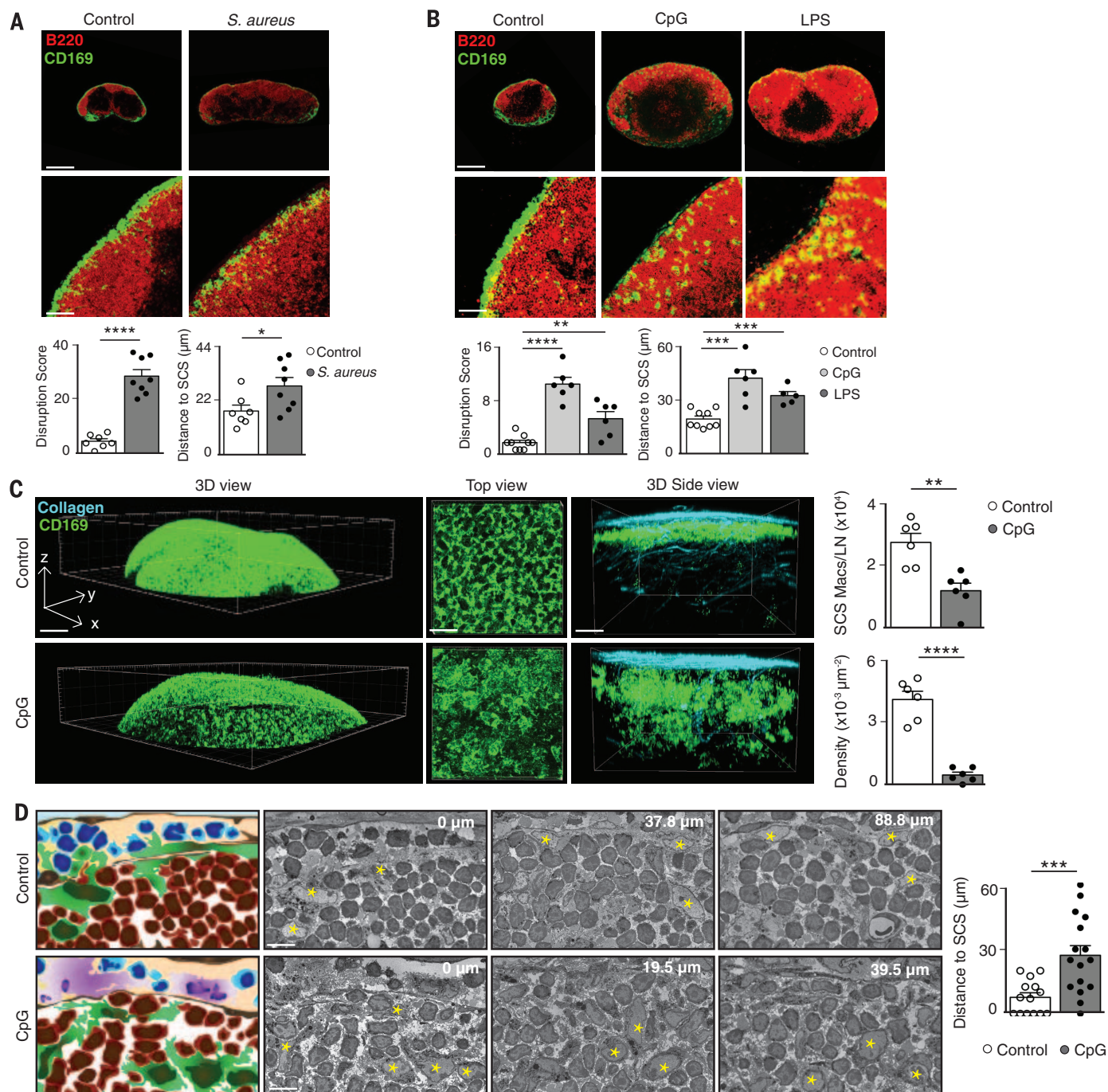


Fig. 1. Infection and inflammation disrupt SCS macrophage organization in draining LNs. (A and B) Draining LN cryosections stained for CD169 (green) and B220 (red) derived from mice administered either PBS (control), (A) 10^7 colony-forming units (CFU) of *S. aureus* in the ear 7 days previously, or (B) 10 μg of CpG or 50 μg of LPS in the footpad 4 days previously. Scale bars, 300 μm (top); 60 μm (bottom). Bar charts show the quantification of SCS macrophage disruption and distance of macrophages to LN border in each condition for an individual experiment (see materials and methods). Each dot represents the analysis of a distinct follicle. Data are shown as mean \pm SEM and are representative of at least three independent experiments. (C) Three-dimensional multiphoton microscopy of explanted popliteal LNs from animals injected in the footpad with either PBS or CpG (4 days) and anti-CD169

(green) 10 min before dissection. Second harmonic signal generated by collagen fibrils is shown (cyan). Scale bars, 500 μm (left); 40 μm (middle and right). Bar charts show the number and density of CD169⁺ macrophages in the SCS in each condition from three independent experiments. Each dot represents an individual LN. Data are shown as mean \pm SEM. (D) Representative Z sections (right) and schematics (left) of 3View electron microscopy analysis of popliteal LNs after 4 days of PBS or CpG administration. Yellow stars indicate macrophages. Scale bar, 5 μm . Bar chart represents the distance of macrophages to LN SCS in an individual experiment. Each dot indicates a single macrophage. Data are shown as mean \pm SEM and are representative of two independent experiments. Student's *t* test, **P* < 0.05, ***P* < 0.01, ****P* < 0.001, *****P* < 0.0001.

overall dimensions of the LNs were increased around fourfold with considerable enlargement of the B220⁺ follicular regions and a marked disruption of the CD169⁺ population at the SCS and interfollicular regions (Fig. 1A). We observed a similar disruption in the SCS macrophage organization after localized infection with influenza A virus, *Vaccinia* virus (VACV), and group B *Streptococcus* (GBS) but not after administration of ultraviolet (UV)-inactivated virus or inert beads (fig. S1, A to C). Notably, mice receiving either the Toll-like receptor 9 (TLR9) agonist CpG or the TLR4 agonist lipopolysaccharide (LPS) in the footpad display similar changes in the LN organization (Fig. 1B and figs. S1D and S2). This is a temporary process as the compact layer of SCS macrophages is reestablished after 28 days (fig. S1E). Overall, these data show that disruption

of SCS macrophages in draining LNs is a frequent feature associated with inflammation and viral or bacterial infections.

We further investigated this loss of integrity in the SCS macrophage layer following inflammation by using two high-resolution technologies. Three-dimensional (3D) multiphoton imaging of whole explanted LNs showed a decrease in the number and density of CD169⁺ macrophages accompanied with a change in morphology and retraction of these cells from the SCS (Fig. 1C and movie S1). Three-dimensional electron tomography, scanning 100-nm LN sections over a distance of 100 μ m, revealed that macrophages are located toward the follicular interior during inflammation, whereas they are positioned longitudinally on the inner wall of the SCS on steady state (Fig. 1D and movie S2). Together, this shows

that the characteristic disruption of SCS macrophages is a result of both cell loss and displacement of cells toward inner follicular areas.

To analyze the mechanism by which inflammation triggers alterations in SCS macrophage organization, we used the CpG-mediated inflammation model and a series of mouse strains in which different components of the TLR signaling pathway have been genetically ablated. Mice deficient in TLR9, MyD88-TRIF adaptors, or MyD88 alone did not exhibit SCS macrophage disruption, concordant with the notion that responses to CpG are mediated by TLR9 signaling via MyD88 (Fig. 2A and fig. S3). To determine which MyD88-expressing immune cell population is required for this process, we deleted MyD88 in B cells (*Myd88^{flax/flax} Cd19^{Cre}* mice), dendritic cells (DCs) (*Myd88^{flax/flax} Cdl1c^{Cre}* mice), and

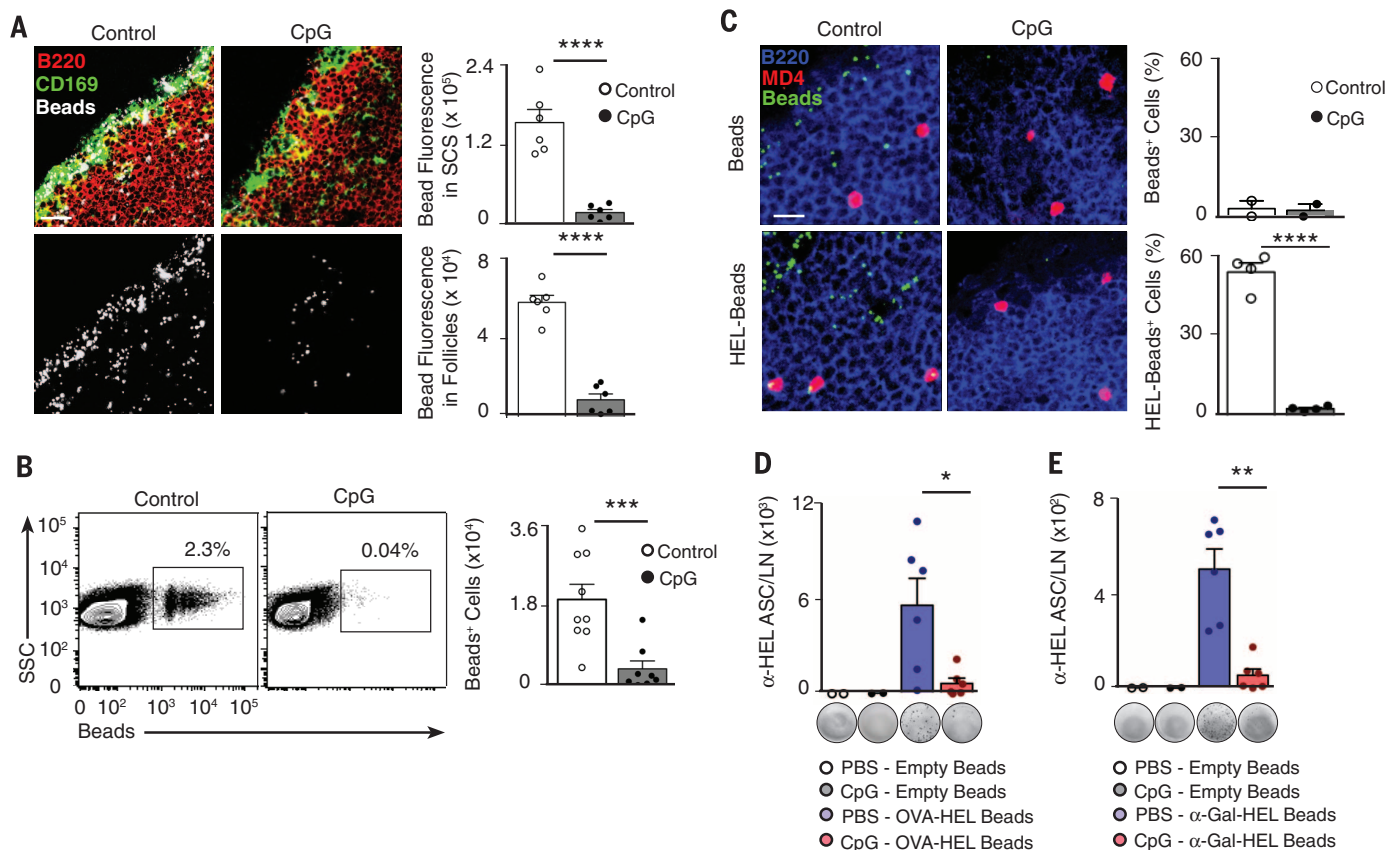


Fig. 3. Inflammation impedes acquisition of subsequent antigen by SCS macrophages and cognate B cells. (A) Confocal microscopy images of popliteal LNs from mice injected in the footpad with PBS or CpG and 4 days later injected again with 8×10^8 fluorescent microspheres (0.2 μ m, white). Sections were labeled with antibodies to B220 (red) and CD169 (green). Scale bar, 70 μ m. Bar charts represent beads fluorescence quantification in SCS and follicles from three independent experiments. (B) Flow cytometry analysis of popliteal LNs from animals treated as in (A). Representative dot plots depict beads acquisition by B220⁺CD3⁺ cells. Quantification of beads-positive cells from three independent experiments is shown in the bar chart. (C) Confocal microscopy images of LNs from mice that were (i) adoptively transferred with 5×10^6 SNARF-labeled MD4⁺ *Tlr9*^{-/-} B cells (red) on day 0, (ii) administered PBS or CpG in the footpad on day 1, (iii) injected again with 8×10^8 avidin fluorescent

particles (green) coated or not with HEL on day 5, and (iv) killed after 6 hours. Sections were stained with B220 antibody (blue). Scale bar, 20 μ m. Bar charts represent the proportion of MD4 B cells loaded with particles for an individual experiment. Data are representative of three independent experiments. (D and E) ELISPOT analysis of HEL-specific ASCs (day 14) in popliteal LNs of animals that were (i) adoptively transferred with (D) 5×10^6 MD4 *Tlr9*^{-/-} B cells and 5×10^6 OT-II T cells or (E) 2×10^6 MD4 *Tlr9*^{-/-} B cells, (ii) injected with PBS or CpG in the footpad on day 1, and (iii) injected again with (D) OVA-HEL beads or (E) α GalCer-HEL beads on day 7. Bar charts represent the number of HEL-specific ASCs in each condition for an individual experiment. Data are representative of three independent experiments. In all panels, each dot in bar charts represents a single mouse. Data are shown as mean \pm SEM. Student's *t* test, **P* < 0.05, ***P* < 0.01, ****P* < 0.001, *****P* < 0.0001.

neutrophils (*Myd88^{flax/flax} Lyz2 Cre⁺* mice) (fig. S4). As revealed by flow cytometry, MyD88 abundance in SCS macrophages remains unchanged in the different transgenic models (fig. S4). B cells are not required for SCS macrophage disruption, as this process was observed in *Myd88^{flax/flax} Cdl9 Cre⁺* and Rag2-deficient mice (Fig. 2A and fig. S5A). Furthermore, the disruption was not prevented by lack of expression of MyD88 in

neutrophils or their in vivo depletion with an antibody against Ly6G (anti-Ly6G) (Fig. 2A and fig. S5, B and C). In contrast, whereas draining LNs were enlarged in *Myd88^{flax/flax} Cdl1c Cre⁺* mice following inflammation, disruption of the SCS macrophage layer was significantly reduced (Fig. 2A and fig. S3B). These observations demonstrate that SCS macrophage disruption during inflammation is not simply due to associated

enlargement of draining LNs but requires the expression of MyD88 in the DC population.

In line with these observations, we found a significant accumulation of DCs in the SCS following inflammation (Fig. 2, B and C, and fig. S6, A and B). Therefore, to determine if DC arrival is necessary for the disruption of the SCS macrophage layer, we injected phosphate-buffered saline (PBS) or CpG into either wild-type mice

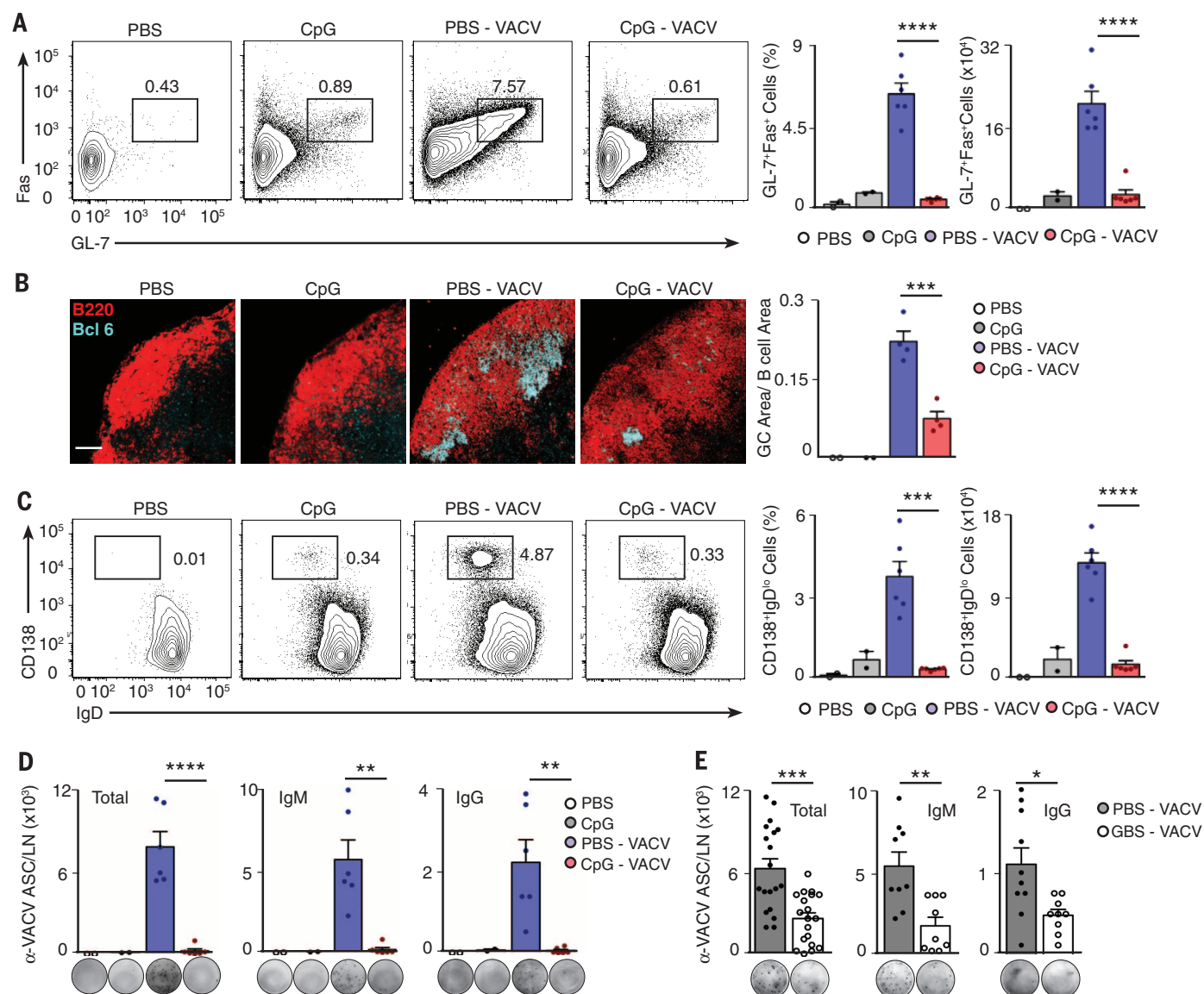


Fig. 4. Inflammation and primary infection shut down B cell responses to subsequent pathogens. (A) Flow cytometry analysis of GC formation (day 14) in popliteal LNs from mice that were administered PBS or CpG in the footpad and 7 days later infected with 10^4 plaque-forming units (PFU) of VACV. Representative contour plots display the percentage of B220⁺ cells that are GL-7⁺Fas⁺. Bar charts display the quantification of GL-7⁺Fas⁺ B cells in the different conditions for a single experiment. (B) Confocal microscopy analysis of popliteal LNs from mice treated as in (A). Sections were stained with mAbs to B220 (red) and Bcl-6 (cyan). Scale bar, 60 μ m. Quantification of the GC area for an individual experiment is depicted on the right bar chart. (C) Flow cytometry analysis of PC formation in mice treated as in (A). Representative contour plots show the

percentage of B220⁺ cells that are also CD138⁺IgD^{low}. The quantification of CD138⁺IgD^{low} B cells for a single experiment is shown on the right bar charts. (D) ELISPOT analysis of total, immunoglobulin M (IgM) and IgG VACV-specific ASCs in popliteal LNs from mice that were treated as in (A). Bar charts represent the number of VACV-specific ASCs for an individual experiment. (E) ELISPOT analysis of total, IgM, and IgG VACV-specific ASCs (day 14) from mice that were administered PBS or 10^6 CFU of GBS in the footpad and then infected with 10^4 PFU of VACV on day 7. Bar charts represent the number of VACV-specific ASCs from three independent experiments. In all panels, experiments were performed at least three times and each dot represents a different mouse. Data are shown as mean \pm SEM. Student's *t* test, **P* < 0.05, ***P* < 0.01, ****P* < 0.001, and *****P* < 0.0001.

or mice lacking CCR7, the main LN-homing chemokine receptor for DCs (fig. S6, C and D) (11). Indeed, disruption of the macrophage layer was significantly reduced in CCR7-deficient animals (Fig. 2D). To evaluate whether DC arrival to the LN is sufficient for this disruption, we adoptively transferred into the footpad bone marrow-derived DCs (BM-DCs) that were previously treated with CpG *in vitro*. We observed disruption of the SCS macrophage layer in draining LNs of animals receiving CpG-treated BM-DCs but not control DCs; neither PBS-treated nor TLR9-deficient DCs (Fig. 2E and fig. S6E). Noticeably, a marked disruption was also observed when BM-DC migration was induced independently of TLR signaling with prostaglandin E2 (12), suggesting that DC migration per se can alter SCS macrophage organization (fig. S6F). Our observations suggest that the arrival of mature DCs during inflammation plays an important role in the disruption of SCS macrophages.

We next examined the functional implications of the impaired integrity of SCS macrophages for the retention and presentation of antigen arriving in a subsequent wave. We treated mice with PBS (control), CpG, VACV, or GBS and then challenged them with fluorescent microspheres (0.2 μ m) or fluorescently labeled GBS. As described previously (6), antigen particles localized at the SCS of LNs from control mice after 6 hours (Fig. 3A). However, this accumulation was diminished in mice that had previously received CpG, VACV, or GBS (Fig. 3, A and B, and fig. S7, A to D). Antigen retention was not impaired owing to disruption in lymphatic flow or antigen transport (fig. S7, E and F) and was restored by 4 weeks after initiation of inflammation (fig. S7G). Thus, infection or inflammation has a temporary, functional impact on the capacity of SCS macrophages to retain antigen from a subsequent wave.

Antigen retained by SCS macrophages can be presented to follicular B cells, so we examined the effect of inflammation on the ability of cognate B cells to acquire antigen arriving at the LN in a subsequent wave. SNARF-labeled *Tlr9*^{-/-} MD4 B cells, expressing a transgenic B cell receptor specific for hen egg lysozyme (HEL) but unable to respond to CpG, were adoptively transferred into recipient animals. These mice were treated with either PBS (control) or CpG and later received either uncoated or HEL-coated fluorescent microspheres. In control mice, ~50% of MD4 B cells acquired one to five HEL-coated microspheres, whereas in CpG-treated mice, only 3% of B cells acquire HEL-coated microspheres and never more than one per cell (Fig. 3C and fig. S7, H and I). Thus, concordant with the reduction in antigen retention by SCS macrophages, the acquisition of cognate antigen by B cells is reduced in draining LNs following inflammation.

Does the observed reduction in antigen acquisition during inflammation affect the capacity of B cells to respond to subsequent antigen challenge *in vivo*? To address this, wild-type mice were adoptively transferred with *Tlr9*^{-/-} MD4 B cells and OT-II T cells (ovalbumin-specific T cell receptor). Afterwards, they were treated with PBS or CpG

followed by administration of HEL-ovalbumin-coated microspheres. LNs from control mice contained ~10³ HEL-specific antibody-secreting cells (ASCs), although this was significantly lower in LNs from CpG-treated mice (Fig. 3D). We observed a similar reduction in HEL-specific ASC formation when mice were adoptively transferred with *Tlr9*^{-/-} MD4 B cells followed by injection of CpG and HEL- α GalCer-coated microspheres (13) (Fig. 3E). These approaches demonstrate that inflammatory signals affect the extent to which B cells can acquire and respond to further antigenic challenge *in vivo*.

We then examined the potential impact that inflammation-mediated disruption of the SCS layer has on B cell responses to a subsequent viral infection. Wild-type mice were treated with PBS (control) or CpG and then infected with VACV. Control LNs exhibited an expansion of GL7⁺Fas⁺Bcl6⁺ germinal center (GC) B cells and CD138⁺IgD^{lo} virus-specific plasma cells (PCs) (Fig. 4, A to D). Instead, both GC and PC formation were impaired when infection was initiated after inflammation induction (Fig. 4, A to D). B cell responses to VACV were restored to control levels when infection occurred 4 weeks after CpG administration (fig. S8), a time frame consistent with the recovery of the structural integrity of the SCS macrophage layer (fig. S1E). Similar reductions in B cell responses were observed when *Diphtheria* toxin or clodronate liposomes were used to deplete SCS macrophages (14, 15) before VACV infection (fig. S9) or when mice received CpG or clodronate in the ear before infection with *S. aureus* (fig. S10). Therefore, it appears that the SCS macrophage disruption triggered by inflammation affects the ability of B cells to mount responses to viral or bacterial antigen arriving in a secondary wave.

Finally, we asked whether SCS macrophage disruption during a primary infection impedes the ability of B cells to respond to a secondary pathogen. After PBS (control) or GBS administration, mice were infected with VACV. The formation of VACV-specific PCs was significantly reduced in GBS-infected mice (Fig. 4E). This is consistent with the notion that loss of integrity of the SCS macrophage layer during primary infections severely affects the capacity of B cells to respond to secondary pathogens.

SCS macrophages have been placed at the heart of antipathogen responses because of their key role in antigen trapping and immune response initiation (1–8, 16–20). We found that infection or inflammation leads to a significant loss of CD169⁺ macrophages at the SCS and to a displacement of these cells toward inner follicular areas. Regardless of whether this is due to cell death (5) and/or macrophage redistribution, these observations raise the important question of the potential benefit of such a phenomenon. We speculate that this marked architectural reorganization might be beneficial in allowing the entry of afferent lymph-derived immune cells directly through the SCS floor (21); it may facilitate antigen relay to follicular DCs (7) or it might maximize presentation of antigen to B cells.

However, although these scenarios would be likely to enhance immune responses in a primary infection, the disruption of SCS macrophages would also render draining LNs temporarily refractory to newly arriving pathogens. This inability to respond to subsequent pathogens parallels recent findings that the failure of host defenses to counteract secondary infections results from loss of lymphoid tissue integrity or compromised innate host defense (22, 23). Here, we propose a model in which SCS macrophages function as a valve that senses inflammation within draining LNs, triggering the temporary shutdown of humoral responses to secondary infections to prioritize the effective control of contemporaneous lymph-borne infecting pathogens (fig. S11).

REFERENCES AND NOTES

1. F. D. Batista, N. E. Harwood, *Nat. Rev. Immunol.* **9**, 15–27 (2009).
2. T. Junt *et al.*, *Nature* **450**, 110–114 (2007).
3. M. Iannaccone *et al.*, *Nature* **465**, 1079–1083 (2010).
4. S. F. Gonzalez *et al.*, *Nat. Immunol.* **11**, 427–434 (2010).
5. W. Kastentmüller, P. Torabi-Parizi, N. Subramanian, T. Lämmermann, R. N. Germain, *Cell* **150**, 1235–1248 (2012).
6. Y. R. Carrasco, F. D. Batista, *Immunity* **27**, 160–171 (2007).
7. T. G. Phan, I. Grigoriou, T. Okada, J. G. Cyster, *Nat. Immunol.* **8**, 992–1000 (2007).
8. T. G. Phan, J. A. Green, E. E. Gray, Y. Xu, J. G. Cyster, *Nat. Immunol.* **10**, 786–793 (2009).
9. T. Junt, E. Scandella, B. Ludewig, *Nat. Rev. Immunol.* **8**, 764–775 (2008).
10. V. Kumar *et al.*, *Blood* **115**, 4725–4733 (2010).
11. G. J. Randolph, V. Angeli, M. A. Swartz, *Nat. Rev. Immunol.* **5**, 617–628 (2005).
12. J.-H. Yen, T. Khayrullina, D. Ganea, *Blood* **111**, 260–270 (2008).
13. P. Barral *et al.*, *Proc. Natl. Acad. Sci. U.S.A.* **105**, 8345–8350 (2008).
14. Y. Miyake *et al.*, *J. Clin. Invest.* **117**, 2268–2278 (2007).
15. F. G. Delemarre, N. Kors, G. Kraal, N. van Rooijen, *J. Leukoc. Biol.* **47**, 251–257 (1990).
16. P. Barral *et al.*, *Nat. Immunol.* **11**, 303–312 (2010).
17. T. Chtanova *et al.*, *Immunity* **31**, 342–355 (2009).
18. J. L. Coombes, S.-J. Han, N. van Rooijen, D. H. Raulet, E. A. Robey, *Cell Reports* **2**, 124–135 (2012).
19. Z. Garcia *et al.*, *Blood* **120**, 4744–4750 (2012).
20. T. Chtanova *et al.*, *Immunity* **29**, 487–496 (2008).
21. A. Braun *et al.*, *Nat. Immunol.* **12**, 879–887 (2011).
22. E. Scandella *et al.*, *Nat. Immunol.* **9**, 667–675 (2008).
23. A. M. Jamieson, S. Yu, C. H. Annicelli, R. Medzhitov, *Cell Host Microbe* **7**, 103–114 (2010).

ACKNOWLEDGMENTS

We thank A. Rot and D. Withers for the CCR7 knockout mouse strain. We thank L. Collinson, H. Armer, and C. Peddie from the electron microscopy facility for electron microscopy and 3View analysis of lymph nodes; the experimental histopathology facility for the initial preparation of tissue cryosections; and S. Lutter for assistance with whole-body imaging. We thank N. Harwood and J. Coleman for editing of the manuscript, and P. Barral, J. Caamaño, R. Germain, and the members of the Lymphocyte Interaction Laboratory for critical reading of the manuscript. We thank F. Sallusto for feedback and suggestion of the term “shut down.” The data presented in this manuscript are tabulated in the main paper and in the supplementary materials. Supported by Cancer Research UK.

SUPPLEMENTARY MATERIALS

www.sciencemag.org/content/347/6222/667/suppl/DC1
Materials and Methods
Figs. S1 to S11
References (24–29)
Movies S1 and S2

21 October 2014; accepted 11 December 2014
10.1126/science.1230000

PROTEIN EVOLUTION

Pervasive degeneracy and epistasis in a protein-protein interface

Anna I. Podgornaia^{1,2,*} and Michael T. Laub^{2,3,†}

Mapping protein sequence space is a difficult problem that necessitates the analysis of 20^N combinations for sequences of length N . We systematically mapped the sequence space of four key residues in the *Escherichia coli* protein kinase PhoQ that drive recognition of its substrate PhoP. We generated a library containing all 160,000 variants of PhoQ at these positions and used a two-step selection coupled to next-generation sequencing to identify 1659 functional variants. Our results reveal extensive degeneracy in the PhoQ-PhoP interface and epistasis, with the effect of individual substitutions often highly dependent on context. Together, epistasis and the genetic code create a pattern of connectivity of functional variants in sequence space that likely constrains PhoQ evolution. Consequently, the diversity of PhoQ orthologs is substantially lower than that of functional PhoQ variants.

Protein-protein interactions drive the operation and function of cells. These interactions involve a molecular interface formed by a subset of amino acids from each protein. Interfacial residues often vary between orthologs, indicating some mutational tolerance or degeneracy (1, 2), but such natural variability may not capture the full plasticity of interfaces. Thus, it remains unclear how many combinations of interface residues will support a given interaction and how these com-

binations are distributed and connected in sequence space (3) (fig. S1A). It is also unknown whether all functional variants can be reached through a series of mutations that retain function, or whether evolution is fundamentally constrained, limiting the natural diversity in orthologous proteins. Several studies have examined the mutational intermediates separating two proteins, but these typically exclude residues not present in either protein (4). Assays that couple genotype to phenotype along with deep

sequencing have enabled the interrogation of large numbers of mutants, including saturation mutagenesis of individual positions. These deep mutational scans have also tested many double and higher-order mutants, although not comprehensively, impeding the systematic analysis of functional variants and mutational paths in sequence space (5–10).

We mapped the sequence space underlying the interface formed by bacterial two-component signaling proteins in vivo (Fig. 1A and fig. S1, B and C). *E. coli* PhoQ is a sensor histidine kinase that is stimulated by low extracellular magnesium concentrations to phosphorylate the response regulator PhoP (11). When not stimulated to autophosphorylate, PhoQ binds to and drives the dephosphorylation of PhoP. The interface formed by two-component signaling proteins, such as PhoQ-PhoP, involves a limited number of residues from each protein (12, 13) (fig. S1B). For histidine kinases, mutating just three or four interfacial residues to match those in another kinase is often sufficient to reprogram partner specificity (12, 14).

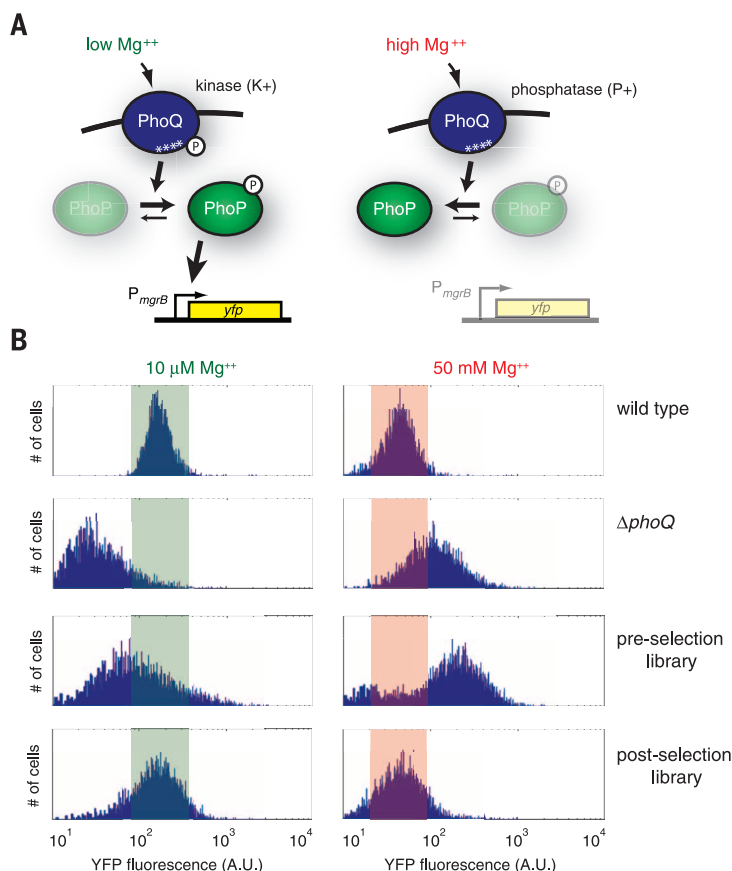


Fig. 1. Mapping sequence space. (A) PhoQ phosphorylates or dephosphorylates PhoP depending on extracellular magnesium concentration. White asterisks indicate interfacial residues randomized in the *phoQ* library. (B) YFP levels measured by flow cytometry for cells expressing wild-type *phoQ*, lacking *phoQ*, or harboring the *phoQ* library, before and after selection. Shaded regions indicate wild-type YFP levels.

For PhoQ, these key interfacial residues are Ala²⁸⁴, Val²⁸⁵, Ser²⁸⁸, and Thr²⁸⁹ (AVST), which is just one of 160,000 possible combinations at these four positions. To assess the ability of each combination to promote a functional PhoQ-PhoP interface in *E. coli*, we developed a high-throughput screen using a strain where *yfp* is expressed from a PhoP-dependent promoter, *P_{mgrB}* (Fig. 1A and fig. S1, B and C). When extracellular Mg²⁺ concentration is low, PhoQ is predominantly a kinase, driving PhoP phosphorylation and YFP (yellow fluorescent protein) production; in high extracellular Mg²⁺, PhoQ is mainly a phosphatase, stimulating PhoP dephosphorylation and preventing YFP production (11) (fig. S2A). To systematically probe the PhoQ interface, we constructed a library in which the four key interfacial residues were fully randomized and then transformed this library into a Δ *phoQ* strain harboring the *P_{mgrB}-yfp* reporter. The library was grown for 6 hours in medium with low or high extracellular Mg²⁺ to stimulate PhoQ kinase or phosphatase activity, respectively, and was then subjected to fluorescence-activated cell sorting to isolate those

mutants that behaved similarly to wild-type PhoQ (fig. S3A). This screen proved more stringent in selecting mutants with wild-type phosphatase activity because cells deficient in PhoQ kinase activity still accumulate some phosphorylated PhoP via acetyl-phosphate (fig. S2B). We therefore performed a second screen in which cells selected for phosphatase activity were starved of extracellular Mg²⁺ for 18 hours and then recovered in Mg²⁺-replete medium for 6 hours (figs. S4 and S5). Kinase activity comparable to that of the wild type was required to induce the PhoP regulon and survive without Mg²⁺ (fig. S2C). To identify interfacial residues that promote a PhoQ-PhoP interaction, we deep-sequenced the relevant region of *phoQ* from cells that passed our two-step selection (Fig. 1B and fig. S4). The starting library used NNS codons to randomize the four interfacial residues (where N = any nucleotide and S = G or C). Hence, the theoretical diversity of the library is 194,481, with 160,000 combinations lacking stop codons. Sequencing of the starting library indicated that 93% of 160,000

possible protein variants had more than three reads (fig. S3). For the postselection library, we used an unbiased binary classifier to identify sequences that were enriched relative to the starting library. The training set for the classifier consisted of (i) library data for the 34,481 PhoQ variants harboring one or more stop codons, each of which produces a nonfunctional PhoQ, and (ii) data collected individually for each single mutant of PhoQ at the first three positions randomized in our library. Of these 57 single point mutants, 13 exhibited nearly wild-type flow cytometry profiles and could successfully compete with the wild type under conditions of Mg²⁺ starvation (Fig. 2A and fig. S6). The binary classifier identified 1659 unique, functional PhoQ variants with an estimated false positive rate of <0.01% and false negative rate of ~7% (table S1). To validate the functionality of the PhoQ variants identified, we isolated and tested 20 individual mutants. Each mutant enabled PhoP-dependent gene expression at approximately wild-type levels in the presence of low Mg²⁺ and each suppressed PhoP activity in high Mg²⁺,

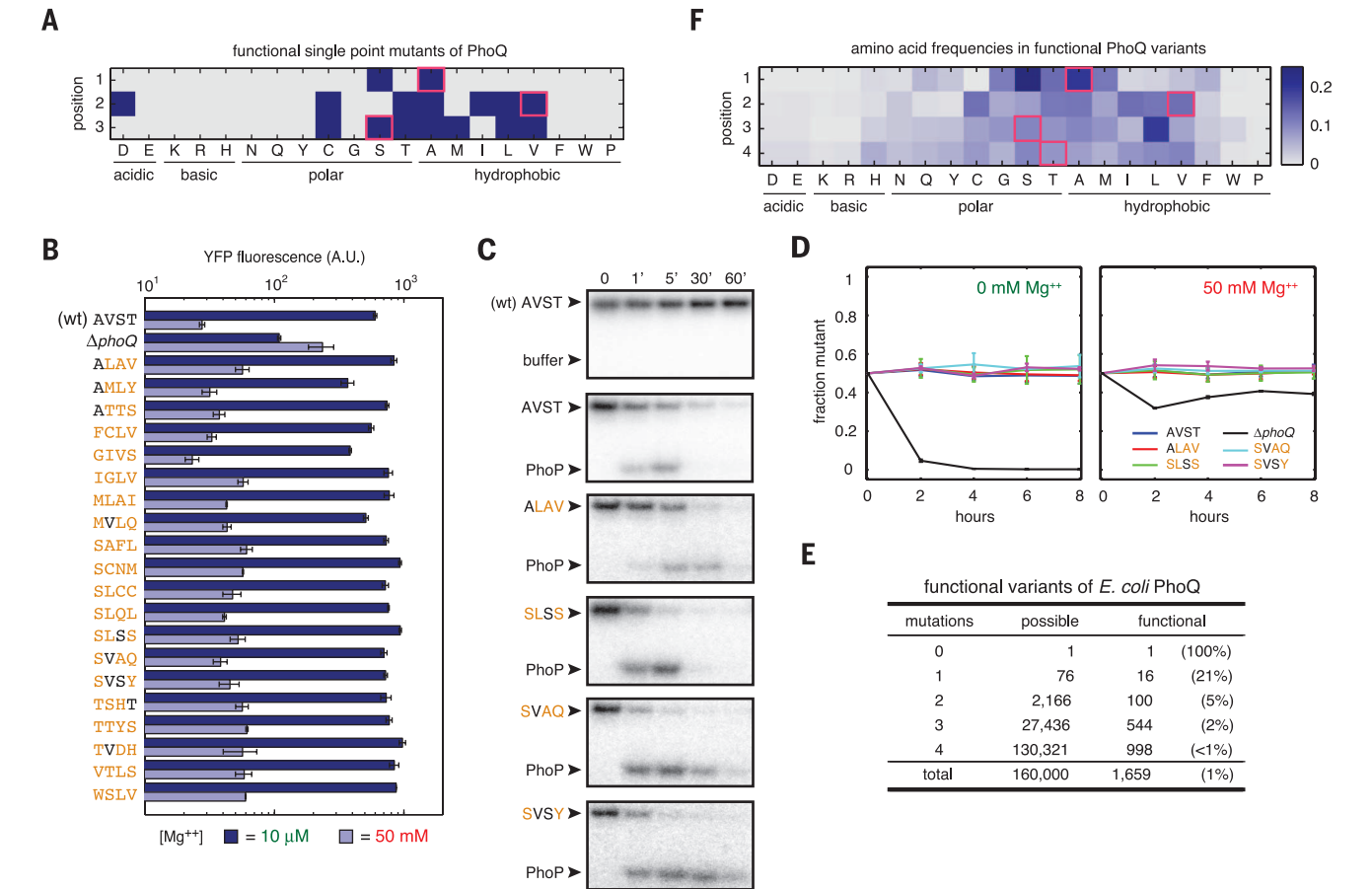


Fig. 2. Functional degeneracy of PhoQ interfacial residues. (A) Functionality of point mutations assessed individually. Blue indicates functional variants; magenta boxes indicate wild-type residues. Amino acid abbreviations: A, Ala; C, Cys; D, Asp; E, Glu; F, Phe; G, Gly; H, His; I, Ile; K, Lys; L, Leu; M, Met; N, Asn; P, Pro; Q, Gln; R, Arg; S, Ser; T, Thr; V, Val; W, Trp; Y, Tyr. (B) Flow cytometry measurements of YFP levels for 20 PhoQ variants.

Error bars indicate SD; *n* = 2. (C) PhoQ variants indicated were auto-phosphorylated in vitro and tested for phosphotransfer to and dephosphorylation of PhoP. (D) Head-to-head competitions of wild-type against strains expressing the indicated PhoQ variant. (E) Summary of functional PhoQ variants. (F) Heat map indicating amino acid frequencies in the 1659 functional PhoQ variants.

indicating that these PhoQ variants harbored kinase and phosphatase activity (Fig. 2B). We purified four of these variants, harboring the residues ALAV, SLSS, SVAQ, and SVSY, and confirmed that each exhibited kinase and phosphatase activity in vitro and in vivo (Fig. 2, C and D, and fig. S2D).

The identification of 1659 functional PhoQ variants that are signal-responsive in vivo and that survived magnesium starvation indicates extensive degeneracy of the PhoQ-PhoP interfacial residues. In addition to 16 single mutants, there were 100 double, 544 triple, and 998 quadruple mutants; this finding demonstrates that many diverse combinations of residues can support a functional interaction with PhoP (Fig. 2E and table S1). The set of 1659 functional variants showed an enrichment of hydrophobic and small polar residues at each position (Fig. 2F). Most bulky and charged residues appeared at low frequencies, which indicates that they can only be tolerated in certain contexts (Fig. 3, A to C). For example, the substitution A284H (variant HVST) abolished the phosphatase activity of PhoQ. However, the mutant HSLV was functional, indicating that A284H can be tolerated in this context. Similarly, the

substitution S288Q alone (AVQT) was nonfunctional but permissible in some variants harboring the A284S substitution, such as SIQC.

Conversely, some substitutions were permissible individually but not in combination. For instance, A284S, V285T, S288L, and T289V individually support a functional PhoQ-PhoP interface but are nonfunctional when combined (STLV) (Fig. 3D). Similarly, the combinations ACLV, TISV, and SILS, each involving residues found individually at high frequency, were severely impaired in competition against wild-type PhoQ (Fig. 3D and fig. S7A). Thus, the effects of individual substitutions are often context-dependent, or epistatic (15–19).

This epistasis implies that the functionality of variants with multiple substitutions cannot be easily predicted from the behavior of single point mutants or site-saturation mutagenesis. If each position contributed independently, our single-mutant data (Fig. 2A) would predict $2 \times 7 \times 7 \times 5 = 490$ functional combinations: [AS][ACDILTV][ACLMSTV][RTVWY]. However, our screen recovered only 104 of these and revealed an additional 1555 functional combinations (Fig. 3E), emphasizing the interdependency of individual positions.

To further assess interdependencies in PhoQ, we measured mutual information between each pair of positions in the set of 1659 functional variants (Fig. 3F and fig. S7B). The strongest coupling occurs between positions 1 and 2 and positions 1 and 3. For instance, a histidine at position 1 in functional PhoQ variants is highly correlated with a leucine or methionine at position 3 (Fig. 3, F and G), occurring three times as often as expected if these substitutions occurred independently. Similarly, a glutamine at position 3 correlates with a serine or threonine at position 1 (Fig. 3, F and G). These dependencies likely arise from constraints on the packing of adjacent residues. Positions 1 and 3 are separated by three residues in the primary sequence but are adjacent on α helix 1 in PhoQ.

The epistasis observed significantly constrains the mutational paths that PhoQ can follow through sequence space, assuming that PhoQ must retain a productive interaction with PhoP. For instance, of the 100 functional double mutants of PhoQ, only 23 represent cases where both single mutants are functional (Fig. 4A and fig. S8A). In 46 cases, only one of the single mutants is functional; thus, the mutational paths to these double mutants

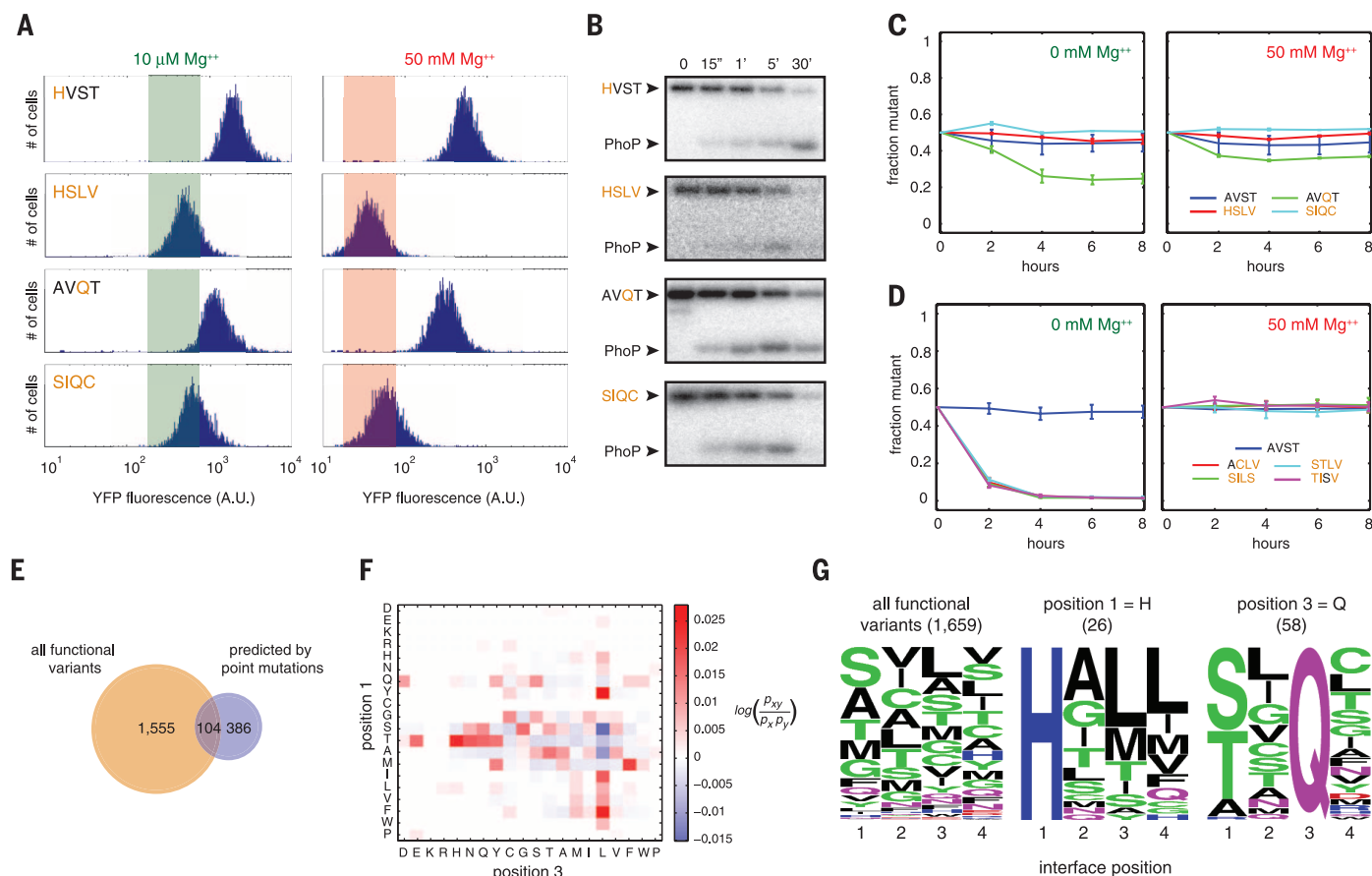


Fig. 3. Epistasis of PhoQ interfacial residues. (A and B) Flow cytometry (A) and in vitro analysis (B) of the PhoQ variants indicated. Shaded regions indicate wild-type YFP levels. (C and D) Head-to-head competitions of the wild type against strains producing the indicated PhoQ variant. (E) Venn diagram comparing the number of functional PhoQ variants identified with that predicted from single mutants, assuming position independence. (F) Heat map showing frequency of residue pairs at positions 1 and 3 relative to frequency expected if residues occurred independently. (G) Frequency logos for residues at each position in the PhoQ sets indicated. The height of each letter is proportional to its frequency in each set.

are constrained, requiring a certain order of substitutions. In the remaining 31 cases, the double mutant is functional even though neither single mutant is functional. Paths connecting the wild-type combination AVST to such double mutants, if they exist, must be indirect.

To systematically explore the impact of epistasis on mutational paths, we quantified the shortest path connecting the wild-type combination AVST with each of the 1658 functional variants (Fig. 4B). There are 79 PhoQ variants that cannot be reached from AVST without passing through a nonfunctional intermediate. For 428 variants, the Hamming distance from AVST equals the shortest path length. For example, AVST can convert to MLAI using four consecutive substitutions, with

each intermediate being functional. However, because of epistasis, only 3 of 24 possible direct paths are permissible (Fig. 4C). Of the 1658 functional PhoQ variants, 1151 (~70%) would require more mutational steps than their Hamming distance from AVST (Fig. 4B), indicating that many paths in sequence space are indirect and require the transient introduction of other residues (Fig. 4, B and D). Similar results were obtained when considering all possible starting points, not just AVST (fig. S8B).

To visualize connectivity in sequence space, we generated a force-directed graph in which nodes represent functional PhoQ variants and edges connect nodes differing by one residue (Fig. 4E). This graph revealed five primary clusters, each with

high internal connectivity. Functional variants have an average of seven neighbors (Hamming distance 1), ranging from 0 to 20 (fig. S8). The wild-type combination AVST has 16 neighbors and resides within a densely interconnected region of sequence space. Epistasis helps drive the separation of clusters; for example, clusters 1 and 2, featuring an A or S at position 1, are distal to cluster 5, which contains an L at position 3 that is incompatible with A/S at position 1 (Figs. 3F and 4E).

We also generated a force-directed graph in which edges connect functional variants separated by a single nucleotide substitution, following the codon table (Fig. 4F and fig. S9, A and B). This resulted in 260 variants that could not be reached from AVST without passing through

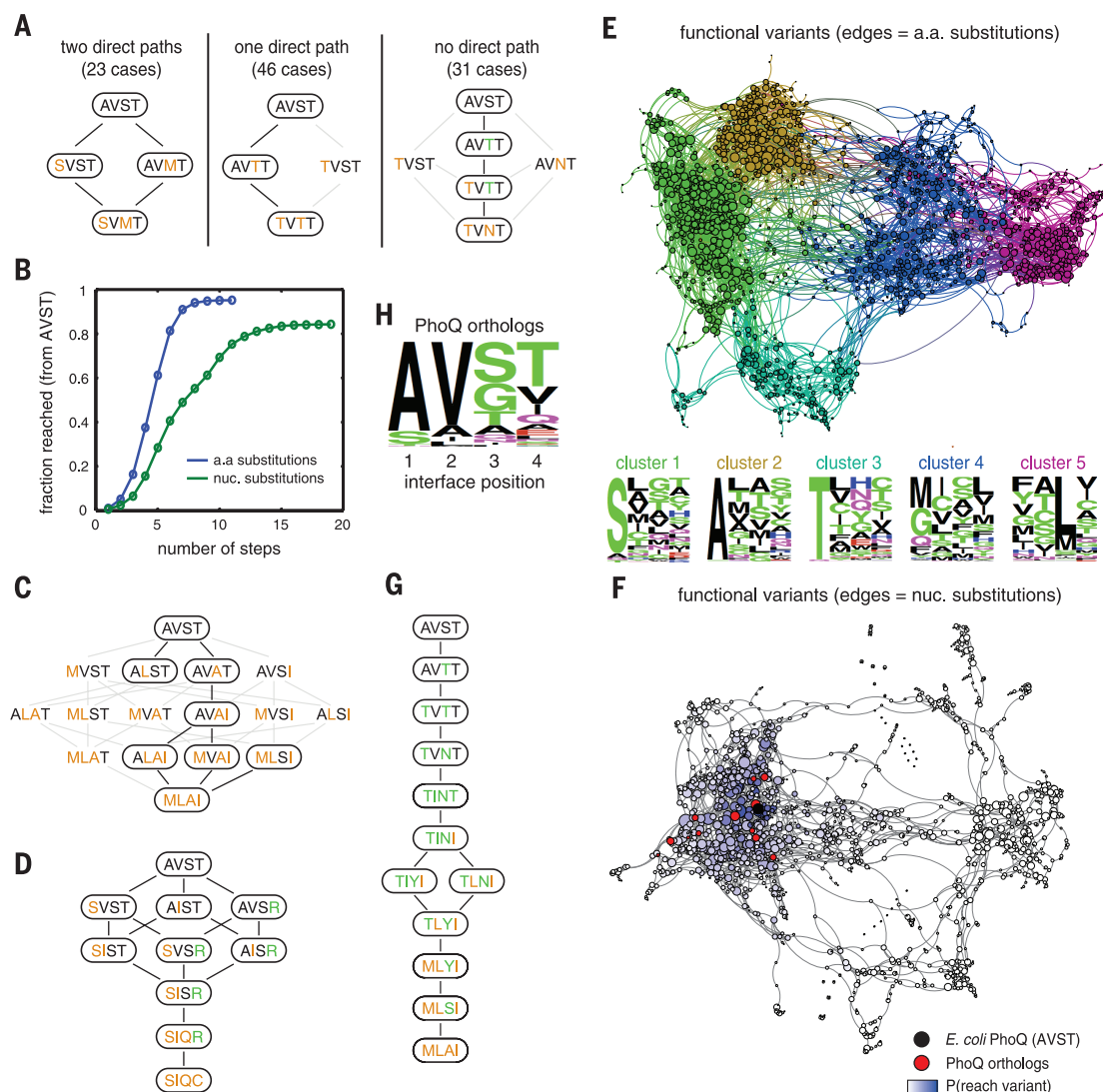


Fig. 4. PhoQ sequence space. (A) Tabulation and examples of double mutants reached by 2, 1, or 0 direct paths from AVST. Functional variants are circled. Lines connect variants differing by one residue (black, accessible paths; gray, inaccessible paths). (B) Cumulative fraction of functional variants reached from wild-type PhoQ in a given number of amino acid (blue) or nucleotide (green) substitutions. (C and D) Examples of shortest paths connecting AVST (wild type) to MLAI and SIQC. Green text indicates residues not in either terminal node. (E and F) Force-

directed graphs of functional PhoQ variants (nodes) with edges connecting variants differing by one residue (E) or one nucleotide (F). Node size is proportional to number of neighbors. In (E), clusters are colored with corresponding frequency logos shown. In (F), the color scale represents the probability of reaching a node after 20 mutational steps, with red nodes indicating variants found in PhoQ orthologs. (G) Shortest paths connecting AVST and MLAI via nucleotide substitutions. (H) Frequency logo for interfacial residues of PhoQ orthologs from γ -proteobacteria.

nonfunctional intermediates, as well as a substantial increase in the length of shortest paths connecting functional variants (Fig. 4B and fig. S8). For example, the shortest path from AVST to MLAI increased from 4 to 10 (Fig. 4G). Shortest path lengths now exceeded Hamming distances for >97% of all connected variant pairs (fig. S8B). Together, the genetic code and epistasis severely constrain mutational paths in sequence space for PhoQ.

The set of functional variants includes 13 residue combinations found in PhoQ orthologs. Some residue combinations found in PhoQ orthologs are not included, possibly because these orthologs have widely divergent PhoP partners (fig. S9C) and are thus constrained differently from *E. coli* PhoQ. In general, the natural diversity in PhoQ orthologs (Fig. 4H and fig. S9C), even those with divergent PhoP partners, is much more limited than the diversity in our selected, functional variants. This difference may indicate that some PhoQ variants identified as functional have subtle defects that confer a disadvantage in the wild on long time scales. However, there was no obvious correlation between the enrichment ratios of variants after magnesium starvation and their sequences (figs. S5 and S10) (20). Alternatively, mutational paths may be fundamentally constrained by the nonuniform interconnectivity of variants in sequence space, such that nature has not sampled certain sequences. To test this idea,

we simulated PhoQ mutational paths starting from AVST and making one nucleotide change at each step. Even after 20 simulated steps, a relatively limited region of sequence space was explored (Fig. 4F and fig. S9D), with the region most densely sampled including all of the 13 PhoQ ortholog residue combinations. Collectively, our results suggest greater functional degeneracy for PhoQ than would be expected by site-saturation mutagenesis. However, the interconnectivity of functional variants, which results from epistasis and the structure of the genetic code, has likely limited nature's exploration of sequence space (2, 15–18, 21), as reflected in the limited diversity of PhoQ orthologs (Fig. 4H).

REFERENCES AND NOTES

1. M. J. Harms, J. W. Thornton, *Nat. Rev. Genet.* **14**, 559–571 (2013).
2. M. A. DePristo, D. M. Weinreich, D. L. Hartl, *Nat. Rev. Genet.* **6**, 678–687 (2005).
3. J. Maynard Smith, *Nature* **225**, 563–564 (1970).
4. D. M. Weinreich, N. F. Delaney, M. A. DePristo, D. L. Hartl, *Science* **312**, 111–114 (2006).
5. D. M. Fowler *et al.*, *Nat. Methods* **7**, 741–746 (2010).
6. T. A. Whitehead *et al.*, *Nat. Biotechnol.* **30**, 543–548 (2012).
7. R. N. McLaughlin Jr., F. J. Poelwijk, A. Raman, W. S. Gosal, R. Ranganathan, *Nature* **491**, 138–142 (2012).
8. R. T. Hietpas, J. D. Jensen, D. N. Bolon, *Proc. Natl. Acad. Sci. U.S.A.* **108**, 7896–7901 (2011).
9. D. M. Fowler, S. Fields, *Nat. Methods* **11**, 801–807 (2014).
10. D. Melamed, D. L. Young, C. E. Gamble, C. R. Miller, S. Fields, *RNA* **19**, 1537–1551 (2013).
11. E. A. Groisman, *J. Bacteriol.* **183**, 1835–1842 (2001).
12. J. M. Skerker *et al.*, *Cell* **133**, 1043–1054 (2008).
13. P. Casino, V. Rubio, A. Marina, *Cell* **139**, 325–336 (2009).
14. E. J. Capra *et al.*, *PLOS Genet.* **6**, e1001220 (2010).
15. M. S. Breen, C. Kemena, P. K. Vlasov, C. Notredame, F. A. Kondrashov, *Nature* **490**, 535–538 (2012).
16. B. Lehner, *Trends Genet.* **27**, 323–331 (2011).
17. E. A. Ortlund, J. T. Bridgham, M. R. Redinbo, J. W. Thornton, *Science* **317**, 1544–1548 (2007).
18. D. M. Weinreich, R. A. Watson, L. Chao, *Evolution* **59**, 1165–1174 (2005).
19. D. M. Weinreich, Y. Lan, C. S. Wylie, R. B. Heckendorn, *Curr. Opin. Genet. Dev.* **23**, 700–707 (2013).
20. C. Bank, R. T. Hietpas, A. Wong, D. N. Bolon, J. D. Jensen, *Genetics* **196**, 841–852 (2014).
21. I. S. Povolotskaya, F. A. Kondrashov, *Nature* **465**, 922–926 (2010).

ACKNOWLEDGMENTS

We thank B. Fiske, A. Murray, B. Sauer, and the Laub laboratory for discussions. Supported by Human Frontier Science Program and Office of Naval Research grants (M.T.L.) and an NSF Graduate Fellowship (A.I.P.). Author contributions: A.I.P. and M.T.L. conceived the approach, analyzed data, and wrote the paper. A.I.P. performed all experiments.

SUPPLEMENTARY MATERIALS

www.sciencemag.org/content/347/6222/673/suppl/DC1
Materials and Methods
Tables S1 and S2
Figs. S1 to S10
References (22–32)

12 June 2014; accepted 8 December 2014
10.1126/science.1257360

“《科学》职业” 已经与Cernet/赛尔互联开展合作。中国大陆的高校可以直接联系Cernet/赛尔互联进行国际人才招聘。



请访问 Sciencecareers.org/CER
点得联系信息。

招募学术精英,《科学》是您的不二之选 **Science**



SCHOOL OF MEDICINE

INDIANA UNIVERSITY

The Diabetes Research Center (DRC) at Indiana University School of Medicine is seeking applications for tenure track/tenured faculty positions at the Assistant/Associate/Full Professor level positions in the area of diabetes research. This search continues a vigorous commitment to expand upon and develop a world-class diabetes research program at the University. There are currently 65 principal investigators in the DRC, and NIH funded areas include: islet cell biology, metabolism and physiology of obesity, cardiovascular complications of obesity and diabetes, renal and retinal complications of diabetes, and clinical trials research. The DRC is supported by state-of-the-art Core facilities, including an islet isolation and characterization core, a rodent phenotyping core, a swine physiology core, a microscopy/imaging core, and a human in vivo studies core. In addition, the DRC is supported by a Signature Centers Initiative to fund innovative projects and encourage collaboration, and by 3 dedicated T32 grants to support pre- and post-doctoral trainees.

Candidates with research interests in any area of diabetes, including islet biology, stem cell and developmental biology, insulin action, diabetes complications, and obesity research are invited to apply. Successful applicants are expected to have/develop a strong, independent extramurally funded research program and participate in training students and fellows and engage in research interactions with the clinical diabetes program. A competitive salary, startup funds, and space will be provided. Applicants must have an MD and/or PhD degree (or equivalent degrees), post-doctoral research experience, and clear evidence of research productivity. The search committee will begin considering applications immediately and on an on-going basis until positions are filled. Applicants should submit a curriculum vitae, summary of past accomplishments and future plans, and names and email addresses of three references electronically to **Dr. Raghu G. Mirmira, MD, PhD** at islets@iupui.edu (Fax: 317-278-8910).

Indiana University is an EEO/AA Employer, M/F/D.

For your career in science, there's only one

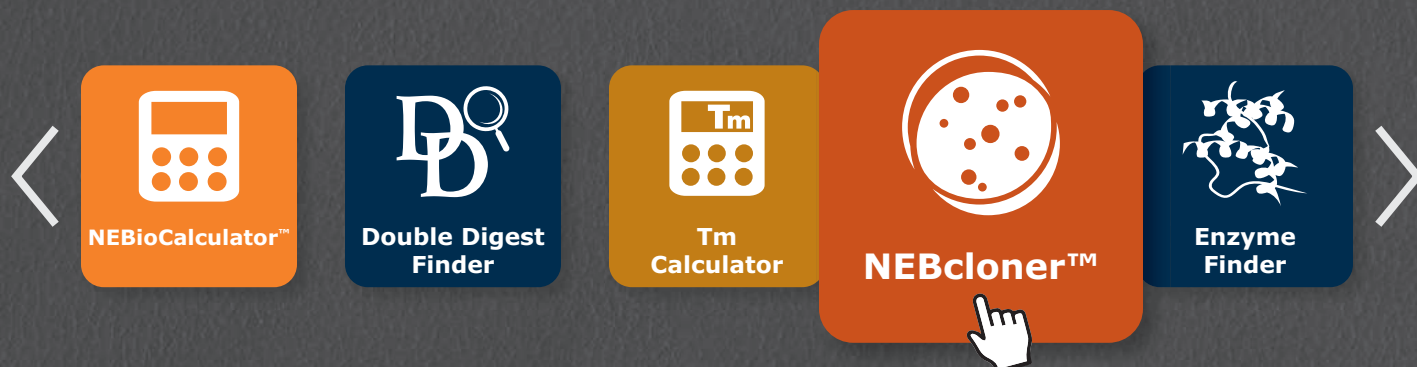
Science

Introducing myIDP: A career plan customized for you, by you.

- The first and only online app that helps scientists prepare their very own individual development plan.
- Recommended by leading professional societies and the NIH.
- Developed by scientists at FASEB, UCSF, and the Medical College of Wisconsin in collaboration with AAAS and Science Careers, with support from the Burroughs Wellcome Fund.



Visit the website and
start planning today!
myIDP.sciencecareers.org

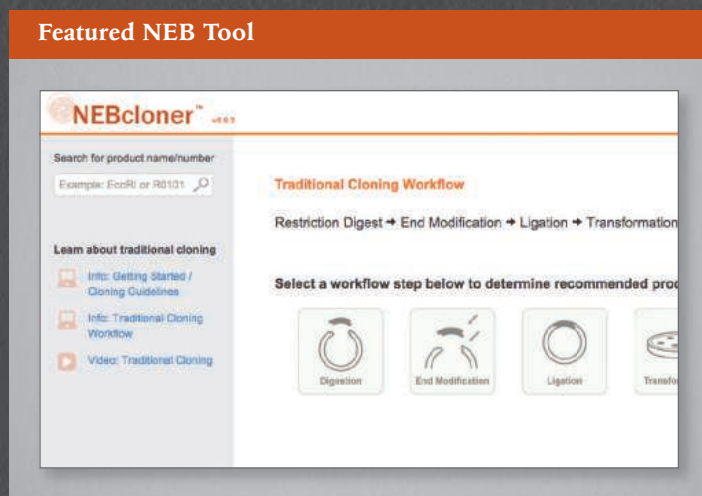


Expand your toolbox

with NEB's interactive tool, NEBcloner[™].

Find the right product and protocol for your next cloning experiment with NEBcloner. Answer a few simple questions, and our latest NEBtool will find a solution for you. Or, select the protocol you need, and get started. With NEB's online tools, easier experimental design is right at your fingertips.

- For help with scientific conversions and calculations, try **NEBioCalculator**[™].
- Identify the restriction enzyme cut sites within your DNA sequence with **NEBcutter**[®].
- Calculate the optimal annealing temperature for your PCR with NEB's **Tm calculator**.

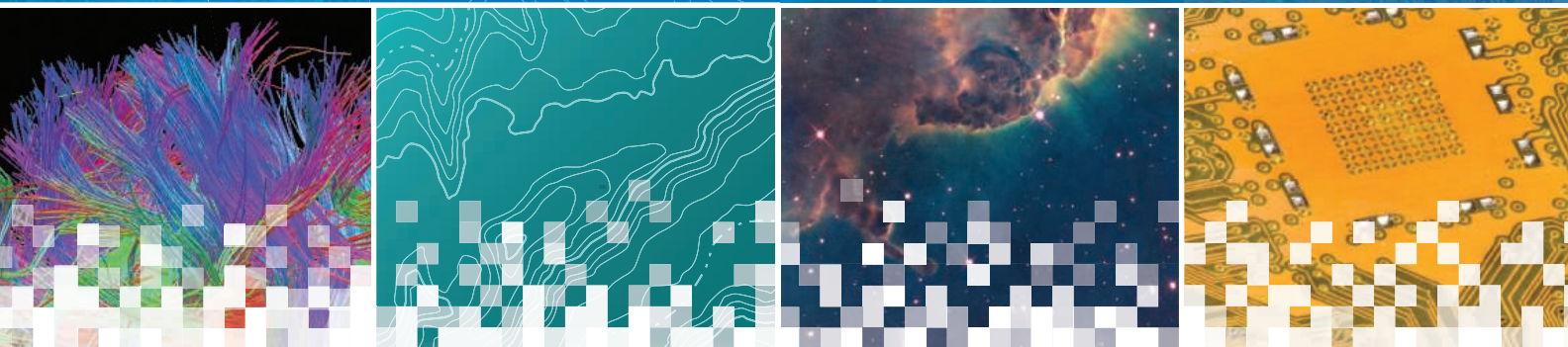


Explore NEB's entire suite of interactive online tools at
www.neb.com/nebtools

AAAS | 2015 ANNUAL MEETING

12–16 FEBRUARY • SAN JOSE, CA

INNOVATIONS, INFORMATION, AND IMAGING



AAAS, publisher of *Science*, thanks the sponsors and supporters of the 2015 Annual Meeting

As of 15 January 2015



Johnson & Johnson



Genentech
A Member of the Roche Group



the Lemelson foundation
improving lives through invention



DIGITAL
science



for its generous support of
the Science Journalism Awards

THE GEORGE
WASHINGTON
UNIVERSITY
WASHINGTON, DC

ScienceAdvances

Mobile app, meeting program, and all the
information you need for the Annual Meeting

www.aaas.org/meetings

China's National Key Laboratory of Medical Immunology

At the Forefront of Immunology Research

At the western gate of the Second Military Medical University (SMMU) in Shanghai, there stands a five-story building. In 1999, when the Department of Immunology—the predecessor of the National Key Laboratory of Medical Immunology (LOMI)—moved into this building, Dr. Xuetao Cao, the director and founder, said to his colleagues, “It is our historical responsibility to establish a lab with an international reputation.” At that time, the Chinese economy was growing at an astonishing speed and attracting international attention; however, scientific research in China, especially the basic sciences, had yet to make a name in the world.

Fifteen years have now passed and Cao's dream is beginning to come true. The Department of Immunology has blossomed from a small department to the only National Key Laboratory in the field of immunology in China. Focusing on basic research for the functional regulation of innate and adaptive immunity and on translational research for cancer immunotherapies, LOMI has been conducting innovative research and exploration, and is becoming a rising star in the international immunology community.



Laboratory staff members gathered outside the SMMU guest house.

When the Institute of Immunology at SMMU won the title of National Key Laboratory of Medical Immunology in 2006, it was considered well deserved by Chinese colleagues. Though relatively young at just 15 years old, the institute has fast established itself at the forefront of immunology research worldwide.

This recognition is, in part, due to LOMI's reputation for pioneering research. Director Cao has long followed the Chinese traditional philosophy of Yin-Yang while investigating immune regulation. For example, he has focused LOMI's research not only on how the immune response is initiated to eliminate invading pathogens, but also on how immune responses are negatively regulated to avoid excessive activation that may cause damage. Such studies have resulted in the publication of over 250 peer-reviewed papers and China's Ministry of Science and Technology choosing LOMI's discovery of prognostic biomarkers for patients with cancer as one of the top ten scientific achievements of 2011.

The institute's leadership has also worked hard to promote Chinese immunology research on the international stage, contributing greatly to its growing recognition. For example, LOMI has hosted several international immunology conferences in Shanghai to help its international colleagues learn more about Chinese research and scientists. Alongside such efforts to develop global relationships, Cao has been elected as the president of Global Alliance for Chronic Disease, president of the Federation of Immunological Societies of Asia-Oceania, and an editorial board member for the journals *Annual Review of Immunology* and *Cell*.

A unique history

Prior to being awarded its National Key Laboratory status in 2006, LOMI's predecessor, the Department of Immunology, existed as part of the School of Basic Medical Sciences at SMMU. In 1990, Cao graduated from SMMU as the university's youngest Ph.D. student. He turned down a postdoctoral training opportunity at Yale University to stay on at SMMU as a lecturer in the department to keep a promise to his mentor, Dr. Tianxing Ye, to grow the Department of Immunology into the most productive lab at SMMU. Cao quickly advanced, becoming the vice director of the department and full professor in 1992, and director in 1995. During that time, the department experienced its first round of rapid development and was focused on adoptive cellular immunotherapy for cancer.

However, in contrast to today's funding climate, support for the basic sciences was limited at the time. Therefore, to create a better research environment, Cao sought out venture capital funding to set up a new building for his quickly expanding team. “I wished to establish a top-level lab. Inspired by my visits to top universities in Western countries, I worked with an architect to design a building with academic style for a new institute,” recalls Cao. In October 1999, he moved the lab into the five-story brick red building. One year later, he established a new institute, mainly from the Department of Immunology: the Institute of Immunology.

With the slow progress of cancer immunotherapy research, Cao was struggling to find ways to carry out basic research to develop new strategies for cancer treatment. Yu Yizhi, a professor at LOMI, recalls Cao's astute decision regarding the department's direction: “In the mid-1990s, Dr. Cao asked us to

investigate antigen-presenting cells [APCs], particularly dendritic cells," says Yu. "During that time this field was not as popular, but Dr. Cao thought these cells could be important for the field of immunology, so we began researching them."

This decision opened a new chapter for the institute. Starting in 1997, LOMI researchers began identifying novel genes from human immune cells (mainly dendritic cells) by random sequencing of cDNA libraries and bioinformatics analysis. Since then, 23 new gene names have been approved by the Human Genome Organization Gene Nomenclature Committee. These advances, along with studies on the functional regulation of dendritic cells, have led to a number of publications in high-impact journals—with the first *Nature Immunology* paper from China being published by LOMI researchers. LOMI underwent a second rapid growth period and was subsequently designated as China's National Key Laboratory of Medical Immunology in 2006.

The following eight years brought stable financial support from the central government specifically for the National Key Laboratory, over 60 scientific publications, and a number of significant discoveries, including the unique function of long noncoding RNAs and the novel function of major histocompatibility complex class I and II molecules in toll-like receptor signaling. LOMI is now entering its third round of rapid expansion.

Research highlights

The institute's success is largely due to the faculty's creative research. The director's office door bears the motto: "Time is precious, spend more time thinking." It is in this spirit that Cao, who is also the past president of the Chinese Society for Immunology, leads his team of scientists and students. Cao says, "We are a young laboratory with great energy, and we focus on the frontiers of this field, which is why I think we have made some significant discoveries in the past years. Most importantly, our final goal is not only to produce publications, but also translate what we find into disease treatments."

Understanding the regulation of immune system responses is one such frontier. Early on, Cao's group discovered that the immune microenvironment could drive mature dendritic cells to differentiate into a unique type of regulatory dendritic cell, challenging the dogma that mature dendritic cells are terminally differentiated. This research became the cover story of a November 2004 issue of *Nature Immunology*. Cao's team continues to study how immune system homeostasis is maintained and the role of the immune microenvironment.

LOMI researchers continue to cover novel immune cell-specific genes. Nan Li, who has been a professor at LOMI since 1996, has investigated the function of over 30 new proteins, including immune receptors, tumor antigens, and signaling molecules. "Most of these molecules have important roles in dendritic cell function, such as migration and activation of T cells," she explains. "So they may be targets for the design of therapeutic approaches to infection and cancer."

To investigate immune defenses against pathogen infections, Huazhang An, a professor who has worked at LOMI since 2000, explores the effects of innate immune receptors on inflammation. Invading pathogens can activate proinflammatory responses and cause tissue damage as well. "If we can find a way to inhibit inflammation but also enhance immunity against a virus, it would be much better for patients," explains An. His group discovered that activating phosphatase SHP-1 inhibits inflammation while simultaneously increasing antiviral activity. This discovery could generate new treatments for autoimmune and viral diseases.

Though such innate immune responses are key to combating foreign invaders, these cellular responses are disruptive when activated during organ transplantation. Professor Quanxing Wang explores ways to alter these responses. "We believe that the main limitation in organ transplantation is chronic rejection," says Wang, "because it takes place over several months or years." Wang's team is searching for ways to treat chronic rejection by genetically modifying APCs, such as dendritic cells, to promote tolerance of transplanted tissue.

Translational research at LOMI also focuses on using basic research findings to develop new cancer therapeutics. For example, Professor Tao Wan's team is trying to establish a new approach to chemoimmunotherapy. "Over the past ten years, we have been developing a new vaccine for colorectal cancer," says Wan. This type of vaccine could greatly benefit these patients, who often show resistance to 5-fluorouracil, a major chemotherapy agent used to treat colorectal cancer.

A creative approach to research

Taoyong Chen, a young professor who also investigates the molecular mechanisms underlying host innate immune responses to pathogens, says that a unique and valued trait about the laboratory is that creativity is encouraged.

Chen is developing strategies to enhance innate immune responses against infection and is searching for novel signaling mechanisms underlying inflammation in autoimmune diseases such as arthritis and multiple sclerosis. "If you are interested in a field, any field, you can research it," he says. "The work time in our lab is very flexible, and I like to work in this style."

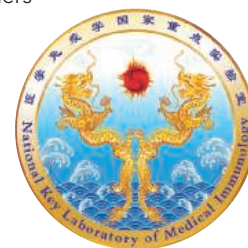
This progressive work environment emanates from Cao's leadership style. "If one of my faculty has a creative idea, I encourage them to go forward, even if it is not successful in the end," says Cao. "Being a scientist means having an open mind and respecting the creativity of the individual. Coming from different directions with different views means we can collaborate. This is why our lab is so efficient."

Collaboration is not only limited to the lab, but broadened to the global community. To facilitate such interactions, immunologists are invited from abroad to give lectures—and heated discussions often follow. Additionally, LOMI researchers are encouraged to study abroad. "They need to broaden their horizons," says Cao. "We should pay attention to the frontiers in the field and learn new technologies, and then integrate what we learn into our own system."

The institute has been successfully integrating basic immunology and translational research over the past decade and will continue to emphasize this strategy in the future. Cao believes that the challenges ahead lie in disseminating information to the medical community and forming new collaborations. "The future of LOMI lies in translating our scientific knowledge into clinical applications," says Cao. "There's a gap in communication between scientists and doctors, which we aim to fill by creating translational-focused projects."

"We still have a long way to go before becoming a top-level lab; however, with the increasing support from the government, the timing is right for LOMI and its researchers to achieve our goals of contributing to the global understanding of immunology and developing new immunotherapeutic strategies to treat diseases," says Cao.

**National Key Laboratory of Medical Immunology,
Second Military Medical University**
800 Xiangyin Road
Shanghai, 200433
China



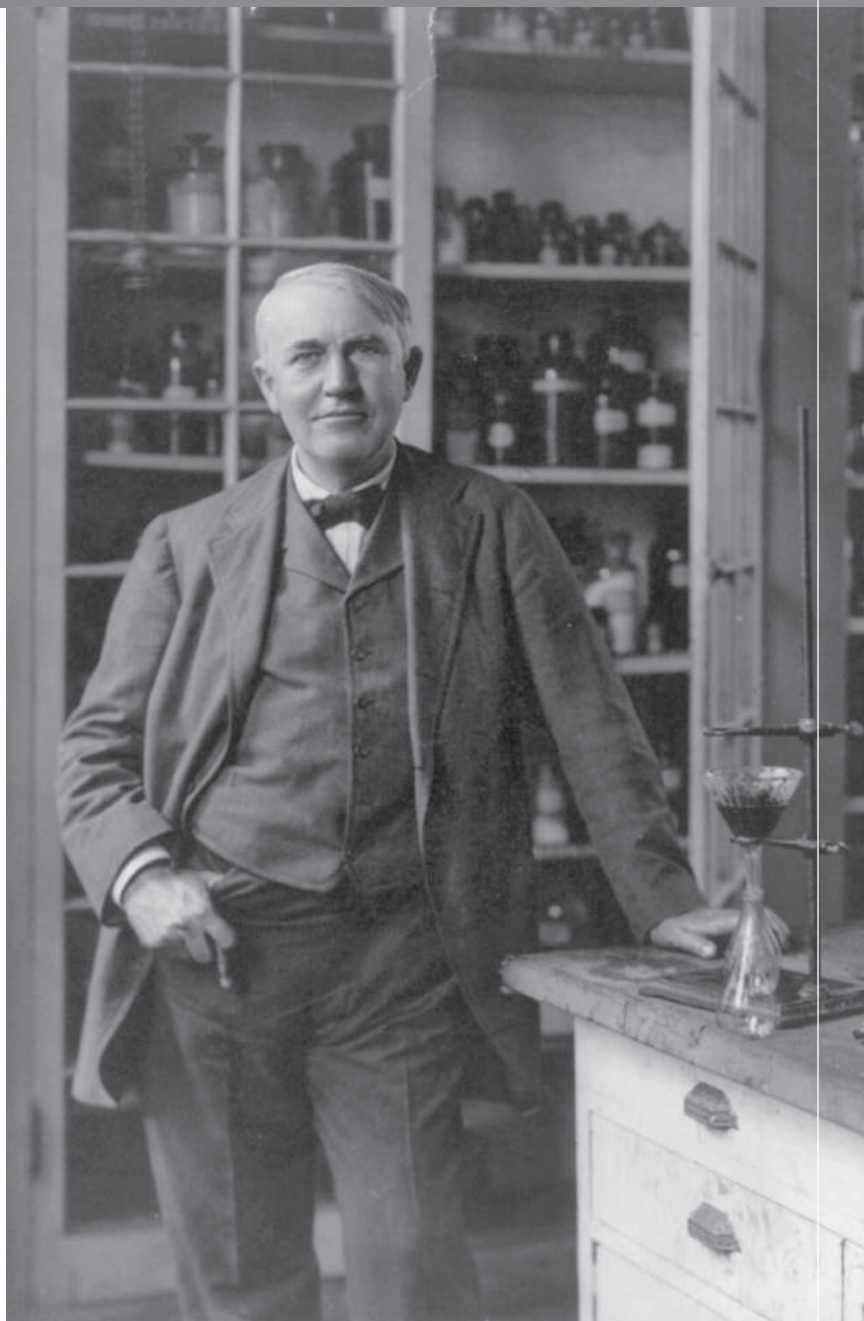
WHAT DO YOU AND THOMAS EDISON HAVE IN COMMON?

AAAS.

By investing in AAAS you join Thomas Edison and the many distinguished individuals whose vision led to the creation of AAAS and our world-renowned journal, *Science*, more than 150 years ago.

Like Edison, you can create a legacy that will last well into the future through planned giving to AAAS. By making AAAS a beneficiary of your will, trust, retirement plan, or life insurance policy, you make a strong investment in our ability to advance science in the service of society for years to come.

To discuss your legacy planning, contact Juli Staiano, Director of Development, at (202) 326-6636, or jstaiano@aaas.org, or visit www.aaas.org/1848 for more information.



"I feel great knowing that I will leave behind a legacy that will be channeled through the AAAS. It also means a lot to me to be able to honor my late parents, too."

—PETER ECKEL
Member, 1848 Society and AAAS Member since 1988

AAAS *Travels*



MADAGASCAR

August 20–September 4, 2016
See the Annular Solar Eclipse Sept. 1, 2016!



Explore the unique heritage of this enchanting land including the Annular Solar Eclipse. Madagascar is home to thousands of unique species including lemurs and reptiles, flowering plants, palms, and many birds. This is an exceptional opportunity to become acquainted with Madagascar and experience the Annular Solar Eclipse in 2016! \$4,995 pp + air

For a detailed brochure, call (800) 252-4910

All prices are per person twin share + air



BETCHART EXPEDITIONS Inc.
17050 Montebello Rd, Cupertino, CA 95014
Email: AAASInfo@betchartexpeditions.com
www.betchartexpeditions.com



AAAS is here – bringing scientific expertise to policy making.

Good science policy is the result of politicians understanding science and scientists understanding policy. Toward this end, AAAS manages the Science & Technology Policy Fellowships program, which embeds scientists and engineers in the federal government for up to two years. From Congress to the State Department, each class of Fellows contributes to the policy-making process while getting hands-on experience at the intersection of science and policy. As a AAAS member your dues support these efforts. If you're not yet a AAAS member, join us. Together we can make a difference.

To learn more, visit aaas.org/plusyou/fellows



"MOST OF THE PEOPLE THINK THEY'VE REACHED THE END OF EARTH
WHEN THEY GET TO THE REINDEER CAMP. BUT WE GO BEYOND THAT."

Paula T. DePriest

Lichenologist and Mongolian
cultural conservationist
Paula DePriest, AAAS Member



Every scientist
has a *story*

Read her story at membercentral.aaas.org, the website
that opens up new worlds. Connect with others who share
your passion.



Hot Plate Stirrer

The new Analog Hotplate Stirrer with a 7"x7" ceramic coated hot plate has a maximum hot temperature surface rating of 380°C with stirring speeds that can be precisely controlled between 100–1,500 rpm at maximum capacity of 5 L. A large control panel includes two easily visible lamps, which indicate when the heating and stirring functions are activated as well as a third lamp to indicate when the unit is powered on. Safety features include an on/off switch conveniently located on the side of the unit, as well as an angled control panel, which extends away from the hot surface. Hotplate stirrers are popular for both biology and chemistry applications, and can be purchased separately as hotplate, magnetic stirrer, or combined hotplate stirrer.

Labnet International

Phone: 732-417-0700
www.labnetinternational.com

Pipette Tips

BrandTech is introducing the new line of BRAND pipette tips from BRAND GMBH + CO KG, including sterile, nonsterile, filtered, and ultralow retention tips. The line features a new, environmentally-friendly box and insert system with lids that can hinge or lift off. Tips are manufactured in BRAND's new state-of-the-art clean room and packaged DNA-, RNase-, ATP-, and endotoxin-free. Tips fit pipettes from all major manufacturers, including the BRAND Transferpette S.

BrandTech Scientific

For info: 888-522-2726
www.brandtech.com

Luteinizing Hormone ELISA Kit

The new LH ELISA Kit for Sensitive and Rapid Detection of luteinizing hormone (LH) can be used to quantify human LH in serum and plasma samples as well as tissue culture media. This sensitive assay is fully quantitative, with the ability to detect as low as 5.2 mIU/mL of LH, surpassing semi-quantitative Western blot analysis. This assay produces rapid results in less than 2 hours with negligible reactivity to similar glycoprotein hormones. With this new kit, Enzo Life Sciences extends its line of ELISAs for endocrine analysis, including angiotensin I & II, corticosterone, cortisol, DHEA, 17 β estradiol, estriol, big endothelin-1, gastrin I, GLP-1, leptin, oxytocin, progesterone, serotonin, substance P, testosterone, Arg8 vasopressin, and 25(OH) vitamin D.

Enzo Life Sciences

For info: 800-942-0430
www.enzolifesciences.com



Transcriptome Solution

Translational researchers who previously could not obtain global gene expression profiles from biobank samples due to limited amounts of tissue now have access to a wealth of valuable RNA data with the launch of the Ion AmpliSeq Transcriptome Solution for the Ion Proton System. Its ability to draw gene expression profiles from just 10 ng of RNA sets the Ion AmpliSeq Transcriptome Solution apart from other solutions in the market, and it is compatible with formalin-fixed, paraffin-embedded samples. The Ion AmpliSeq Solution also provides a faster and more cost-effective workflow without the sample manipulation required for microarrays or analytical complexity normally associated with whole transcriptome RNA-sequencing. The solution is designed with simplicity and flexibility in mind. Differential expression profiles are generated through a push button analysis application within Ion Torrent Suite Software. After primary analysis, current microarray and next generation sequencing users are able to conveniently export data into their existing downstream analysis software app.

Thermo Fisher Scientific

For info: 800-955-6288
www.thermofisher.com

Highly Validated Antibody Conjugates

An exclusive range of highly validated conjugated antibodies is now available for use in key imaging applications including immunofluorescence, flow cytometry, and fluorescent Western blotting. Abcam's conjugated antibodies enable scientists to easily perform multi-protein analysis. It is essential for scientists to study and image proteins in their multi-component state rather than individually, as research findings indicate that proteins rarely operate in isolation but function within multi-protein complexes. The majority of the new antibodies are developed using Abcam's RabMAb technology, and are conjugated to Alexa Fluor dyes, HRP, or biotin, combining high signal to noise ratios with high specificity. Each antibody has been produced and extensively validated by Abcam's scientists. Performance data including images, references and customer reviews is provided with each product.

Abcam

For info: 888-772-2226
www.abcam.com/conjugates

Gamma-H2AX Assay

A gamma H2AX Pharmacodynamic assay kit for the study of double strand DNA breaks through the detection of gamma H2AX—a phosphorylated histone historically proven to be a highly specific and sensitive molecular marker for double strand DNA damage detection. This new assay has been developed for anticancer drug screening, basic research, and upcoming clinical trials providing one of many tools needed to support hypothesis-driven drug design strategies. Documented variability in DNA double-strand break repair among different segments of the human population may contribute to patient-specific therapeutic toxicities, enabling a more personalized approach

to treatment. A quantitative determination of gamma-H2AX levels in response to treatment would help to establish patient-specific dose regimens minimizing the toxicity, while maximizing the efficacy of therapy. The new 96-well nonradioactive enzyme-linked immunosorbent assay documents differences in gamma H2AX levels in peripheral blood mononuclear cells, cultured cells, and tissue biopsies.

AMS Biotechnology

For info: +44-(0)-1235-828200
www.amsbio.com

Electronically submit your new product description or product literature information! Go to www.sciencemag.org/products/newproducts.dtl for more information.

Newly offered instrumentation, apparatus, and laboratory materials of interest to researchers in all disciplines in academic, industrial, and governmental organizations are featured in this space. Emphasis is given to purpose, chief characteristics, and availability of products and materials. Endorsement by *Science* or AAAS of any products or materials mentioned is not implied. Additional information may be obtained from the manufacturer or supplier.

want new technologies?

antibodies

apoptosis

biomarkers

cancer

cytometry

data

diseases

DNA

epigenetics

genomics

immunotherapies

medicine

microbiomics

microfluidics

microscopy

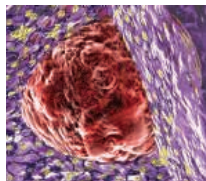
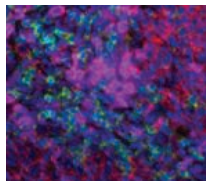
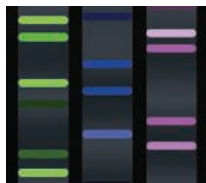
neuroscience

proteomics

sequencing

toxicology

transcriptomics



watch our **webinars**

Learn about the latest breakthroughs, new technologies, and ground-breaking research in a variety of fields. Our expert speakers explain their quality research to you and answer questions submitted by live viewers.

VIEW NOW!

webinar.sciencemag.org

Science
AAAS

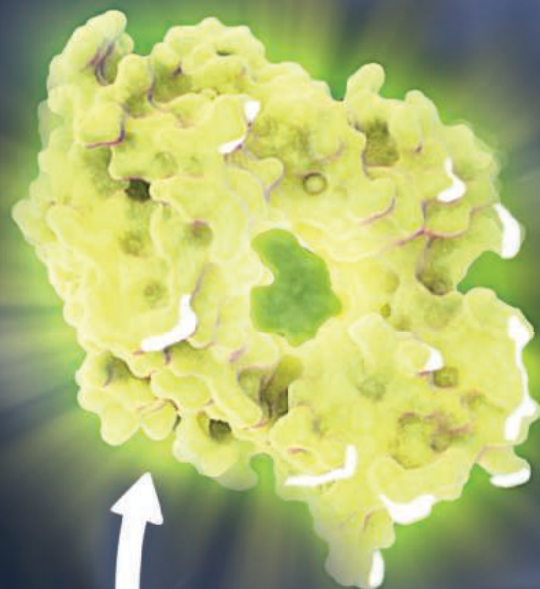
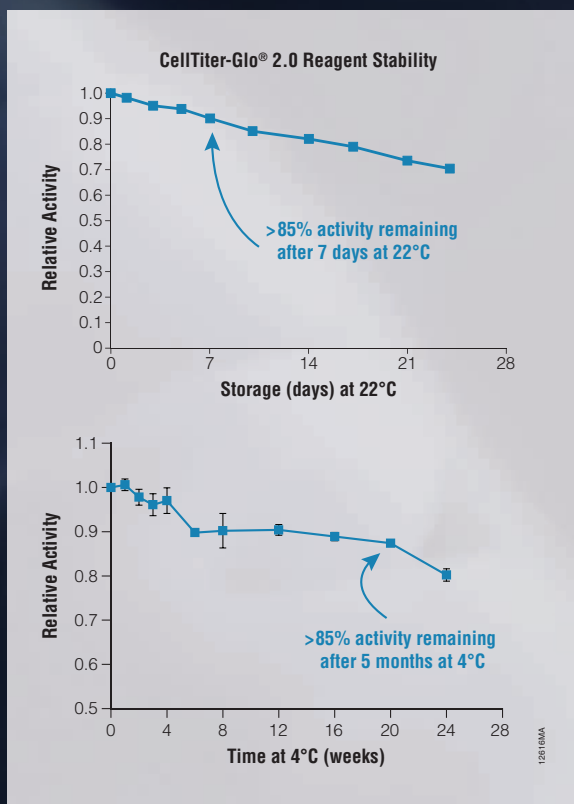
Brought to you by the *Science*/AAAS
Custom Publishing Office



@SciMagWebinars

NEW CellTiter-Glo® 2.0 Ready When You Are

Same high performance and sensitivity as the original CellTiter-Glo® Assay, now as a single reagent ready to use with storage stability at 4°C or room temperature. No mixing. No thawing. No waste.



Luciferin +
Ultra-Glo™ rLuciferase



Cellular ATP

To learn more and request
a **FREE SAMPLE**, visit:
www.promega.com/Glo2



Scan QR code
to directly
access the free
sample form.



There's only one **Science**

Science Careers Advertising

For full advertising details, go to ScienceCareers.org and click For Employers, or call one of our representatives.

Tracy Holmes

Worldwide Associate Director
Science Careers
Phone: +44 (0) 1223 326525

THE AMERICAS

E-mail: advertise@sciencecareers.org
Fax: 202 289 6742

Tina Burks

Phone: 202 326 6577

Nancy Toema

Phone: 202 326 6578

Marci Gallun

Sales Administrator
Phone: 202 326 6582

Online Job Posting Questions

Phone: 202 312 6375

EUROPE / INDIA / AUSTRALIA / NEW ZEALAND / REST OF WORLD

E-mail: ads@science-int.co.uk
Fax: +44 (0) 1223 326532

Axel Gesatzki

Phone: +44 (0) 1223 326529

Sarah Lelarge

Phone: +44 (0) 1223 326527

Kelly Grace

Phone: +44 (0) 1223 326528

JAPAN

Katsuyoshi Fukamizu (Tokyo)

E-mail: kfukamizu@aaas.org
Phone: +81 3 3219 5777

Hiroyuki Mashiki (Kyoto)

E-mail: hmashiki@aaas.org
Phone: +81 75 823 1109

CHINA / KOREA / SINGAPORE / TAIWAN / THAILAND

Ruolei Wu

Phone: +86 186 0082 9345
E-mail: rwu@aaas.org

All ads submitted for publication must comply with applicable U.S. and non-U.S. laws. *Science* reserves the right to refuse any advertisement at its sole discretion for any reason, including without limitation for offensive language or inappropriate content, and all advertising is subject to publisher approval. *Science* encourages our readers to alert us to any ads that they feel may be discriminatory or offensive.

Science Careers

FROM THE JOURNAL SCIENCE **MAAAS**

ScienceCareers.org



Cellular and Molecular Neuroscience Faculty Position

The Department of Integrative Physiology and Neuroscience (IPN) at Washington State University in Pullman, WA is seeking an outstanding academic scientist to fill a full-time, tenure-track faculty position in cellular and/or molecular neuroscience at the rank of Assistant/Associate/Full Professor. The position is a permanent 12-month appointment.

Requirements: Must have one of the following earned degrees: PhD in neuroscience or related biomedical discipline, MD, or DVM, and at least two years post-doctoral research experience. Ability to support and mentor graduate students and postdoctoral trainees is essential. Must be able to communicate effectively and work in a highly collegial and collaborative environment with a diverse population of colleagues and students.

Applicants for associate/full professor positions must have an established/active extramurally funded independent research program, and a record of peer-reviewed publications and national/international recognition commensurate with rank. Candidates considered for associate professor must have 6 years of experience or equivalent at the assistant professor rank. Candidates considered for full professor must have 6 years of experience or equivalent at the associate professor rank.

Applicants for an assistant professor position must have demonstrated potential to establish and maintain an externally funded faculty research program. The successful applicant will have a record of peer-reviewed publications and will be able to articulate an innovative agenda for their future research program in cellular/molecular neuroscience.

Duties: Maintain an innovative, extramurally funded research program in cellular/molecular neuroscience that can interface with current faculty scholarship in such areas as drug abuse, food intake/energy homeostasis, circadian rhythms/sleep, neurodevelopment, synaptic plasticity, neurodegenerative disease and/or affective neuroscience. Teaching in the graduate and/or undergraduate Programs in Neuroscience. Salary and rank will be commensurate with experience and qualifications. A competitive start-up package will be available, along with laboratory space in a newly completed, state-of-the-art research building specifically designed and equipped for neuroscience research. This facility includes behavioral, imaging and protein/genetic analysis in common equipment cores.

Washington State University has a vibrant neuroscience community plus the collaborative environment of a large research university, and is located in a region having a high quality of life with excellent access to outdoor activities and the arts.

Screening of applications will begin **March 9, 2015**. Applications must include a cover letter that states the rank being sought, a current curriculum vitae, a statement of research interests and goals, a description of teaching experience and/or philosophy, and the names and contact information (including email addresses) for three references. The application must be submitted online at www.wsujobs.com (job listing #42016). Direct questions to kinslow@vetmed.wsu.edu; <http://ipn.vetmed.wsu.edu/>

EEO/AA

Faculty Position in Immunology Department of Microbiology-Immunology Northwestern University Feinberg School of Medicine

A tenure-track position is open for a full-time faculty researcher (PhD, MD/PhD or MD) in Immunology. Areas of particular interest include immune regulation, lymphocyte activation and differentiation, and innate and adaptive immunity to microorganisms. Rank is open, and salary, start-up packages and lab space will be competitive. All applicants should have substantial peer-reviewed publications that demonstrate productivity and the ability to perform cutting edge research. Candidates for an Assistant Professor position should have postdoctoral research experience and current or pending external funding. Candidates seeking appointment at the Associate Professor or Full Professor level should have substantial research productivity, current grant support and academic service. Candidates should have an interest in teaching graduate and medical students. Starting date is negotiable.

Application materials will be reviewed as received, but to receive full consideration, should be received by **August 1, 2015**. Please send a complete CV, a one page research plan along with the name and contact information of at least three references by email to: immunologysearch@northwestern.edu.

Northwestern University is an Equal Opportunity, Affirmative Action Employer of all protected classes, including veterans and individuals with disabilities. Women and minorities are encouraged to apply. Hiring is contingent upon eligibility to work in the United States.



A Unique opportunity for Research Careers in Science & Technology in CSIR-IMTECH, INDIA

CSIR-INSTITUTE OF
MICROBIAL
TECHNOLOGY
CHANDIGARH, INDIA

Applications for Scientists positions are sought from Indian Nationals for R&D in various areas in Microbiology / Biotechnology / Synthetic Biology, etc.

**Applications' deadline is
12th March, 2015.**

(For details, see our website:
www.imtech.res.in)

ONLINE CAREER FAIR

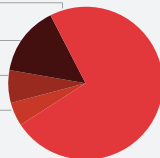
March 4, 2015 | 10:00 AM – 4 PM EST



Register now for this exciting virtual career fair and engage, screen, and recruit hundreds of targeted candidates.

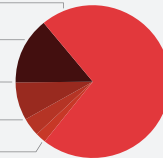
ATTENDEE DEMOGRAPHICS

Life Sciences – 75%
Physical Sciences – 15%
Health Sciences – 7%
Other – 5%



Field Experience

PhD – 71%
Masters – 14%
BA/BS – 8%
PhD/MD – 4%
Other – 2%



Degree Type

Over 3,000 pre-registrants; over 900 live participants

HOW THE EVENT WILL WORK

Employers receive a fully customized “booth” tailored to meet their recruiting needs. This landing page can include open positions, company information, testimonials and branding videos.

During the live event, candidates browse your booth and then choose to chat one-on-one. The conversations are timed to allow companies to meet as many candidates as possible.

- No travel or accommodation costs
- Get access to resumes to build your talent community
- Candidate information is displayed during the chat
- Powerful follow up tools to move top candidates through the hiring process
- Screen candidates with pre-qualifying questions to connect with the most relevant candidates

BENEFITS OF EXHIBITING

- Connect with candidates from the comfort of your own desk
- Showcase your employer brand online to your target audience

Book your booth today!

For more information, please visit:
ScienceCareers.org/onlinecareerfairemployers

SCIENCECAREERS.ORG

ScienceCareers

FROM THE JOURNAL SCIENCE 



Assistant, Associate or Full Professor in Biomedical Sciences

The Division of Biomedical Sciences within the School of Medicine at the University of California Riverside is seeking to hire two new faculty members at the rank of Assistant, Associate or Full Professor. We are looking for accomplished research scientists with expertise in physiology or molecular pharmacology as applied to biomedical research in pulmonary or renal disease, the microbiome, medical bacteriology or cancer (CNS or GI preferred). Preference will be given to those individuals examining the molecular mechanisms of human disease who are committed to a collaborative approach to research, and who are expert in their specific disease model.

The successful candidates will be appointed in the Division of Biomedical Sciences. The School of Medicine at UCR is the sixth University of California Medical School and serves the rapidly growing and dynamic Inland Southern California region by training a much-needed physician workforce and catalyzing innovations in research, education, and health care delivery that will improve the health of medically underserved populations. Laboratory and office space will be in the School of Medicine Research Building. Areas of research within the Division include diseases of epithelial biology, ion transport, signal transduction, mucosal immunology, host-pathogen interactions, vaccine development, neurodevelopmental disorders, neurodegeneration, neuroendocrinology and cancer biology. Particular strengths on the campus pertinent to this recruitment include genetics, epigenetics, genomics/bioinformatics, microRNAs, vector biology, bioengineering, nanotechnology, synthetic and analytic chemistry.

The Division of Biomedical Sciences sponsors an innovative Ph.D. program that integrates the core medical curriculum with biomedical sciences graduate training and research. The successful candidate will be expected to teach in the medical curriculum and actively participate in the Biomedical Sciences Ph.D. program. Preference will be given to candidates who indicate an ability to contribute to teaching in general areas of pharmacology, histology, pathology or physiology.

The University of California, Riverside is centrally located within Riverside and situated in an historic citrus growing area surrounded by mountain ranges. Riverside is about an hour away from ski slopes, surfing, or hiking in mountain or desert environments, and housing in the area is very affordable. The campus is also located in a prime position to take advantage of the other universities, research institutes, and biotech industries present in Southern California. Applicants must hold a Ph.D., M.D., Pharm D., or equivalent degree and qualify for a tenure track or tenured faculty appointment at the University of California. Applications will be reviewed beginning **March 1, 2015** and the positions will remain open until filled.

To Apply: Please submit the following items electronically through the APRecruit system: Cover Letter, Curriculum vitae, statement of research accomplishments and goals, statement of teaching expertise. Choose the appropriate link based on qualifications:

Assistant Professor - <https://aprecruit.ucr.edu/apply/JPF00304>

Associate/Full Professor - <https://aprecruit.ucr.edu/apply/JPF00303>

The University of California is an Equal Opportunity/Affirmative Action Employer. All qualified applicants will receive consideration of employment without regard to race, color, religion, sex, national origin, age, disability; protected veteran status, or any other characteristic protected by law.

Max-Planck-Institut für Biophysik



The Max Planck Institute of Biophysics invites expressions of interest and nominations for the position of

Director

We are looking for an outstanding scientist to lead a department and establish a world-leading research programme in the areas of (1) structure and mechanisms of membrane proteins or (2) advanced techniques in studying membrane proteins and biological membranes. We seek individuals with an international reputation and a proven track record in these areas who are capable of inspiring the research of junior scientists including graduate students, post-doctoral fellows and group leaders. Excellent resources will be provided in terms of laboratory infrastructure, equipment and running costs. The appointed individual will contribute to the scientific direction and management of the Institute (<http://www.biophys.mpg.de/en.html>) by working closely with the other three Directors. Qualified individuals of all nationalities will be considered.

Remuneration is internationally competitive and negotiable.

The Max Planck Society seeks to increase the number of women in areas where they are underrepresented and explicitly encourages the application and nomination of women. A new childcare facility is available on site. The Max Planck Society is committed to increasing the number of individuals with disabilities in its workforce and encourages applications and nominations of such qualified individuals.

Expressions of interest should include a full CV including a complete list of publications, a summary of research experience and a short description of future goals as a single PDF file. Written nominations must include a short description of the nominee's background and most significant scientific accomplishments.

Expressions of interest and nominations will be treated in strict confidence and should be sent by **31 March 2015** to Dr. Werner Kühlbrandt (Managing Director, assistant: Monika Hobrack, monika.hobrack@biophys.mpg.de).



University of Washington, Seattle Department of Pediatrics Seattle Children's Research Institute

The Center for Global Infectious Disease Research at the Seattle Children's Research Institute invites applications for a full-time faculty position as a Professor, Associate Professor, or Assistant Professor, without tenure, in the Department of Pediatrics, Division of Infectious Diseases, University of Washington.

Applicants should have a grant-supported research program that complements those of current faculty, whose research spans infection-associated cancers, mechanisms of pathogen persistence and virulence, novel cure strategies, immunopathogenesis, antibiotic resistance and pathogen diagnostics. Responsibilities of the position include maintaining an independent, extramurally-funded research program and teaching and mentoring graduate students, postdoctoral fellows, and junior faculty investigators. The successful candidate must have a PhD, MD, or MD/PhD (or foreign equivalent).

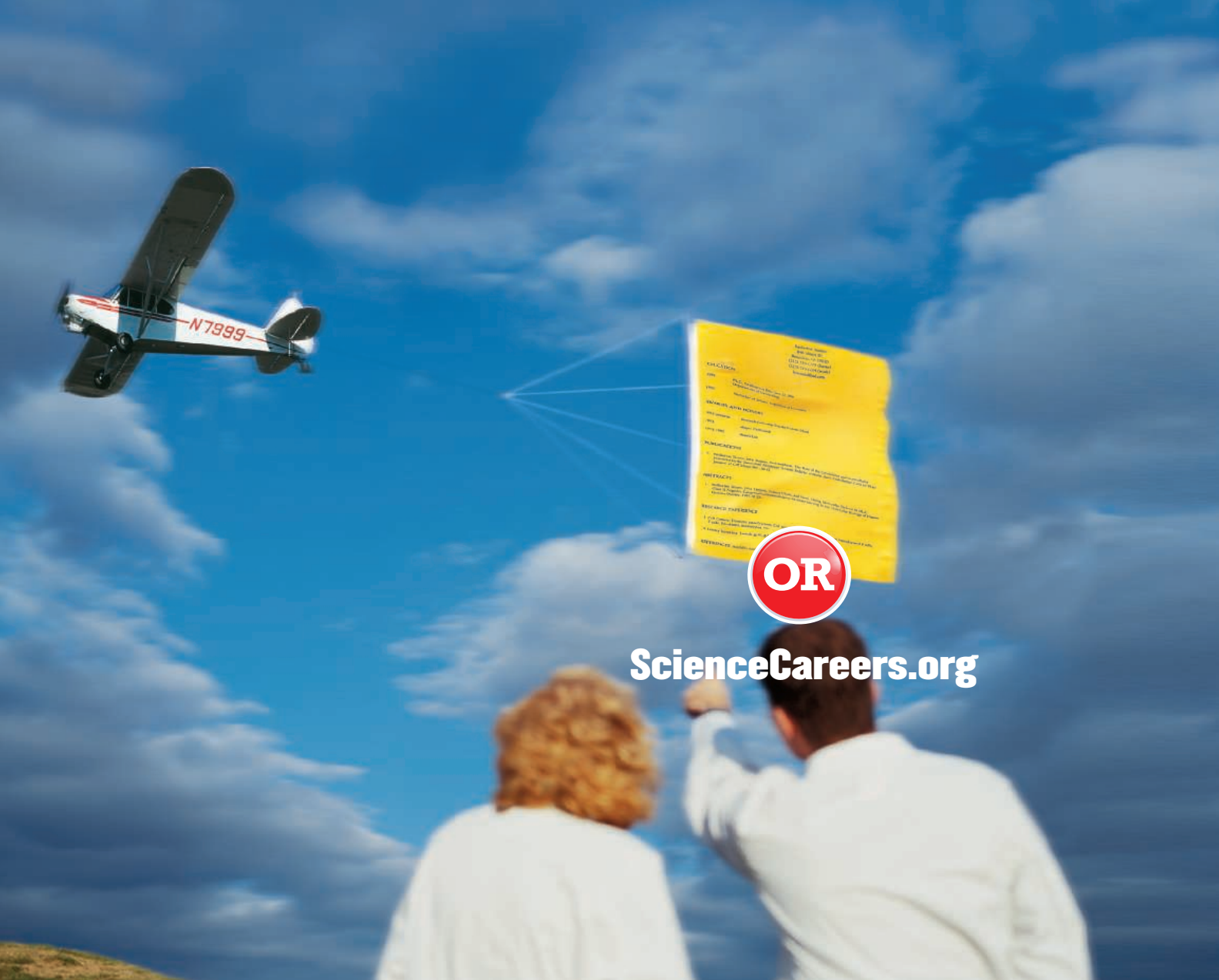
Please direct a letter of interest and curriculum vitae to: **Dr. Timothy Rose and Dr. Lisa Frenkel** at: CGIDRadmin@seattlechildrens.org, Seattle Children's Research Institute, 1900 Ninth Avenue, Seattle, WA 98101.

University of Washington faculty engage in teaching, research and service.

In order to be eligible for University sponsorship for an H-1B visa, graduates of foreign (non-U.S.) medical schools must show successful completion of all three steps of the U.S. Medical Licensing Exam (USMLE), or equivalent as determined by the Secretary of Health and Human Services. The University of Washington is an Affirmative Action and Equal Opportunity Employer. All qualified applicants will receive consideration for employment without regard to, among other things, race, religion, color, national origin, sex, age, status as protected veterans, or status as qualified individuals with disabilities.



Seattle Children's
HOSPITAL · RESEARCH · FOUNDATION



ScienceCareers.org

Learn more and bring your job search in for a smooth landing.

- Search thousands of job postings
- Create job alerts based on your criteria
- Get career advice from our Career Forum experts
- Download career advice articles and webinars
- Complete an individual development plan at “myIDP”

Target your job search using relevant resources on **ScienceCareers.org**.

ScienceCareers

FROM THE JOURNAL SCIENCE  AAAS

Science by any means necessary

As a child of mixed ancestry growing up 5 decades ago in the Harlem and Bronx neighborhoods of New York City, Erich Jarvis was immersed in the teachings of civil rights leaders. From Martin Luther King Jr., he took the precept to “love everybody, accept everybody.” Malcolm X inspired him to succeed “by any means necessary.” Both principles have served him well in science, says Jarvis, now a prominent neurobiologist. Jarvis is a natural collaborator and also an opportunist. “I try to accept any kind of tool or any type of technology that I need to use to answer my questions,” he says.

These days, the Duke University professor and Howard Hughes Medical Institute investigator studies the molecular mechanisms underlying the capacity for spoken language, a uniquely human trait. His work was featured prominently in the 12 December *Science* special issue. (You can read it at scim.ag/1v9GcNv.) It required an unusual collaboration with researchers studying a seemingly different topic: the evolution of birds.

Parrots, songbirds, and hummingbirds are among the few animals capable of imitating sounds they hear, a trait called vocal learning. Jarvis wanted to compare the genomes of vocal-learning birds with their non-vocal-learning evolutionary cousins. He first teamed up with Genome 10K, a project aiming to sequence the genomes for 10,000 vertebrate species, and when he heard about another parallel bird-sequencing project, he helped bring everyone together to create a coalition. “Some people say competition leads to greater advances, but I’ve found that coordinating, and forming collaborations and cooperating, actually works just as well if not better,” he says.

Jarvis took an indirect route to science. A student at New York City’s High School of Performing Arts, the setting for the 1980 movie *Fame*, he earned an audition with Alvin Ailey American Dance Theater, a prestigious modern dance company. He chose science instead. “My mother always taught me to do something that has a positive impact on the planet, and I felt I could do that better as a scientist than as a dancer,” he explains. “Science and dance are very similar to me. They both require discipline, creativity, invention, and lots of effort that in the end rewards you with something new.”

His undergraduate research at Hunter College produced six papers. “A lot of people were surprised that a person of



“My mother always taught me to do something that has a positive impact on the planet.”

color could do this,” he says. “I remember people telling me that directly; they weren’t shy about it.” He encountered similar sentiments in graduate school at Rockefeller University, where some implied he was only there because of a quota, he says. “I remember internalizing this feeling that I’m not as good as others here and that I don’t belong here.”

When the time came to apply for faculty jobs, “I felt like I suddenly became a commodity because of the successes I had, like I was being sought after almost like a basketball player.” Yet his minority status continues to present challenges. “Anything that has to do with any kind of diversity issue, I’m called upon because I’m an under-represented minority,” he says. “I am expected to hold two jobs. One is to be the best scientist I can be, like anybody else, and the other is

to cure society’s disease. ... I had to learn how to say ‘no’ to a lot of things in order for it to not take up my time and sink my science career.”

It’s not that he believes the issue is unimportant or solved. He says he could not have succeeded as a scientist without special programs and awards for minority researchers, “no matter how much talent I had.” He just wants more company—more researchers from underrepresented-minority backgrounds in faculty positions in the basic sciences, where they can “lead by example.” Science needs to be more visible as a career option, he says. “In my old neighborhoods, people haven’t heard the word Ph.D. that much. ... They say, ‘What’s a Ph.D.?’ ” ■

Rachel Bernstein is a staff writer for Science Careers. For more on life and careers, visit www.sciencereaders.org. Send your story to SciCareerEditor@aaas.org.